Magnetic Anisotropy Control in Rare Earth Iron Garnet Thin Films for Spintronic Devices and All-optical Ultrafast Manipulation of Magnetization

by

Saeedeh Mokarian Zanjani

A Dissertation Submitted to
the Graduate School of Sciences and Engineering
in Partial Fulfillment of the Requirements for
the Degree of
Doctor of Philosophy
in

Materials Science and Engineering

KOÇ ÜNİVERSİTESİ

July, 2021

Magnetic Anisotropy Control in Rare Earth Iron Garnet Thin Films for Spintronic Devices
and
All-optical Ultrafast Manipulation of Magnetization

Koç University

Graduate School of Sciences and Engineering

This is to certify that I have examined this copy of a doctoral dissertation by

Saeedeh Mokarian Zanjani

and have found that it is complete and satisfactory in all respects, and that any and all revisions required by the final examining committee have been made.

Committee Members:

Assist. Prof. Mehmet Cengiz Onbaşlı (Advisor)

Prof. Özgür Müstecaplıoğlu

Asst. Prof. Safacan Kölemen

Assoc. Prof. Eyüp Duman

Assoc. Prof. Emre Erdem

Date: 06/07/2021

I dedicate this Ph.D. thesis to my beloved parents…and to my amazing husband, Sadra, my wings to fly…

ABSTRACT
Magnetic Anisotropy Control in Rare Earth Iron Garnet Thin Films for Spintronic Devices and All-optical Ultrafast Manipulation of Magnetization

PhD thesis

Saeedeh Mokarian Zanjani
Ph.D. in Material Science and Engineering
Supervisor: Asst. Prof. Dr. Mehmet Cengiz Onbaşlı
July 2021

Spin-based memory and logic devices might provide a promising route for fast, nonvolatile and power-efficient operation using magnetic insulators with minimal Joule heating and ultrafast spin dynamics, which can be controlled all optically. There are very few magnetic insulator iron garnets, whose magnetic properties cannot be tuned easily and limit spintronic device applications. Thus, new iron garnets with perpendicular magnetic anisotropy and low saturation fields are needed for ultra-low power spintronics. In this thesis, we present theory, modelling and experimental studies on controlling magnetic anisotropy in epitaxial iron garnet thin films and all-optical control of magnetization dynamics in quantum-confined metallic nanolayers.

First, we developed an anisotropy model for describing the magnetic anisotropy characteristics of insulating rare earth iron garnet (REIG) films ($Re_3Fe_5O_{12}$, Re; rare-earth ions Y, Tm, Dy, Ho, Er, Yb, Tb, Gd, Sm, Eu). We construct an effective anisotropy energy using shape, magnetocrystalline, and magnetoelastic terms for ten different REIG films grown epitaxially and lattice-matched on five commercially-available garnet substrates. We calculated their magnetic easy axes and predict that 20 different pairs out of 50 to possess out-of-plane magnetic easy axis (PMA). Only 7 of them were experimentally tested and confirmed. We predict that the magnetic saturation fields of PMA garnets could span two orders of magnitude (300 Oe to 12.6 T), significantly expanding the available PMA garnet class. To test our predictions, we grew 420 and 67 nm-thick Holmium iron garnet films on $Gd_3Ga_5O_{12}$ and $Tb_3Ga_5O_{12}$ substrates using pulsed laser deposition at 800°C and 650°C. X-ray diffraction and magnetic hysteresis loop measurements indicate phase purity and PMA, respectively, for 67 nm HoIG, confirming our prediction.

Using a modified microscopic three temperature model, we investigate the effect of laser pulse parameters and magnetic elemental metal thin film properties on the femto- and picosecond magnetization dynamics. We model the coupled energy transfer between electrons, phonons and spin baths. A magnetization quenching (in sub-200 fs) and recovery (a few ps) was found for metals with high Curie temperature (Fe, Co, and Ni). In the quantum-confined thickness regime ($t < 50$ Å), spin-phonon scattering in magnetic metals are significantly reduced due to the reduced density of states. Thus, THz spin wave emission might become feasible with three orders of magnitude lower laser fluence compared with the previously reported experimental values.

Our models and experiments could expand the available PMA iron garnets with minimal Joule heating for spintronics and help control ultrafast spin dynamics much more efficiently.

ÖZETÇE

Spintronik Uygulamaları için Nadir Toprak Demir Garnet İnce Filmlerde Manyetik Anizotropi Kontrolü ve Tam Optik Ultra Hızlı Manyetizma Kontrolü

Doktora tezi

Saeedeh Mokarian Zanjani
Malzeme Bilimi ve Mühendisliği Doktora
Tez Yöneticisi: Dr. Mehmet Cengiz Onbaşlı
Temmuz 2021

Spine dayalı bellek ve mantık devreleri; Joule ısınmasını azaltan manyetik yalıtkanlar ve ultrahızlı spin dinamikleri sayesinde hızlı, kalıcı ve verimli çalışabilme potansiyelini içermektedir. Manyetik yalıtkan demir garnetlerden çok az sayıda bulunmaktadır ve bunların manyetik özelliklerinin kolayca ayarlanamamaları nedeniyle spintronik aygıt uygulamaları kısıtlanmaktadır. Bu nedenle, düşük güç tüketimli spintronik uygulamaları için düşey manyetik eşyönsüzlüğe ve manyetik doyum alanına sahip yeni demir garnet filmlerin geliştirilmesi gerekmektedir. Bu tezde, kuramsal, modelleme ve deneysel çalışmalarla epitaksiyel demir garnet ince filmlerin manyetik eşyönsüzlüklerin kontrolü ve kuantum sınırlandırmalı metalik nanokatmanlarda tam optik manyetizma dinamiklerinin kontrolü sunulmaktadır.

İlk olarak, yalıtkan nadir toprak demir garnet (REIG) filmlerinin ($Re_3Fe_5O_{12}$, Re; nadir toprak iyonları Y, Tm, Dy, Ho, Er, Yb, Tb, Gd, Sm, Eu) manyetik anizotropi özelliklerini tanımlamak için bir anizotropi modeli geliştirdik. Beş garnet alttaşı üzerinde örgüleri uyumlu ve epitaksiyel olarak büyütülecek on farklı REIG filmi için şekil, manyetokristal ve manyetoelastik terimlerini kullanarak efektik manyetik anizotropi fonksiyonunu hesapladık. Manyetik kolay eksenlerinin 50 film/alttaş çiftinden yirmisinin düzleme dik manyetik kolay eksene (PMA) sahip olacağını tespit ettik. Bunlardan sadece 7 tanesi deneysel olarak bugüne kadar test edilmiş ve doğrulanmıştır. PMA garnetlerinin manyetik doygunluk alanlarının neredeyse 100 kat aralığı kapsayabileceğini (300 Oe ilâ 12.6 T) ve mevcut PMA garnet sınıfını önemli ölçüde genişleteceğini öngörmekteyiz. Öngörülerimizi test etmek için 800°C ve 650°C'de darbeli lazer biriktirme kullanarak $Gd_3Ga_5O_{12}$ ve $Tb_3Ga_5O_{12}$ alttaşlar üzerinde 420 ve 67 nm kalınlığında Holmium demir garnet filmleri büyüttük. X-ışını girişimi ve manyetik histerezis (ardılizlem) ölçümleri,

67 nm HoIG için faz saflığını ve PMA'yı göstermektedir ve modellerimizdeki öngörümüzü doğrulamaktadır.

Güncellenmiş mikroskopik üç sıcaklık modelini kullanarak lazer darbe parametrelerinin ve manyetik elemental metal ince film özelliklerinin femto- ve pikosaniye manyetizasyon dinamikleri üzerindeki etkisini sistematik olarak inceledik. Elektron, fonon ve spin banyoları arasındaki enerji transferini modelledik. Yüksek Curie sıcaklığına sahip metaller (Fe, Co ve Ni) için bir manyetizasyon inişi (ilk 200 fs) ve geri kazanımı (sonraki birkaç ps) olacağı öngörülmektedir. Kuantumla sınırlandırılmış kalınlık rejiminde ($t < 50$ Å), manyetik metallerdeki spin-fonon saçılmasının, durum yoğunluğunun azalması nedeniyle önemli ölçüde azalabileceği öngörmekteyiz. Bu nedenle, THz spin dalgası üretiminin, daha önce bildirilen deneysel değerlerle karşılaştırıldığında, yaklaşık bin kata kadar daha düşük lazer akısı ile uygulanabilir hâle gelebileceği tespit edilmiştir.

Modellerimiz ve deneylerimizin, spintronik uygulamalar için asgari Joule ısınması gösteren PMA demir garnet sınıfını genişleteceğini ve ultra hızlı manyetizma dinamiklerini çok daha verimli bir şekilde kontrol etmeye yardımcı olabileceğini öngörmekteyiz.

ACKNOWLEDGMENTS

During my Ph.D. studies at Koç University, I had the chance to work with numerous talented people in a productive and fun environment. My family members, advisors, professors, colleagues, and friends each had their unique and undeniable impact on this thesis.

First, my sincere gratitude goes to Prof. Mehmet Cengiz Onbaşlı for being not only my thesis advisor but at the same time a great and caring consultant in all aspects, who always boosted my motivation during the times I got cold feet. His superior knowledge, great patience and understanding, positive and friendly character, valuable guidance, limitless motivation and encouragement, and endless support always pushed me towards more success and recognition. It was and always will be my great honor to be one of his first Ph.D. students. I will never forget his endless efforts to improve my academic levels along with strengthening my personality. I learned so much from him and I owe him many thanks.

I am unexplainably grateful to my intelligent, caring, and kind husband, Dr. Sadra Sadeghi, for his unconditional support and love, for eight years in all happiness and sadness. He never stopped standing by my side and supporting me to be a successful, independent, and strong woman with his hardworking, understanding, patience, and high spirit. He was one of the first motivating people for me to pursue my Ph.D. studies tirelessly with his helpful advice, academic success, and endless consensus. I could never thank him enough for his undeniable role in my graduate studies. This journey has been much easier to go through with his presence.

My appreciation also extends to my beloved parents, who have done more than their bests to support me mentally, financially, and spiritually; I can never put a price on their sacrifices and efforts. I am also thankful to my elder sisters and brother for always taking care of me as their little sister, even from far beyond the geographic borders. I am always inspired by them to aim big and work hard with conscientiousness.

I would like to sincerely thank Prof. Özgür Müstecaplıoğlu for his significant scientific contribution and helpful discussions, which led to the composition and submission of one of my best studies in Ph.D. I am grateful to him and Prof. Safacan Köleman and also Prof. Alper Uzun for helpful scientific discussions as my thesis committee members. I would

like to also thank Prof. Emre Erdem and Prof. Eyüp Duman for giving me the honor to be my thesis committee members for helpful suggestions and useful comments to improve my thesis.

I would like to appreciate Mr. Mohammadreza Alipour Sormoli for his assistance in my analytical calculations. I appreciate the valuable help from Dr. Amir Motallebzadeh, Dr. Hadi Jahangiri, Ms. Dilara Arıbuğa, and all of the members at Koç University Surface Science and Technology Center (KUYTAM) and Koç University Boron and Advanced Materials Application and Research Center (KUBAM), who significantly assisted me for my measurements and characterizations. I owe many thanks to the professors, researchers, students, and staff in the Graduate School of Materials Science and Engineering, Department of Physics, Department of Chemical and Biological Engineering, Department of Electrical and Electronics Engineering, and Department of Mechanical Engineering at Koç University.

Finally, I would like to acknowledge the generous financial support from the Graduate School of Science and Engineering at Koç University, the Scientific and Technological Research Council of Turkey (TÜBİTAK) (grant no. 117F416, and 120F230), and European Research Council (ERC) starting project SKYNOLIMIT (Grant No. 948063).

TABLE OF CONTENTS

LIST OF TABLES

LIST OF FIGURES

ABBREVIATIONS

ICT	Information communication technology
IC	Integrated circuit
DRAM	Dynamic random access memory
HDD	Hard disk drive
MRAM	Magnetic random access memory
GMR	Giant magnetoresistance
IMA	In-plane magnetic anisotropy
PMA	Perpendicular magnetic anisotropy
REIG	Rare earth iron garnet
PLD	Pulsed laser deposition
LPE	Liquid phase epitaxy
CVD	Chemical vapor deposition
VSM	Vibrating sample magnetometer
FMR	Ferromagnetic resonance
SEM	Scanning electron microscopy
HRXRD	High resolution X-ray diffraction
HAADF-TEM	High angle annular dark field transmission electron microscopy
HRXRR	High resolution X-ray reflectometry
XPS	X-ray photoelectron spectroscopy
AFM	Atomic force microscopy
MA	Magnetic anisotropy
EA	Easy axis
IP	In-plane
OP	Out-of-plane
ME	Magnetoelastic
YIG	Yttrium iron garnet
TmIG	Thulium iron garnet
DyIG	Dysprosium iron garnet
HoIG	Holmium iron garnet

ErIG	Erbium iron garnet
YbIG	Ytterbium iron garnet
TbIG	Terbium iron garnet
SmIG	Samarium iron garnet
EuIG	Europium iron garnet
GdIG	Gadolinium iron garnet
GGG	Gadolinium gallium garnet
SGGG	substituted-Gadolinium gallium garnet
TGG	Terbium gallium garnet
NGG	Neodymium gallium garnet
YAG	Yttrium aluminum garnet
SOI	Silicon on insulator
SOT	Spin-orbit-torque
MO	Magneto-optical
SHE	Spin-Hall effect
AO	All-optical
T_C	Curie temperature
RT	Room temperature
M3TM	Microscopic three temperature model
3TM	Three Temperature Model
LLB	Landau-Liftshitz-Bloch
THz	Terahertz
FWHM	Full width at half maximum
fs	Femtosecond
ps	Picosecond
nm	Nanometer
FEM	Free electron model
DOS	Density of states

Chapter 1

INTRODUCTION

1.1 Today's conventional electronics devices and the emergence of the spintronics

Information communication technologies (ICT), in the electronics devices such as smart phone, computers, memories and storage devices, music players, is one of the most important issues of the decade [1]. These devices have two separate parts: hard disk memory as permanent data storage unit and microprocessors and MRAM as semiconductor integrated circuits (IC) [2, 3]. These circuits consist of millions of electronic components such as diodes, capacitors, transistors, resistors, etc. [4], while the data storage unit consists of magnetic medium[5]. The information is processed in microprocessor and MRAM based on binary (0 and 1) system [6]. Every single bit needs one transistor and one capacitor (1 memory cell), which means that for a large data process and storage, billions of transistors and capacitors are required [7].Therefore, increasing the capacity, speed, and the efficiency of the storage devices relies on the number of transistors used in the devices. Based on Moore's law the number of transistors in the ICs doubles each 2-year, the number of which in 2019 is 39.54 Billions of transistors with 7 nm in size fabricated by (Taiwan Semiconductor Manufacturing Company) (Figure 1.1).

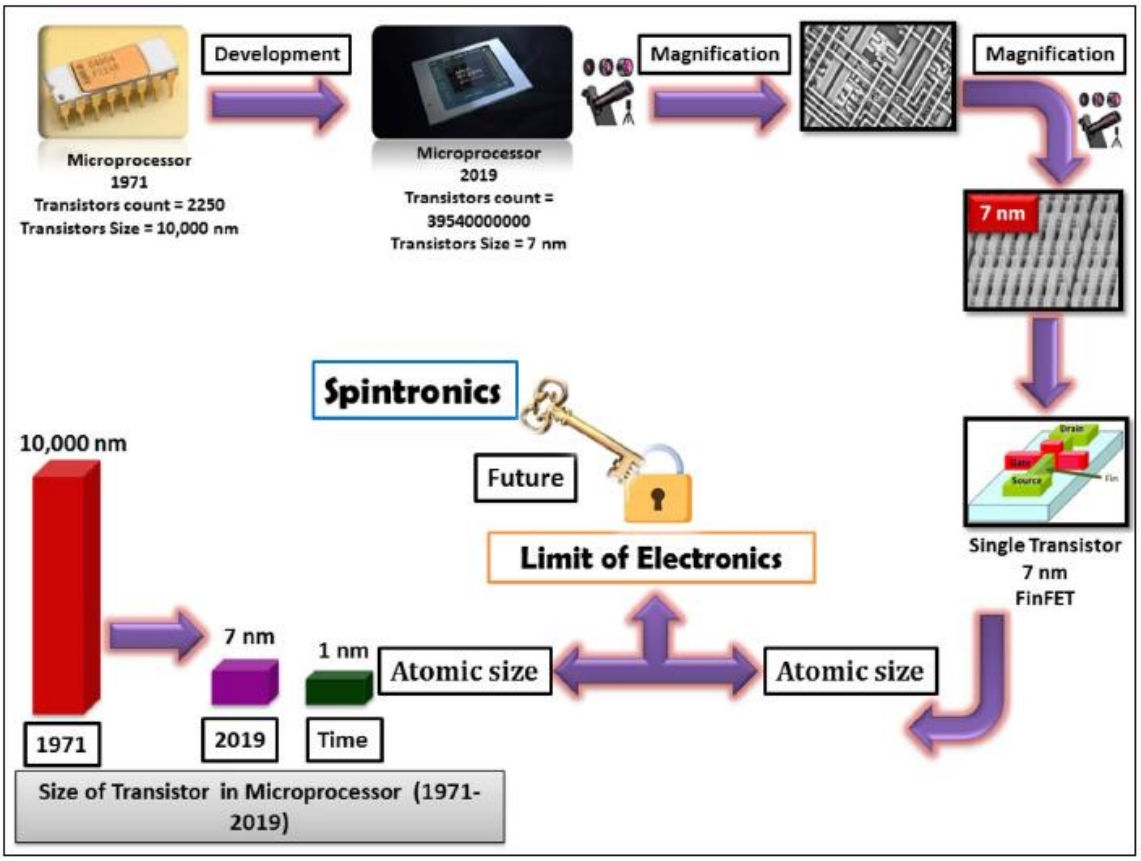

Figure 1.1: Evolution of number of transistors from 1971 to 2019, and limitation of charge-based devices [1].

Decreasing the transistor size is predicted to reach the atomic size which is not possible to fabricate, and the writing and processing will become challenging due to the heat dissipation in case the effect of quantum confinement effect (<10 nm) [8-10]. Therefore, the development of charge based electronic devices will be terminated in near future [11]. Figure 1.2 shows the charge-based devices development with size reduction in transistors of ICs.

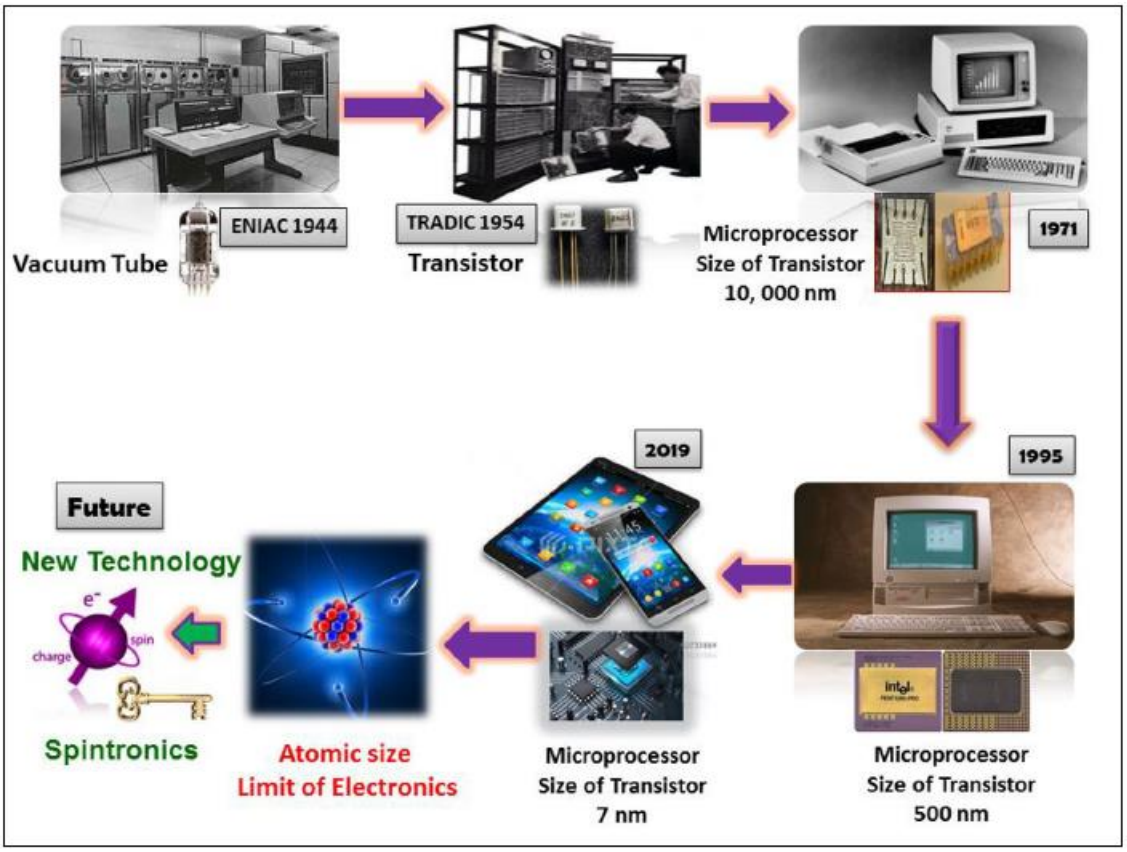

Figure 1.2: The size reduction in transistors of ICs in the developed charge-based [1].

The emerging field of spintronics is a solution to the abovementioned major problem in the conventional electronic storage and computational devices, which use the charge of the electron for their operations [12-14]. Spintronics uses the spin of electron in addition to the electron charge to carry and store the information in 0 and 1 binary form [15]. Another problem with the semiconductor based digital information storage such as dynamic random access memory (DRAM) is that despite its faster read/write operation compared to hard disk drives (HDD), it is a volatile memory, such that when the power is off, it results in the charge leakage in the capacitor of the memory and the information is endurance is limited [16]. But computers with magnetic random access memory (MRAM) operating based on the spintronics technologies are non-volatile and reliable and these components use electronic spins to store information [8, 17].

Drastic increase in the data storage and generation is ever increasing, while the size of the memory devices have been reduced, for a facile data carrying in the computers and cell phones. With the discovery of giant magneto resistance (GMR) in the late 1980's [18, 19], the critical breakthrough of the spintronics was developed by professor Albert Fert and Peter Grünberg who won the physics Nobel prize in 2007 [20, 21]. Two ferromagnetic

(FM) layers with localized spins are separated by another non-magnetic layer, through which the digital binary (0 and 1) information is recorded as the result of the magnetization of the spins in FM and electronic conduction [16]. Apple was the first technological incorporation which developed the iPod device based on the use of GMR [22].

The field of spintronics combined the charge based ICs with the spin based magnetic media on a single chip (Figure 1.3).

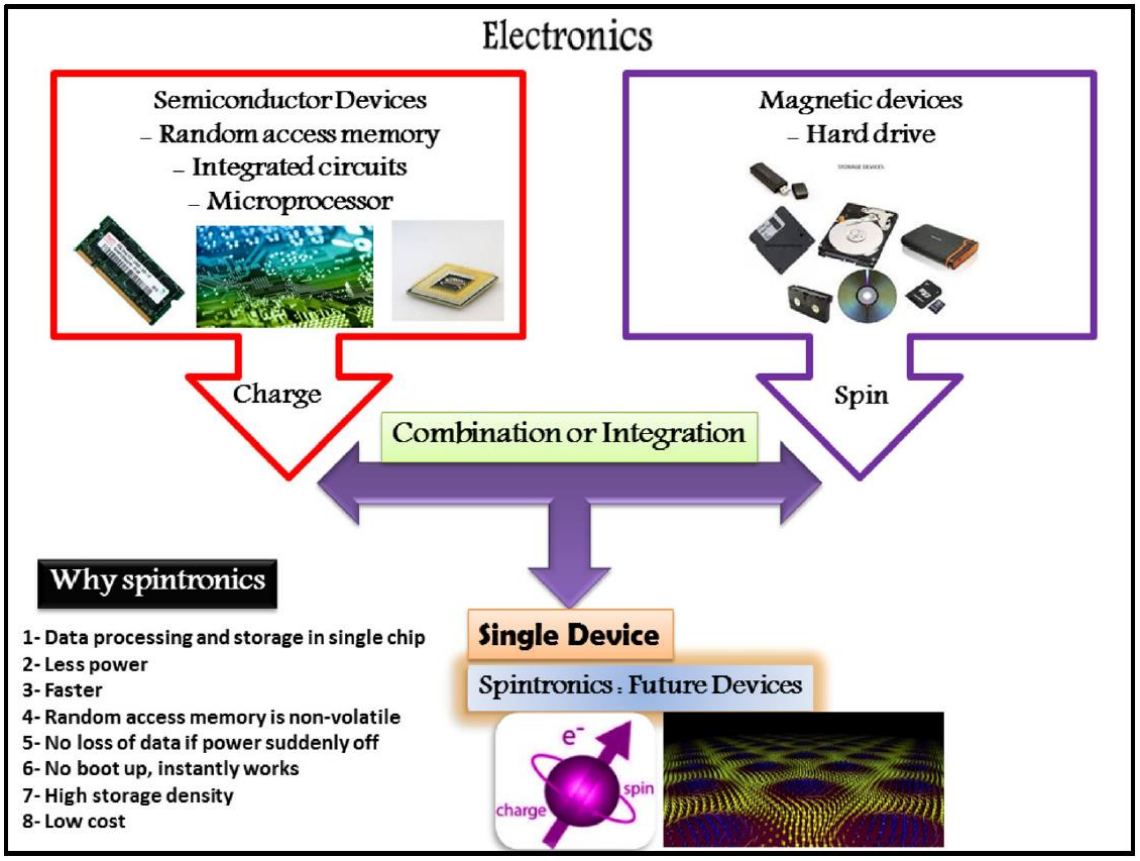

Figure 1.3: Integrated circuits combined with magnetic medium (hard disk) [1].

1.2 Spintronics for fast, energy efficient, and non-volatile memory and recording

Moreover, increasing the capacity of the data storage causes a considerable energy consumption. For example in 2010 online cloud and information sharing consume an estimably 1-1.5% of the total global electricity [23, 24], and is predicted to increase up to 3-13% in 2030 [25]. Consequently, novel materials and methods in the spintronics field are required to be developed for more energy efficient data storage and transfer. Different high endurance and non-volatile mechanisms of magnetic memories in spintronics such as Spin-Hall effect (SHE), spin diffusion in plane magnetic anisotropy (SD-IMA),

magneto electric effect (ME), spin diffusion and spin transfer torque perpendicular magnetic anisotropy (SD-PMA and STT-PMA), and domain wall (DW) motion have various speed and energy cost based on their underlying mechanisms. Figure 1.4 compares the various spintronic memory mechanisms based on the energy and time consumption. Current driven mechanisms based on spin diffusion perpendicular magnetic anisotropy are more low energy cost and faster compared to the IMA [16]. Despite the other current driven mechanisms which operate based on a torques generated by current, voltage driven ME works based on charging a capacitor and consumes the least writing energy; nevertheless, it is slower than PMA based current generated torque mechanisms. The desired memory performance is shown by star in the Figure 1.4.

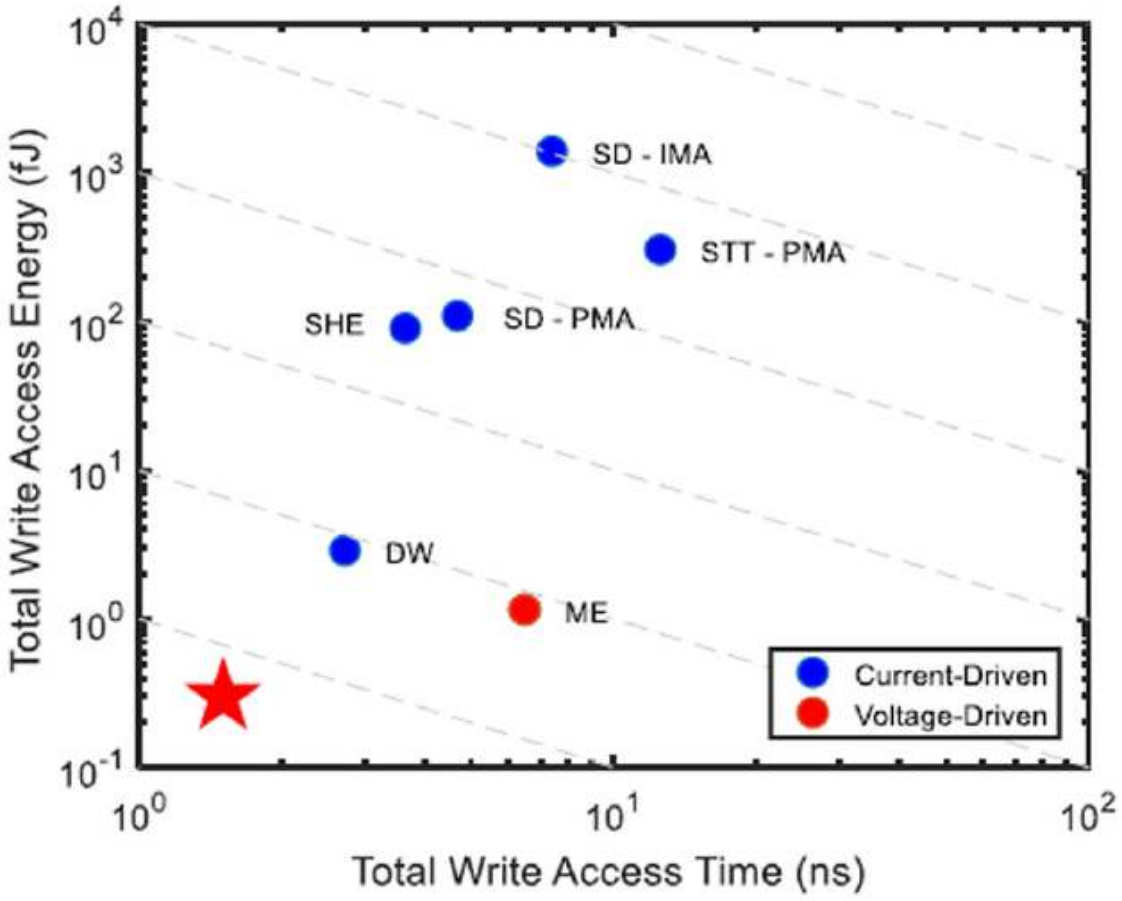

Figure 1.4: Comparison between the various mechanism of spintronic memories, from the energy and time consumption point of view [16, 26].

Among the mechanisms, only spin transfer torque (STT) memories have found their way in the commercial world, while the others are at the research stage. Most of the research on magnetic memories have been done on magnetic tunnel junctions (MTJ) [27, 28]. For magnetic data writing magnetization is needed to be switched in MTJ by which spin-

polarized current penetrates through an oxide barrier in between two ferromagnetic layer via STT [29, 30]. The first MTJ with high stability and scalability by perpendicularly aligned ferromagnetic layers (PMA), was achieved in 2010 [31]. The drawback of the STT-MTJ is the need of a response time for beginning of the writing which slows the memory writing down to 10 ns, and consequently the operating power is lowered. The solution was performing the spin switching in PMA layers by the spin conversion or spin orbit torque, instead of spin transfer torque [32-34]. The spin conversion using spin Hall Effect (SHE) has been experimentally demonstrated in various materials such as topological insulators [35, 36], and magnetic heterostructures (i.e. TmIG/Pt) using heavy metals like Pt, Ta, W [37].

1.3 Perpendicular magnetic anisotropy in spintronics

Numerous spintronic applications necessitate the use of layers with perpendicular magnetic anisotropy (PMA). These applications include memory, spin-orbit torque switching, and logic devices. Iron garnets, which have reduced Gilbert damping, low and tunable saturation magnetization, lower exchange constants than magnetic metals, are magnetic insulators which may help reduce the power consumption, extend operation bandwidth and be a part of spintronic memory and logic devices using spin-orbit torques. Not many PMA garnets have so far been experimentally demonstrated or reported. Some demonstrated cases are samarium, thulium and terbium iron garnet [38-40]. In order to be able to study novel phenomena with low damping, high spin Hall angles, low or tunable saturation fields, switching on silicon-based substrates, high frequency switching, control of magnetism near compensation temperatures, enhanced magnetotransport characteristics with topological protection, more PMA garnets are required.

Researchers have been able to investigate a wide variety of spin wave phenomena and magnetization switching thanks to the development of sputtering and pulsed laser deposition of high-quality iron garnet thin films with ultralow Gilbert damping [41-43]. Sputtering and pulsed laser deposition have developed the growth of magnetic iron garnet thin films with high quality and reduced Gilbert damping. Therefore, it has provided the opportunity for researchers to study an extensive range of novel spin wave phenomena and magnetization switching [41-43]. YIG (Yttrium iron garnet, $Y_3Fe_5O_{12}$) is one of the most extensively studied REIG for such applications [44]. YIG's very low Gilbert damping allows on-chip propagation of spin waves up to millimeters for multi-GHz spin wave excitations. However, the magnetization easy axis of YIG is parallel to the film

plane; so, they cannot be used in various spin mechanisms like Rashba-Edelstein effect, spin-orbit torques, forward volume magnetostatic spin waves, and logic devices [41]. On the other hand, PMA is a necessary condition for fast and reliable response in spin-orbit torque switching using low current densities [33]. In addition, the Dzyaloshinskii–Moriya interaction (DMI) in thulium iron garnet grown on GGG substrate enables the skyrmions stabilization and skyrmion motion by spin currents [45]. The ability to stabilize topologically-protected chiral spin structures or skyrmions, along PMA garnet/non-magnetic heavy metal interfaces and potentially along other magnetic iron garnet/2D metallic interfaces opens up significant opportunities for spintronic logic, memory and sensing devices. As a result, the range of PMA iron garnets with tunable magnetic characteristics (saturation moment, exchange constant, uniaxial and magnetoelastic anisotropy, DMI constant) need to be significantly extended.

In order to tune the magnetic anisotropy for PMA in magnetic insulating thin films numerous studies have been conducted [38, 46-50]. Insulating magnetic iron garnets with their tunable magnetic properties have appealed a wide interest [51-53]. Their reduced damping and high magneto-optical Faraday rotation make them significant candidates among the materials investigated. Engineering the magnetic anisotropy terms is a method of obtaining a total effective magnetic field with out-of-plane magnetic easy axis. Magnetic anisotropy energy is defined as the angle-dependent effective magnetization energy density which includes shape, strain-induced and magnetocrystalline anisotropy contributions. Thermodynamic energy minimization dictates that the total energy of a magnetic material is minimized by relaxation of magnetization vector orientation along its lowest energy axis when there is no external magnetic field. Magnetic easy axis is defined as the real-space spin orientation along which a magnetic material minimizes its total effective magnetic energy (or effective magnetic field). Magnetization switching rates and the stability of total magnetization vector are derived by this energy minimization. By tuning the magnetic anisotropy in REIG thin films the researchers in the field of spintronic could test novel switching phenomena based on PMA. In addition, the study of ultrafast spin dynamics and magnetic response in thin films and nanostructures which is driven by magnetic anisotropy become feasible.

In this thesis, we report twenty new iron garnet film-substrate pairs which exhibit PMA. We calculated the total anisotropy energies of ten different stoichiometric rare-earth iron garnet thin films when they are grown lattice-matched on five different garnet substrates.

The parameters that determine the PMA state of the magnetic iron garnet are compressive or tensile strain states, which depend on the substrate choice, magnetostriction constants value and their signs. We provide the conditions for obtaining PMA in magnetic rare earth iron garnet films. PMA iron garnet thin films with different saturation moments could help develop magnonic devices and spin-orbit torque memory elements.

The unique properties of garnets enable spintronic devices based on pure spin currents or spin wave transport including:

1. **Spin wave excitation and detection:** Spin Seebeck effect [54], spin Hall effect [41], spin injection, spin torque oscillators [55, 56] are major applications. Excellent reviews [57] cover this subject comprehensively.
2. **Efficient on-chip magnon transport:** Spin transport across long distances on-chip (many wave vectors) [58] and over magnonic crystals [42] are promising for integrated logic devices.
3. **Magnetooptical devices**: Optical isolators and circulators using low-loss garnets [59] allow investigating nonreciprocal band structures as well as integrating with lasers for telecommunication applications.
4. **Ultrafast spintronics:** Generation and control of multi-GHz and terahertz spin-waves [60] using femtosecond (fs) laser pulses are interesting for THz range communications. Using fs laser pulses, one can trigger ultrafast spin and electron transport with sub-picosecond rise times.

   Room temperature compensated ferrimagnetic garnets, like DyIG and GdIG [54], are one of the emerging materials for ultrafast spintronics. These garnets have magnetic compensation at room temperature. Compensated or antiferromagnetic behavior in garnets could allow for sub-picosecond spin transport mediated through exchange interactions.
5. **2D spintronics**: Giant spin-orbit torques (SOT) are generated and spin-polarized currents are injected from a non-magnetic 2D material to a magnetic garnet, like YIG. In this case, large charge-to-spin conversion efficiencies could be observed [61].
6. **Integrating garnets on silicon platforms:** Integrating garnets on silicon is useful for technological applications such as magnetooptical isolators on silicon photonics and magnonic logic gates and memory addressable with CMOS. Optical isolators are nonreciprocal silicon photonic components developed for protecting

telecommunication lasers on chip. Breaking time-reversal symmetry in these components is achieved by using magnetooptical iron garnets with high figure-of-merit (high Faraday rotation degree per dB optical loss) on silicon resonators. Integrated magnonic logic gates use silicon CMOS transistors for spin injection and readout of magnon signals propagating in garnets on silicon. In both cases, structural, magnetic, optical and magnetotransport properties of garnet on silicon become critical for device performance. Growing garnets on silicon resonators or transistors is challenging due to the thermal expansion and lattice parameter mismatch between these materials. Due to their large unit cell volumes, garnets also have large formation enthalpy, which necessitates crystallizing garnets only using large thermal budget. As a result, the final optical isolator chip or magnonic circuit undergoes cracking and exhibits enhanced optical loss or enhanced Gilbert damping. Either optimized monolithic growth [62] or wafer bonding of garnet on silicon [63] would be necessary to solve this problem.

Epitaxial holmium iron garnet (HoIG) as a REIG thin film which was not extensively explored previously for spintronics, is a promising candidate for such applications including PMA-based [64, 65] SOT and tunable saturation field, high magnetooptical response [46] low temperature quantum spintronics (due to its low compensation point, 120 K) [66], chemotherapy and cancer radiotherapy [67] and multiferroicity [68] the potential use of which is to miniaturize the electronic components [69-71].

Coupling between magnetic and electric orders is called magneto electric (ME) effect. This effect enables the control of magnetic order by magnetic field (direct ME effect), or electric field (converse ME effect) [72, 73] for data storage devices, piezoelectric device controlled by magnetization, actuators, sensors and detectors with high sensitivity to magnetic field, microwave phase shifters, and magnetic memories [74-76]. Ferrimagnetic REIG (RE: Ho, Dy, Tb, Er) have shown low magnetic field room temperature magnetodielectric coupling [77, 78]. Based on our systematic modelling and calculation results of magnetic anisotropy control in REIG thin films, HoIG with perpendicular magnetic anisotropy on GGG and TGG substrates, was chosen to be grown on and characterized on four different substrates including GGG, TGG, Si, and SOI. The lack of experimentally studied PMA garnets in spintronics highlights the need for more and novel garnet single crystalline thin films with higher structural and magnetic qualities for both spintronic device applications and integrated spintronics for CMOS devices.

1.4 Ultrafast control of magnetization in quantum confined metallic nanolayers

While PMA garnets are useful and needed for fast spin-orbit torque switching and other spintronic applications, magnetic metals may also provide significant opportunities for ultrafast control of magnetization [79]. To probe the temporal and energy limits of magnetization switching, Heisenberg exchange, longer-range dipolar spin interactions, magnon-phonon, spin-phonon or spin-spin scattering as well as for increasing memory speed and computation, femtosecond lasers have been used by pumping and probing the spin transport characteristics of magnetic materials.

All-optical control of magnetization using femtosecond pulses is a challenge in spintronics [80] to reduce switching times and energies. Femtosecond (fs) laser pulses allow for ultrafast control of magnetization at picosecond timescales [79]. In these experiments, fs lasers could be used for triggering magnetization reversal or spin waves or these lasers could be used for probing ultrafast magnetization switching driven by other means, such as ps electric pulses in nm-thick ferromagnetic metallic thin films [81]. In these probing experiments, the ultrafast manipulation of the magnetization is monitored due to the spin-orbit torques which is induced by change of magnetic anisotropy after interaction with the effective field of the femtosecond laser pulse. Low energy and picosecond control and switching of magnetization was achieved [33]. In our study, we theoretically show that by exposing magnetized films with femtosecond laser pulses only, one can manipulate magnetization with three orders of magnitude lower energies than in bulk-like magnetic metallic thin films in fs to ps timescale.

Optical control of ferromagnetic order at femtosecond timescales have attracted considerable interest among the spintronics researchers [82, 83]. At these non-equilibrium fs regimes, magnetization quenching and also magnetization switching by a single fs laser pulse were shown to be feasible [84, 85]. These pulses lead to spin current generation which can propagate through the device in several tens of nanometers, which opens a novel window in the femto-magnetism and terahertz (THz) spintronic phenomena. In previous experiments, fs laser pulse-induced spin-transfer torques (STT) were found to generate spin currents. These THz spin wave currents were absorbed in a few nanometers [86, 87]. In layered ferrimagnetic metallic structures, so called ‘on-the-fly” magnetic bits were written by fs laser pulses and transported with a DC charge current. These experiments demonstrate that ultrafast laser pulses could be used for writing data into magnetic domains [88].

Laser-driven magnetization dynamics have emerged to study the magnetization of the magnetic materials in the timescales where new spin dynamics and phenomena emerge in the field of magnetism [79, 89-91]. To be able to explain mechanisms such as exchange interactions, spin-orbit interaction, which take place at sub-picosecond timescales, laser pulse excitation and detection is necessary, since such mechanisms cannot be explained with magnetostatic fields. In addition, using femtosecond laser pulses eliminate the need for integrating complex electronics on chip. The future applications of the all-optical magnetization control by femtosecond laser pulses are data storage, spintronic logic devices, sensing, and quantum computation. Understanding the interaction among photons, electrons, phonons, and magnons could lead to the discovery of more efficient energy and angular momentum transfer mechanisms among these wave-particles.

All-optical magnetization dynamics of metallic magnetic thin films depend on intrinsic magnetic properties such as Curie temperature, spin-flip ratio and laser pulse parameters. Type I films (Fe, Co, and Ni with Curie temperatures (T_C) > room temperature, RT) could recover their magnetic moments unlike type II films (Gd and Ni_2MnSn with $T_C \approx$ RT). In this thesis, we show by numerical modeling that ultrafast magnetization control could be achieved when laser fluence is within [30-100] $J \cdot m^{-2}$ for type I films thicker than 20 nm. Recovered fraction of magnetization is higher for type I thin films with higher Curie temperatures. Magnetization drop and recovery occurs in shorter timescales in films with larger spin-flip ratio.

All-optical control dynamics of magnetization in sub-10 nm metallic thin films with quantum confinement undergo unique interactions with fs laser pulses. Our theoretical derivations based on the free electron model show that the density of states at Fermi level (DOS_F) and electron-phonon coupling coefficients (G_{ep}) in ultrathin metals have very high sensitivity to film thickness within a few Angstroms. As DOS_F and G_{ep} depend strongly on thickness due to quantum confinement, we show that completely different magnetization dynamics characteristics emerge compared with bulk metals. Our model suggests highly-efficient energy transfer from fs laser photons to spin waves due to minimal energy absorption by phonons. Quantum confined magnetic metallic nanolayers might there offer opportunities for obtaining ultrafast and efficient laser-to-spin wave energy transfer.

1.5 Thesis contribution and plan

This thesis demonstrates the investigation of magnetic thin films in: i) Theoretical modelling for tuning perpendicular magnetic anisotropy in rare earth iron garnets (REIG), ii) Pulsed laser deposition growth and characterization of the Holmium iron garnet (HoIG) iii) Analytical modelling of all-optical control (AOC) of magnetization dynamics in magnetic metallic thin films and quantum-confined ultrathin magnetic films. The organization of the thesis is as follows:

In this first chapter (introduction), we introduced magnetic thin films including rare earth iron garnets (REIG), PMA in REIGs, spintronic applications of magnetic thin films, and ultrafast control of magnetization in magnetic metallic thin films.

In chapter two (methods), we provide the basic background knowledge about REIGs, their growth procedures, structural and magnetic properties, as well as structural and magnetic analysis and measurement techniques for each of the REIG thin film based devices. Then, we provide a theoretical background about magnetic anisotropy control. Finally, we provide the scientific background about fs laser control of magnetization in metallic magnetic thin films.

In chapter three (predicting PMA in REIGs), we conduct a systematic calculation of the anisotropy energies of ten epitaxial lattice-matched RE iron garnet thin films ($X_3Fe_5O_{12}$, X = Y, Tm, Dy, Ho, Er, Yb, Tb, Gd, Sm, Eu) on five (111)-oriented and commercially-available garnet substrates. These substrates are $Gd_3Ga_5O_{12}$ (GGG), $Nd_3Ga_5O_{12}$ (NGG), $Y_3Al_5O_{12}$ (YAG), $Gd_3Sc_2Ga_3O_{12}$ (SGGG), and $Tb_3Ga_5O_{12}$ (TGG). Among fifty different film-substrate combinations, we predict twenty cases to exhibit PMA at room temperature. Only seven of these twenty PMA film-substrate cases have been tested and verified experimentally to show PMA. The thirteen remaining pairs have not been experimentally tested for their PMA characteristics. We show by means of systematic magnetic anisotropy (MA) calculations that to overcome shape anisotropy, large magnetoelastic anisotropy term is needed in highly strained thin films. Only the RT values of λ_{111} [92] were used in this study and our predictions are valid for RT (300K). To distinguish REIG thin films based on the RE element we labelled them as XIG (X = Y, Gd, Er, Dy, Tb, Tm, Sm, Ho, Yb, Eu), i.e. SmIG (Samarium iron garnet) etc., through the rest of this chapter. Our model accurately predicts the magnetic easy axes (EA) in almost all REIG thin film-substrate combinations, which were experimentally tested. Our

calculations are done based on the real (not tabulated) film properties in our model and we assume the experimentally grown films possess cubic lattice matched film structure.

In chapter four (experimental testing for chapter three), we provide for the first time an experimental procedure for pulsed laser deposition of HoIG on two different (111)-oriented GGG nad TGGG garnet substrates as well as Si (001) and SOI substrates. We investigate the effect of film thickness and growth parameters such as substrate temperature and oxygen partial pressure on the thin film structural (XRD, SEM, AFM) and magnetic properties (VSM) of HoIG. We provide optimized PLD growth parameters for better film quality which provides robust perpendicular magnetic anisotropy (PMA).

In the fifth chapter (ultrafast and efficient magnetization control in quantum confined metallic nanolayers), we present an energy balance model to study the effect of laser fluence and pulse width for single Gaussian laser pulse on magnetization dynamics in five different magnetic metallic thin films: Iron, Cobalt, Nickel, Gadolinium and Ni_2MnSn Heusler alloy. We investigate the effect of film thickness on magnetization and lattice temperature after interaction with the ultrashort laser pulse. The model captures the energy transfer rates from femtosecond laser pulse to electron bath coupled with phonon, spin, and magnetization. Then, we theoretically investigate the magnetization dynamics for sub-10 nm metallic thin films when they are exposed to a femtosecond laser pulse. First, we calculate the electron density of state at Fermi level (DOS_F), electron-phonon coupling (G_{ep}), and electron heat capacity constant (Sommerfeld coefficient: γ) and magnetization dynamics in quantum-confined magnetic metals using M3TM (microscopic three temperature model) [93, 94]. Finally, we investigated the variability of these parameters and magnetization dynamics as a functions of film thickness.

In the sixth chapter, we conclude by describing our achievements, future work and potential applications originating from this thesis.

Chapter 2

SCIENTIFIC BACKGROUND AND METHODS

2.1 Rare earth iron garnets (REIG)

Magnetic insulators (MIs) are a large family of materials which include magnetic rare earth iron garnets (REIG). REIG have been studied for more than 60 years [95, 96]. Their properties in the bulk form are very well-understood and well-known thanks to the extensive research in 1960s to 1980s [92, 97]. After 1980s, there was the discovery of the GMR and perpendicular magnetic anisotropy. So the focus has shifted to metallic magnetic layers but before then, the popular materials were magnetic insulators.

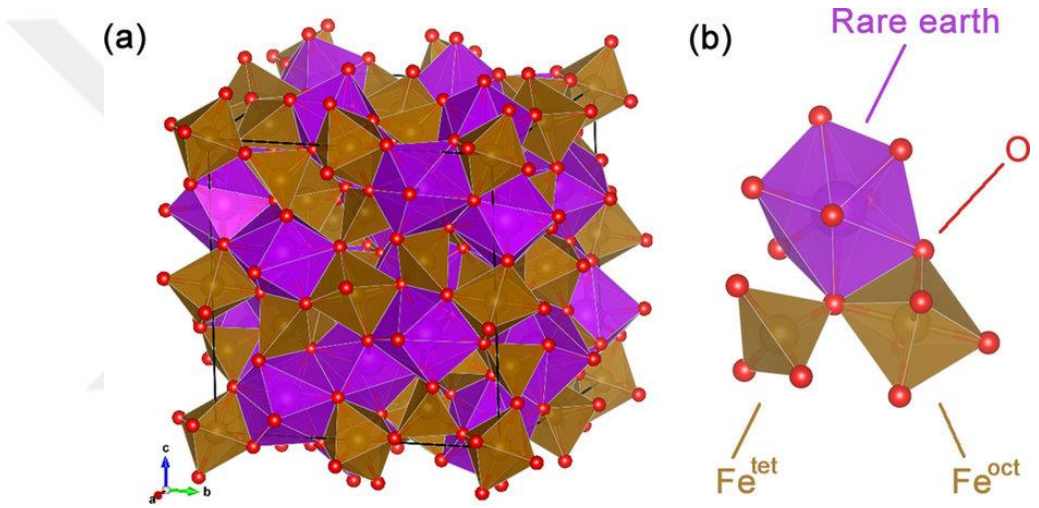

Figure 2.1: (a) The schematic representation of crystal structure of rare earth iron garnets [98]

REIGs are advantageous from two different point of view:

1) Tunable magnetic properties such as:

- Saturation magnetization (M_s): Depending on the RE ion used, there could be different M_s values due to the different electronic lone pair configurations [99].
- The strain state is different using different RE ions, which leads to rise in tunable magnetic anisotropy [64, 65].
- Magnetization damping (α): Depending on the composition and stoichiometry, magnetic damping can be tuned [100].
- Compensation temperature (T_M): Magnetic iron garnets have T_M near room temperature, where the iron ions with opposing spins in tetrahedral and octahedral sublattices cancel to yield antiferromagnet-like behavior [98].

The complexity of the unit cell of REIGs could be advantageous for tuning the above parameters via the RE choice, substitution, substrate choice, varying temperature, and materials grown on top.

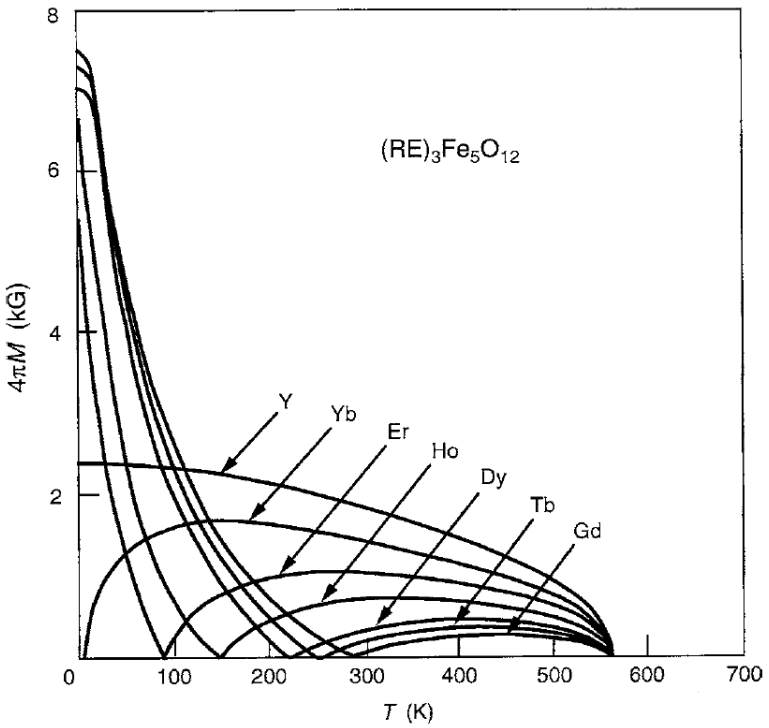

Figure 2.2: Thermomagnetism curves of REIGs. Dependence of the saturation magnetization of different REIG to the temperature and RE ion [101].

2) General properties:

- Each REIG might be grown epitaxially on a garnet substrate in single crystal form.
- Since REIGs are oxides, these materials are naturally protected from oxidation from the ambient. Therefore, REIGs are structurally robust.
- They give high flexibility of growing many types of materials like nonmagnetic heavy metallic contacts, other garnets, topological insulators or other magnetic oxides or metals on top, without compromising their properties.
- Bulk forms of REIGs are commonly grown by liquid phase epitaxy (LPE), but (ultra)thin films are typically grown by pulsed laser deposition (PLD) or sputtering.

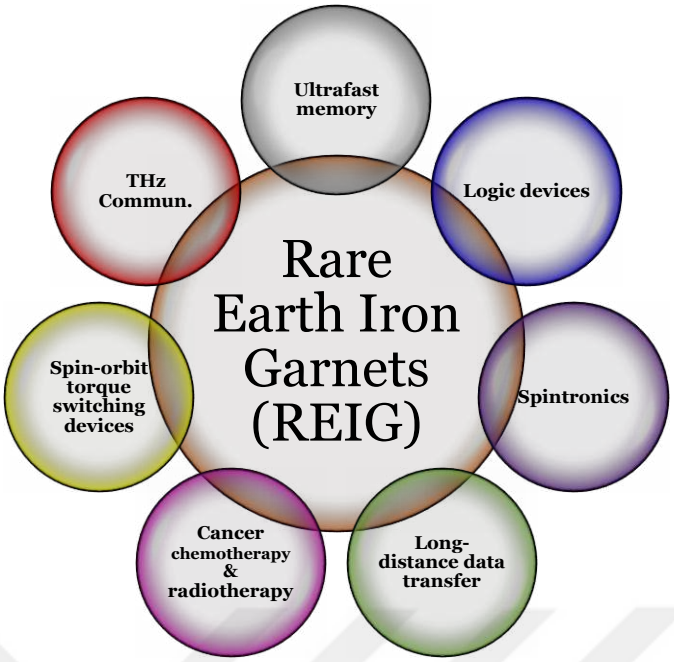

Figure 2.3: Different applications of REIGs.

REIGs are proper candidates for spintronic applications due to:

- Tunable perpendicular magnetic anisotropy in REIGs [64, 65].
- Possibility of getting efficient spin current generation by coherent magnons or incoherent magnonic excitations or other mechanisms such as spin Seebeck effect, or spin pumping [41, 102].
- Possibility to combine a wide range of materials as a spin current source or detector (metals, alloys, transition metal dichalcogenide (TMD)s, topological insulators, etc.) with magnetic insulators [103].
- High structural quality of REIGs gives minimal magnetic pinning, which eases the efficient domain wall (DW) and skyrmion motion [104].
- With REIGs low switching currents are feasible; magnetization is tunable even though these materials can be thicker than their metallic counterparts. One may still use lower current densities for spin-orbit torque switching of magnetization in these materials compared with the currents needed for magnetic metals [33, 104].
- Ultrafast dynamics could be obtained by engineering REIGs to get the angular momentum compensation temperature near room temperature [105].
- The lowest reported damping material is YIG [106] and other REIG materials could be used for long range on-chip spin signal transmission.

- Possibility of lithographical patterning of magnetic REIGs for engineered magnetization orientations and for desired device geometries [107] .

2.2 Fabrication and Growth of Magnetic Thin films

Magnetic thin film interfaces are crucial due to the strong exchange interaction between their atomic layers. As a result, magnetic ultrathin films have unique magnetic properties which may not necessarily be available in bulk. In order to benefit from the magnetic properties of thin films, the interface and film structural properties become important. These properties are controlled by growth kinetics and techniques as well as thermodynamics. The atomic layers are formed by nucleation of the islands and the deposited atoms are grown on these layers by surface diffusion, the kinetics of which determines the properties of the film [108]. Different synthesis procedures have been developed in order to grow REIG thin films with various thicknesses and stoichiometries. In recent decades, pulsed laser deposition (PLD) method has been investigated to synthesize epitaxial single crystalline REIGs which is preferable compared to other physical or chemical vapor deposition techniques. Some of the epitaxial, single crystalline thin film growth techniques are liquid phase epitaxy (LPE), chemical vapor deposition (CVD), pulsed laser deposition (PLD), molecular beam epitaxy (MBE), and atomic layer deposition (ALD). These methods are explained briefly and compared in Table 2.1.

2.2.1 Pulsed laser Deposition (PLD)

PLD is a useful for growing homogeneous, high-quality, epitaxial and nm-to-few μm-thick complex oxide films [109]. This technique enables:

- Good stoichiometry transfer from targets to films
- The ability to eliminate secondary phases in the films due to ultrahigh vacuum and purity of target
- Process control over growth temperature, oxygen pressure, laser fluence, and annealing conditions
- Wafer-scale thickness uniformity and target stoichiometry

In this technique, repeatable short pulses from a high power laser source such as KrF excimer source impinge on the surface of the ceramic target and evaporate the target surface in nanoseconds. Following target ablation, a plume of dimers and atoms is ejected from the target to substrate surface. Large distance between target and substrate, rotation of the target during deposition, and also keeping the laser power above the ablation

threshold prevents the splashing of target plume as particulates and the formation of micrometer-sized undesirable droplets on substrates [110]. In this research, targets are bought from commercial suppliers to start with good stoichiometry and to achieve high-purity REIG thin films.

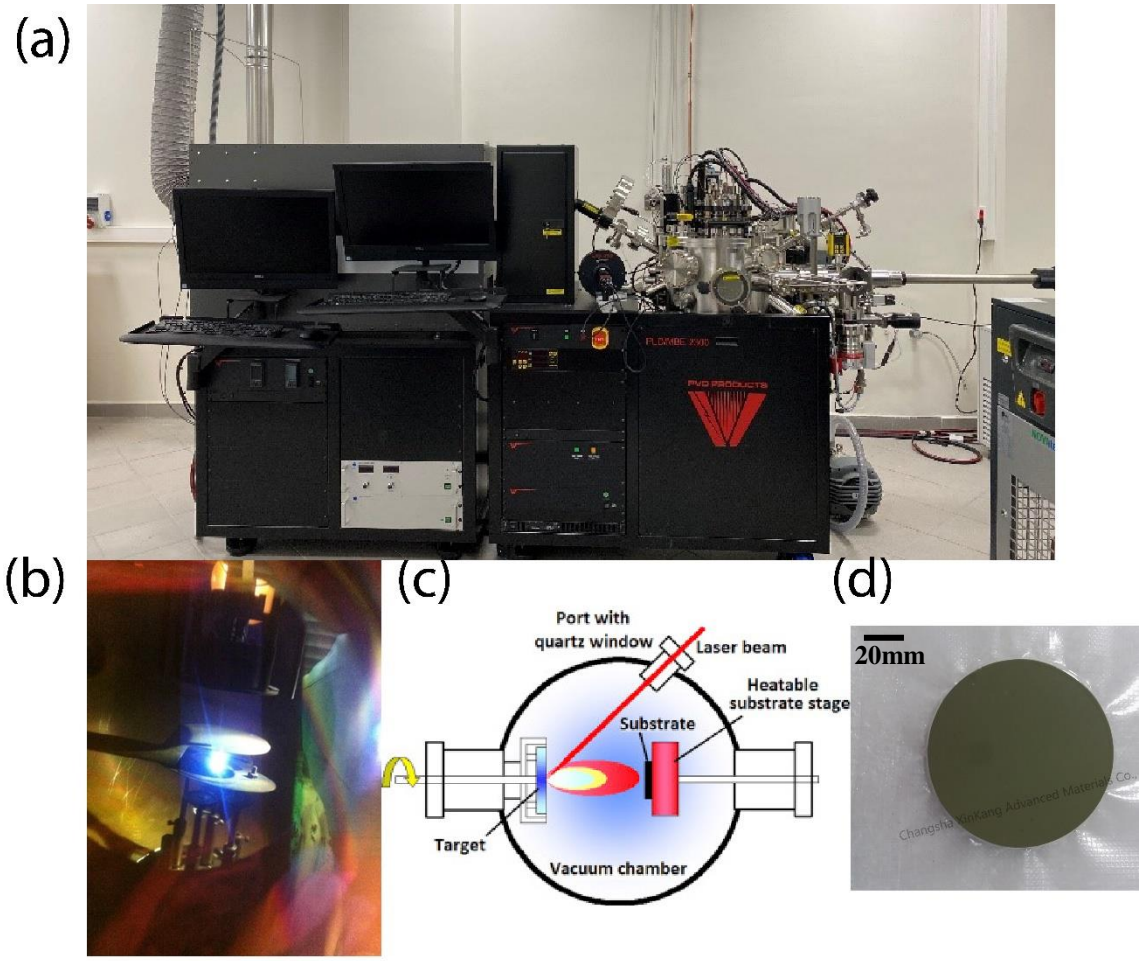

Figure 2.4: (a) Pulsed laser deposition instrument at Koç University, (b) plasma plume formed as the result of target evaporation by laser pulse (c) vacuum chamber of PLD [111]. (d) Yttrium iron garnet (YIG) target for PLD.

The deposition rate in the pulsed laser deposition is not high (0.2-5 nm/min), however the evaporation rate is extremely high, even more than that in the thermal deposition techniques [110]. This offers the feasibility of the nucleation of the first monolayer and diffusion of the second monolayer and growth of the layer by layer structure. The deposition rate in PLD varies between a fraction of monolayer per minute up to 100 MLs^{-1}; very high deposition rates effect the growth and structures such that layer by layer deposition of metastable structures are reported [110, 112]. Improved morphology and structures, stability, is another property of the films grown by PLD [113].

2.2.2 Chemical Vapor deposition (CVD)

In this technique, targets are placed into a heated chamber, then a precursor gas is flown through the chamber. Near the substrate, chemical reactions of the gaseous precursors occur and the solid thin film is deposited on the surface of substrates, while the reaction by-products are pumped out of the chamber with the unreacted precursor gases (Fig. 2.5).

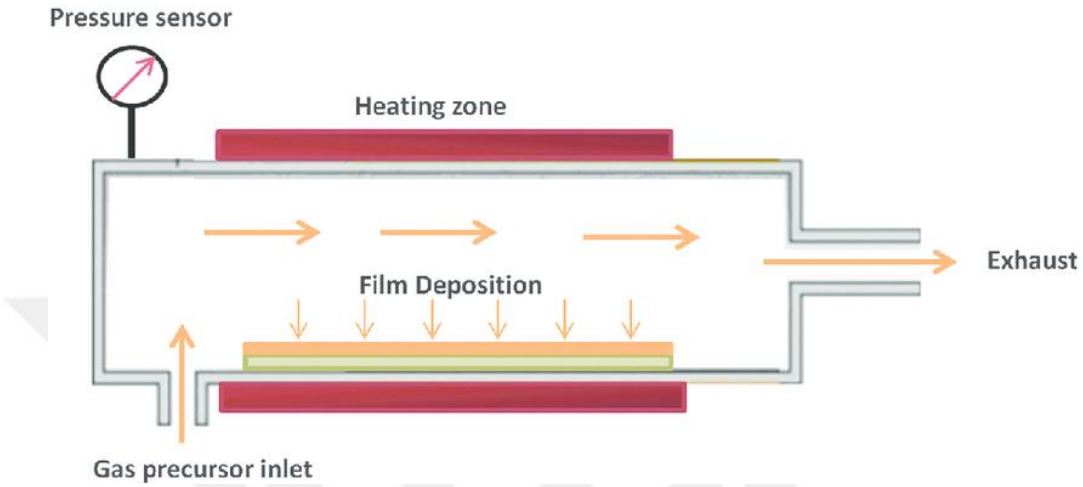

Figure 2.5: The schematic representation of thin film growth by CVD [114].

2.2.3 Liquid phase epitaxy (LPE)

The liquid phase epitaxy (LPE) is a technique for the growth of micrometer-thick epitaxial thin film materials with high crystallinity. A garnet precursor mixture is placed in a high temperature furnace with a crucible (usually platinum). First, the furnace temperature is raised up to above the melting point of the sample and kept for several hours. The melted mixture is stirred continuously with a paddle. The substrate is lowered by the substrate holder and rotated during growth till it is removed from the solution [115]. Many REIG samples have been prepared in the previous studies by LPE method [116, 117]. The schematic diagram of LPE is shown in Figure 2.6.

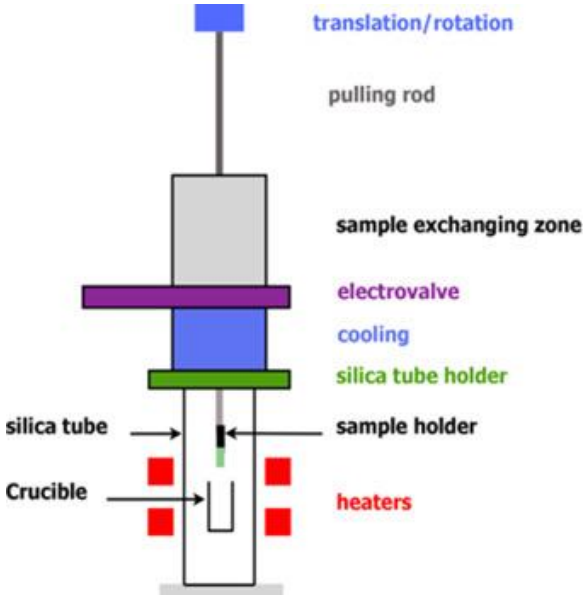

Figure 2.6: The schematic representation of thin film growth by LPE [118].

2.2.4 *Sputtering*

Sputtering is commonly used for thin film deposition for a wide range of thin film materials and applications like magnetic read head surfaces. Sputtering is a process of physical vapor deposition with which typically inert gas ions in a DC or RF plasma, eject atoms from the surface of a sputtering target. The evaporated atoms are attracted electrostatically towards a substrate to form a thin film. When sputtering thin films, an ionizing gas, usually argon, is used to create a plasma. For sputtering metallic nitrides or oxides, nitrogen or oxygen are used as process gases. The basic schematic of sputtering is shown in Figure 2.7. The atoms from target (cathode) are ejected by ion bombardment and the driven atoms travel towards the substrate [119].

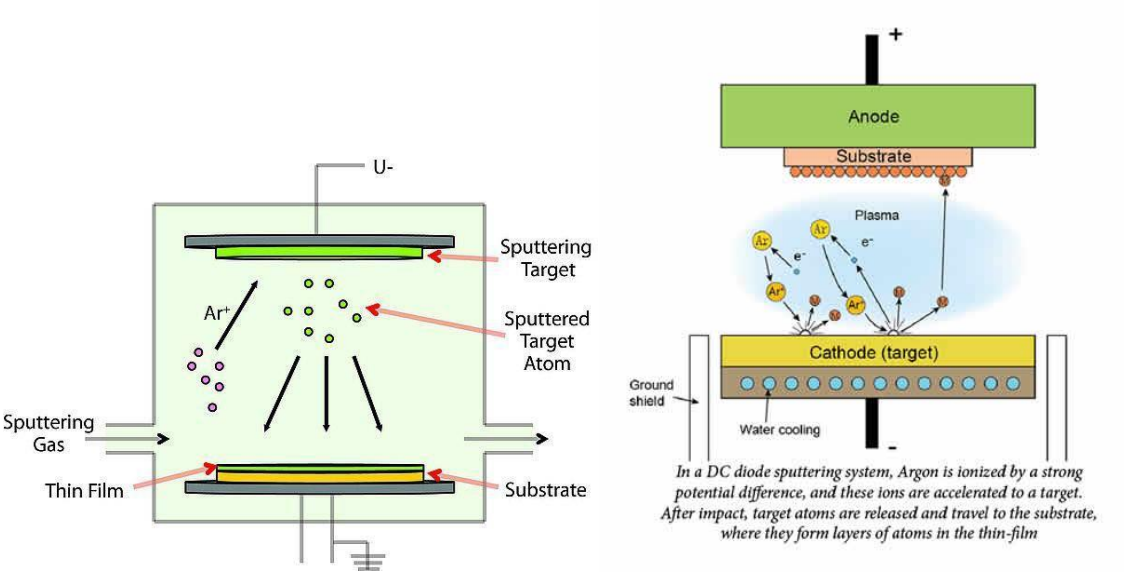

Figure 2.7: The schematic representation of thin film growth by sputtering [120].

2.2.5 *Molecular Beam Epitaxy (MBE)*

One of the advanced thin film growth methods with high control is MBE. MBE technique is a very powerful tool for the study of basic science and the production of very high-quality materials and devices. This method has been used for synthesis of transition metal dichalcogenides (TMD), topological insulators and complex oxides, selenides, and sulphides. Due to ultra-high vacuum ($<10^{-14}$ Torr) the purity of the films grown by this method is very high. Besides, one could control the interface formation, alloy compositions, and doping concentrations [121].

In MBE, the substrate is heated and non-interacting molecular beams are evaporated and sublimed on the substrate. Their mean free paths are much longer than the typical 20–30 cm source-to-substrate distance due to the UHV conditions. The reason for very pure epitaxial growth and the simplified chemistry during the growth is the use of pure solid-source. MBE is extremely good at producing very sharp interfaces. The molecular beams of source materials can quickly start or stop, via effusion cells, in much shorter time than it takes to grow an atomic layer of material.

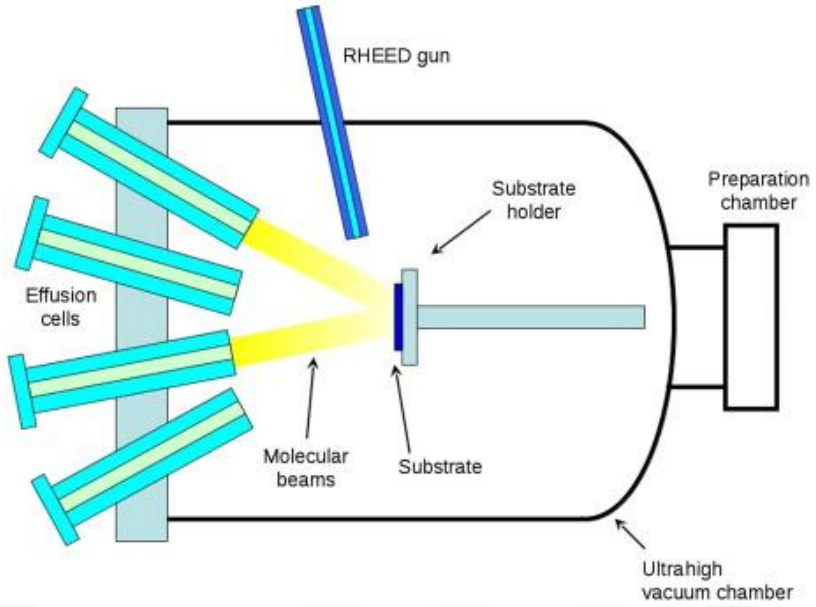

Figure 2.8: The schematic representation of thin film growth by MBE [122].

Table 2.1: Comparison between epitaxial thin film growth techniques

Growth Technique	**Stoichiometry control**	**Scalable**	**Flexible**	**Typical uses**
Pulsed laser deposition	***	*	***	Epitaxy of complex oxide films
Liquid phase epitaxy (LPE)	**	**	**	Growing μm-thick oxide films
Sputtering	***	***	***	Metal or oxide film deposition
Chemical vapor deposition (CVD)	*	**	**	Deposition of simple oxides, nitrides
Molecular beam epitaxy (MBE)	**	**	**	Ultrathin epitaxial elemental or oxide films, selenides, sulphides, tellurides

2.3 The structural properties of REIGs

As mentioned in section 2.1, the unit cell of the REIGs are very complex which contains 160 ions per unit cell; 24 RE^{3+} (dodecahedral↓), 40 Fe^{3+} (24 tetrahedral↓, 16 octahedral↑), and 96 O^{2-}. The magnetization of the REIGs originates from the exchange interaction between the tetrahedral and octahedral sites of Fe, through the oxygen ion connecting them together (Figure 2.9). This is the strongest interaction in this material. There is antiferromagnetic coupling between the Fe sites, however, due to the larger number of tetrahedral sites than the octahedral sites, it leads to partial cancellation of spins and thus a finite net magnetization arises. In addition, RE ion and sometimes oxygen deficiencies also contribute to magnetization. The main exchange coupling of this RE is to the tetrahedral site (Fe); however, the interaction between those two sites are very weak and is negligible. Due to the different contribution of the RE in the magnetization of the REIG sample, there is different saturation magnetization depending on the temperature for each RE ion. In addition, in case of the REIG, the magnetization of the RE ion vanishes at the Curie temperature, which is relatively high compared to the room temperature [123, 124]. Above room Curie temperature is advantageous for device applications under ambient conditions.

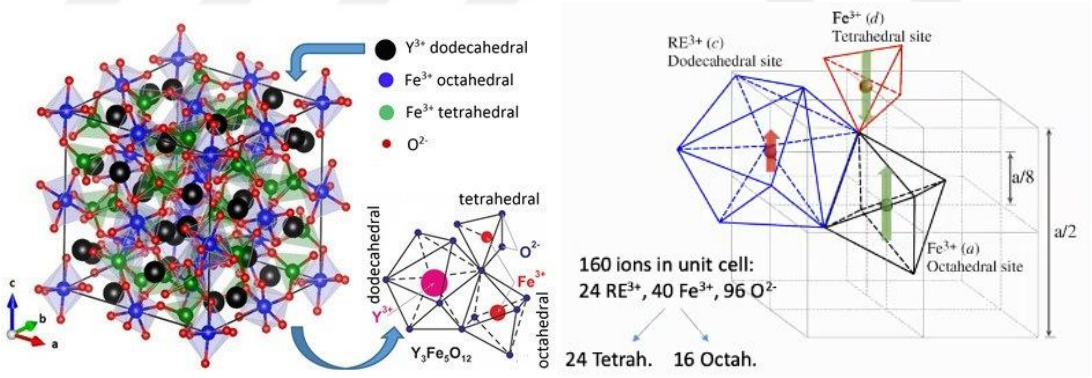

Figure 2.9: (Left) The schematic representation of crystal structure of rare earth iron garnets. (Right) Dodecahedron vacancy of the RE (24 sites) are shown as well as the tetrahedron (24) and octahedron (16) Fe^{3+} ions sites [95, 96].

Based on the crystalline nature of the REIG thin films, different techniques can be used in order to structurally characterize the synthesized REIGs such as, high-resolution X-ray diffraction (HRXRD), high-resolution X-ray reflectometry (HRXRR), atomic force microscopy (AFM), high-angle annular dark field scanning transmission electron microscopy (HAADF-STEM), and high-resolution transmission electron microscopy (HR-TEM).

2.3.1 X-Ray diffraction (XRD) and X-ray Reflectometry (XRR)

XRD is one of the common techniques to study the atomic spacing and the crystal structures of crystalline materials. X-ray diffraction is based on constructive interference of monochromatic X-rays and a crystalline sample. These X-rays are generated by a cathode ray tube, filtered to produce monochromatic radiation, collimated to concentrate, and directed toward a sample. The interaction of the incident rays with a sample produces constructive interference (and a diffracted ray) when conditions satisfy Bragg's Law ($n\lambda=2d\sin\theta$). This law relates the wavelength of electromagnetic radiation to the diffraction angle and the lattice spacing in a crystalline sample. These diffracted X-rays are then detected, processed and counted. By scanning the sample through a range of 2θ angles, all possible diffraction directions of the lattice should be attained due to the random orientation of the material. Conversion of the diffraction peaks to d-spacing allows identification of the element or compound because each material has a set of unique d-spacings. Typically, this is achieved by comparison of d-spacings with standard reference patterns measured for each compound crystalline material.

All x-ray diffraction methods are based on generation of x-rays in an x-ray tube. These x-rays are directed towards a sample and the diffracted rays are collected. A key component of all diffraction is the angle between the incident and diffracted rays. As the sample and detector are rotated, the intensity of the reflected x-rays is recorded. When the geometry of the incident X-rays impinging the sample satisfies the Bragg's equation, constructive interference occurs and an intense peak is visible. A detector records and processes this x-ray signal and converts the signal to a count rate which is then output to a device such as a printer or computer monitor.

One measurement configuration of an x-ray diffractometer is called Bragg-Brentano configuration shown in Figure 2.10. In this geometry, the x-ray source and the detector rotates around a fixed sample and the θ angle of measurement is gradually incremented for every next diffraction measurement. A goniometer is used to maintain the coupled angle between the source and the detector and rotate the source and the detector on the circular path. For typical powder patterns, data is collected at 2θ from ~5° to 70°, angles that are preset in an x-ray diffractometer scan.

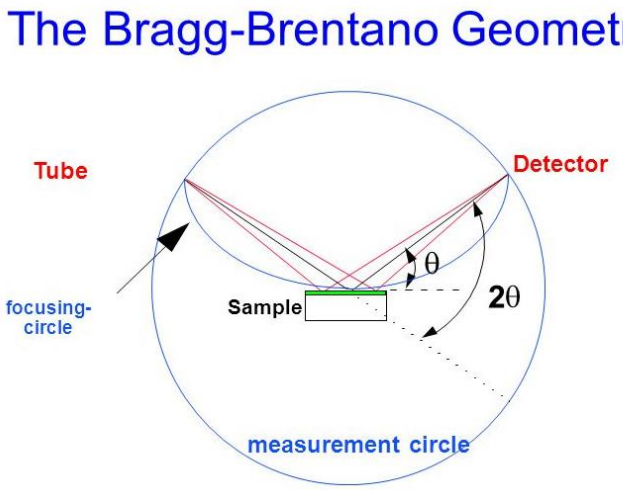

Figure 2.10: The Bragg-Brantano geometry in XRD measurement.

For characterization of the single crystalline REIGs, high resolution XRD (HRXRD) is used as shown in Figure 2.11a. Due to the nm range thickness of the REIG thin films, the uniformity of the epitaxial film and also the thickness of the film is determined by high resolution X-ray reflectometry (HRXRR). In this technique, the peak full width at half maximum (FWHM) is proportional to reciprocal of the film thickness. In the very high quality epitaxial films, the HRXRR peaks are similar in shape and position, shown in Figure 2.11b [43].

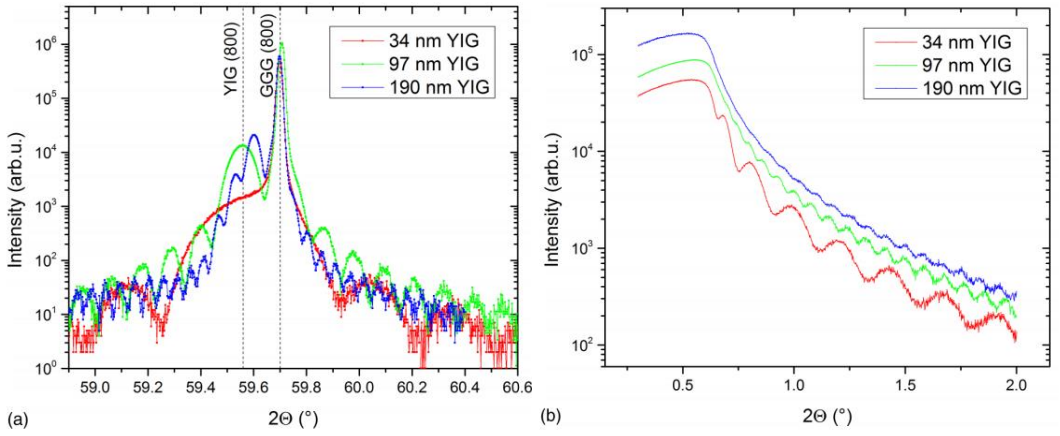

Figure 2.11: (Left) HRXRD 2θ/θ plot around YIG (800) and GGG (800) peaks. (Right) HRXRR plot for 34, 97, and 190 nm thick YIG films [43].

2.3.2 *Atomic force microscopy (AFM)*

AFM is a technique for characterization of surface topography. Surface roughness and also films thickness can be characterized with a resolution of less than 0.1 nm. In AFM method, a current develops between an electrode and a cantilever, a deflection is caused by interaction between the tip and the surface, whose the electrical response is measured.

For investigating the surface features, AFM uses columbic or van der Waals forces between the surface and the probe tip. The movement of the cantilever is converted into image as the probe is moved across the surface [125]. The schematic of working principle of AFM method is shown in Figure 2.12.

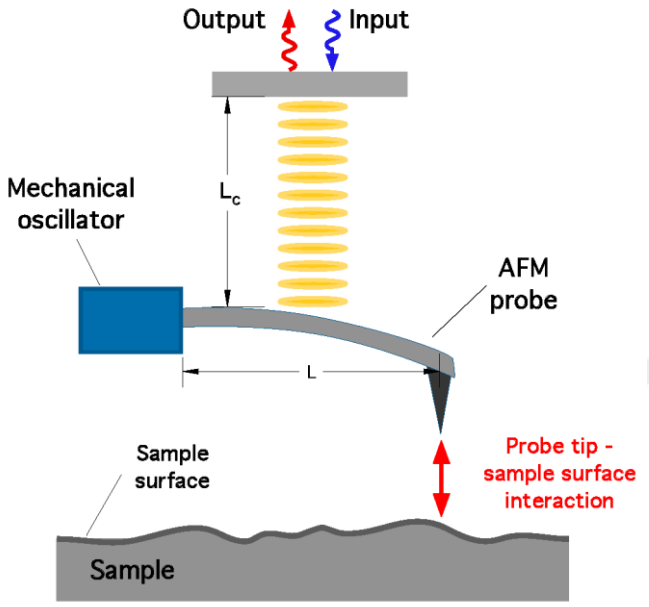

Figure 2.12: Schematic of the AFM [126].

The surface roughness of the epitaxial REIG thin films is measured and reported as the RMS value which is usually less than 1 nm, as shown in Figure 2.13.

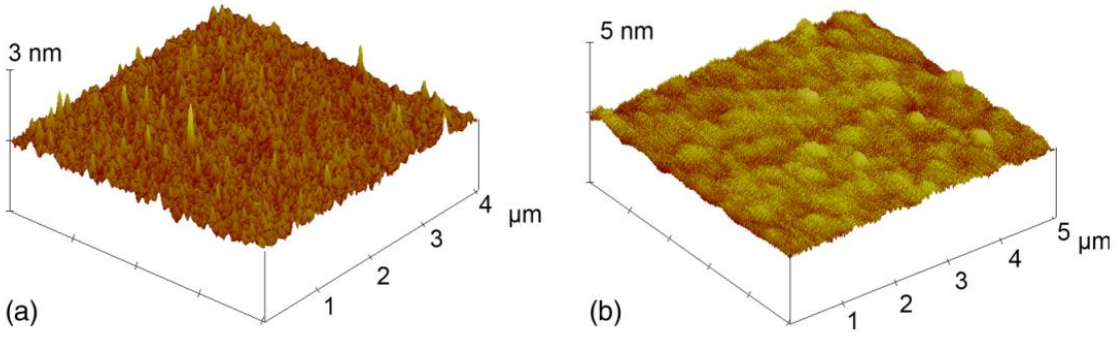

Figure 2.13: AFM surface profiles of (a) 17 nm YIG film with RMS surface roughness of 0.14 nm and (b) 79 nm thick YIG film with RMS surface roughness of 0.20 nm [43].

2.3.3 Scanning electron microscopy

Scanning electron microscopy (SEM) uses focused high energy electron beams for 2D and 3D characterization of surface topography, thickness (in SEM cross sectional imaging), elemental composition, as well as imaging the surface of the materials with up to nm resolution [127]. The scanning mechanism is rastering through the surface to take

image. High vacuum inside the chamber where the primary electrons are produced, prevents sample contamination [128]. The non-conductive samples are coated with a thin conductive layer such as Gold, for interaction of the electron with surface and to avoid imaging artefacts due to electrostatic charging of insulating surfaces.

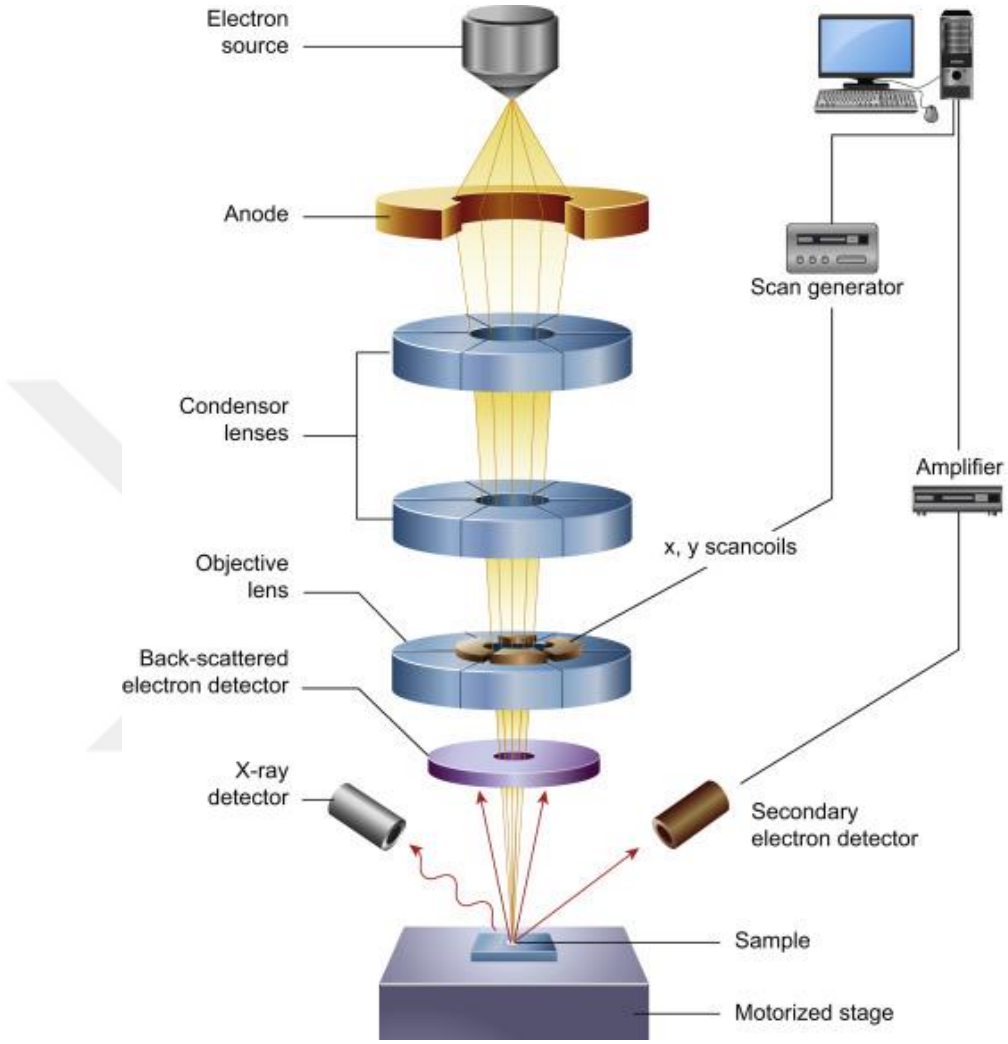

Figure 2.14: Schematic of SEM chamber [129].

The working principle of SEM is based on electrons as charged particles which are accelerated and focused precisely by electromagnetic (EM) fields. Figure 2.14 shows a schematic of SEM. The scattered beams are collected by a lens, and refocused that results in formation of true real-space image, where each point in the image is corresponding to a specific point in the object. Furthermore, electrons are able to form more strong interaction with matter which result in electron diffraction in nanometer scale materials. Since the electron wavelength lies in the range an order of magnitude smaller than the atomic spacing materials (0.004 to 0.001 nm), using accelerating voltages of 100-1000 kV, material imaging with atomic resolution becomes a routine procedure [130].

SEM has different functionalities based on the depth of the electron emission, such as back scattered electrons (BSE) or secondary electrons (SE). BSE are reflected as the result of elastic scattering when the electron beam strikes the sample. This mechanism provides information about the elemental distribution based on the atomic number. By application of high electric fields, the cathode emits electrons in the field-emission SEM function which provides images with higher resolution [131]. Despite conventional SEM in which the electron beam is under high vacuum, the FESEM provides gaseous environment into the specimen chamber. Moreover, non-conductive surfaces could be imaged without application of a conductive coating. Figure 2.15 shows a cross sectional SEM image of porous YIG films grown by sol-gel method [132].

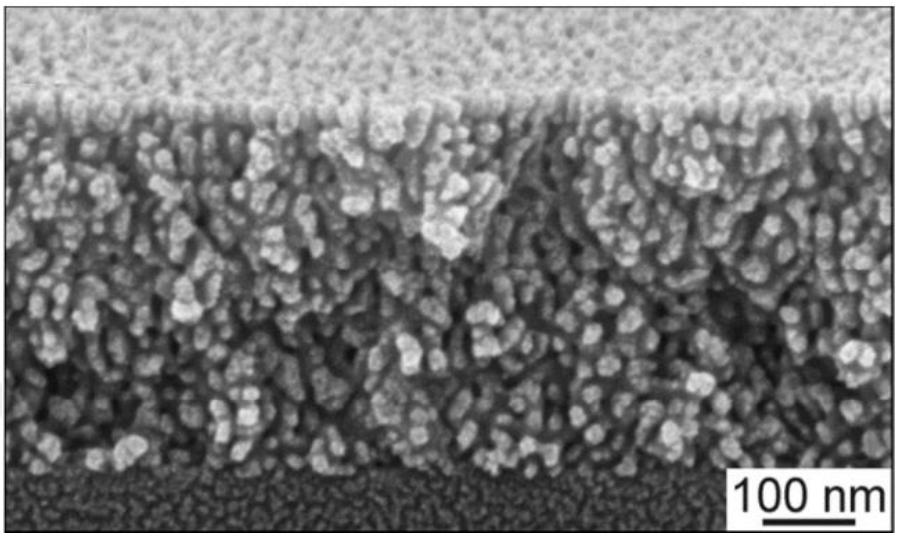

Figure 2.15: Cross sectional SEM image of porous YIG film grown by sol-gel method [132].

2.4 Magnetic properties of REIGs

2.4.1 Vibrating sample magnetometer (VSM)

One of the most important measurements in characterization of magnetic materials is the measurement of their magnetic hysteresis loops. These measurements determine information such as magnetic coercivity (H_c), remenant state (M_r), saturation magnetization (M_s), and also indirect information such as magnetic anisotropy of the magnetic material, depending on the orientation of the applied magnetic field. The sample is attached to the sample holder which is vibrated with an AC current inside the pickup coils. A constant magnetic field is applied by the electromagnets to the sample. The vibrating sample generates an AC magnetic flux oscillation on the pickup coil. The AC voltage in the pickup coils is recorded. VSM calibration before measurement yields

"emu/Volt" proportion factor. The induced voltage in the pickup coil is proportional to the sample's magnetic moment for each applied field.

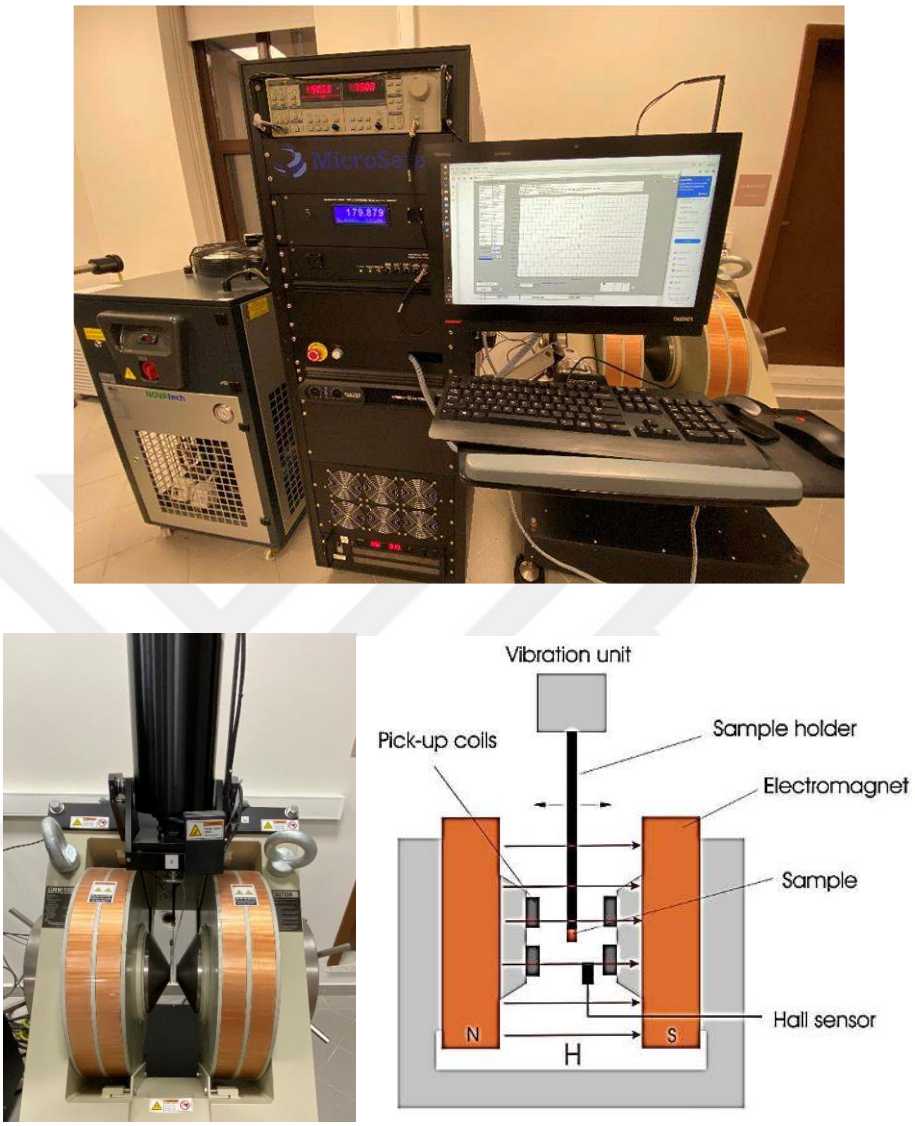

Figure 2.16: Vibrating sample magnetometer for measurement of hysteresis loop of the magnetic samples. Electromagnet, sample holder, vibrating unit, and pickup coils in the VSM device [133].

With VSM, the magnetic moment of a thin film is measured, usually at room temperature, and plotted with respect to the applied field. In publication, the diamagnetic or paramagnetic contribution of a substrate is subtracted from the data as shown in Figure 2.17. In this figure, the external magnetic field is applied parallel to the sample plane.

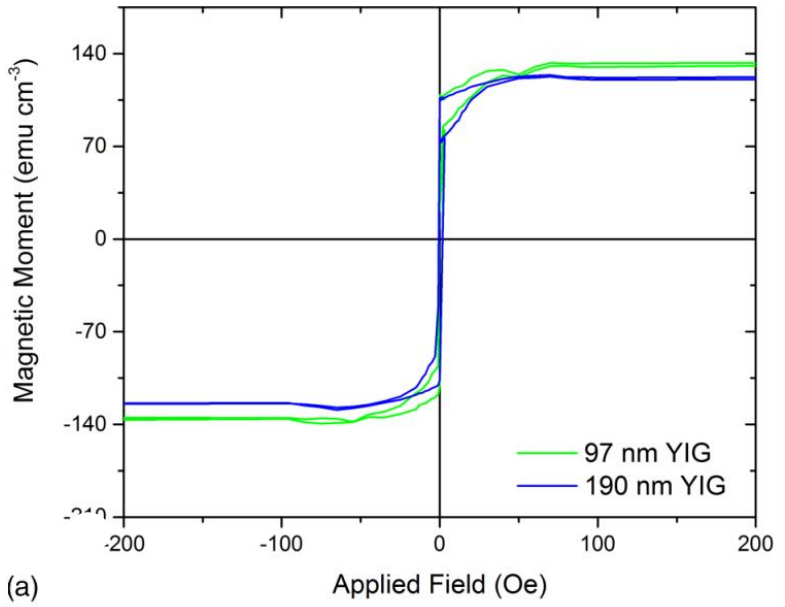

Figure 2.17: Hysteresis loop (Magnetization as a function of applied in plane magnetic field) for YIG films with different thicknesses (97 and 190 nm) [43].

2.5 *Magnetic anisotropy*

Magnetic anisotropy (MA) is defined as the directional dependence of the magnetic properties of the materials. The magnetization easy axis is the energetically favorable axis along with the material could be magnetized, which arises from the interaction of the spin with the crystal lattice (spin-orbit coupling). The magnetic anisotropy state of magnetic materials can be extracted from the magnetization curves, B-H or M-H hysteresis loops, when measured under different directions of the applied magnetic field; however measuring the external magnetic field-induced torques on a spherical or disk shaped crystalline sample, as the function of the angle between the preferred crystallographic direction and the magnetic field orientation, is also introduced as a method for determining the magnetic anisotropy state of magnetic materials [134].

A free magnetic moment when there is no external magnetic field, does not possess a preferred orientation, as shown in Figure 2.18a. The tendency to orient along a preferable axis, or magnetic anisotropy, arises from breaking the symmetry in the crystal of the magnetic materials. Figure 2.18b shows a schematic of magnetic anisotropy in the crystalline magnetic materials.

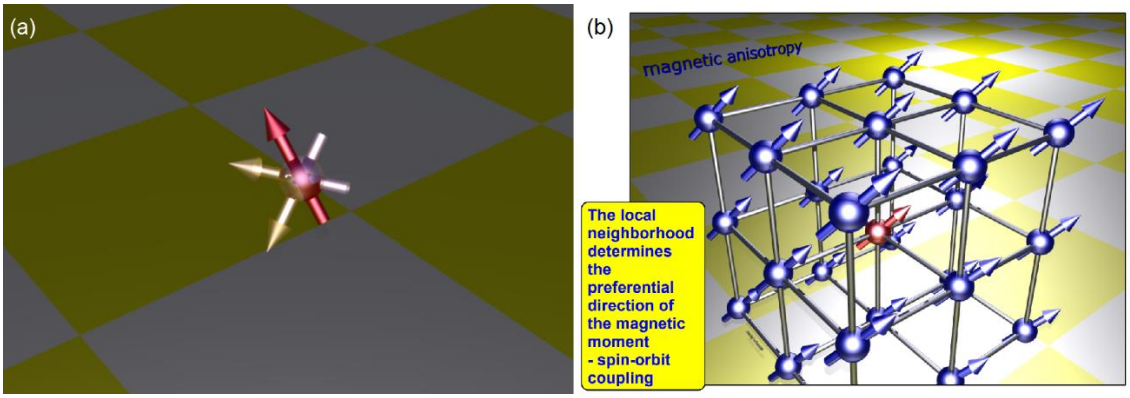

Figure 2.18: (a) The orientation of a single magnetic moment in a free space in absence of external magnetic field, and (b) The magnetic anisotropy in the crystal due to the spin orbit coupling under the influence of the neighboring atoms [135].

2.5.1 Magnetic anisotropy in a cubic crystal-Magnetocrystalline anisotropy

The energy density related to the orientation of the magnetic moment can be written as the power series of direction cosines in the crystalline structures as expressed in equation 2.1 [136-138].

$$E_{cryst}(\vec{M}) = b_0 + \sum_{i=1,2,3} b_i\alpha_i + \sum_{i=1,2,3} b_{ij}\alpha_i\alpha_j + \sum_{i=1,2,3} b_{ijk}\alpha_i\,\alpha_j\alpha_k + \ldots \qquad (2.1)$$

Where, α_1, α_2, and α_3 are direction cosines of magnetization as $(\alpha_1, \alpha_2, \alpha_3) = (\sin(\theta)\cos(\varphi), \sin(\theta)\sin(\varphi), \cos(\theta))$, with θ and φ polar and azimuthal angels, respectively.

Magnetocrystalline anisotropy depends on the even powers of the cosine direction α. By substituting the tensor b in the equation 2.2 the anisotropy energy for the cubic crystals are

$$E_{cryst}(\vec{M}, T) = K_0(T) + K_1(T)(\alpha_1^2\alpha_2^2 + \alpha_2^2\alpha_3^2 + \alpha_3^2\alpha_1^2) + K_2(T)\alpha_1^2\alpha_2^2\alpha_3^2 \qquad (2.2)$$

Where K_0, K_1, and K_2 are the linear combinations of n tensor components, known as zeroth, first, and second order magnetocrystalline anisotropy. Considering uniaxial anisotropy in the cubic sustems, the magnetocrystalline anisotropy of the magnetic medium is $K_1(T)$. Since K_2 is usually two orders of magnitude smaller compared to K_1, it can be neglected in the magnetic anisotropy calculations [137-139]. For temperature-dependent changes in magnetic anisotropy, K_2 may become important especially when K_1 becomes lower.

Figure 2.19 shows the magnetic anisotropy in the hysteresis loop of the Ni, Fe, and Co crystalline magnetic materials with different magnetization easy axes [135].

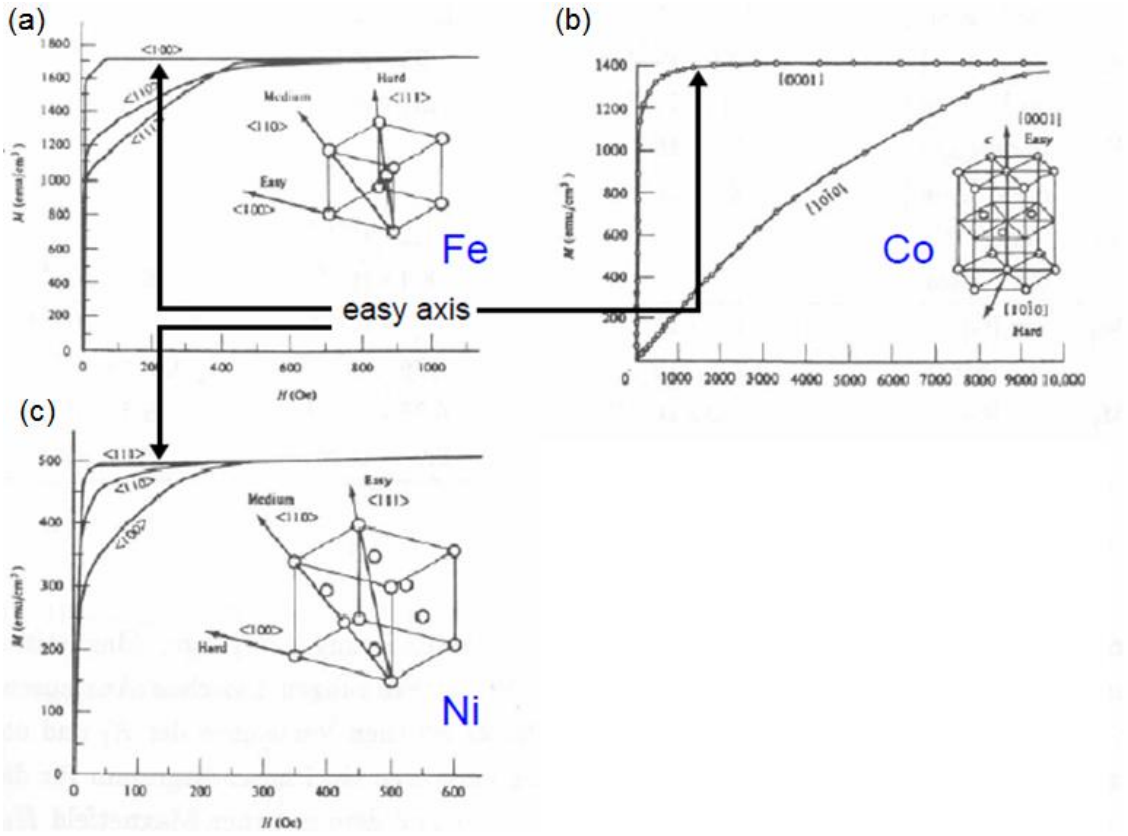

Figure 2.19: The magnetic anisotropy in the hysteresis loop of (a)Fe, (b) Ni, and (c) Co along their easy and hard axes [140].

The main contributing terms in the magnetic anisotropy energy density calculations of the magnetic materials are shape, magnetocrystalline and magnetoelastic anisotropy energy densities.

The microscopic mechanism of the existence of the magnetocrystalline anisotropy is described by the spin-orbit coupling [141]. The orientation of a spin of an atom in the magnetic material is dependent of the orientation of its relevant atomic orbitals in the crystalline structure, (shown in Figure 2.20) which gives rise to the favorable magnetization direction, so called easy axis.

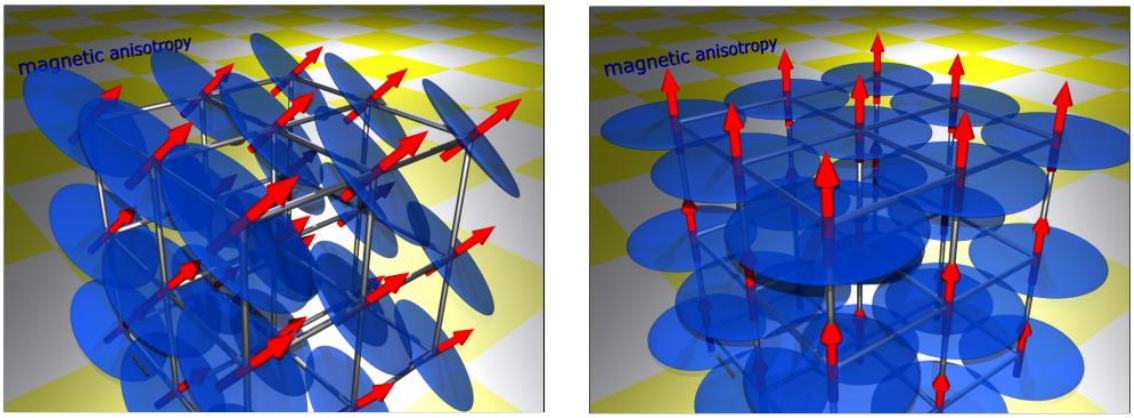

Figure 2.20: Schematic of the magnetocrystalline anisotropy. Dependence of the easy axis to the orbital orientation of each atomic spin [135].

2.5.2 *Shape anisotropy*

The shape anisotropy originates from the magnetostatic energies, due to the non-spherical shape of the magnetic medium; therefore the shape anisotropy is always taken into account in the MA of samples. Since shape anisotropy changes with sample geometry, one could prepare permanent magnets by engineering shape anisotropy. In 1950, magnetic needles with single domain have been fabricated from the perfect cubic magnetic iron [142].

Magnetic induction in a uniformly magnetized body is expressed as equation 2.3

$$\vec{B} = \mu_0(-N.\vec{M} + \vec{M}) \qquad (2.3)$$

N is the demagnetizing tensor [143]. Due to the non-uniform charge distribution in the magnetic medium, demagnetization reduces the field inside the ferromagnetic medium. If the magnetization is along the easy axis of the ellipsoid, the demagnetizing tensor is $N_x+N_y+N_z=1$.

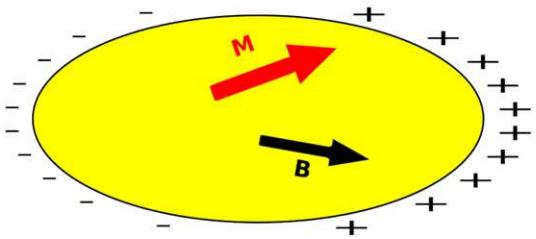

Figure 2.21: The demagnetization effect of the magnetostatic shape anisotropy [135].

The demagnetization energy of a sample, due to the shape anisotropy contributes to the total energy of the sample as [143]:

$$E_{demag} = -\frac{1}{2}\int \vec{B}_{demag} \cdot \vec{M}\, dV = \frac{1}{2}\int \mu_0\left(N \cdot \vec{M}\right) \cdot \vec{M}\, dV = \frac{1}{2} V \mu_0\left(N\vec{M}\right) \cdot \vec{M} \qquad (2.4)$$

Where V is sample volume, and B is the magnetic induction. By substituting this energy term in the uniaxial anisotropy energy and Stoner-Wohlfarth model [144, 145], which describes the magnetization reversal in a single domain magnetic material, and considering that for an infinitely expanded very thin ellipsoid N tensor is written as N= $\begin{pmatrix} 0 & 0 & 0 \\ 0 & 0 & 0 \\ 0 & 0 & 1 \end{pmatrix}$, the demagnetizing shape anisotropy energy density is defined as $K_{shape}=2\pi M_s^2$. The magnitude of shape anisotropy term usually overcomes that of the magnetocrystalline anisotropy, and tends to orient the magnetic moment of the sample towards in-plane direction.

The schematic of the shape anisotropy is shown in Figure 2.22. The effect of shape anisotropy on an infinite square plane is eliminated.

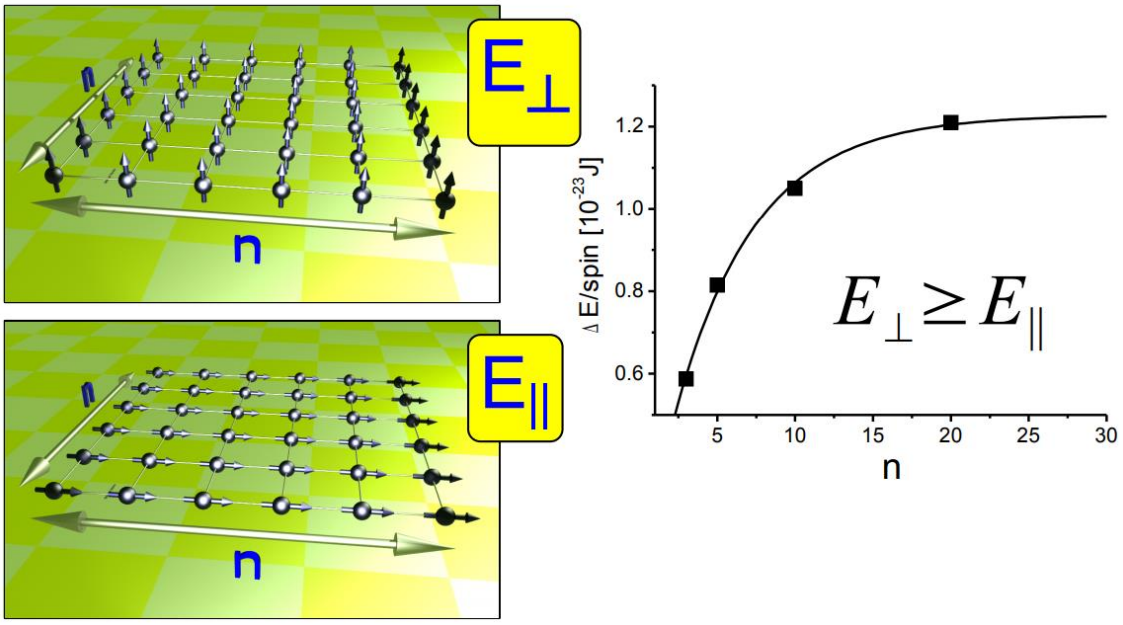

Figure 2.22: The schematic of the shape anisotropy [135].

2.5.3 *Magnetoelastic anisotropy*

Magnetoelastic, or strain-induced magnetic anisotropy arises from magnetostriction coupling in the magnetic medium which results in favorable magnetization direction. Due to the magnetostriction, the dimensions of a magnetic material changes under an external magnetic field. Magnetostriction constant, λ, is defined as the magnetic field dependence of the strain change inside the magnetoelastic material, shown in Figure 2.23a. The

magnitude of λ is different for various crystal orientations. Inverse magnetostrictive effect describes the change in the magnetization orientation (easy axis) of a sample, under mechanical stress/strain (Figure 2.23b).

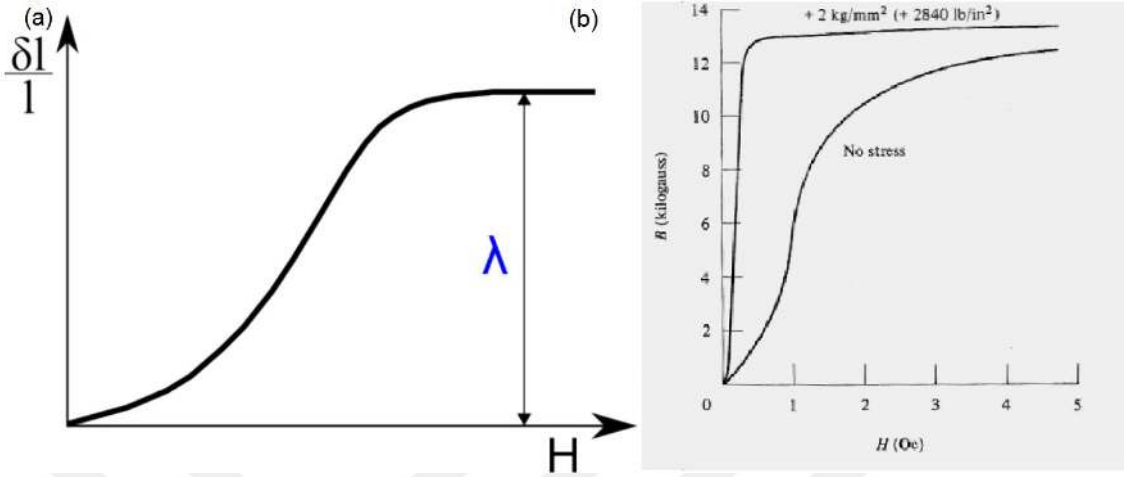

Figure 2.23: (a) The definition of magnetostriction constant, and (b) Inverse magnetostrictive effect. Influence of the stress on the magnetization of the permalloy [146].

For a crystalline material oriented in (hkl) direction, with isotropic λ the magnetoelastic anisotropy energy density is defined as $K_{ME} = -\frac{3}{2}\lambda_{hkl}\sigma \cos^2\theta$; where σ is the stress, and θ is the angle between the applied stress and the easy axis.

2.6 Ultrafast all-optical control of magnetization in metallic thin films

2.6.1 Magnetization dynamics and Landau-Liftshitz-Gilbert (LLG) equation

In absence of damping, the angular momentum of a magnetic material is:

$$L = \frac{m}{\gamma} \tag{2.5}$$

The transient change of this angular momentum induces a torque on the magnetic moment equal to

$$T = m \times H \tag{2.6}$$

$$\frac{dL}{dt} = \frac{d}{dt}\frac{m}{\gamma} = m \times H \tag{2.7}$$

, which describes the precession motion of magnetic moment as shown in Figure 2.24a. In this formula H is the effective field as

$$H_{eff} = H_{ext} + H_{ani} + H_{dem} + \cdots \tag{2.8}$$

The precessional motion time of the magnetic moment is not infinite. A dissipative term is present that slows down this precessional motion towards effective field as shown in Figure 2.24b.

$$\frac{\partial \mathrm{m}}{\partial \mathrm{t}} = \gamma \mathrm{m} \times \mathrm{H}_{\mathrm{eff}} + \frac{\alpha}{|\mathrm{m}|} \times \frac{\partial \mathrm{m}}{\partial \mathrm{t}} \tag{2.9}$$

The equation 2.9 describes the magnetization dynamics of a magnetic material in presence of an effective magnetic field, and is known as Landau-Liftshitz-Gilbert (LLG) equation. In this formula γ is the gyromagnetic ratio and α is Gilbert damping parameter.

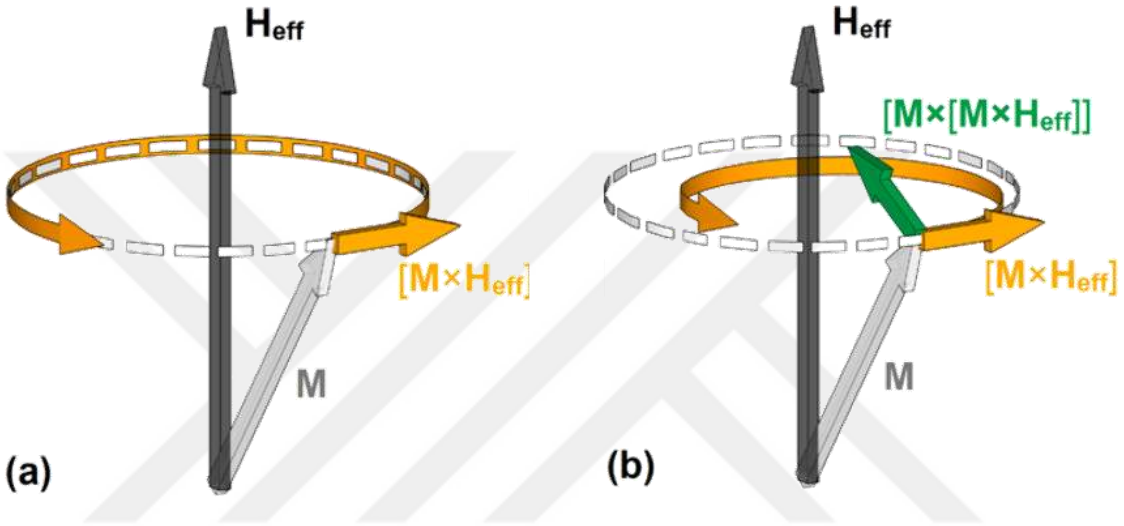

Figure 2.24: (a) Precession of magnetic moment induced by the effective field and (b) damping of the precessional motion [147].

2.6.2 Ultrashort laser-induced manipulation of magnetization dynamics

The interaction of ultrashort laser pulses with magnetic materials has been an appealing research area in spintronics and modern magnetism. The presence of ultrafast events in the field of magnetism urges the use of femtosecond lasers both for excitation and detection. Figure 2.25 shows the timescales of the magnetic phenomena with fs laser pulses compared to magnetic field. The laser pulses are attractive alternative for manipulation of the magnetization due to their short duration.

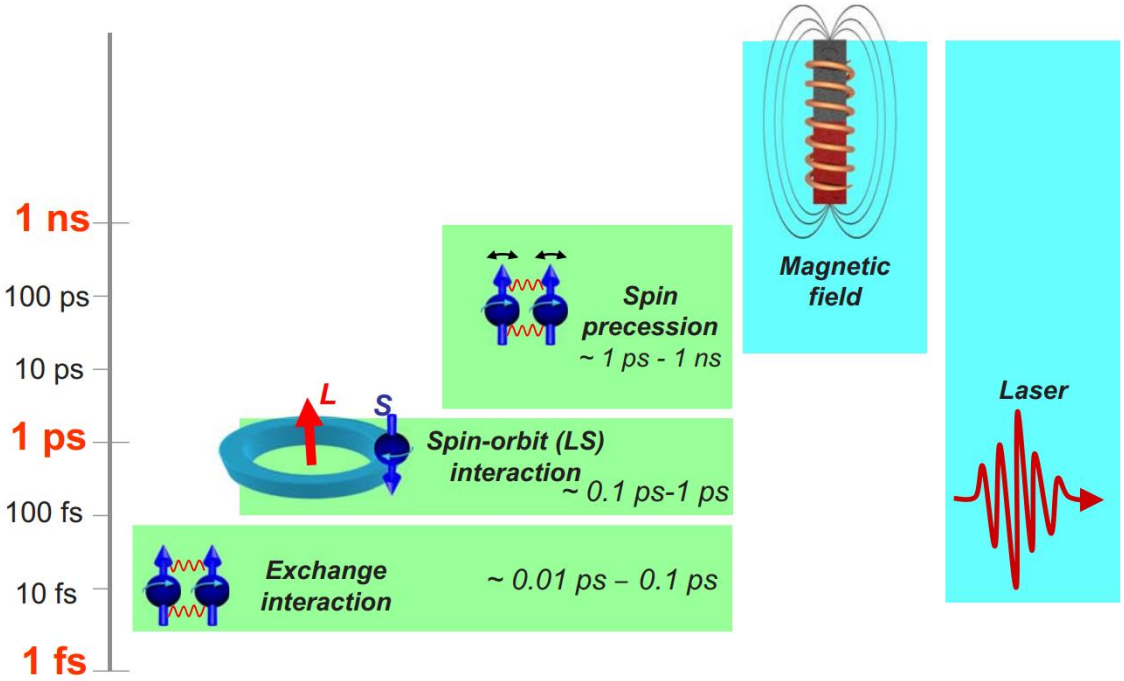

Figure 2.25: Comparison of the time scales in magnetism with magnetic field and laser pulses [79].

The ultrafast manipulation of magnetization in the femtosecond timescales (femtomagnetism) was discovered, as it is a method for accelerating the magnetization reversal. It was experimentally observed that the magnetization of the Ni thin film was quenched to around 50% of its maximum value in sub-picoseconds after illumination of an ultrashort laser pulse of 60 fs width, as shown in Figure 2.26a. This magnetization quenching mechanism was not feasible to describe by conventional electromagnetism, since the speed of the changes was an order of magnitude higher than the precessional motion of the magnetization. After a few picoseconds, the magnetization of Ni film is reversed back to its original state as the system cools down. The demagnetization of the various metallic thin films was studied previously with different theories to understand the origin of such processes [83, 148-152]. Magnetization quenching has now been understood to be a thermal process in which the material is heated in sub-picosecond timescale.

The sub-picosecond demagnetization of Ni in 1996 [89], introduced the manipulation of magnetic order by ultrashort laser pulses as a fundamentally challenging topic. By illumination with a fs laser pulse, first, the material is heated due to the laser energy absorption by electron bath. The non-equilibrium state is induced in the system and the energy absorbed by electrons is distributed to the phonon and spin baths in the following

picoseconds until the material reaches to thermal equilibrium. The schematic of the coupled interaction between electron, phonon and spin baths are shown on Figure 2.26b. The experimental observation of the ultrafast demagnetization and recovery of the Ni thin film was first demonstrated by Beaurepaire and explained by three temperature model (3TM) shown as Figure 2.26c.

The energy balance model describes that the fs laser pulse injects energy into the coupled baths and the transient electron, phonon, and spin temperatures (T_e, T_l, T_s) and magnetization are described with the rate equations 2.10-2.12 [83, 89]

$$C_e \frac{dT_e}{dt} = -G_{el}(T_e - T_l) - G_{es}(T_e - T_s) + P(t) \quad (2.10)$$

$$C_l \frac{dT_l}{dt} = -G_{el}(T_l - T_e) - G_{sl}(T_l - T_s) \quad (2.11)$$

$$C_s \frac{dT_s}{dt} = -G_{es}(T_s - T_e) - G_{sl}(T_s - T_l) \quad (2.12)$$

In these equations, T_e, T_l, T_s, are electron, phonon, and spin temperatures, respectively. The electron-phonon, electron-spin, and phonon-spin coupling constants G_{el}, G_{es}, G_{sl}, follow a similar formalism described in ref. [83] and [153]. The heat capacities of phonon and spin are C_l and C_s. In this model, the electron, phonon and spin baths are in thermodynamic equilibrium. Due to the smaller heat capacity of electron, C_e, the electron temperature rises in around 200 femtoseconds. The energy transfer coefficients between electron-phonon/lattice (G_{el}), electron-spin (G_{es}), and spin- phonon/lattice (G_{sl}), determine the kinetics of thermodynamics equilibrium between the baths which takes place in a few picoseconds after illumination of the fs laser pulse. In equation 2.10, the laser energy absorption by only the electron bath is shown. The temporal electron, phonon, and spin temperatures (T_e, T_l, and T_s, respectively) in the Beaurepaire experiments are estimated and shown in Figure 2.26c. The time of the laser pulse incidence on the surface of the thin film is shown as t=0 on the x-axis.

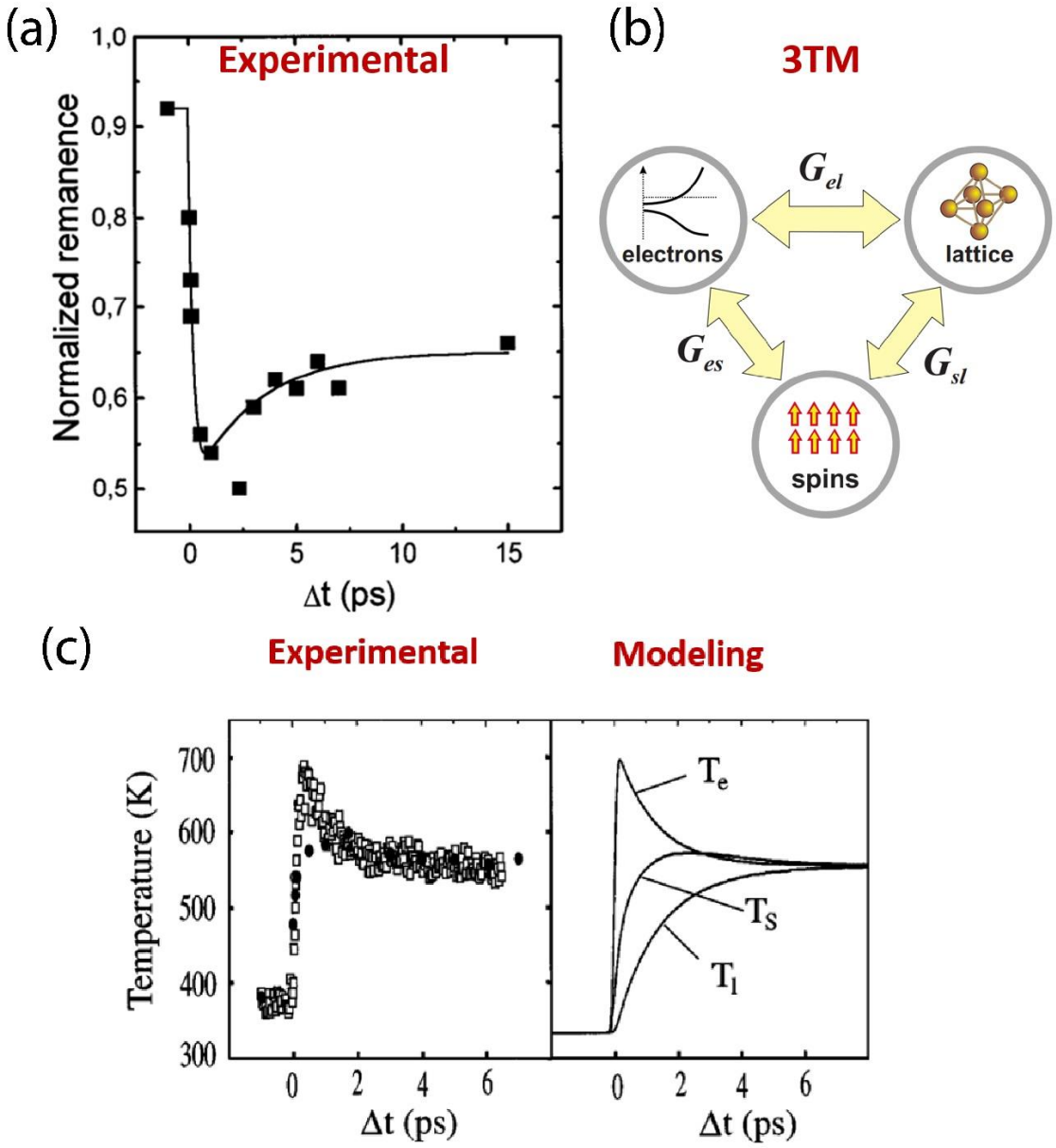

Figure 2.26: (a) Demonstration of the ultrafast demagnetization of Ni, (b) schematic 3TM [154], (c) experimental, and modeling results of three temperature model [89].

Figure 2.27 shows the sequential events after the fs laser pulse hits a magnetic metal. First, the electron excitation after absorption of the fs laser pulse takes place in a few femtoseconds [155], which stirs the equilibrium state. The non-equilibrium state dictates a non-thermal distribution in the electron bath, where the Fermi-Dirac statistics ($F(E) = \frac{1}{1+\exp(\frac{E_F}{kT_e})}$) cannot explain (Figure 2.27a). E_F, is the electron energy at Fermi state and k is the Boltzmann's constant. In the following few femtoseconds the thermalized electrons reach an equilibrium with each other within the Fermi-Dirac distribution. At this point, the electron temperature can rise up to the temperatures well above the room temperature such as 1000-2000K (Figure 2.27b). In the following few picoseconds, the non-

equilibrium among the electron, phonon and spin baths reaches to the equilibrium with energy exchange between baths (G_{ij}), as shown in Figure 2.27c. This energy exchange occurs through scattering phenomena such as Elliot-Yafet scattering [31]. In Elliot-Yafet scattering, electron spin flips upon scattering by a phonon. This scattering has a critical role in the laser induced thermalization of the three baths. Upon reaching an an equilibrium temperature (T) among the baths, the cooling process follows the Curie-Weiss Law [6] as the equation 2.13.

$$M_s(T) = M_s(t = 0)[1 - \left(\frac{T}{T_C}\right)^{\zeta}] \quad (2.13)$$

In this equation, $M_s(T)$ is the recovered magnetization at the equilibrium temperature T, and ζ is a material-dependent parameter. The ultrafast manipulation of magnetization forms a highly non-equilibrium state among the thermal baths and there are multiple different ways of thermal relaxation. There is ongoing debate and rigorous research on the origin of the ultrafast demagnetization [83, 149, 156, 157]. The spin-phonon or electron-phonon scattering and angular momentum transfer mechanisms need to be elucidated clearly in the ultrafast manipulation of magnetization in magnetic metals. Two different approaches have been explained for ultrafast loss of magnetization; first, the transfer of local angular momentum by super-diffusive spin currents [149]. The second mechanism is Elliot-Yafet scattering, which explains the spin flip by spin-phonon scattering. Despite the considerable success in both approaches, a theory which clearly explains such ultrafast excitation mechanisms is missing in femto-magnetism.

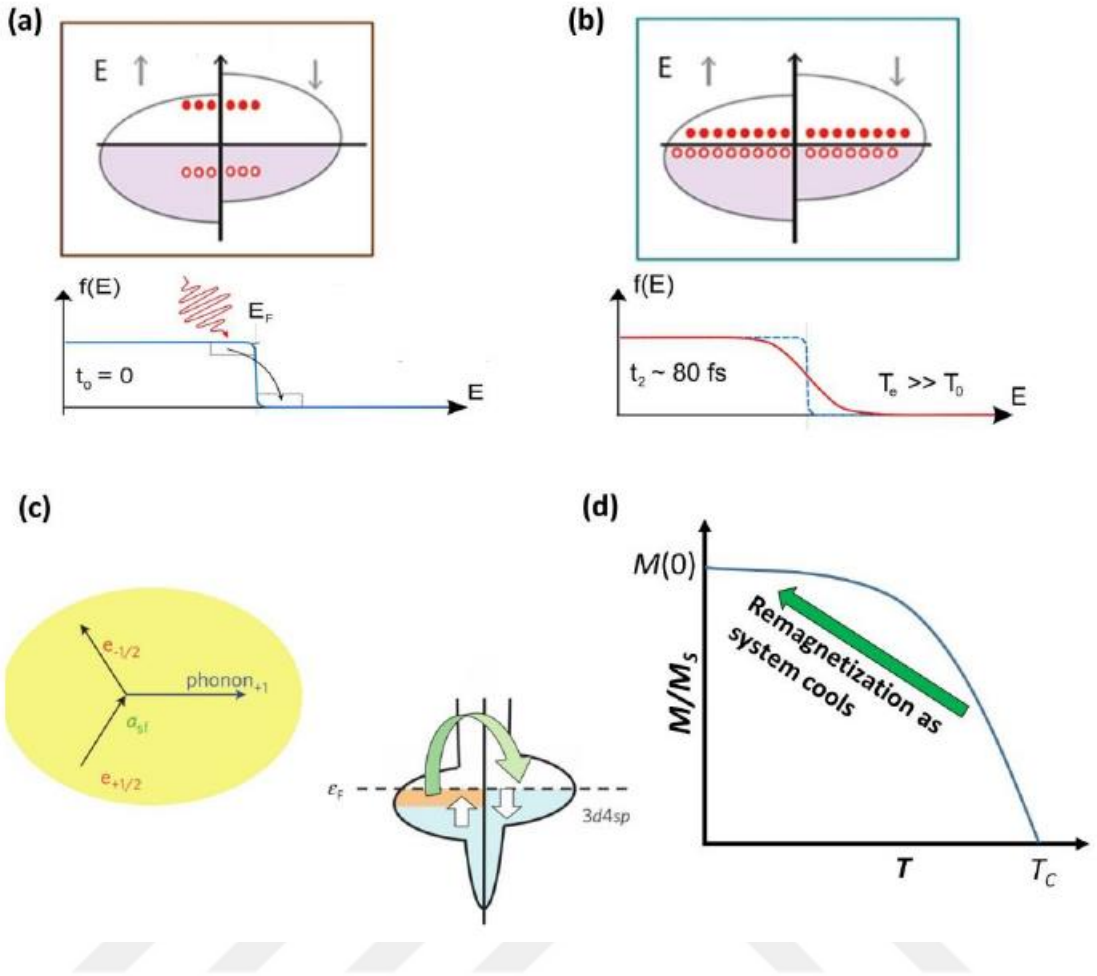

Figure 2.27: The sequential events in ultrafast thermal demagnetization (a) non-thermal excitation of a few electrons due to the absorption of laser energy (a few femtosecond), (b) Fermi-Dirac distribution of electrons due to laser thermalization (sub-picosecond) [14], (c) Elliot-Yafet scattering and spin flip of the electrons by phonons [83], (d) Thermal baths equilibrium cool down and magnetization recovery.

An improved understanding of femto-magnetism in metals could enable new applications. Some of these future applications of all-optical magnetization control by femtosecond laser pulses include THz sensing and efficient detection of light for telecommunications, spintronic logic, data storage, and quantum computation. Understanding the underlying mechanisms implies understanding the interaction of photons with charges, spins, and lattice, as well as the angular momentum transfer between them.

Chapter 3

PERPENDICULAR MAGNETIC ANISOTROPY CONTROL IN RARE EARTH IRON GARNETS

3.1 Out of plane magnetic anisotropy in rare earth iron garnet thin films for spintronic applications

This section is based on the publication "*Thin film rare earth iron garnets with perpendicular magnetic anisotropy for spintronic applications"* S. Mokarian Zanjani, M. C. Onbasli, AIP Advances 9, 035024 (2019). Reproduced (or "Reproduced in part") with permission from AIP Publishing Copyright 2019.

Perpendicular magnetic anisotropy (PMA) in iron garnet thin films is important to achieve many spintronic applications such as spin-orbit switching. In this section, we conduct a computational investigation on the PMA control in Holmium Iron Garnet (HoIG) films by tuning substrate strain when the film is grown on five different (111) single crystal garnet substrates of Gadolinium Gallium Garnet (GGG, $Gd_3Ga_5O_{12}$), Substituted Gadolinium Gallium Garnet (sGGG, $Gd_3Sc_2Ga_3O_{12}$), Terbium Gallium Garnet (TGG, $Tb_3Ga_5O_{12}$), Yttrium Aluminum Garnet (YAG, $Y_3Al_5O_{12}$), and Neodymium Gallium Garnet (NGG, $Nd_3Ga_5O_{12}$). The factor that determines the easy magnetization axis of the film to be perpendicular to the film surface, is that the effective anisotropy energy density, $K_{eff} < 0$, and anisotropy field, $H_a < 0$ to have negative sign. We show that magnetoelastic anisotropy energy density can be manipulated by changing the lattice parameter mismatch of the film and its substrate, and it determines the sign of the total anisotropy energy density. Based on our calculations, HoIG grown on GGG, TGG and YAG is predicted to have PMA among all five substrates mentioned. In addition, the magnitude of the saturation field is calculated as an order of several hundreds of Oersteds, which is feasible in practical applications to saturate rare earth iron garnets with perpendicular magnetic anisotropy.

3.1.1 Introduction

It is necessary for magnetization to be perpendicular for low current density spin-orbit switching for fast and reliable response [33]. Due to their low Gilbert damping and their controllable magnetic properties, insulating magnetic iron garnets were subject of interest in the recent decays [51-53]. The most common material for spin wave propagation and

spintronic application is Yttrium Iron Garnet ($Y_3Fe_5O_{12}$, YIG) [44]. The magnetic properties of YIG could can be tuned by substituting other rare earth elements instead of Y sites [158]. YIG films have easy axis parallel to the film plane since they have large shape anisotropy and low magnetocrystalline anisotropy. The latter term is defined as dependence of the magnetic energy to the direction because of the crystal and bonding structure. Due to the challenging fabrication procedures of PMA YIG film with high quality, new iron garnet thin films with easy axis perpendicular to the film plane and also various saturation fields are required.

Using anisotropy energy density terms, one could describe the magnetic properties of magnetic thin films of any kind [139], The magnetic anisotropy energy density is defined as the angle-dependent magnetic energy of a material. According to the second law of thermodynamics, in absence of any external magnetic field, the total energy of a magnetic material is minimized when its magnetization vector orientation is aligned along its minimum total energy direction, also known as the easy axis [159]. There are three terms in the magnetic thin film's anisotropy energy density [160] which may change the easy axis; magnetocrystalline, shape, and magnetoelastic. PMA can be achieved in a magnetic material by engineering these three energy terms. When the in-plane strain ($\varepsilon_{\parallel}$) increases, magnetoelastic anisotropy increases as well which might lead to PMA [161]. The dependence of the magnetic anisotropy to the strain of REIG thin films, such as YIG, has been reported in the former studies [162-165]. When the anisotropy originating from the lattice mismatch could overcome the shape anisotropy term, the magnetic hysteresis loop becomes square with high remanence, low and out-of-plane saturation field [47]. YIG was reported to show PMA when it is grown on SGGG (substituted-Gadolinium Gallium Garnet) substrate [166]. It is important for the researchers to be able to fabricate new cases of iron garnet thin films with different saturation fields, Gilbert damping with PMA to test the influence of changing H_s, and on magnetization and magneto-optical switching as well as other spin-related phenomena [33, 41, 42].

In this part, we conduct a systematic calculation of the anisotropy energy density terms to be able to understand the ways to reach PMA for epitaxial Holmium iron garnet ($Ho_3Fe_5O_{12}$, HoIG) thin films grown on different single crystal garnet substrates with (111) orientation: GGG (Gadolinium Gallium Garnet, $Gd_3Ga_5O_{12}$), NGG (Neodymium Gallium Garnet, $Nd_3Ga_5O_{12}$), YAG (Yttrium Aluminum Garnet, $Y_3Al_5O_{12}$), sGGG (Substituted-Gadolinium Gallium Garnet, $Gd_3Sc_2Ga_3O_{12}$), TGG (Terbium Gallium

Garnet, $Tb_3Ga_5O_{12}$). We demonstrate that by utilizing various substrates, one could change the magnetic anisotropy contributing terms and alter the easy axis of magnetization in these thin films. Altering the magnetic anisotropy energy density is useful to tune the magnetic fields needed to saturate the magnetization in HoIG films, H_a, so called the anisotropy field. At last, we investigate the sensitivity of the magnetic anisotropy terms on the variability in the experimental terms which change the strain of the magnetic thin film.

We chose HoIG since it was not studied extensively in the previous spintronic researches. However, there are numerous promising applications, including magneto-optical response [46], multiferroicity [68], low compensation temperature (near 120 K) which was used in cryogenic ultrafast quantum spintronic experimental studies [66], chemotherapy and cancer radiotherapy [67] alongside with its controllable saturation magnetic fields. Compared with YIG, HoIG is appealing since the stoichiometric thin film was demonstrated to show PMA in a previous experimental studies [167]. Different method for achieving PMA in HoIG was reported by Suchomski et al. [168] in a mesoporous structure in thin film when it was grown on (001)-oriented Si substrate. In this study, due to reduced shape anisotropy and increased magnetoelastic and growth anisotropy, PMA is predicted in HoIG. PMA does not depend on the lattice parameter difference between the film and the substrate. The PMA in HoIG is due to the intrinsic strain induced to the film because of its porous structure. As a result, the strain of the film can be controlled either by choice of substrate, or the synthesis and processing methods.

3.1.2 Methods of calculation of anisotropy energy density

The main terms in the effective anisotropy energy density are shape anisotropy (K_{shape}), magnetoelastic anisotropy (K_{indu}) and magnetocrystalline anisotropy (K_1) shown in equation 3.1 [166];

$$K_{eff} = K_{shape} + K_{indu} + K_1 \tag{3.1}$$

Shape anisotropy, is one of the best-known anisotropy terms related to magnetic materials [169, 170]. It changes due to the variation in the geometry and the intrinsic saturation magnetization (M_s) of the magnetic material. The demagnetizing effect of the shape anisotropy on the effective anisotropy energy density has been determined. In case of the thin films, the shape anisotropy energy is defined as $K_{shape} = 2\pi M_s^2$ [166]. For calculation of shape anisotropy, we consider the M_s as constant with the film thickness,

although it depends on the temperature [101, 171]. In this study, we also use material parameters measured at room temperature (300 K).

Magnetoelastic coupling (or magnetostrictive anisotropy energy density) is due to the strain induced inside the film during the epitaxial growth of the thin film [172]. Depending on the sign of the film lattice strain ($\varepsilon_{\parallel}$) and the (111)-oriented magnetostrictive constants of the films (λ_{111}), the magnetoelastic anisotropy term makes the magnetization vector to align along perpendicular axis. The elastic strain-related magnetic properties of the film is quantified by λ_{111}. Strain-induced anisotropy energy density of a garnet film grown on a (111) substrate, which is magnetized along [111] direction is formulated by $K_{indu} = -\frac{3}{2}\lambda_{111}\sigma_{||}$ [166, 173]. The term $\sigma_{||}$ is the in-plane stress induced in the thin film due to the mismatch between the lattice constaants of the film and the substrate, $\sigma_{||} = \frac{Y}{1-\nu}\varepsilon_{||}$ [174]. Y is the Young's modulus of HoIG, and ν is the poison ratio which are considered 2.00×10^{12} dyne·cm^{-2} and 0.29, respectively [175]. Using $\varepsilon_{||} = \frac{a_s - a_f}{a_f}$, strain inside the film is calculated. In this formula a_s is lattice parameters of the substrate and a_f represent the thin film lattice constant [172].

The magnetocrystalline anisotropy (K_1), contributes the least in the effective anisotropy energy. It is defined as an intrinsic effect which depends on the stoichiometry with the origin of the bonding direction of the magnetic thin film [176]. We used the first order magnetocrystalline anisotropy (K_1) of the HoIG's at room temperature (300K) [177].

The anisotropy field, H_a could be calculated once we obtain the value of effective anisotropy energy density in equation 3.2 [166]. H_a could be defined as the required magnetic field for saturation of the garnet films.

$$H_a = \frac{2K_{eff}}{M_s} \tag{3.2}$$

In Figure 3.1, we show that the elastic strain may lead to the in-plane magnetic easy axis of HoIG from to get out-of-plane. The strain in the lattice originates from the difference between the lattice parameter of the film (a_f) and the substrate (a_s). It is shown that if the lattice parameter of the substrate is smaller than that of the film (a_s-a_f = Δa < 0), compressive in-plane strain is induced inside the film ($\varepsilon_{\parallel}$<0), and the magnetoelastic anisotropy energy density will become negative. Since magnetostrictive term, K_{indu} , is at least one order of magnitude stronger in equation 3.1, $\varepsilon_{\parallel}$ < 0 leads to K_{eff} < 0 and

eventually $H_a < 0$. Also, positive lattice mismatch between the film and the substrate, $\Delta a > 0$, forced the strain inside the film to be tensile, that leads to positive effective anisotropy energy density and field. The unit cell of the film (with lattice parameter of a_f) and the substrate (with the lattice parameter of a_s) are shown Figure 3.1.

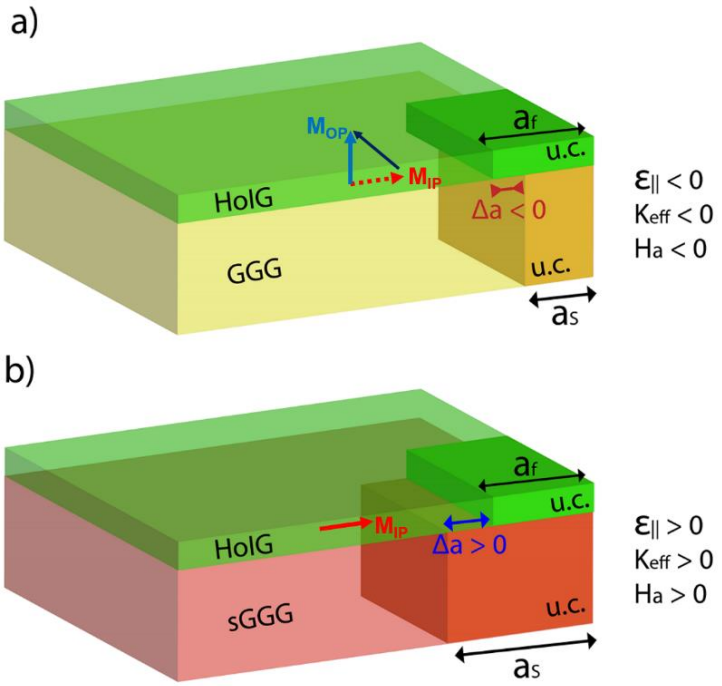

Figure. 3.1: Schematic of IP and OP strain, induced by lattice mismatch of the HoIG film unit cell (a_f) and substrate unit cell (a_s). (a) When $a_f > a_s$, the film strain is compressive and anisotropy energy density and field are negative. (b) Since $a_f < a_s$, the strain inside HoIG film is tensile and leads to positive anisotropy energy density and field. The dark yellow and the red color show the GGG and the sGGG unit cells, respectively.

3.1.3 HoIG magnetic anisotropy field

Each parameter that influences the anisotropy energy density terms of HoIG and also the calculated anisotropy energy density values at room temperature are shown on Table 3.1. Five commercially available substrates, GGG, YAG, TGG, sGGG and NGG have been used in our calculations. The film and the substrates lattice parameters are used from the previous data [98]. The calculated strain using a_s and a_f values for a fully lattice-matched film $\varepsilon_{\parallel}$, and also, magnetostrictive constants along (111) direction, λ_{111}, are presented on columns 5 and 6. The rest of the columns include the calculated magnetoelastic anisotropy K_{indu}, first-order magnetocrystalline anisotropy energy density, K_1, and the effective magnetic anisotropy energy density, K_{eff}. The field needed to saturate the thin film, known as anisotropy field H_a, is calculated on 10^{th} column.

Table 3.1: The effect of substrate on total anisotropy field of Holmium Iron Garnet (HoIG) with lattice parameter of 12.4 Å.

Subs.	**M_s (Oe)**	**K_{shape} (erg/cm^3)**	**a_s(Å)**	**$\varepsilon_{\parallel}$**	**λ_{111}**	**K_{indu} (erg/cm^3)**	**K_1 (300K) (erg/cm^3)**	**K_{eff} (erg/cm^3)**	**H_a (Oe)**
GGG	55.732	1.95×10^{4}	12.383	-1.37×10^{-3}	-4.00×10^{-6}	-2.32×10^{4}	-5.00×10^{3}	-8.66×10^{3}	-3.11×10^{2}
YAG	55.732	1.95×10^{4}	12.005	-3.19×10^{-2}	-4.00×10^{-6}	-5.38×10^{5}	-5.00×10^{3}	-5.24×10^{5}	-1.88×10^{4}
TGG	55.732	1.95×10^{4}	12.355	-3.63×10^{-3}	-4.00×10^{-6}	-6.13×10^{4}	-5.00×10^{3}	-4.68×10^{4}	-1.68×10^{3}
sGGG	55.732	1.95×10^{4}	12.48	6.45×10^{-3}	-4.00×10^{-6}	1.09×10^{5}	-5.00×10^{3}	1.24×10^{5}	4.43×10^{3}
NGG	55.732	1.95×10^{4}	12.509	8.79×10^{-3}	-4.00×10^{-6}	1.49×10^{5}	-5.00×10^{3}	1.63×10^{5}	5.85×10^{3}

We chose the sign convention for H_a according to [175], which states the negative K_{eff} and H_a shows PMA in the magnetic film. To follow this convention in equation 3.1, we should have $K_{indu} < 0$ and large to overcome K_{shape}. Because the room temperature magnetostrictive constant of HoIG, λ_{111}, is negative, the in-plane strain should be negative (compressive, $\varepsilon_{\parallel} < 0$) to have $K_{indu} < 0$.

3.1.4 Effect of substrate on total anisotropy field

The anisotropy term which reflects the effect of substrate on the total anisotropy is the magnetoelastic anisotropy energy density. The strain sign (negative or positive) originating from film-substrate lattice mismatch determines the sign of the magnetoelastic anisotropy term. Epitaxial HoIG with lattice constant of 12.4 Å grown on GGG (12.383 Å), YAG (12.005 Å), and TGG (12.355 Å) substrates, exhibits negative strain since the lattice constants of these garnet substrates are smaller than that of the film. When YAG is considered as a substrate the in-plane strain value is the largest around 3% in HoIG. As a result, the K_{indu} is negative and large enough to overcome shape and magnetocrystalline anisotropies. This leads to PMA in HoIG magnetic thin film, with $H_a < 0$. According to Table 3.1, the required field to saturate the HoIG thin film is experimentally feasible, which could be used in integrated magnonic device applications, especially when the substrate is GGG (with saturation field of -311 Oe). Due to the induced tensile strain ($\varepsilon_{\parallel} > 0$) originating from their larger lattice parameters than that of the HoIG, sGGG and

NGG substrates do not yield PMA combination with HoIG. As a result, $H_a < 0$ and these substrates do not suit HoIG with PMA.

Figure 3.2 shows the influence of various substrates on total anisotropy field of HoIG. According to these graphs, GGG, YAG and TGG substrates are appropriate candidates for negative strain induction inside HoIG thin film, as they yield $H_a < 0$ in HoIG in these film-substrate pairs. In Figure 3.2a, the anisotropy fields and strains of HoIG films on each substrates are compared. The sensitivity of the total anisotropy field to the strain relaxation is shown in Figure 3.2b. Note that thin films exhibiting strains above 1-2% might show spontaneous relation in growth procedure and the experiments.

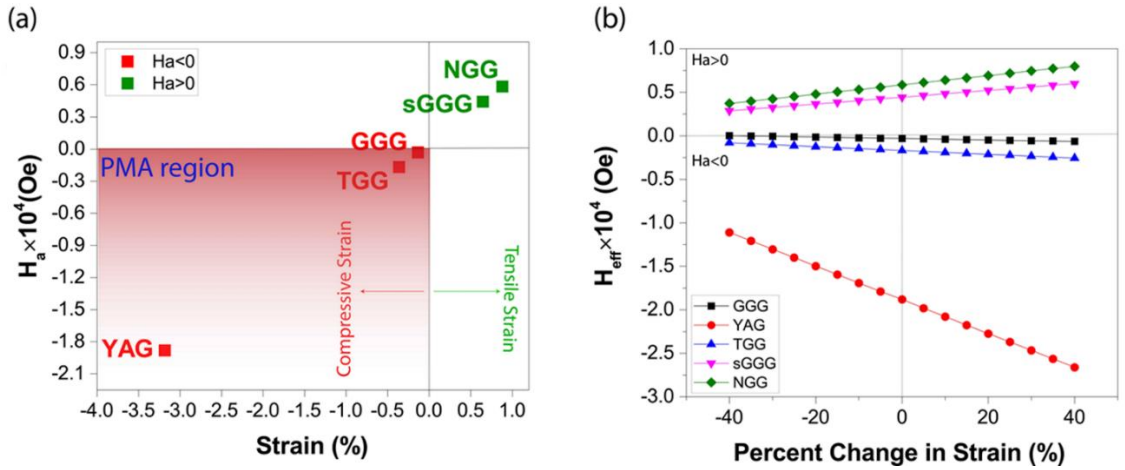

Figure 3.2: (a) The influence of substrate choice on effective magnetic anisotropy field of HoIG. Compressive strain is induced in the film using YAG, TGG and GGG substrates. As a result $H_a < 0$ defines PMA in HoIG thin film. Using NGG and sGGG yields tensile strain inside film, which leads to $H_a > 0$. (b) Anisotropy field is sensitive to the partial strain relaxation due to experimental variations. The easy axis orientation does not change despite the increase in the magnitude of the total anisotropy field with increasing strain, except when HoIG is grown on GGG. In case of thick HoIG grown on GGG with 40% relaxation of strain, the easy axis turns from OP to IP.

According to Figure 3.2a, it is necessary for film lattice parameters to be larger than that of substrate to have $\varepsilon_{\parallel} < 0$ and $K_{indu} < 0$. Hence, the $H_a > 0$ and IP anisotropy in HoIG film is the result of the induced tensile stress in HoIG thin film from sGGG and NGG substrates. It is possible in the experiments and fabrication processes to change strain due to partial strain relaxation. The variability in the film strain might also arise from the tabulated mechanical properties such as Young's modulus and poison ratio of the HoIG film that might alter in different growth conditions. Therefore, the film strain might be variable compared to the ideal lattice mismatch in the film-substrate. In Figure 3.2b, the total anisotropy field values of HoIG thin films grown on the different substrates are shown for the conditions when film is strain-relaxed up to 40% due to the critical film

thickness or presence of the growth-induced microstructures such as oxygen vacancies. So, we studied the influence of partial relaxation in the film strain on magnetic anisotropy in Figure 3.2b. The easy axis orientation does not change despite the increase in the magnitude of the total anisotropy field with increasing strain, except when HoIG is grown on GGG. In case of thick HoIG grown on GGG with 40% or more strain relaxation, the easy axis turns from OP to IP.

3.1.5 Conclusions

In this section, we studied the influence of lattice strain on the total anisotropy field (H_a) required for magnetic saturation of the HoIG thin film. The influence of the induced lattice strain in HoIG by various substrates (GGG, sGGG, TGG, YAG, and NGG) is investigated by substrate-induced strains in HoIG magnetic thin film due to the lattice constant difference in between the substrate and the film. Our calculation results show that if the lattice constant of the substrate is smaller than that of the film, $K_{indu} < 0$ as due to the induced compressive strain in the magnetic thin film. According to the anisotropy field values we calculated, HoIG films are predicted to have PMA ($\varepsilon_{\parallel} < 0$ results $K_{eff} < 0$, and $H_a < 0$), when epitaxially grown on TGG, GGG, and YAG. Considering the strain variations of the substrate, the film exhibits in-plane easy axis grown on sGGG and NGG. Increased film thickness would result in strain relaxation since the lattice matching might vanish in those thickness regimes. Consequently, saturation fields decrease in thicker films, due to their lower strain, and we might reach more feasible fields for spin-orbit or magnonic device applications. HoIG with less than a few nm thickness is PMA, when it is grown on GGG substrate. Above this critical thickness, the film experiences around 40% strain relaxation and its easy axis becomes IP. Thus, to have PMA, it is necessary for HoIG to be grown with thicknesses below a specific critical thickness, to be suitable for spintronic device applications, using GGG substrate.

Our predictions for PMA are experimentally testable. HoIG have more robust PMA than similar REIG thin films such as YIG due to its smaller saturation magnetization. Since the shape anisotropy energy is smaller due to its smaller M_s, the energy barrier to have PMA is smaller and magnetoelastic strain term could used for obtaining PMA in HoIG.

3.2 Novel rare earth iron garnet thin films with out of plane magnetic anisotropy

This section is based on the publication "*Predicting New Iron Garnet Thin Films with Perpendicular Magnetic Anisotropy*" S. Mokarian Zanjani, M. C. Onbasli, Journal of Magnetism and Magnetic Materials, 499 (2020) 1661082. Reproduced (or "Reproduced in part") with permission from Elsevier Copyright 2020.

Numerous spintronic applications necessitates the perpendicular magnetic anisotropy (PMA). These applications include memory, spin-orbit torque switching, and logic devices. Iron garnets, which have reduced Gilbert damping, are significant group of magnetic insulators. There are not many PMA garnets which are experimentally reported so far. Some of the examples are samarium and terbium iron garnet. In order to be able to study novel phenomena in the spintronic field more PMA garnets are required. In this section, we report our prediction of PMA in twenty new iron garnet film-substrate pairs based on our total effective magnetic anisotropy calculations. We calculated the total anisotropy energies of ten various lattice-matched iron garnet thin films on five commercially-available garnet substrates. The parameters that give rise to PMA in magnetic iron garnets are compressive or tensile strain, which depends on the substrate choice, and the magnetostriction constants value and their signs. We provide guidelines for obtaining PMA in magnetic rare earth iron garnet films. New PMA iron garnet thin films with tunable saturation moments could help develop new magnonic devices and spin-orbit torque memory elements.

3.2.1 Introduction

Sputtering and pulsed laser deposition have developed the growth of magnetic iron garnet thin films with high quality and reduced Gilbert damping. Therefore, it has provided the opportunity for researchers to study an extensive range of novel spin wave phenomena and magnetization switching [41-43]. YIG (Yttrium iron garnet, $Y_3Fe_5O_{12}$) is one of the most extensively studied REIG for such applications [44]. Its Gilbert damping is very low that allows the on-chip propagation of spin waves up to millimeters. However, the magnetization easy axis of YIG is parallel to the film plane; so, they cannot be used in various spin mechanisms like Rashba-Edelstein effect, spin-orbit torques, forward volume magnetostatic spin waves, and logic devices [41]. On the other hand, PMA is a necessary condition for fast and reliable response in spin-orbit torque switching using low current densities [33]. In addition, the Dzyaloshinskii–Moriya interaction (DMI) in

thulium iron garnet grown on GGG substrate enables the skyrmions stabilization and skyrmion motion by spin currents [45].

In order to tune the magnetic anisotropy for PMA in magnetic insulating thin films, numerous studies have been conducted [38, 46-50]. Insulating magnetic iron garnets with their tunable magnetic properties have attracted wide research interest previously [51-53]. Their reduced damping and high magneto-optical Faraday rotation make them significant candidates among the materials investigated. Engineering the magnetic anisotropy terms is the method of obtaining out-of-plane magnetic easy axis. The easy axis of the magnetic material dictates the relaxation of magnetization vector orientation along its least energy axis, in the absence of the external magnetic field. The magnetization switching rates and the stability of total magnetization vector are derived by this energy minimization. By tuning the magnetic anisotropy in REIG thin films the researchers in the field of spintronic could test novel switching phenomena based on PMA. In addition, the study of ultrafast spin dynamics and magnetic response in thin films and nanostructures which is driven by magnetic anisotropy become feasible.

Due to its small magnetocrystalline anisotropy and large shape anisotropy, the magnetic easy axis of the most commonly studied YIG films generally lie in-plane [43]. Despite the previous reports of PMA in epitaxial YIG thin films [165, 166], the complexity of their fabrication conditions makes variations in PMA film while strain effects could alter magnetoelastic anisotropy in YIG. Polycrystalline YIG ultrathin have shown magnetic anisotropy controlled by strain [165, 178]. Yet, in case of very high change in oxygen stoichiometry, for YIG magnetic thin film on GGG substrate, it is possible to partially control the magnetic anisotropy [161]. Bu this leads to the increase in the damping. Due to the difficult fabrication of the YIG thin films on GGG with high structural and surface quality, substitution of Y by other RE elements have been the subject of intense research [158, 179, 180]. It is necessary to develop new REIG thin films with PMA that exhibit various saturation fields, compensation points, coercivities, and controllable Gilbert damping for evaluation of their influence in the optimization of the insulator-based spintronic devices.

Several studies include the methods, such as nano-patterning, to reduce the shape anisotropy effect in YIG as it is the dominant contributing magnetic anisotropy [107, 181, 182]. As shown in Figure 3.3 schematic, YIG thin film was patterned by lithography to a

rectangular nano-strips with the thickness of a few nanometers. Therefore, the required saturation magnetic field is minimized along the longest direction of the rectangular pattern. If the thickness of the grown YIG film is very low, the magnetostrictive contribution becomes the dominant energy term which leads to the negative saturation field and out of plane magnetic anisotropy [107]. Due to the reduced influence of the shape term in the anisotropy energy, IP anisotropy is switched to OP when the ratio of the thickness to the length is decreased [165].

Figure 3.2b shows that reduction of the shape anisotropy effect should be accompanied by the increasing the magnetoelastic energy contribution in order to switch the easy axis orientation to the out-of-plane direction. For this, strain inside the REIG films dominates the shape term and yield PMA [163, 165, 166, 183]. A sign of the PMA observation in the magnetic thin film is the square shape of the magnetic hysteresis loop, when the shape anisotropy is small enough to be overcame by strain-induced anisotropy [47]. It is also reported that PMA is achievable in REIG as the result of mismatch between lattice parameters of the film and the substrate. For example in the previous studies, PMA has been achieved by utilizing SGGG substrate and a very thin buffer layer of samarium gallium garnet (SmGG) above and under YIG ultrathin film [166]. When the thickness of the YIG thin film is increased (i.e. 40 nm), the easy axis returns to in-plane again. Kubota et al. [161] showed that by increasing the strain parallel to the film plane ($\varepsilon_{\parallel}$), one could gain PMA. In addition, when the magnetostriction coefficient (λ_{111}) has a large and negative value, it could overcome the shape term and the easy axis gets OP. In the specific case of TmIG (Thulium iron garnet, $Tm_3Fe_5O_{12}$) the tensile strain inside the film ($\varepsilon_{\parallel} > 0$) leads to PMA [47, 161].

Another way of the strain induced anisotropy is the presence of the porosity in the magnetic thin film structure. Holmium Iron Garnet ($Ho_3Fe_5O_{12}$, HoIG) thin film with mesoporous structure grown on Si (001) substrate [168] shows PMA. The reason is that the shape anisotropy is reduced growth-induced and magnetostrictive anisotropies are increased. In fact, the strain induced anisotropy does not rely on the substrate in this case. The pores in the film structure were not dependent on any thermal or mechanical strain as the result of the lattice mismatch between the film and the substrate. On the other hand, the imposed strain inside the film comes from the porous structure during the process. Therefore, for overcoming the shape effect by strain, one could not only control it by choosing a proper substrate, but also can engineer the microstructure of the thin film.

Doping the crystal structure with substitution of other chemical element can be mentioned as another method to tune the magnetic anisotropy. In this case, the strain is induced during the doping process thanks to the growth-induced anisotropy effects, and also lattice distortion. Figure 3.3c shows this effect schematically. By doping the REIG thin films with Bi (Bi:YIG and Bi:GdIG) the high annealing temperature alters the film chemical and yield PMA [106, 180, 184]. Also PMA in such thin films is due to the GGG substrate-induced strain [185]. In addition, doping the He atoms, so called Helium implantation, into the oxides was reported to be method for local and reversible tuning of MA [186]. Another example is $Tb_xY_{3-x}Fe_5O_{12}$ (x=2.5, 2.0, 1.0, 0.37) grown by spontaneous nucleation technique [187], for which the decrease in Tb concentration lead to altering the magnetic easy axis from [111] direction to [100]. The change in the MA could be as the result of the temperature change, which alters the first-order magnetocrystalline anisotropy. Some of the examples could be mentioned as change in the sign of K_1 at around 190 K, and also the K_1 change in the YIG films [188]. Therefore, the highlighted role of the temperature on lattice distortion and change in MA, as well as magnetic compensation, could not be neglected.

In this section, we conduct a systematic calculation of the anisotropy energies of ten various epitaxial lattice-matched RE iron garnet thin films ($X_3Fe_5O_{12}$, X = Y, Tm, Dy, Ho, Er, Yb, Tb, Gd, Sm, Eu) on five garnet substrates which are available commercially and oriented in (111) direction. These substrates include $Gd_3Ga_5O_{12}$ (GGG), $Nd_3Ga_5O_{12}$ (NGG), $Y_3Al_5O_{12}$ (YAG), $Gd_3Sc_2Ga_3O_{12}$ (SGGG), and $Tb_3Ga_5O_{12}$ (TGG). Among fifty different film-substrate combinations, twenty cases were found to be candidates for PMA at room temperature. Only seven out of twenty film-substrate cases have been tested in the previous experimental studies, which show PMA. The thirteen remaining pairs, have not been subjected to the experimental tests for PMA characteristics. We show by means of systematic MA calculations that to overcome shape, large MA induced by strain terms is needed in the highly strained thin films. Only the RT values of λ_{111} [92] were used in this study and our predictions are only valid for RT (300K). To be able to distinguish REIG thin films based on the RE element we labelled them as XIG (X = Y, Gd, Er, Dy, Tb, Tm, Sm, Ho, Yb, Eu), i.e. SmIG (Samarium iron garnet) etc., through the rest of this study. Our model accurately valid for prediction of the magnetic EA in almost all REIG thin film-substrate combinations which are experimentally tested. This is satisfied under

the condition that calculations are done based on the real film properties in our model and also the experimentally grown thin films possess the cubic lattice matched film properties.

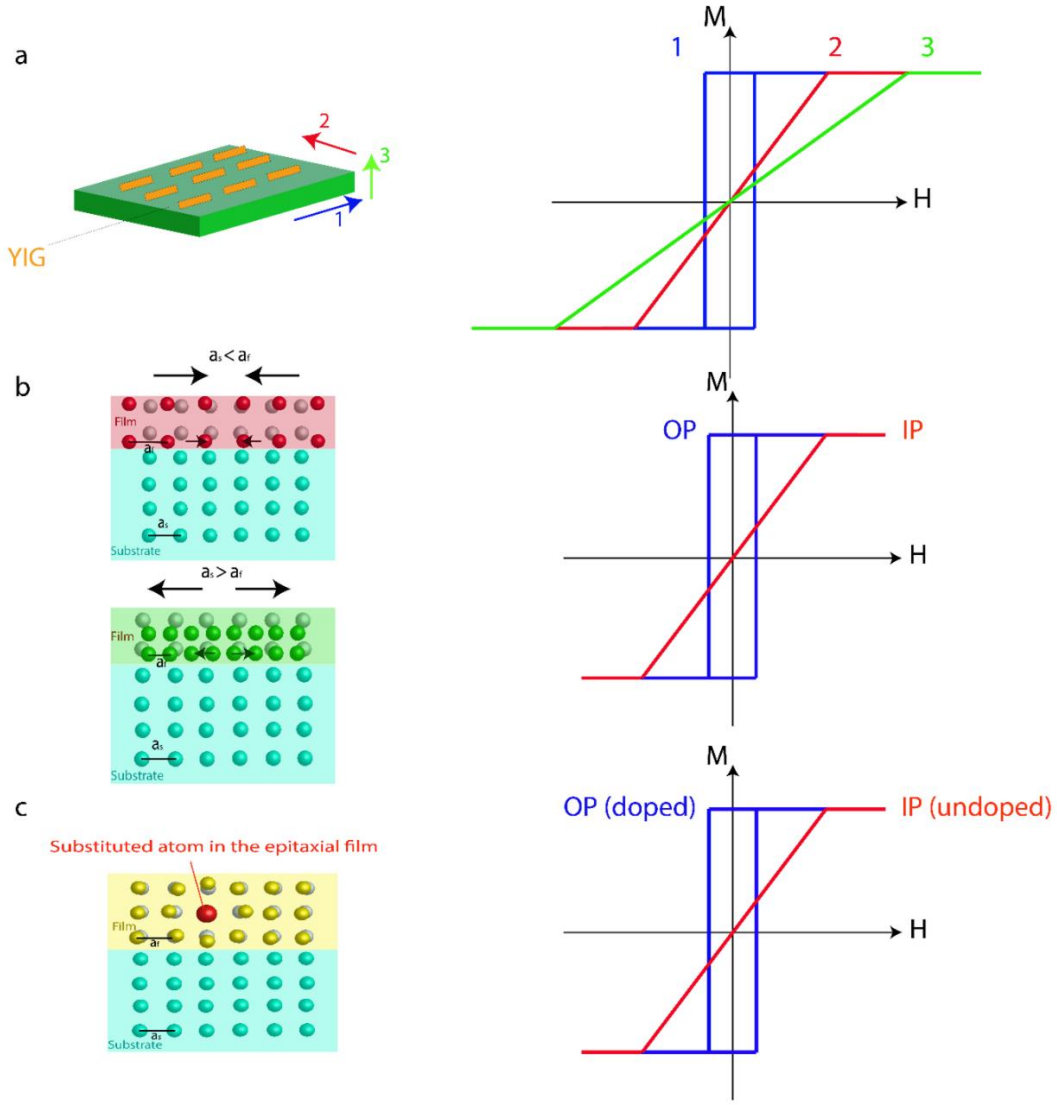

Figure 3.3: Methods of achieving perpendicular magnetic anisotropy in iron garnet thin films. (a) Magnetoelastic anisotropies overcome shape as the result of micro/nano-patterning and shape anisotropy. (b) Shape anisotropy must be overcome by large enough strain-induced anisotropy to result in out-of-plane EA. (c) Enhanced magnetocrystalline contribution exceeds the magnitude of shape anisotropy in the substitutional doping which changes both growth-induced and ME terms.

3.2.2 Calculation of effective anisotropy energy density

In order to determine the magnetic EA of the magnetic thin films we calculated the effective anisotropy energy density, which contains 3 main terms; shown in the equation 3.3 as the first order cubic magnetocrystalline anisotropy (K_1), shape anisotropy (K_{shape}), and strain-induced (ME) anisotropy (K_{indu}) [166].

$$K_{eff} = K_{indu} + K_{shape} + K_1 \tag{3.3}$$

When the garnet thin film is magnetized in [111] direction (i.e. (111) single crystalline substrate orientation), the magneto-elastic anisotropy energy density, resulting from ME coupling is calculated by using equation 3.4:

$$K_{indu} = -\frac{3}{2}\lambda_{111}\sigma_{||} \tag{3.4}$$

In this equation λ_{111} is the RT magnetostriction constant along [111] direction which is a negative value at RT [173]. In equation 3.4, the in-plane stress $\sigma_{||}$ is the result of lattice mismatch between the substrate and the film, and is calculated from equation 3.5 [174]:

$$\sigma_{||} = \frac{Y}{1-\nu}\varepsilon_{||} \tag{3.5}$$

, where ν is Poisson's ratio and Y is elastic modulus [175].

In-plane strain calculation is needed for the extraction of lattice parameters of the films from the XRD characterization. Equation 3.6 shows the strain relation as the difference in the lattice constant between the bulk form and the thin film normalized by the lattice constant of the thin film form of the magnetic material [166].

$$\varepsilon_{||} = \frac{a_{film}-a_{bulk}}{a_{film}} \tag{3.6}$$

We consider the lattice constants of the thin film and the substrate matches, such that the lattice parameter of the substrate could be used instead of the lattice constant of thin film in IP strain using equation 3.7 [172]:

$$\varepsilon_{||} = \frac{a_{sub}-a_{film}}{a_{film}} \tag{3.7}$$

Table 3.2 shows the lattice parameters of the film and the substrates used in calculation of the in plane strain.

The geometry-dependent shape anisotropy energy density is calculated using the intrinsic saturation magnetic moment of the magnetic REIG. With its demagnetizing effect on the effective anisotropy energy density, shape anisotropy has significant effects on magnetic FMR measurements and hysteresis loops [107].

Magneto-crystalline anisotropy and shape anisotropy are the most common anisotropy terms present in the magnetic materials [169, 170]. The shape anisotropy can be calculated for the continuous film, as the following [166]:

$$K_{shape} = 2\pi M_s^2 \tag{3.8}$$

M_s values are obtained from the temperature-dependent graphs for REIG [101, 171], Note that using the bulk M_s values the shape anisotropy energy density could be calculated using equation 3.8.

Magnetocrystalline anisotropy is an intrinsic magnetic anisotropy [176], which has a weak influence on the total anisotropy energy density compared to ME and shape anisotropies [48, 50, 161, 166]. The first order magnetocrystalline anisotropy is a parameter which is mostly considered as a temperature-dependent term and is reported in the former calculations for rare earth iron garnets [177]. The saturation field, or the anisotropy field, defined as the field needed for saturation of the anisotropic magnetic material along its EA is calculated using: $H_A = 2\frac{K_{eff}}{M_s}$.

Table 3.2: List of magnetic iron garnet thin films and garnet substrates used for this study.

Chemical formula	**Garnet material**	**Bulk lattice constant (Å)**	**Purpose**
$Gd_3Sc_2Ga_3O_{12}$	SGGG	12.480	Substrate
$Tb_3Ga_5O_{12}$	TGG	12.355	Substrate
$Y_3Al_5O_{12}$	YAG	1.005	Substrate
$Gd_3Ga_5O_{12}$	GGG	12.383	Substrate
$Nd_3Ga_5O_{12}$	NGG	12.520	Substrate
$Yb_3Fe_5O_{12}$	YbIG	12.300	Film
$Tm_3Fe_5O_{12}$	TmIG	12.324	Film
$Sm_3Fe_5O_{12}$	SmIG	12.530	Film
$Y_3Fe_5O_{12}$	YIG	12.376	Film
$Ho_3Fe_5O_{12}$	HoIG	12.400	Film
$Er_3Fe_5O_{12}$	ErIG	12.350	Film
$Tb_3Fe_5O_{12}$	TbIG	12.460	Film
$Dy_3Fe_5O_{12}$	DyIG	12.440	Film
$Gd_3Fe_5O_{12}$	GdIG	12.480	Film
$Eu_3Fe_5O_{12}$	EuIG	12.500	Film

The detailed parameters used in the calculation of the anisotropy energy density terms for REIG at RT (300K) are shown on Tables 3.2 and 3.3. The Table 3.3 only shows the predicted PMA cases out of the total fifty investigated REIG cases. The complete version of Table 3.3 including all calculated anisotropy energy density terms for all fifty film-substrate combinations are provided in the Appendix A. The M_s values [101, 171] and lattice constants [98] are extracted from the tabulated materials data. In this study, we

assumed the Poisson ratio as 0.29 and the Young's modulus 2.00×10^{12} dyne·cm^{-2} for all REIG thin film types [175]. Another assumption in these calculations is that the M_s does not alter with the film thickness and the room temperature bulk value of M_s is used in calculation of the shape anisotropy for iron garnet.

Table 3.3: Anisotropy energy density parameters calculation results. Rare earth iron garnets on GGG (a_s=12.383Å), YAG ($Y_3Al_5O_{12}$, a_s=12.005Å), SGGG (a_s=12.48Å) and TGG ($Tb_3Ga_5O_{12}$, a_s=12.355Å), and NGG ($Nd_3Ga_5O_{12}$, a_s=12.509Å) substrates, with $K_{eff} < 0$, are presented.

Film	Substrate	λ_{111} ($\times10^{-6}$)	ε ($\times10^{-3}$)	σ (dyn·cm^{-2}) ($\times10^{10}$)	K_{indu} (erg·cm^{-3}) ($\times10^{4}$)	K_1 (300K) (erg·cm^{-3}) ($\times10^{3}$)	M_s (emu·cm^{-3})	K_{shape} (erg·cm^{-3}) ($\times10^{3}$)	K_{eff} (erg·cm^{-3}) ($\times10^{3}$)	H_A (Oe) ($\times10^{3}$)
GdIG	GGG	-3.1	-7.77	-2.19	-10.2	-4.10	7.962	0.398	-106	-26.5
HoIG	TGG	-4	-3.63	-1.02	-6.13	-5.00	55.73	19.5	-46.8	-1.68
TbIG	SGGG	12	1.61	0.452	-8.14	-8.20	15.92	1.59	-88.0	-11.1
HoIG	GGG	-4	-1.37	-0.386	-2.3	-5.00	55.73	19.5	-8.66	-0.311
DyIG	YAG	-5.9	-35.0	-9.85	-87.2	-5.00	31.85	6.37	-870	-54.7
SmIG	YAG	-8.6	-41.9	-11.8	-152.3	-17.4	140	123	-1420	-20.2
SmIG	TGG	-8.6	-14.0	-3.93	-50.8	-17.4	140	123	-402	-5.74
ErIG	YAG	-4.9	-27.9	-7.87	-57.8	-6.00	79.62	39.8	-545	-13.7
YIG	YAG	-2.4	-30.0	-8.44	-30.4	-6.10	141.7	126	-184	-2.60
SmIG	GGG	-8.6	-11.7	-3.30	-42.6	-17.4	140	123	-321	-4.58
HoIG	YAG	-4	-31.9	-8.97	-53.8	-5.00	55.73	19.5	-524	-18.8
GdIG	SGGG	-3.1	0.00	0.00	0.00	-4.10	7.962	0.398	-3.70	-0.930
YbIG	YAG	-4.5	-24.0	-6.76	-45.6	-6.10	127.3	102	-360	-5.66
TmIG	YAG	-5.2	-25.9	-7.29	-56.9	-5.80	110.9	77.2	-497	-8.97
TbIG	NGG	12	3.93	1.11	-19.9	-8.20	15.92	1.59	-206	-25.9
SmIG	SGGG	-8.6	-3.99	-1.12	-14.5	-17.4	140	123	-39.3	-0.562
DyIG	TGG	-5.9	-6.83	-1.92	-17.0	-5.00	31.85	6.37	-169	-10.6
GdIG	YAG	-3.1	-38.1	-10.7	-49.9	-4.10	7.962	0.398	-502	-126
GdIG	TGG	-3.1	-10.0	-2.82	-13.1	-4.10	7.962	0.398	-135	-33.9
DyIG	GGG	-5.9	-4.58	-1.29	-11.4	-5.00	31.85	6.37	-113	-7.09

In this section, we explain how the thin films show PMA characteristic when $K_{eff} < 0$. We use the convention used in ref. [166] for sign of total MA energy. Therefore it is necessary to have negative and large value of K_{eff} to show PMA. Despite all the other garnets, TbIG possesses positive magnetostriction constants at RT, so the tensile stress in this case is desired to exhibit PMA. On the other hand, for the other REIG cases, the $\lambda_{111}$is negative; as a result, it is the sign of the strain (compressive or tensile) which determines the anisotropy state. In several former studies [166, 179, 189, 190], however, PMA was defined for both cases when the effective anisotropy energy density (K_{eff}) is negative or positive. Here, we provide an explanation to clarify this inconsistency which might result in confusion for the reader. From the thermodynamic point of view, the stable state is

defined as the lower energy state with respect to higher energy cases. With this definition, the magnetic EA is the direction along a magnetic material minimizes its energy or could get saturated with the lowest external magnetic field. So the reorientation of the magnetization direction along the EA in the magnetic material happens spontaneously to minimize its total energy. Thus, our convention here is $K_{eff} < 0$ for OP easy axis.

3.2.3 Substrate influence on the magnetic anisotropy energy density

Using different substrates changes strain in films, which also alters the ME anisotropy. Figure 3.4 shows the anisotropy energy density of REIG thin films calculated considering them grown epitaxially on five substrates: Substituted Gadolinium Gallium Garnet ($Gd_3Sc_2Ga_3O_{12}$, SGGG), Terbium Gallium Garnet ($Tb_3Ga_5O_{12}$, TGG), Gadolinium Gallium Garnet ($Gd_3Ga_5O_{12}$, GGG), Neodymium Gallium Garnet ($Nd_3Ga_5O_{12}$, NGG), and Yttrium Aluminum Garnet ($Y_3Al_5O_{12}$, YAG). As shown in Figure 3.4a, the following thin films exhibit compressive strain ($a_{substrate} < a_{film}$) when grown on GGG substrate: Samarium Iron Garnet (SmIG), Holmium Iron Garnet (HoIG), Dysprosium Iron Garnet (DyIG), Gadolinium Iron Garnet (GdIG). These film possess a negative large λ_{111}, and so the ME anisotropy energy densities will lead to the total effective anisotropy energy density to be negative and these films on GGG exhibit PMA.

According to our calculations of ME and RT-magnetocrystalline anisotropy terms (K_1), Thulium iron garnet (TmIG) grown on GGG (111) is predicted to be IP easy axis, despite several experimental studies which clearly indicate that TmIG shows PMA when it is grown on GGG (111) [1,19]. In the special case of the TmIG, considering only the effect of shape, magnetocrystalline and ME anisotropy terms do not reflect similar results compared to that of the experimental studies. In fact, the reason for PMA in TmIG/GGG (111) might originate from other anisotropy contributions like stoichiometry-driven or growth-induced anisotropy and surface anisotropy. Due to the very low thickness of the films used in such experiments (thickness < 10 nm or 5-8 unit cells) surface effects may result in nonlinear effects and might require density functional theory (DFT)-based calculations for surface anisotropy energy.

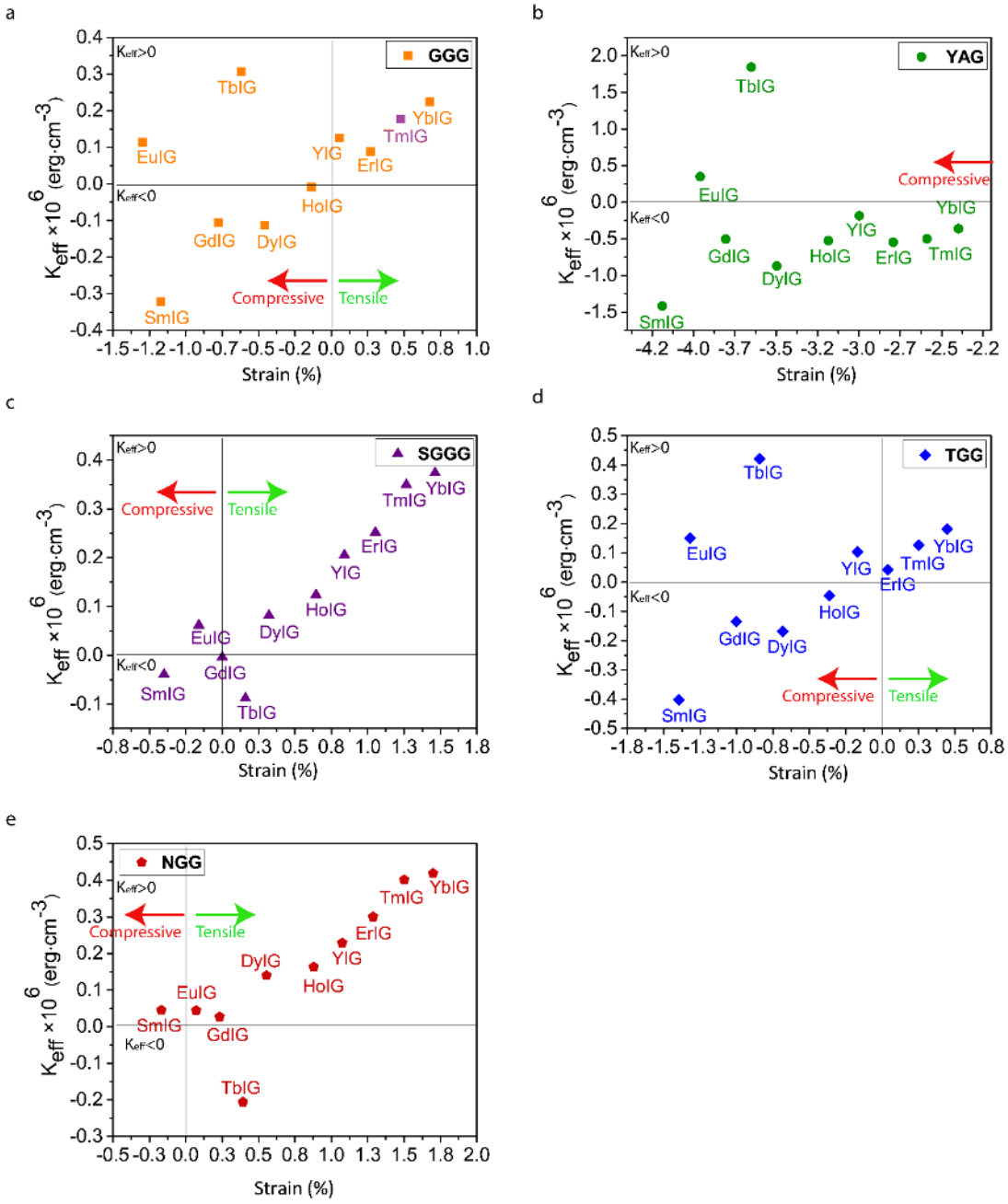

Figure 3.4: Calculated effective anisotropy values for each rare earth iron garnet thin film when they are epitaxially grown on (a) GGG, (b) YAG, (c) SGGG, (d) TGG, and (e) NGG substrates. Note that the scales of the axes are different in each part.

The lattice constant of the Yttrium Aluminum Garnet (YAG) substrate is smaller than all the REIG films in this study (a_s=12.005Å). YAG induces large in plane strain in SmIG (a_f=12.530Å),YIG (a_f=12.376Å), DyIG (a_f=12.440Å), TmIG (a_f=12.324Å), EuIG (a_f=12.500Å), ErIG (a_f=12.350Å), YbIG (a_f=12.300Å), GdIG (a_f=12.480Å), HoIG (a_f=12.400Å), and TbIG (a_f=12.460Å) thin films. As the result, the negative strain coming from YAG substrate leads to negative ME anisotropy energy density for these films. In

these REIG cases the shape anisotropy is overcome by the strain-induced anisotropy. Therefore, the negative sign of total anisotropy energy densities results these garnet films to possess PMA. EuIG (Europium Iron Garnet) and TbIG (Terbium Iron Garnet) are exceptional cases. Because, despite the fact that compressive strain induces negative ME anisotropy, magnetostriction constants of these films are positive. Consequently, they do not yield PMA, as the ME anisotropy terms become positive for both EuIG ($K_{indu\ (EuIG)}$ = 3.01×10^5 erg·cm^{-3}) and TbIG ($K_{indu\ (TbIG)} = 1.85\times10^6$ erg·cm^{-3}).

TbIG, SmIG, and GdIG can be mentioned as potential PMA garnet films grown on SGGG substrate. The growth conditions of TbIG and GdIG could be optimized for obtaining compensation point near RT which leads to zero M_s. Room temperature magnetic compensation could be useful in terahertz magnonics based on PMA garnets. Since the lattice constants of SGGG (a_s=12.48Å) substrate and GdIG (a_f =12.480Å) thin film are exactly the same, the IP strain is zero and the ME anisotropy completely vanishes. In this case, the magnetocrystalline anisotropy (-4.1×10^3 erg·cm^{-3}) is the dominant contributing term, since the M_s of GdIG, leads to small shape anisotropy (3.98×10^2 erg·cm^{-3}) which cannot overcome the magnetocrystalline term. So, the effect of magnetocrystalline anisotropy on MA of the GdIG, cannot be neglected any more. As a result, the negative anisotropy energy density of GdIG grown on SGGG substrate classifies it as a PMA garnet due to the dominant negative magnetocrystalline anisotropy energy density.

Grown on SGGG substrate, another PMA candidate of REIGs is SmIG. The lattice constant of the film is larger the substrate, and the induced strain is compressive (-3.99×10^{-3}) inside the film, which results in $K_{indu} < 0$. The magnitude of the ME anisotropy energy density ($K_{indu} = -1.45\times10^5$ erg·cm^{-3}) is comparable to, but still greater than the shape energy density ($K_{shape}=1.23\times10^5$ erg·cm^{-3}). The magnetocrystalline anisotropy of SmIG is relatively large (-1.74×10^4 erg·cm^{-3}), so it has PMA due to negative total anisotropy energy density ($K_{eff} = -4.80\times10^5$ erg·cm^{-3}). One exceptional case of REIG with positive strain is TbIG film grown on SGGG substrate. This film is experimentally shown to exhibit PMA due to its positive λ_{111} which leads to $K_{indu}<0$ [40].

Since SGGG lattice constant is greater than that of the TbIG thin film, tensile strain of $+1.61\times10^{-3}$ dyn.cm^{-2} is induced inside the film from the substrate. While the λ_{111} of TbIG is positive (in contrast to most of the REIG films listed here), the film possess large and negative ME anisotropy the magnitude of which is greater than the shape anisotropy.

Hence, in TbIG, the relatively large magnetocrystalline anisotropy could only be sufficient to overcome shape and yield PMA on SGGG substrate. The combinatorial effect of ME (-8.14×10^4 erg·cm^{-3}) and magnetocrystalline anisotropies, renders a stable PMA state in TbIG/SGGG pair.

Grown on TGG (Terbium Gallium Garnet) substrate with a_s=12.355Å, YIG, DyIG, HoIG, TbIG, GdIG, SmIG, EuIG have compressive strain, while the induced strain in TmIG, ErIG and YbIG is tensile. Due to the positive sign of the ME anisotropy cases with tensile strain, PMA cannot be achieved. On the other hand, despite its negative value, the weak ME anisotropy in YIG, TbIG and EuIG thin films cannot exceed that of the shape. Therefore, the anisotropy state of YIG, EuIG and TbIG grown on TGG is in-plane. Thanks to the negative λ_{111} values in DyIG, GdIG, HoIG, and SmIG films, the large and negative ME and consequently K_{eff} results in PMA state in these films when grown on TGG. Thus, similar to the conditions where the DyIG, HoIG, GdIG, and SmIG thin films are grown on GGG substrate, only for the cases with $\varepsilon_{\parallel}<0$, one obtains a negative and large ME anisotropy (induced by the IP strain) to overcome shape anisotropy.

Recently [160] NGG (Neodymium gallium garnet) as a substrate a new substrate was introduced for growing RE iron garnet thin films by PLD method. With its large lattice parameter in comparison with most of the bulk RE garnets, NGG induces compressive strain in all REIG except for SmIG. The sign of the ME anisotropy can be determined by the value of λ_{111} for each REIG, except for SmIG. The ME anisotropy of DyIG, TmIG, YIG, YbIG, HoIG, and ErIG is positive, which results in easy axes parallel to the film planes. In case of SmIG and EuIG grown on NGG, the shape anisotropy magnitude is so large that it cannot be overcome by ME strain and magnetocrystalline anisotropy terms. Only Terbium Iron Garnet on NGG could yield PMA, whose compressive strain is large enough to produce negative and large ME anisotropy (-2.44×10^5 erg·cm^{-3}). The tensile strain induced by NGG substrate to GdIG thin film causes IP easy axes since the magnitude of the negative magnetocrystalline anisotropy is not large enough. The combined effect of first order magnetocrystalline anisotropy term (-8.20×10^3 erg·cm^{-3}), along with the large and negative ME anisotropy term, exceeds the value of shape (1.59×10^3 erg·cm^{-3}) in TbIG grown on NGG which leads to a negative and large enough total magnetic anisotropy energy density (K_{eff} = -2.51×10^5 erg·cm^{-3}). Therefore, growing TbIG on NGG substrate is predicted to yield PMA.

From Figure 3.5, we infer that in the rare earth iron garnet films, which show negative K_{eff} originating from strain induced from the substrates, one may expect PMA. Figures 3.5a-d show the comparison between the calculated K_{eff} as a function of in-plane strain (sign and type) for TbIG, YIG, YbIG, and TmIG. We compare our calculation results with the reported experimental values of K_{eff} of TmIG, and its exact value from the experimental data [158] to Figure 3.5b. As shown on Figure 3.5b, the experimental K_{eff} of TmIG thin film is positive due to the tensile IP strain and large negative λ_{111}.

The effective anisotropy energy densities are calculated and shown in Figures 3.6a-f as a function of strain for HoIG, SmIG, EuIG, GdIG, DyIG, and ErIG. The sign of K_{eff} might be positive or a negative under both tensile and compressive strain, depending on the signs of λ_{111} of REIG thin film type. In most of the REIG thin films that exhibit PMA on any given substrates, PMA is achieved under compressive in-plane strain. So compressive strain should be considered in the experimental studies. Due to the positive sign of the magnetostictive constant, TbIG is an exception. In this film PMA is gained as the result of tensile strain when it is grown on SGGG and NGG substrates. In addition to the ME anisotropy, the large and negative magnetocrystalline anisotropy already overcomes shape, in both cases, and yield PMA.

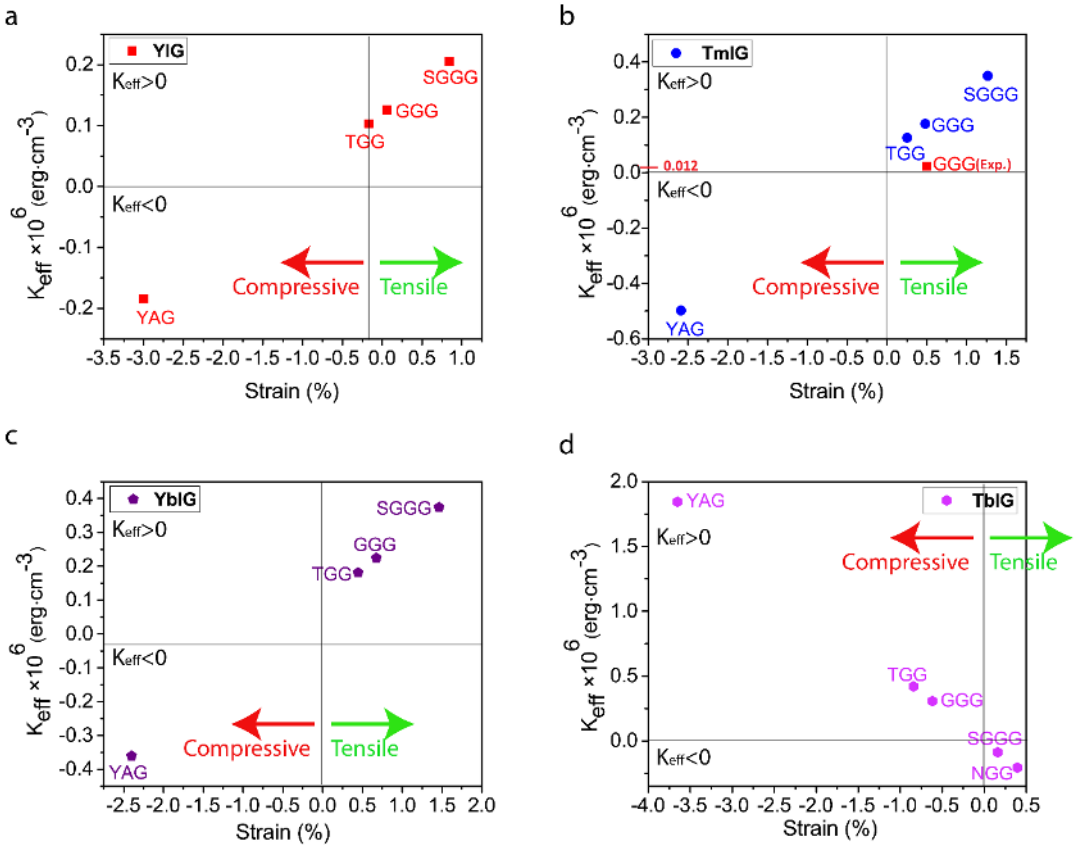

Figure 3.5: Influence of substrate induced strain on the total anisotropy energy densities of (a) YIG, (b) TmIG, the data inserted on the graph, with red square symbol, GGG (Exp.), is the experimental value of effective anisotropy energy of TmIG on GGG based on ref. [158] (c) YbIG, and (d) TbIG. Note that the axes scales are different in each part.

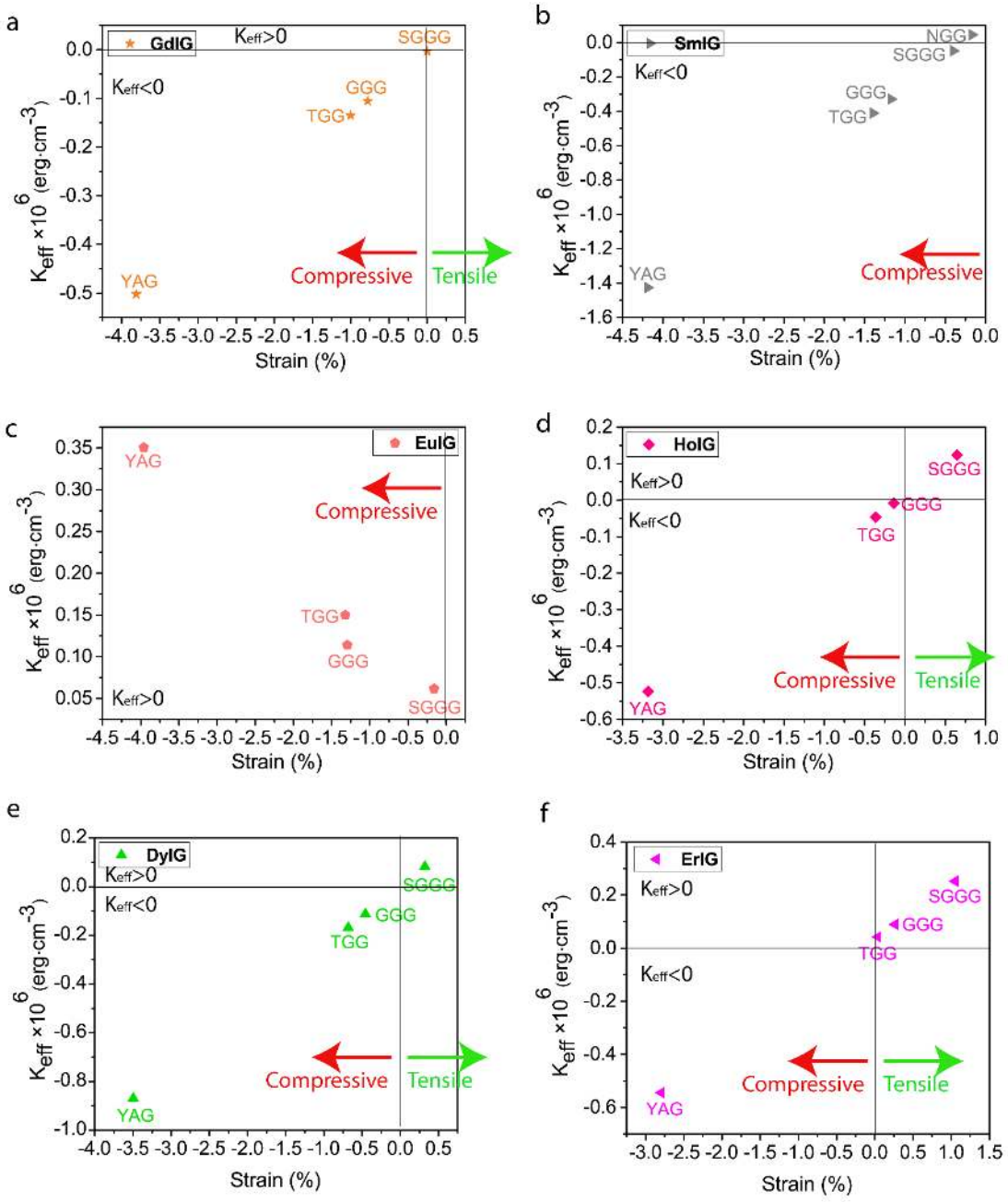

Figure 3.6: Effective anisotropy energy density versus strain in (a) GdIG, (b) SmIG, (c) EuIG, (d) HoIG, (e) DyIG, and (f) ErIG films on GGG, YAG, SGGG, TGG, and NGG substrates. Note that the axes scales are different in each part.

According to the Figures 3.4-3.6, our calculations are numerically consistent, both in order of magnitude and sign, with the previous experimental values. Due to inconsistencies in the PMA sign conventions of REIG film in the literature, some of them might show variability in the anisotropy state despite having the same K_{eff}.

Our model is able to predict the tensile stress-induced anisotropy as the result of the lattice parameter mismatch between the film and the substrate in TmIG on GGG substrate

(Figure 3.5b), along with the film's negative λ_{111}, as reported in the former experimental results of MA in TmIG/GGG [47, 179, 191]. In the previous studies, PMA is identified under the condition of $K_{eff} > 0$. However, this convention causes contradiction when compared with experimental MA in YIG/GGG. This approach yields YIG as PMA on GGG which is not consistent with the well-known IP easy axis reported in the former experimental studies [43, 188, 192]. From a thermodynamic perpective, $K_{eff} < 0$ convention for defining PMA would yield more reasonable description and it is also able to explain most of the REIG/garnet substrate cases accurately, such as YIG/GGG pair.

3.2.4 Magnetic anisotropy sensitivity to variations in M_s and film strain relaxation

The variability in the process conditions and fabrication may lead to different conclusion in the magnetic anisotropy state of the magnetic thin films than the predicted state of effective anisotropy energy density and field. The thin film stoichiometry (RE:Fe as well as oxygen deficiency) and non-equilibrium phases in the garnet thin film structures which are induced by the process, could also make divergence in the magnetic anisotropy state with respect to the theoretical predictions. These structural differences might cause complete or partial strain relaxation in the thin film or may cause rise in the strain magnitude because of the presence of secondary crystalline phases. These minimal changes in strain may cause dramatic changes to magnitude and the sign of ME anisotropy energy and change the prediction result of a PMA film become in-plane EA. In other words, off-stoichiometry may reduce the in M_s and consequently the shape anisotropy term in a quadratic scale ($K_{shape} = 2\pi M_s^2$). It means that if the M_s is reduced by 10%, K_{shape} decreases around 19%, so the anisotropy field increases according to $H_A = 2K_{eff}/M_s$. Thus, the anisotropy field and the easy axis prediction of the samples might be effected by the imperfections in sample fabrication and other anisotropy energy terms. Although these unintentional imperfections might evolve, they could be used deliberately to engineer the garnet films for any desired properties in devices working principle. Consequently, it is necessary to evaluate the sensitivity of MA and the saturation field (H_a) to such parameters like in plane mechanical strain and saturation magnetic moment.

Figure 3.7 shows the influence of strain and M_s deviations on the effective MA energy density for 5 PMA film-substrate combinations in which the anisotropy state might alter due to the : change in the experimental parameters. These film-substrate pairs are: HoIG/GGG, SmIG/NGG, YIG/YAG, SmIG/SGGG, and HoIG/TGG. It is worth to remind that in our convention $K_{eff} < 0$ indicates PMA. The sign change of magnetic

anisotropy energy from $K_{eff} < 0$ to $K_{eff} > 0$ shows OP to IP magnetization easy axis transition. In these graphs, for M_s and in plane strains ranging from 60% to 140% of the bulk values of M_s and lattice matched strains inside the thin film, the total MA energy densities are calculated. The MA energy density in erg·cm^{-3} scale is shown by the color scale. In the sign consideration of K_{eff}, only the effect of K_{indu} and K_{shape} are considered, despite the negative first order magnetocrystalline anisotropy energies of almost all the REIG thin films. So the ME anisotropy should be negative and larger than shape anisotropy energy density, because K_1 (300 K) ~ -5% of K_{shape}. The equations 3.9-3.12 show the M_s and strain related derivation of MA energy which shows $\lambda_{111} < 0$ and compressive strain ($\varepsilon_{||} < 0$) for garnet films (HoIG, YIG, SmIG) lead to PMA in Figures 3.7a-e. The conditions for obtaining PMA state; $\lambda_{111} < 0$ and large assuming Young's modulus and the ν are constant as shown in equation 3.12.

$$K_{eff} = K_{indu} + K_{shape} + K_1 \tag{3.9}$$

$$K_{eff} = -\frac{3}{2}\lambda_{111}\frac{Y}{1-\nu}\varepsilon_{||} + 2\pi {M_s}^2 + K_1 \tag{3.10}$$

$$K_{eff} = \frac{3}{2}\lambda_{111}\frac{Y}{1-\nu}|\varepsilon_{||}| + 2\pi {M_s}^2 + K_1 \tag{3.11}$$

$$K_{eff} < 0 \quad \text{if} \quad \left|\frac{3}{2}\lambda_{111}\frac{Y}{1-\nu}|\varepsilon_{||}| + K_1\right| > 2\pi {M_s}^2 \tag{3.12}$$

If we move from left to right on each plot in Figure 3.7, we relax the thin films from fully strained thin film to unstrained state ($\varepsilon \rightarrow 0$) which reduces the ME anisotropy energy term and then gradually vanishes. At constant M_s with decreasing strain the total MA energy reduces. On the other hand, as the result of increasing M_s, K_{shape} term also increases and exceeds the value of ME anisotropy term. Thus, for strain-relaxed thin films (i.e. increased thickness or low RE:Fe) higher M_s may cause PMA. So, optimization of the film stoichiometry during the controlled growth and deposition process, is required to ensure the strained and stoichiometric films. These deposition conditions include oxygen partial pressure, growth temperature, and film thickness. The film with strains less than 1% in Figures 3.7a and 3.7c-e are experimentally more reproducible. However the strain is around 3% in case of YIG on YAG (as shown in Figure 3.7b), the reproduction of which might be challenging. Only the cases shown in Figures 3.7a-e are the PMA ones among 50 film-substrate combinations, in case of which an increase in M_s and strain might result in the PMA to vanish. The remaining REIG cases are not sensitive to M_s and strain change and they show stabilized magnetic anisotropy. Total anisotropy energy and field

plots similar to that of Figures 3.7a-e are included in the Appendix A figures for all 50 film-substrate pairs.

While $K_{eff} < 0$ is a proper metric for determining PMA, K_{eff} of the REIG thin films should also not be higher than a few 10^5 erg·cm^{-3} for experimental feasibility. If saturation fields exceed 5000 Oe, the films may not be compatible with device architectures. In Appendix A figures, we present both K_{eff} and H_a values for all the 50 film-substrate combinations considering the M_s and strain changes. These figures show that the anisotropy fields could span from about 300 Oe up to 12.6 T in PMA RE iron garnets. In applications such as integrated magnonics, to have stable and robust PMA, the K_{eff} should be a negative large value, still, it should not be too high to prevent very large saturation fields. By optimizing IP strain and M_s and by controlling oxygen partial pressure and Fe stoichiometry, one could keep the H_a low at the same time with a stable PMA. Hence, sustainable lattice matching in case of some thicker REIG such as HoIG [65], is challenging due to the strain relaxation inside the HoIG film. As a result, anisotropy field decreases in case of such low strain state, which could be utilized for spin-orbit torque or magnonic devices. PMA is achievable for HoIG using GGG substrate grown with a thickness below a critical limit. On the other hand, above the critical thickness the strain relaxation inside the film reaches 40% which makes the EA to switch from OP to in-plane. So in case of integrated devices, the thinner REIG films are preferred.

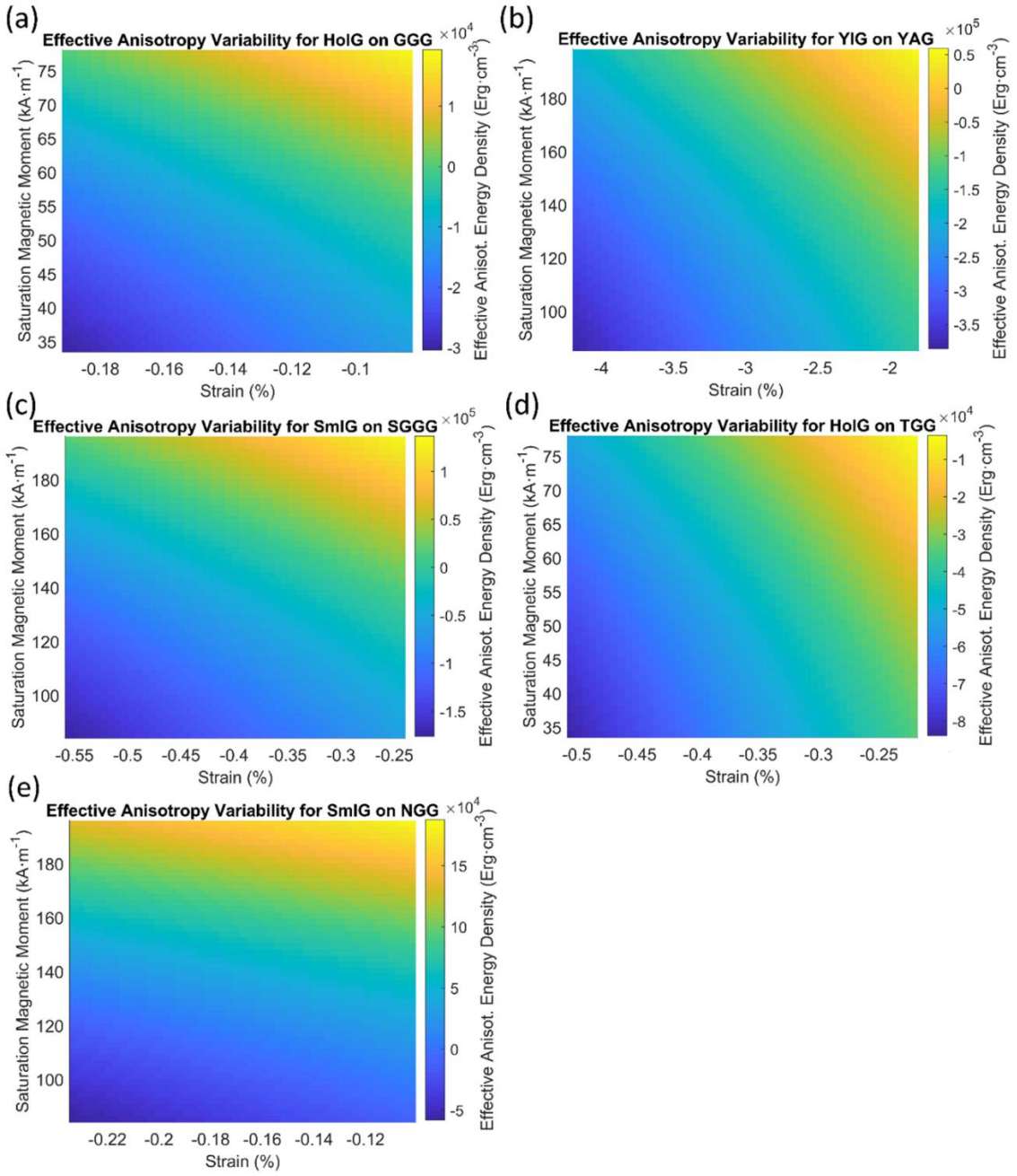

Figure 3.7: Effect of thin film relaxation and M_s variability on the effective MA energy density (K_{eff}) of the REIG. Variation of K_{eff} for (a) HoIG on GGG, (b) YIG on YAG, (c) SmIG on SGGG, (d) HoIG on TGG and (e) SmIG on NGG are presented shown for independent change of magnetic saturation moments and strain relaxation. Film strain may vary from a completely highly strained lattice-matched position to a strain-relaxed state. Strain variability changes ME anisotropy and leads to PMA film become in plane EA. Besides, M_s values may be different from their tabulated values due to the off-stoichiometry in the films induced by the growth process (i.e. higher or lower RE:Fe ratio and or deficiency in oxygen partial pressure or excess oxygen). Strain relaxation reduces the ME anisotropy term and weakens the PMA. On the other hand, increased M_s strengthens shape anisotropy for low enough strains and eliminates PMA.

The former studies on the physical origins of magnetic Gilbert damping show that [193] lower saturation magnetic moment results in lower Gilbert damping, which is advantageous for the device applications in spintronics. Considering this prediction, one could predict some of the REIG thin films listed in this study such as GdIG, DyIG, and

HoIG to have lower Gilbert damping compared to the others. Another practical applications of such garnets are the optimization of the compensation temperature near RT to engineer the magnetic damping for terahertz (THz)-range bandwidths in the magnons or spin wave propagation [54]. It is also indicated by the first principles predictions that reduced magnetic Gilbert damping could be achieved by having higher χ_m (magnetic susceptibility), which leads to lower saturation fields. Therefore, the PMA RE iron garnets with higher H_a values are predicted to have higher Gilbert damping parameters with respect to PMA garnets with lower anisotropy fields (H_a).

3.2.5 Conclusions

In this part, we presented a systematic calculation of shape, magnetocrystalline anisotropy magnetoelastic and energy density terms for 10 various epitaxial rare earth iron garnet thin films when grown on 5 different garnet substrates. We used the convention of $K_{eff} < 0$ to define perpendicular magnetic anisotropy (PMA). The substrate choice that has a smaller lattice constant than that of the film, helps induce compressive in-plane strain inside the thin films along with the negative and large λ_{111}, to eliminate the magnetostatic effect of the shape anisotropy and obtain PMA. Among the 20 new PMA REIG films we have predicted, SmIG thin film (grown on all 5 substrates) possesses a more robust PMA due to its high MA energy density.

To have magnetic thin films with PMA, it is necessary to ME anisotropy energy density to be negative and large to eliminate the demagnetizing effect of shape anisotropy. ME term could exceed the shape term when both λ_{111} and the strain type (compressive or tensile) have the correct signs (the same). So in both compressive ($\lambda_{111} < 0$) and tensile strain ($\lambda_{111} > 0$) states, thin films can have PMA as long as shape anisotropy can be lower than the negative ME effects. Here, except for TbIG on NGG and TbIG on SGGG with positive magnetostriction constant, the compressive strain was the reason for PMA in all the other REIG cases. In these two cases the (relatively) large and negative magnetocrystalline term and the tensile strain and, could result in PMA thin film. Therefore, the experiments should mainly target compressive in-plane lattice strain.

Based on our calculation results listed on Table 3.3, twenty different REIG thin film-garnet substrate are predicted to show. Only 7 cases among these potential PMA combinations, were experimentally demonstrated so far. In addition, YIG/YAG, HoIG/GGG, SmIG/NGG, HoIG/TGG and SmIG/SGGG, among the twenty PMA pairs,

are sensitive to variations in strain and M_s induced by stoichiometry or growth and fabrication process. By doping garnet thin films with other elements such as Ce [194], Tb [187] and Bi [195] or by lithography (nano)patterning, one could control shape anisotropy to tuned K_{eff} in REIGs. On the other hand, M_s value could also significantly increase as the result of doping, which consequently increases the magnitude of shape anisotropy in the magnetic thin films. In the REIG which were predicted to show PMA, the saturation fields were calculated from 310 Oe to 12.6 T. By engineering the stoichiometry, strain, and substrate choice, one could span such a wide range in calculation of the anisotropy field. The lower magnitude of the anisotropy fields (H_a < 0.5 T) and M_s values are desired as they require less energy for magnetization switching and possess lower Gilbert damping which make them appropriate candidates for integrated magnonic devices and circuits.

3.3 Data validity for modeling and prediction of novel REIG with PMA

This section is based on the publication "*Modelling Data for Predicting New Iron Garnet Thin Films with Perpendicular Magnetic Anisotropy*" S. Mokarian Zanjani, M. C. Onbasli, Data in Brief, 28 (2020) 104937. Reproduced (or "Reproduced in part") with permission from Elsevier Copyright 2020.

This section includes detailed calculations and graphs based on our manuscript submitted to Journal of Magnetism and Magnetic Materials, entitled "Predicting New Iron Garnet Thin Films with Perpendicular Magnetic Anisotropy". The comparison with the previous experimental demonstrations is also shown in the Table 3.4 with an accompanying discussion confirming the reliability of our model.

3.3.1 Introduction

The development of magnetic iron garnets with perpendicular magnetic easy axis (PMA) has been a major materials research area, which enabled researchers to start expanding the physics of spintronics and spin wave devices. Spintronic devices, especially emerging spin-orbit torque memory and logic devices, are expected to benefit from the development of rare earth iron garnets with tunable magnetic properties, magnetic anisotropy, crystal strain, and magnetooptical properties. There are very few studies in the literature which systematically investigate the ways in which one can change the composition of rare earth iron garnet thin films to tune magnetic anisotropy and achieve room temperature PMA. The PMA rare earth iron garnet films presented in this study are expected to be of interest for materials scientists working on magnetic oxides and devices, spintronic device researchers working on spin Seebeck effect, spin wave devices, spin logic, spin-orbit torques, all-optical switching, current-controlled magnetism, tunneling magnetoresistance studies, tunnel junctions and other spintronic effects involving unique transport and magnetooptical properties of thin film garnets.

These predicted films offer materials scientists multiple material options to test under a variety of growth and post-processing conditions. This study will be of interest also for spintronics, complex oxide, magnetooptics, and spin logic and magnetism researchers.

3.3.2 Predictive capability and validity of our Model

The model presented here is useful for the experimental researchers because:

1) A simple model, as presented here, helps elucidate the cases where off-stoichiometry, oxygen deficiency, interface effects, and non-equilibrium microstructure effects become significant on magnetic anisotropy; thus, one can better model nanostructured or few-nm-thick magnetic insulator garnets. Since our model can accurately predict most of the magnetic anisotropy cases for experimentally tested REIG film/substrate pairs given the right film parameters and that the films have cube-on-cube epitaxy, we believe comparing our model outcomes with the experiments may help identify experimental issues.
2) For modeling garnet properties, a general investigation helps validate and re-evaluate earlier tabulated magnetic materials data (such as λ_{111}, K_1, M_s, …). Applications of rare earth iron garnets in spintronics are growing very rapidly. Apart from prediction of magnetic anisotropy states in iron garnet thin films, our model highlights and provides a detailed investigation on the role of each individual material parameter including lattice parameters, shear/uniaxial strain, magnetostriction constant, saturation magnetization, and intrinsic magnetocrystalline anisotropy.
3) The model is also useful in anisotropy state prediction of doped iron garnet thin films, which could be highly utilized for all-optical switching, magnetooptical devices, spin Seebeck devices etc. Doping in garnets expand or contract lattice parameters and would change the strain states in films. Thus, our model can help researchers rapidly identify the parameters which need to be experimentally optimized for obtaining the desired anisotropy state.
4) In case of thin films, the fabrication process parameters deviate the film properties from bulk. So, the parameters used in the former experiments cannot be perfectly applicable for every sample with different thickness. Annealing time and temperature, oxygen partial pressure, film thickness, are a few examples of parameters that affect the thin film properties, like M_s which directly affects the demagnetizing anisotropy energy density and shape anisotropy terms.

3.3.3 Prediction accuracy of our model compared to the experimental demonstration

The model presented here could accurately predict the magnetic anisotropy state in almost all cases of garnet film/substrate combinations. The partial differences between our predictions and the experimental outcomes in a few cases rise from the deviation of experimentally measured film parameters from the tabulated properties used in our model (like M_s, λ_{111}, strain, Young's modulus, Poisson's ratio). We reviewed all of the previous

experimental studies related to perpendicular magnetic anisotropy of thin film rare earth iron garnets and evaluated the predictive capability of our model based on experimental outcomes. In almost all cases except for TmIG/GGG (among 20 predicted PMA cases), the model can accurately predict the anisotropy state provided that the material properties are accurately entered in the model. Our model has highlighted the sensitivity of magnetic anisotropy to the films' magnetic and structural properties. As a result of this sensitivity, we believe more precise and explicit reporting of experimental characterization results of film properties could help understand anisotropy much better.

TmIG/GGG case is a special outlier that could not be reproduced by our model, and in our study, we point out that there should be a different anisotropy term originating from either off-stoichiometry, surface strain gradients or process-induced variability in film properties. As the anisotropy of TmIG/GGG strongly depends on process oxygen gas pressure and cooling rate, the films are likely to be in an out-of-equilibrium state within a special window of strain and stoichiometry. As a result, further studies on understanding TmIG/GGG anisotropy might be needed.

Easy axis, by definition, is the axis along which the film can be saturated with lowest external field or lowest total energy. A film would thus spontaneously minimize its energy and reorient its magnetic moment along the easy axis. As a result, defining the easy axis to be out-of-plane by requiring $K_{eff} < 0$ would be thermodynamically more appropriate, unlike previous studies [47, 179]. We would like to present a more detailed and a longer discussion of the points below:

We tested the prediction accuracy of our model by going through each available experimental demonstration of garnet thin film/substrate anisotropy study and comparing their measured anisotropy with the predictions of our model. Below, we show the prediction accuracy and cases where experiments are different from our predictions. We explain why some of these experimental results deviate from our model predictions and why these results do not necessarily invalidate our model.

Table 3.4: Comparison of experimental demonstrations of magnetic anisotropy and our model predictions (IP: in-plane, OP: out-of-plane, NA: Not Available).

No.	Thin Film-Substrate combination	Predicted anisotropy	Published Experimental Studies	Does our prediction match the experiment?	Justification if model does not predict
1	YIG/GGG	IP	[160]	YES	

2	TmIG/GGG	IP	[158]	NO	See our discussion below.
3	DyIG/GGG	OP	[196](doped stoichiometry)	YES	
4	HoIG/GGG	OP	[46]	YES	
5	ErIG/GGG	IP	[197]-not thin film	YES	
6	YbIG/GGG	IP	NA		
7	TbIG/GGG	IP	[40]	NO	The samples in ref. [40] contain significant shear stress which causes reduced magnetoelastic anisotropy. Significant off-stoichiometry changes M_s, K_1 and λ_{111}.
8	GdIG/GGG	OP	[48]	YES	
9	SmIG/GGG	OP	[38]	YES	
10	EuIG/GGG	IP	[40]	NO	The samples in ref. [40] contain significant shear stress which causes reduced magnetoelastic anisotropy. Significant off-stoichiometry changes M_s, K_1 and λ_{111}.
11	YIG/YAG	OP	NA		
12	TmIG/YAG	OP	NA		
13	DyIG/YAG	OP	NA		
14	HoIG/YAG	OP	NA		
15	ErIG/YAG	OP	NA		
16	YbIG/YAG	OP	NA		
17	TbIG/YAG	IP	NA		
18	GdIG/YAG	OP	NA		
19	SmIG/YAG	OP	NA		
20	EuIG/YAG	IP	NA		
21	YIG/SGGG	IP	[160]	NO	Larger λ_{111}, strain and M_s used in the ref. [160]
22	TmIG/SGGG	IP	[39]	NO	See our discussion below.
23	DyIG/SGGG	IP	NA		
24	HoIG/SGGG	IP	NA		

25	ErIG/SGGG	IP	NA		
26	YbIG/SGGG	IP	NA		
27	TbIG/SGGG	OP	[40]	NO	The samples in ref. [40] contain significant shear stress which causes reduced magnetoelastic anisotropy. Significant off-stoichiometry changes M_s, K_1 and λ_{111}.
28	GdIG/SGGG	OP	NA		
29	SmIG/SGGG	OP	NA		
30	EuIG/SGGG	IP	NA		
31	YIG/TGG	IP	NA		
32	TmIG/TGG	IP	NA		
33	DyIG/TGG	OP	NA		
34	HoIG/TGG	OP	NA		
35	ErIG/TGG	IP	NA		
36	YbIG/TGG	IP	NA		
37	TbIG/TGG	IP	NA		
38	GdIG/TGG	OP	NA		
39	SmIG/TGG	OP	NA		
40	EuIG/TGG	IP	NA		
41	YIG/NGG	IP	[160]	NO	Larger λ_{111}, strain and M_s used in the ref. [160]
42	TmIG/NGG	IP	NA		
43	DyIG/NGG	IP	NA		
44	HoIG/NGG	IP	NA		
45	ErIG/NGG	IP	NA		
46	YbIG/NGG	IP	NA		
47	TbIG/NGG	OP	NA		
48	GdIG/NGG	IP	NA		
49	SmIG/NGG	IP	NA		
50	EuIG/NGG	IP	NA		

As shown in the Table 3.4, our model is able to predict the magnetic anisotropy state of many garnet/substrate combinations. Column six of the table provides brief explanations.

Ref. [40] presents an experimental study on the magnetic and magnetotransport properties of TbIG/GGG and TbIG/SGGG (rows 7 and 27). In this study, the authors obtain in-plane compressive strain in TbIG/GGG as we initially entered into our model.

TbIG/GGG (row 7 on Table 3.4): The experimental results indicate PMA in TbIG/GGG, while our model predicts the opposite for this case. The authors in ref. [40] found that

TbIG has rhombohedral lattice structure which is accompanied with significant iron deficiency (RE:Fe = 0.7-0.72 instead of 0.6). Due to this structural distortion and off-stoichiometry, the lattice would likely have oxygen deficiency to preserve charge neutrality of the unit cell. As a result, the measured M_s for the TbIG thin films (19 emu·cm^{-3}) differs from the bulk value we used (15.9 emu·cm^{-3}) in our calculation. Because of off-stoichiometry and structural distortion, the films are no longer cubic. Since our model assumes cubic film on cubic substrate epitaxy with in-plane lattice matching, the presented film does not satisfy the assumptions built into our model. Nevertheless, the fact that our model does not predict the anisotropy state originates from the large magnetoelastic (ME) anisotropy term calculated for our model. Our model only considers Young's modulus and cube-on-cube strains but not shear stresses originating due to rhombohedral distortions on the lattice. Such distortions help reduce the ME anisotropy term by two orders of magnitude (shear stress instead of uniaxial stress) and lead to prediction of PMA in TbIG/GGG by using our model. For our model to work for rhombohedral film lattice structures as well, the ME term would need to account for shear stresses.

TbIG/SGGG (row 27 on Table 3.4): The authors in ref. [40] measure IP easy axis in TbIG/SGGG. This film also demonstrates tensile in-plane strain as we entered into our model. Since TbIG has rhombohedral lattice distortion, significant iron deficiency (RE:Fe = 0.7-0.72) and oxygen deficiency as in TbIG/GGG case, the film properties in the experiments do not satisfy the assumptions built into our model.

Our model overestimates the ME anisotropy term because of our cube-on-cube epitaxy assumption. When the model considers shear stresses instead of uniaxial stress, the ME term decreases by two orders of magnitude. For TbIG/SGGG, magnetocrystalline anisotropy term (K_1) must be lower than that for the tabulated and stoichiometric TbIG K_1 values. Thus, our model can conclude IP easy axis for TbIG/SGGG case by relaxing our cube-on-cube epitaxy assumption and considering the realistic K_1 value for the off-stoichiometric film.

EuIG/GGG (111) (row 10 on Table 3.4): Our model's effective anisotropy prediction is different from the experimental outcome because of three main reasons:

(1) Our model overestimates the ME anisotropy energy since it assumes cube-on-cube epitaxy and uniaxial stresses instead of shear stresses which become the main and much

weaker magnetoelastic effects in the unit cell of the EuIG/GGG (111). These films have rhombohedral unit cells and their ME terms are two orders of magnitude lower than in our predicted case due to shear stresses.

(2) The films in the ref. [40] have significant differences with respect to bulk EuIG including off-stoichiometry (RE:Fe>0.6) and oxygen deficiency. As a result, off-stoichiometry and oxygen deficiency would cause anisotropic lattice contraction which would also cause major deviation from the tabulated magnetocrystalline anisotropy (K_1) of EuIG.

In ref. [40], the authors did not include magnetocrystalline anisotropy in their calculations, which we believe cannot be neglected for EuIG, since it is an order of magnitude larger (-3.8×10^4 erg·cm^{-3}) compared to the other REIG (about -10^3 erg·cm^{-3}).

(3) Since K_1 for EuIG is an order of magnitude larger than that for the other REIG, variability in K_1 for EuIG becomes much more important to accurately model anisotropy in EuIG films. We confirm that our model can predict PMA in EuIG/GGG (111) given the shear stresses (two orders of magnitude lower ME anisotropy) become the main driver and magnetocrystalline anisotropy of EuIG also increases by about 40-50% due to off-stoichiometry, oxygen deficiency and rhombohedral distortion.

YIG/SGGG and YIG/NGG (rows 21 and 41, respectively, on Table 3.4): For YIG/SGGG and YIG/NGG, the measured film M_s (147 emu·cm^{-3} < 141.7 emu·cm^{-3} bulk M_s) is higher than that used in our model. The authors explain the origin of the increase in M_s from the uncertainty in estimation of unit cell volume. According to the hysteresis loop in Figure 2b of ref. [160], the saturation field for YIG/NGG is smaller than that of YIG/SGGG and YIG/GGG, and they conclude that YIG/NGG is PMA. However, considering Figure 2a in ref. [160], the saturation field for in-plane hysteresis loop is lower than of the out-of-plane loop in Figure 2b. So PMA cannot be unambiguously concluded from the hysteresis curves. Their experimental results of out-of-plane anisotropy based on the strain state of the film shows that the saturation field in case of YIG/NGG and YIG/SGGG is smaller than that of YIG/GGG. So, a partial out-of-plane component of magnetization state can be inferred, but complete PMA cannot be concluded. Besides, the experimental values of the lattice parameter of YIG (1.245 nm)/SGGG (1.250 nm), YIG (1.247 nm)/NGG (1.252 nm) results in-plane tensile strain (calculations are provided below) in the film which

agrees with our model's estimates, but the experimental strain is larger in these cases. Young's modulus and Poison ratio might be taken as larger value, which are not reported in the literature by the experimentalists. In addition, the value of λ_{111} used in the [160] (-3×10^{-6}) is also larger than that used in our calculation based on the reported values in the literature (-2.4×10^{-6}); these two inconsistencies result in larger magnetoelastic anisotropy.

Magnetoelastic anisotropy energy calculation of YIG/NGG based on the parameters used in the ref. [160]:

Measured H_s=1225 Oe =H_{eff}

$H_A = 2\frac{K_{eff}}{M_s}$ =====> $K_{eff}=1.1\times10^6$ erg·cm^{-3}

$K_{eff} = K_{indu} + K_{shape} + K_1$

1.1×10^6 erg·cm^{-3} $= K_{indu} + 2\pi(147)^2 + (-6.1\times10^3$ erg·cm^{-3}) ===> $K_{indu}= 9.1\times10^5$ erg·cm^{-3}

In the ref. [160], the RSM data show strain gradient within the substrate which would cause M_s, λ_{111}, Young's modulus, Poison ratio, and even stoichiometry. The parameters we took for our calculations are different from the values used in the reference. Thus, our prediction is not wrong in that we can predict the in-plane component of the easy axis. If the film properties are fully characterized including Young's modulus, Poisson's ratio, λ_{111}, lattice parameters and stoichiometry, then the accurate material parameters would help the model be accurate.

TmIG/GGG and TmIG/SGGG (rows 2 and 22 on Table 3.4): In case of TmIG/GGG and TmIG/SGGG, several main points needed to be considered as follows:

1) In the experimental studies of magnetic anisotropy in TmIG [47, 198], the value of anisotropy energy density/anisotropy field has been reported as a positive value; considering the large negative magnetostriction constant of TmIG and tensile in-plane strain in the TmIG grown on GGG substrate. Our calculations completely agree with the results reported in the literature, both in the order of magnitude and the sign of the anisotropy energy density/field.

2) Considering our experimental background in growth and characterization of rare earth iron garnets including TmIG/GGG [41, 179], while growing the TmIG thin films on GGG substrate, there are different process and post-process annealing conditions to be

optimized to obtain reproducible film properties. The most important parameters are growth time (thickness), oxygen partial pressure (stoichiometry and growth kinetics), annealing time (defect density and Tm:Fe ratio) and temperature (growth rate and microstructure), which affect the film properties including lattice parameters, M_s, λ_{111}, and K_1. On the other hand, film M_s values may deviate from the ideal bulk M_s and this variability affects shape anisotropy directly. In other words, for sub-30 nm films the interface effects become more significant with respect to other anisotropy terms. Thus, non-optimum process conditions may lead to off-stoichiometry or Tm:Fe ratio shift for the ultrathin films.

3) Changing the stoichiometry directly affects the saturation magnetic moment, as explained in [191]. According to this paper, the total magnetic moment of the iron garnet sample can be calculated by calculating the total magnetic moment of the iron ions in tetrahedral and octahedral sites, in addition to the magnetic moment of the rear earth ion as in $\Sigma m = \Sigma \mathrm{m}_{\mathrm{Fe\ tet}} - \Sigma \mathrm{m}_{\mathrm{Fe\ oct}} - \Sigma \mathrm{m}_{\mathrm{rare}\ earth}$ formula. In the Fe-rich samples the saturation moment is reduced because Fe occupy the Tm site and its magnetic moment is larger than that of Tm. In the Tm-rich films there is a possibility of Fe off-stoichiometry either in tetrahedral or octahedral sites. Fe off-stoichiometry in tetrahedral sites reduces M_s, however, the Fe off-stoichiometry in the octahedral sites increases the total M_s. Consequently, the M_s and shape anisotropy of the iron garnet sample is changed with film thickness, which changes the equilibrium stoichiometry in ultrathin films. The shape anisotropy of the thin films become smaller as M_s decreases with off-stoichiometry. Thus, magnetoelastic anisotropy can overcome shape anisotropy and yield PMA in TmIG, consistent with the experimentally reported anisotropy data [198]. As demonstrated in Figure 2c in ref. [191] of our SI file, the M_s values obtained for the different stoichiometries of TmIG thin film samples, are all smaller than that for the bulk. Since shape anisotropy energy density is proportional to M_s^2, the demagnetizing anisotropy term is smaller and easier to overcome by the magnetoelastic anisotropy term in lattice-matched thin films. In our calculations, the bulk garnet M_s values are used, since these values are more reliable than those of the thin films.

4) The experimentally measured ultrathin film M_s are generally less than the bulk M_s [158, 179, 191]. So, shape anisotropy becomes smaller than that of an equivalent sample with bulk M_s. Therefore, the ME anisotropy can overcome shape anisotropy and lead to PMA in TmIG, as reported in the experimental data [198].

5) Apart from the M_s value, the magnetostriction constant, λ_{111}, is also a significant factor which affects the ME anisotropy energy density. In the calculation of ME anisotropy, we used the tabulated λ_{111} values, which were calculated or measured in the literature. So in case of thin films, in which the microstructure, stoichiometry, and process parameters may exhibit variability, those bulk values may no longer be applicable to films.

3.3.4 Conclusions

Our model is able to predict magnetic anisotropy in almost all cases of garnet/substrate combinations and partial differences in a few cases rise from the deviation of experimentally measured parameters from the tabulated values used in our model including M_s, λ_{111}, lattice parameter (strain), Young's modulus, Poisson's ratio. Once the correct material properties are used in the model, under cube-on-cube epitaxy conditions, the anisotropy state and field values can be estimated very accurately. Therefore, the model can help capture the contributing factors with high quantitative accuracy. Besides, our model has highlighted the sensitivity of film anisotropy to the process parameters and film properties. Thus, we highlighted the need for reporting more precise and detailed characterization results for magnetic iron garnet films for reliable anisotropy analysis.

Chapter 4

EPITAXIAL GROWTH AND CHARACTERIZATION OF HOLMIUM IRON GARNET

4.1 Optimization of PLD growth of Holmium iron garnet (HoIG) for PMA

We provide an experimental procedure for pulsed laser deposition of HoIG on two different (111)-oriented GGG and TGG garnet substrates as well as Si (001) and SOI substrates. We investigate the effect of film thickness and growth parameters such as substrate temperature and oxygen partial pressure on the thin film structural (XRD, SEM, AFM) and magnetic properties (VSM) of HoIG. We run two PLD growth procedures as calibration runs to provide optimized growth parameters such as oxygen partial pressure, substrate temperature, as well as number of laser shots for the desired film thickness, in order to achieve better film quality which exhibits perpendicular magnetic anisotropy (PMA). HoIG/GGG (111) film obtained with 67 nm thickness shows better epitaxial and film quality. The surface roughness measured by AFM, was less than 0.3 nm, while the 420 nm HoIG film showed a 1.74 nm surface roughness. XRD results of 420 nm HoIG/Si showed the creation of oxide secondary phases which arises from the increased oxygen partial pressure, and increased film thickness. The IP hysteresis loop measurements of HoIG/GGG showed that the 67 nm film exhibit bulk like saturation magnetic moment of 62 emu·cm^{-3} with very low coercivities and remanence. Relatively large M_r/M_s ratio in the OP hysteresis loop measurements of 67 nm HoIG is an indicator of out of plane magnetic anisotropy in this sample, which is in agreement with our previous theoretical predictions and PMA hypothesis on this material.

4.1.1 Introduction

Epitaxial rare-earth iron garnets ($RE_3Fe_5O_{12}$, REIG) thin films, especially yttrium iron garnet ($Y_3Fe_5O_{12}$,YIG), have been studied recently in variety research fields such as spin waves [58, 106, 199, 200], spin torques [33, 201-203], and magneto-optical (Faraday and Kerr) effects [203-205]. Due to its low magnetization Gilbert damping ($\alpha \sim 10^{-4}$), which enables the millimeter range spin wave generation and transmission, YIG has attracted considerable attention in spintronics and magnonics [43, 206, 207]. Low Ohmic losses of REIG ferrimagnetic insulators, enables ultrafast magnetization dynamics and low heat dissipation in terahertz (THz) spin wave generation, as well as spin-wave logic devices with low power consumption [208, 209]. Furthermore, YIG's high and tunable Curie

temperature [210, 211] enables propagation of spin current, in absence of charge current, considering its long range magnetic order. Nevertheless, YIG with magnetization easy axis parallel to the film plane is not completely a suitable candidate for applications such as spin-orbit-torque (SOT) in spin-transfer-torque oscillators [212], domain wall motion in high density magnetic memories [213], and skyrmion memory elements with chiral magnetic architectures [214].

Perpendicular magnetic anisotropy (PMA) is necessary for some spintronic applications such as spin transport devices and spin wave generation and detection [203] in REIG/heavy metal configurations, via spin Hall effect (SHE) [201, 215-218], or large Hall angle spin-orbit- torque from topological insulators [36, 219]. Due to the complexity of growing YIG with perpendicular magnetic anisotropy (PMA), more REIG with robust PMA are required for such applications. Substitution of Y^{3+} with other rare earth elements provides the opportunity to tune magnetic properties such as Gilbert damping [220, 221], saturation magnetic moment [64, 171, 222], magnetostriction constant (λ) [92], magnetocrystalline and magnetoelastic anisotropy due to variation of strain state by choice of substrate [64, 223, 224], and magnetooptical spectral response [225].

Epitaxial holmium iron garnet (HoIG) as a REIG thin film which was not extensively explored previously for spintronics, is a promising candidate for such applications including PMA-based [64, 65] SOT and tunable saturation field, high magnetooptical response [46] low temperature quantum spintronics (due to its low compensation point, 120 K) [66], chemotherapy and cancer radiotherapy [67] and multiferroicity [68] the potential use of which is to miniaturize the electronic components [69-71].

Coupling between magnetic and electric orders is called magnetoelectric (ME) effect; this effect enables the control of magnetic order by magnetic field (direct ME effect), or electric field (converse ME effect) [72, 73] for data storage devices, piezoelectric device controlled by magnetization, actuators, sensors and detectors with high sensitivity of magnetic field, microwave phase shifters, magnetic memories [74-76]. Ferrimagnetic REIG (RE: Ho, Dy, Tb, Er) have shown low magnetic field room temperature magnetodielectric coupling [77, 78].

4.1.2 Pulsed laser deposition (PLD) of HoIG thin film

Epitaxial HoIG magnetic thin films have been grown by pulsed laser deposition (PLD) technique. The 99.99% pure, 2-inch HoIG target was purchased from PVD Products Co.,

and the thin films have been grown on 10 mm×10 mm garnet and Si single crystalline substrates, purchased from MTI Crystals. For designing the optimized growth process parameters, first, two growth procedures were conducted as calibration runs. Figure 4.1 shows the HoIG target and the HoIG/GGG (111) sample. The circular curvatures on the target after the PLD process shows that the target is rotated in the process chamber during the growth, in order to achieve more uniform deposition and higher film quality.

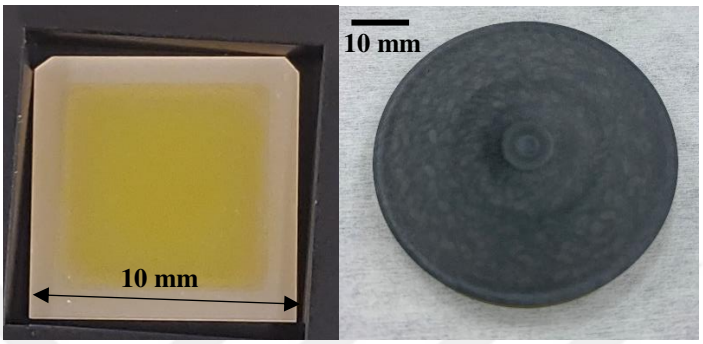

Figure 4.1: (Left) HoIG epitaxial thin film grown on GGG by PLD. (Right) the HoIG target.

The thin films were grown with 25 nm and 40 nm thickness on two different (111)-oriented single side polished substrates: Gadolinium Gallium Garnet (GGG: $Gd_3Ga_5O_{12}$), Terbium Gallium Garnet (TGG: $Tb_3Ga_5O_{12}$), and also Si (001) and Silicon on insulator (SOI) substrates, shown in Figure 4.2, from left to right, respectively. The first and second rows are 40 nm and 25 nm thick sample grown on the substrates with 650 ˚C temperature, respectively. The third and fourth rows are 40 nm and 25 nm thick HoIG thin films grown on the substrates with 800 ˚C temperature, respectively.

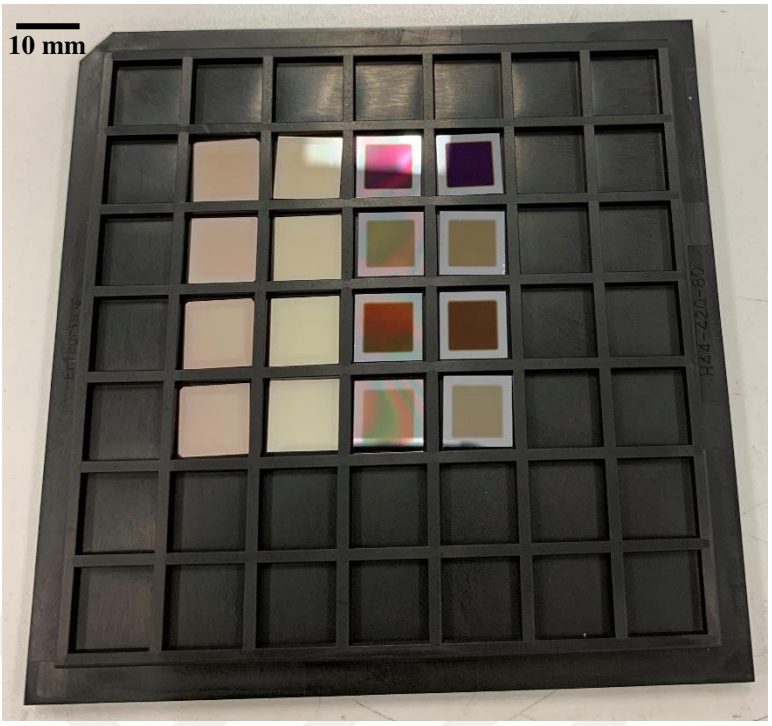

Figure 4.2: HoIG thin films of 25 and 40 nm thick on GGG, TGG, Si, and SOI substrates with substrate with 650 ˚C (first and second rows), and 800 ˚C (third and fourth rows).

Each sample was prepared at 650 ˚C or 800 ˚C substrate temperatures. The oxygen partial pressure was set to 10 mTorr with the base pressure of 10^{-7} Torr. KrF excimer laser pulses with 400 mJ energy per pulse, λ = 248 nm and 10 Hz pulse repetition frequency evaporated the target which was 8 cm below the substrate. All samples were cooled down to 300 ˚C with a 2 ˚C/min rate. The PLD growth parameters are presented in Table 4.1.

Table 4.1: PLD growth parameters of epitaxial HoIG

Thickness (nm)	**Oxygen Pressure (mTorr)**	**Base Pressure (Torr)**	**Substrate Temperature (˚C)**	**Laser Energy (mJ)**	**Laser Wavelength (nm)**	**Laser Frequency (Hz)**	**Number of Pulses**	**Cooling Rate (˚C /min)**	**Target-Substrate Distance (cm)**
25	10	10^{-7}	650	400	248	10	8900	2 (up to 300 ˚C under 10 mTorr O_2 atmosphere)	8
40	10	10^{-7}	650	400	248	10	14200	2 (up to 300 ˚C under 10 mTorr O_2 atmosphere)	8
25	10	10^{-7}	800	400	248	10	7500	2 (up to 300 ˚C	8

								under 10 mTorr O_2 atmosphere)	
40	10	10^{-7}	800	400	248	10	12000	2 (up to 300 ˚C under 10 mTorr O_2 atmosphere)	8

The number of laser pulses have been calculated based on two calibrations runs which were designed to optimize the PLD growth parameters with the best thin film crystalline and magnetic properties.

4.1.3 Structural characterization of HoIG

HoIG thin films were grown on GGG (111) and Si (001) substrate with an oxygen partial pressure of 150 mTorr using 150000 laser shots, with the energy and wavelength of 400 mJ and 248 nm, respectively. The laser repetition rate was 10 Hz, and the samples were cooled down to 300 ˚C with the rate of 2 ˚C in oxygen atmosphere. The substrate temperature was 650˚C. The scanning electron microscopy (SEM) cross-sectional images taken from the thin film/Si substrate show that the thickness of the film was 420 nm, as shown in Figure 4.3a. Moreover, a second calibration run was conducted with oxygen partial pressure of 10 mTorr using 20000 laser shots, and substrate temperature of 800 ˚C, which results in 67 nm film thickness in the SEM cross sectional image, shown in Figure 4.3b. Both films exhibit sharp interfaces with the substrate with a quite uniform thickness all over the scanned area.

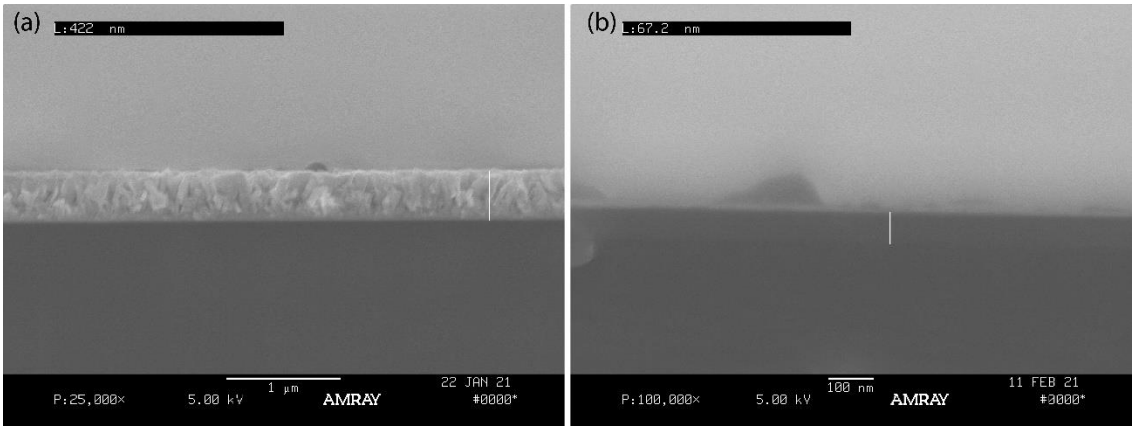

Figure 4.3: SEM cross-sectional image of HoIG grown under (a) 150 mTorr oxygen partial pressure using 150000 laser shots and substrate temperature of 650 ˚C, and (b) P_{O2}=10 mTorr, 20000 laser shots and substrate temperature of 800 ˚C.

In order to characterize the structural properties of the HoIG thin film, x-ray diffraction (XRD) was done in Bragg-Brentano configuration with λ=1.54 Å Cu $K_{\alpha 1}$ x-ray source. The XRD pattern of the HoIG of 420 nm is shown in Figure 4.4.

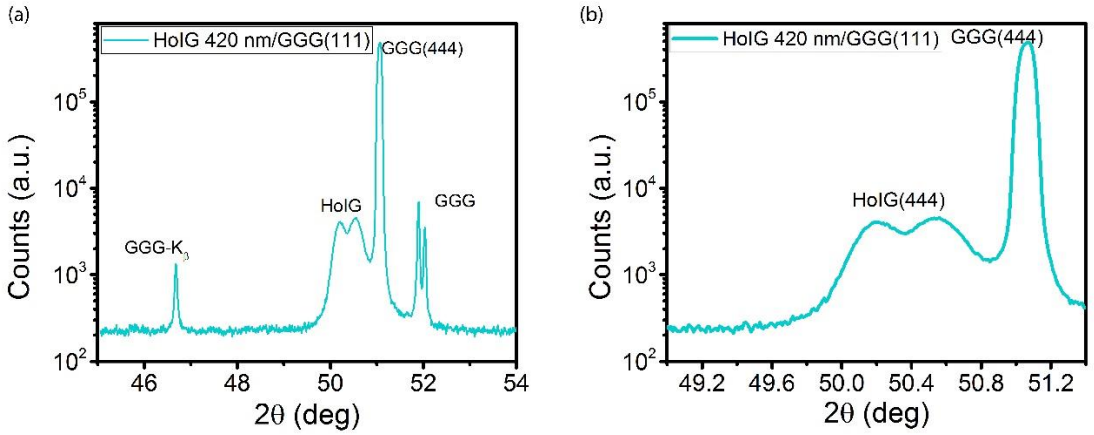

Figure 4.4: (a) XRD of 420 nm thick HoIG grown on GGG (111) substrate, under 150 mTorr oxygen partial pressure, and 650˚C substrate temperature. (b) Zoomed-in version of the left graph.

According to Figure 4.4, HoIG grown on GGG (111) substrate shows an epitaxial single crystalline property. The XRD pattern shown in Figure 4.4 shows the absence of any additional oxide or secondary phases in the thin film. The peaks near 2θ = 46.7˚, and 2θ = 52˚ show K_α and K_β peaks coming from the substrate. The plot on the left side of the Figure 4.4 corresponds to the fourth order reflection of HoIG peaks and GGG (111) substrate near 2θ = 50.4˚ and 2θ = 51˚, respectively. According to JCPDS card number 00-023-0282 of HoIG, the peak position of (444) plane of HoIG belongs to 2θ = 51˚. Therefore, our thin film has a shift towards left on the XRD pattern, which could be due to the strain inside the thin film. We calculated the out-of-plane lattice parameter using the XRD peak positions. We modified the PLD growth parameters and designed the second calibration run for HoIG on GGG (111) substrate, such that, the oxygen partial pressure was decreased to 10mTorr, and the number of laser shots was 20000. The substrate temperature of 800 ˚C was chosen for an improved epitaxial and crystalline quality of the film. The rest of the growth parameters were kept unchanged. The elevated temperature of the substrate leads to the increased diffusion of the atoms on the surface. Figure 4.5 shows the XRD measurement results of the HoIG/GGG (111) substrate. Due to the decreased number of laser shots, the measured thickness of HoIG decreased to 67 nm (Figure 4.3b).

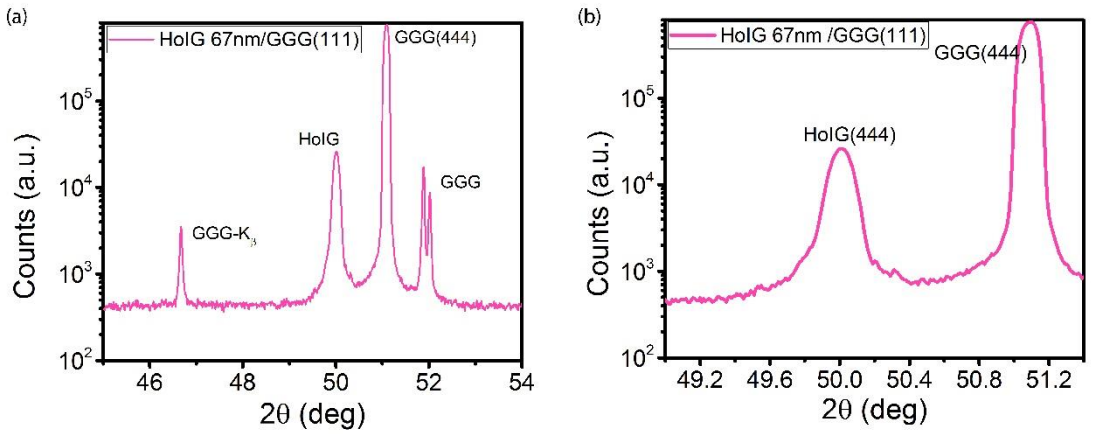

Figure 4.5: (a) XRD of 67 nm thick HoIG grown on GGG (111) substrate, under 10 mTorr oxygen partial pressure, and 800˚C substrate temperature. (b) Zoomed-in version of the left graph.

Similar to 420 nm HoIG XRD pattern, the substrate K_α and K_β peaks are near $2\theta = 46.7^\circ$, and $2\theta = 52^\circ$ are coming from the substrate. In the 67 nm film the HoIG (444) peak position is $2\theta = 50^\circ$ which is shifted even more towards the left. The absence of the peak shoulder and the narrow width of the HoIG (444) peak is an indicator of a higher epitaxial quality of the single crystalline thin film, which is due to the higher substrate temperature reduced oxygen pressure, and film thickness. Figure 4.6, shows the comparison between the XRD peaks of two calibration runs. The blue curve shows the XRD pattern of the 420 nm HoIG/GGG sample which was grown on the 650˚C hot substrate, and the pink pattern is for 67 nm HoIG/GGG sample grown on the 800˚C hot substrate.

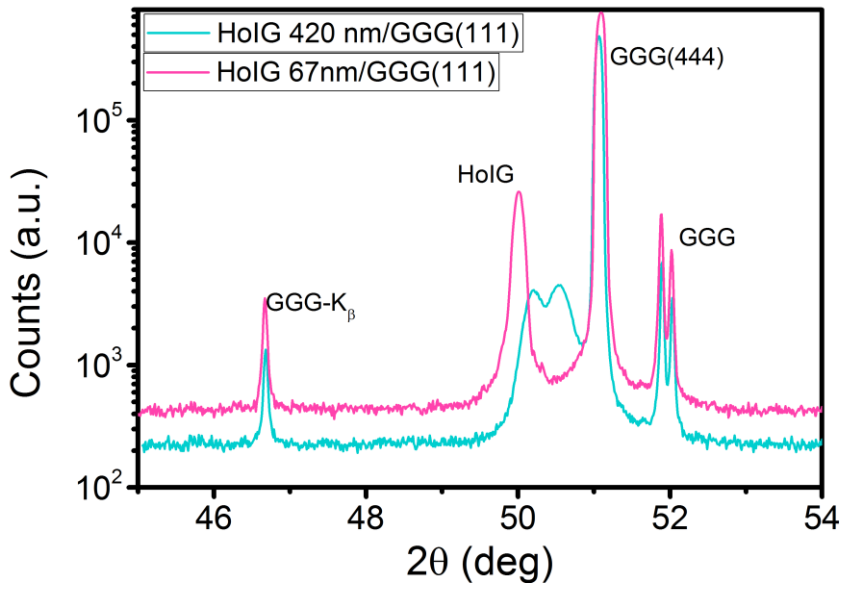

Figure 4.6: The XRD peaks of 420 nm and 67 nm HoIG/GGG (111) substrate.

Comparison between the two HoIG thin films XRD patterns shows that increasing the substrate temperature increases the epitaxial quality of the films for the given temperature range which is reflected in the sharp single peaks of the 67 nm HoIG thin film. Using Bragg's law ($n\lambda = 2d \sin\theta$), we calculated the in-plane lattice parameters of both 420 nm and 67 nm HoIG thin films, as shown in Table 4.2.

Table 4.2: The peak position and lattice parameters of HoIG/GGG samples.

Thin film	HoIG (420 nm)	HoIG (67 nm)
Peak position (˚)	50.4	50.0
Lattice parameter (Å)	12.53	12.62

Considering the bulk lattice parameter of HoIG as 12.40 Å, we conclude that the HoIG thin film is under in plane compressive strain. According to ref. [64] HoIG, may potentially show perpendicular magnetic anisotropy (PMA).

Figure 4.7 shows the XRD pattern of HoIG on Si (001) substrate. Due to the large difference between the lattice parameters of HoIG and Si substrate, the HoIG/Si is not a lattice-matched structure. Moreover, large thickness of the film results in relaxation and disturbance in the crystal structure. Along with the polycrystalline HoIG other secondary compound phases and also elemental metallic crystals may have formed inside the film. Excess oxygen partial pressure inside the chamber reacts with the metallic elements such as Fe and Ho, and form other unwanted secondary phases such as Fe_3O_4, Ho_2O_3, and $HoFeO_3$ orthoferrite in addition to HoIG.

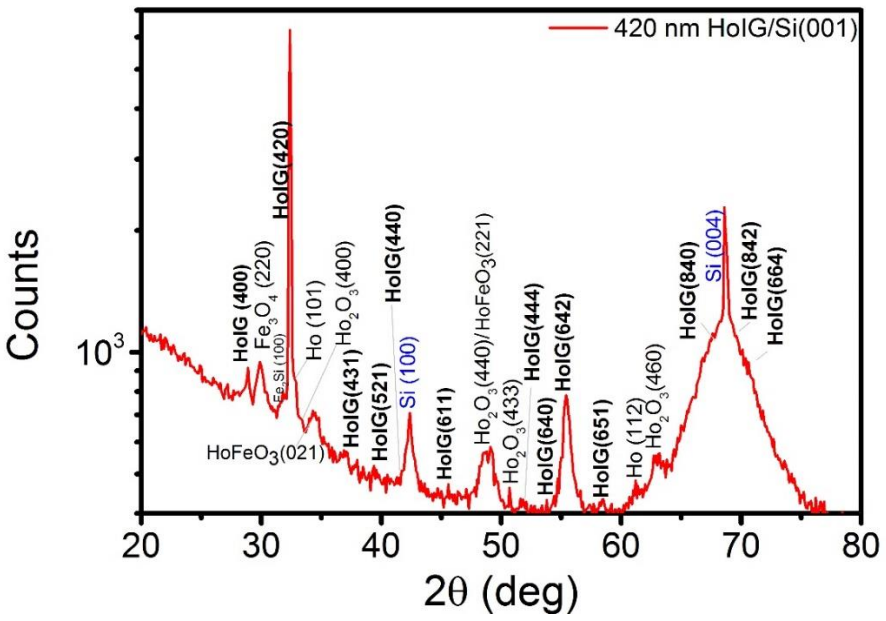

Figure 4.7: The XRD peaks of 420 nm HoIG/Si (001) substrate.

In order to characterize the surface quality of the films, atomic force microscopy (AFM) measurement was done on both 420 nm and 67 nm HoIG films grown on GGG substrates. Figure 4.8a shows the AFM measurement results of 420 nm thick HoIG/GGG, and Figure 4.9a is a 3D image of the same sample. According to the AFM results of 67 nm HoIG film, shown in Figure 4.8b, there are line-shaped structures on the surface of the sample, which might arise from the target rastering during the growth process. The linear line aperture of the target shutter might be a reason for these features. The samples have been scanned with an area of 5μm × 5μm on different areas and an average value of RMS surface roughness have been measured, which yields and RMS surface roughness of the 420 nm thick HoIG as1.74 nm.

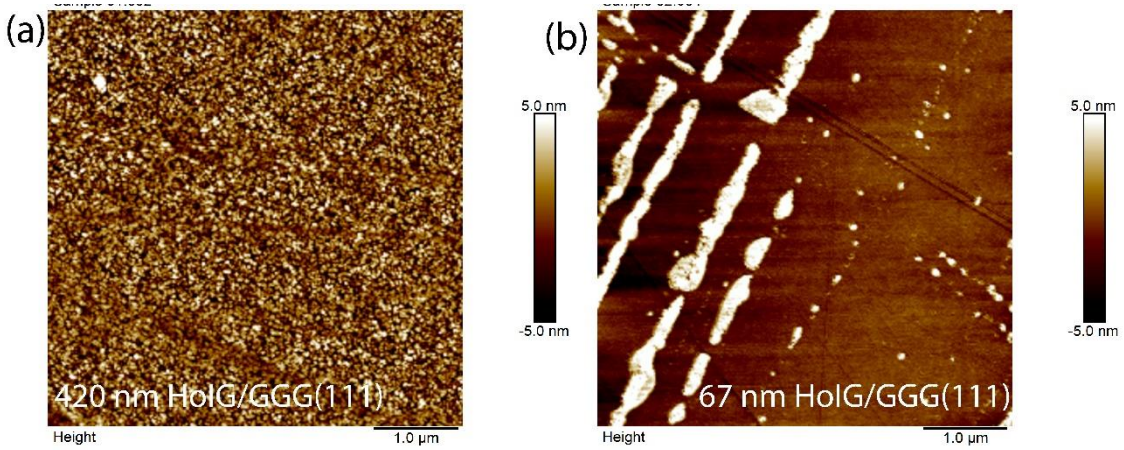

Figure 4.8: The AFM image of HoIG/GGG (111) with (a) 420 nm, and (b) 67 nm thickness.

Due to the unwanted features in the 5 × 5 μm^2 AFM images of the 67 nm HoIG film, we chose a smaller surface area of 1.5 × 1.5μm^2 to show the 3D AFM image of the thinner sample (Figure 4.9b). The RMS roughness of that area is 0.27 nm, however in the wide area scan, due to the unwanted process-induced structures on the film surface, the roughness becomes 1.28 nm for the 67 nm HoIG/GGG film. For thinner films, such as 67 nm and below (as shown on Table 4.1), the lower surface roughness is an indicator of higher epitaxial quality of the HoIG thin films grown on garnet substrates.

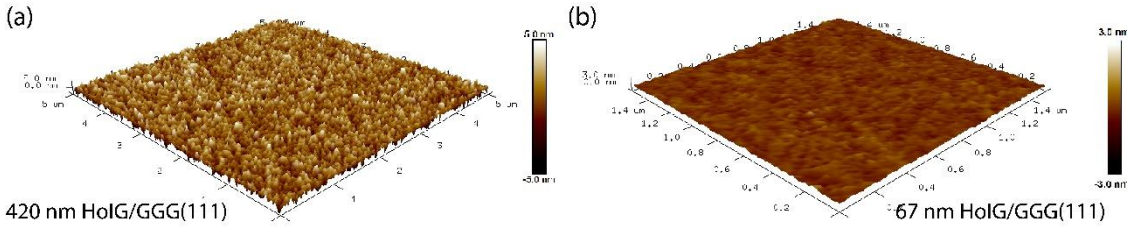

Figure 4.9: The AFM image of HoIG/GGG (111) with (a) 420 nm, and (b) 67 nm thickness. Note that the Z-scales are different.

4.1.4 Magnetic properties characterization of epitaxial HoIG

The magnetic hysteresis loop of both 420 nm and 67 nm epitaxial HoIG/GGG (111) thin films was measured by vibrating sample magnetometer (VSM) with in-plane (IP), and out of plane (OP) applied magnetic field. The higher substrate temperature in case of 67 nm thin film could also assist the better epitaxial quality of the film, since it provides the required thermal energy for atomic diffusion and crystal growth. Figure 4.10 shows the magnetic hysteresis loops of 420 nm and 67 nm HoIG/GGG (111) substrate under 250 Oe applied field. The VSM measurement results are shown on Table 4.3.

Table 4.3: Magnetic hysteresis loops of 420 nm and 67 nm thick of HoIG/GGG (111) with a 250 Oe (a) in-plane (IP) and (b) out-of-plane (OP) magnetic field.

Thickness	Magnetic Field Orientation	H_c (Oe)	M_s (emu/cm^3)	M_r (emu/cm^3)	H_s (Oe)
420 nm	IP	7	29	20	100
420 nm	OP	37	3.9	1.5	250
67 nm	IP	0	62	0	30
67 nm	OP	11	8.7	3.5	150

Figure 4.10a shows the in-plane (IP) magnetic hysteresis curves for both film thicknesses. According to this figure, the 67 nm thick HoIG film shows a saturation magnetic moment (M_s) of 62 emu·cm^{-3} (near bulk M_s of HoIG [65]) with around 30 Oe saturation field. The coercivity and remanence values of the 67 nm thin film is very low, such that almost no IP remanence is detectable in the IP magnetic hysteresis loops. On the other hand, the 420 nm thick film shows M_s ~ 29 emu·cm^{-3} at 100 Oe saturation field. The coercivity of this film is around 7 Oe, with a remanence of 20 emu·cm^{-3}. Large remanence of the 420 nm HoIG under IP applied field shows that, despite 67 nm film, the IP component of the total magnetic moment of this film is dominant, which could be due to the polycrystallinity and multiple grain orientations that retain remanence magnetization at zero magnetic field. Besides, strain relaxation due to increased film thickness may also alter the intrinsic HoIG magnetic hysteresis loop shape. The smaller M_s of the thicker film could be due to the spin cancellation of iron ions via super exchange mechanism inside the thin film lattice, or random distribution and cancellation of magnetic moments in the sub-lattices due to the increased film thickness. Figure 4.10b shows the OP magnetic hysteresis loops for both HoIG thin films. According to this figure, 67 nm HoIG film with a M_r/M_s ~0.5 exhibits an OP magnetic anisotropy which is in agreement with our previous theoretical predictions [64, 65]. The M_s and coercivity values of 8.7 emu·cm^{-3} and 11 Oe,

respectively. The small M_s of the OP hysteresis loop in the 67 nm sample is an advantageous condition for magnetization switching since lower energy is needed for magnetization switching in the sample. Moreover, the small coercivity of the HoIG thin film which is at the range of YIG's coercivity [43], might lead to low Gilbert damping in FMR characterization. 420 nm thick HoIG shows even lower saturation magnetic moment of around 4 emu·cm^{-3} with a coercivity of around 37 Oe, under OP magnetic field. The M_r/M_s value of around 0.3 in the OP hysteresis curve of the 420 nm HoIG film might be an indicator of a tilted magnetic anisotropy. However, the remanence value of the thicker sample is smaller than that of the 67 nm OP hysteresis curve (1.5 emu·cm^{-3}). The tilted magnetic moment is another advantage for spin wave FMR, which can be done using both IP and OP spin orbit torque switching.

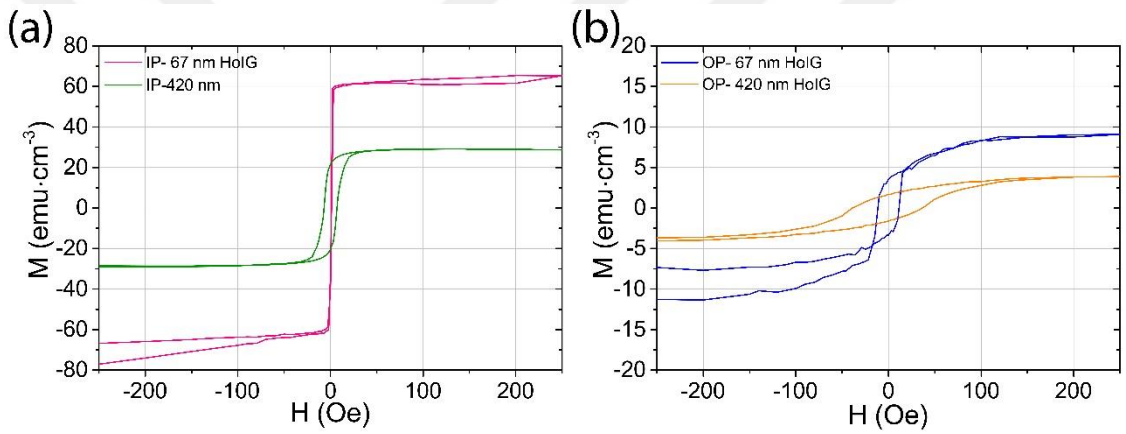

Figure 4.10: Magnetic hysteresis loops of 420 nm and 67 nm thick of HoIG/GGG (111) with a 250 Oe (a) in plane and (b) out of plane magnetic field.

The failure in closing the hysteresis loops might arise from the variations during the measurements such as nonlinear mechanical vibrations of the samples especially under the high magnetic fields or thermal drift during the measurements.

4.1.5 Conclusions

We provided, for the first time, an optimized method for pulsed laser deposition of HoIG epitaxial thin films on GGG (111) and TGG (111) garnet substrates. In addition, HoIG thin film was grown on Si (001) and SOI substrate, for integrated photonic applications. We optimized the growth procedure and the film quality by running two calibration processes: first, HoIG was grown under 150 mTorr, 650 ˚C substrate temperature, and 150000 laser shots which yielded 420 nm film thickness. Second, the oxygen partial pressure, substrate temperature, and the number of laser shots have been reduced to 10

mTorr, 800 ˚C, and 20000 shots, respectively. The second calibration run resulted in 67 nm film thickness. We show that despite 420 nm thick HoIG, the 67 nm HoIG which is grown under lower oxygen partial pressure and higher substrate temperature, shows better epitaxial single crystalline structure with a compressive in-plane strain which might assist PMA. The surface roughness of the film gained from AFM characterization, also shows a better epitaxial quality in case of 67 nm (RMS surface roughness ~ 0.3 nm), compared to the thicker film.

IP and OP magnetic hysteresis loops for 67 nm and 420 nm show OP magnetic anisotropy in the thinner film with bulk-like M_s, low M_r and coercivity values which is advantageous both for low energy spin switching and low Gilbert damping in FMR measurements. Overall, the IP hysteresis loop measurements show a coercivity around 7 Oe and M_s ~29 emu·cm^{-3} for the 420 nm HoIG film, with a tilted magnetic moment, the IP component of which is dominant. The 67 nm film exhibits perpendicular (out-of-plane) magnetic anisotropy. Its IP hysteresis loop curves show a coercivity of less than 1 Oe and M_s of 62 emu·cm^{-3} which is near the bulk M_s value of the HoIG. OP hysteresis loop of 67 nm film shows PMA due to M_r/M_s ~0.5, with a coercivity of around 11 Oe. The 420 nm film with a dominant IP magnetic moment component showed a coercivity higher than the 67 nm film (7 Oe). The smaller M_s of the thicker film could be due to the spin cancellation of iron ions via super exchange mechanism inside the film lattice, or random distribution and cancellation of magnetic moments in the sub-lattices due to the increased film thickness. These results suggest that decreased film thicknesses with higher epitaxial qualities will result in more robust perpendicular magnetic anisotropy in HoIG films, which is in agreement with our earlier theoretical predictions [64, 65]. Our predictions in Table 3.3 show that HoIG/GGG (111) could have about 311 Oe saturation field and we obtained 150 and 250 Oe saturation fields, experimentally. These experimental results confirm our model and PMA hypothesis on HoIG/GGG.

Chapter 5

ALL-OPTICAL CONTROL OF MAGNETIZATION IN METALLIC MAGNETIC THIN FILMS

5.1 Effect of Laser and Magnetic Properties on Ultrafast All-Optical Magnetization Control in Metallic Thin Films

This section is based on the manuscript *"Ultrafast All Optical Magnetization Control for Broadband Terahertz Spin Wave Generation",* S. Mokarian Zanjani, M. C. Onbasli, arXiv preprint arXiv:2005.03493 (2020).

All-optical magnetization dynamics of metallic magnetic thin films depend on intrinsic magnetic properties such as Curie temperature, exchange constant, magnetic moment and spin-flip ratio as well as laser pulse parameters. Here, we present an energy balance model to study the effect of laser fluence and pulse width for single Gaussian laser pulse on magnetization dynamics in five different magnetic metallic thin films: Iron, Cobalt, Nickel, Gadolinium and Ni_2MnSn Heusler alloy. We investigate the effect of film thickness on magnetization and lattice temperature after interaction with the ultrashort laser pulse. The model captures the energy transfer rates from femtosecond laser pulse to electron bath coupled with phonon, spin, and magnetization. Type I films (Fe, Co, and Ni with Curie temperatures (T_C) > room temperature, RT) could recover their magnetic moments unlike type II films (Gd and Ni_2MnSn with $T_C \approx$ RT). Our numerical modeling shows that ultrafast magnetization control could be achieved when laser fluence is within [30-100] $J \cdot m^{-2}$ for type I films thicker than 20 nm. Recovered fraction of magnetization is higher for type I thin films with higher Curie temperatures. The magnetization drop and recovery occurs in a shorter timescales in the films with larger spin-flip ratio.

5.1.1 Introduction

Magnetization control in metallic magnetic thin films with ultrashort laser pulse has been a subject of rigorous research in past decades [226-228] . Laser-driven magnetization dynamics [229-231] and all-optical switching (AOS) of magnetization [152, 232, 233] are based on femtosecond (fs) laser pulse interaction with metallic magnetic thin films and their phonon, spin and electron baths. Such effects could lay the foundations for promising future spintronic applications such as high-precision sensing, spectroscopy

[234], and on-chip communications [235, 236] using THz spin waves generated as a result of ultrafast magnetization control [237-245].

A detailed understanding of how the key material and laser parameters determine the laser-driven magnetization dynamics is essential for understanding phonon, spin and photon interactions for faster and more energy-efficient response in spintronic device design. In this section, we present an energy balance study based on Koopmans' model [83], which describes the coupled interaction between electron, phonon, and spin temperatures with normalized magnetization (extended M3TM) after illumination with fs Gaussian single laser pulse. Our study analyzes the influence of laser pulse parameters and thin film magnetic properties for more energy-efficient and faster response using laser-driven magnetization manipulation for five different metallic magnetic thin films: Iron (Fe), Cobalt (Co), Nickel (Ni), Gadolinium (Gd), and Ni_2MnSn Heusler alloy. We investigated the effect of the thin film thickness, Curie temperature, and spin-flip ratio as well as the fs laser pulse characteristics (laser fluence and pulse width) on magnetization dynamics. We provide the guidelines for obtaining fast magnetization response using the appropriate metallic film type, thickness, laser pulse width and fluence. By identifying the regimes in which T_C, phonon scattering, thermal mass and spin-flip scattering dominates, we quantitatively describe the mechanisms that determine magnetization response and life time.

The interaction of fs laser pulse with Nickel (Ni) metallic magnetic materials was first captured using three temperature model (3TM) [89]. The temperature-dependent microscopic spin and magnetization dynamics of magnetic thin films was independently explained by Landau-Liftshitz-Bloch (LLB) equation [246] to model the laser-matter interaction. The LLB model explains the thermal effects of laser pulse on magnetization dynamics. Nevertheless, this model does not capture the thermal interaction of laser pulse with electron, phonon, and spin temperatures and their interactions. This model also uses temperature-dependent damping parameter, which was not measured for most materials as functions of temperature. Koopmans et al. [83] developed a model considering the coupling of magnetization dynamics with electron and phonon temperatures. Here, we extended that model by adding the spin temperature to those of phonon and electron to describe each of these effects for different pulse fluences, widths, film thicknesses and metal types. Spin temperature is the averaged energy distributed over the spins exposed to the laser pulse. The investigation of spin temperature dynamics is necessary because in

the longer time delays the heat exchange between spin and lattice and electrons may have their own dynamics, independent of electrons, in such temporal regime. These dynamics become more important especially when reaching Curie temperature. As a result, spin phase transitions are triggered with diverging spin heat capacity and longer non-equilibrium spin interaction times.

In experimental studies of laser-matter interaction such as single pulse Kerr or Faraday effects, the interactions of photons with spins have been investigated by measuring FR [148, 150-152]. Using spin temperature and temperature dependence of ferromagnetic metals (Curie's Law), one can calculate the temporal evolution of local magnetic moment interacting with the laser pulse. Using temporal evolution of magnetic moments due to interaction with a fs laser pulse, one could control the local magnetic moment orientation of a material for different magnetization behaviors. These behaviors such as spin canting or controlled partial demagnetization with multiple laser pulses could be used for sensing and memory applications. By capturing the thermal equilibrium between electron, phonon and spin baths, their heat exchanges, the magnetization dynamics, our model provides the experimental conditions needed for ultrafast manipulation of magnetization for spintronic device design.

5.1.2 Energy Balance Model and Magnetization Dynamics

We developed an extended three-temperature model coupled with transient magnetization dynamics to capture the energy transfer rates between spin, phonon and electron thermal baths. These thermal baths are assumed to behave in the classical or semi-bulk regime (i.e. films are sufficiently thick with no quantum confinement effects, d > 20 nm). The energy balance model describes that the fs laser pulse injects energy into the coupled baths and the transient electron, phonon, and spin temperatures (T_e, T_p, T_s) and magnetization are described with the rate equations 5.1-5.4 [83, 89].

$$C_e \frac{dT_e}{dt} = -G_{ep}(T_e - T_p) - G_{es}(T_e - T_s) + P(t) \tag{5.1}$$

$$C_p \frac{dT_p}{dt} = -G_{ep}(T_p - T_e) - G_{ps}(T_p - T_s) \tag{5.2}$$

$$C_s \frac{dT_s}{dt} = -G_{es}(T_s - T_e) - G_{ps}(T_s - T_p) \tag{5.3}$$

$$\frac{dm}{dt} = Rm\frac{T_p}{T_C}\left(1 - m\coth\left(m\frac{T_C}{T_e}\right)\right) \tag{5.4}$$

In these equations, T_e, T_p, T_s, and T_C are electron, phonon, spin, and Curie temperatures, respectively. R is the spin-flip ratio [83] and determines the kinetics of transient changes of T_e, T_p, T_s, and magnetization. The electron-phonon, electron-spin, and phonon-spin coupling constants G_{ep}, G_{es}, G_{ps}, follow a similar formalism described in ref. [83] and [153]. The heat capacities of phonon and spin are C_p and C_s. The electron heat capacity is a temperature-dependent parameter and is defined as $C_e=\gamma T_e$, where γ is a parameter that depends on free electron density and Fermi energy level [247], used in ref. [83] as $C_p=5\ \gamma T_C$). We consider the incoming laser pulse power as a Gaussian single pulse per unit volume as $P(t) = \frac{P_0}{\sqrt{2\pi}} \exp\left(-\frac{1}{2}\left(\frac{t}{t_0}\right)^2\right)$ where $P_0 = \frac{I_0}{d.t_0}$, I_0 and t_0 are the laser pulse fluence in $J\cdot m^{-2}$, pulse width (fs), respectively. The thickness dependence of the injected laser pulse-driven magnetization dynamics in metal thin film is captured by normalizing the laser fluence to the film thickness, d. Here, m is the normalized vertical magnetization defined as $|M_z|/M_s$. The material parameters and constants used in the numerical solutions to the equations 5.1-5.4 for Ni, Co, Fe, Gd, and Ni_2MnSn are shown on Table 5.1.

Table 5.1: Material parameters used in the extended M3TM model. C_p, C_s are in ($J\cdot m^{-3}\cdot K^{-1}$); G_{ep}, G_{es}, G_{ps} are in ($W\cdot m^{-3}\cdot K^{-1}$), T_C is the Curie temperature (K), R: spin-flip ratio (s^{-1}), γ in ($J\cdot m^{-3}\cdot K^{-2}$) [83, 89, 153, 247].

Film	**C_p $\times10^6$**	**C_s $\times10^6$**	**G_{ep} $\times10^{18}$**	**G_{es} $\times10^{18}$**	**G_{ps} $\times10^{18}$**	**T_C**	**R$\times10^{12}$**	**$\gamma = C_p/(5T_C)$**
Ni	2.33	0.2	4.05	0.6	0.03	627	17.2	743.22
Co	2.07	0.2	4.05	0.6	0.03	1388	25.3	298.28
Fe	3.46	0.17	0.7	0.06	0.03	1043	1.86	663.47
Gd	1.78	0.2	0.21	0.6	0.03	297	0.092	1200
Ni_2MnSn	0.615	0.2	0.24	0.6	0.03	319	0.1	385.58

5.1.3 Effect of fs laser pulse on metallic magnetic thin films.

Figure 5.1a shows a schematic of THz spin wave generation inside the metallic magnetic thin film. As the fs laser pulse hits the metallic film, the film's magnetic moment undergoes heat exchange within phonon, spin and electron baths. These exchanges trigger ultrafast relaxation of spins, which could be eventually lead to terahertz spin waves [79]. Here, we analyze only the local heat exchange directly exposed to the laser pulse using our modified three-temperature model, while a rigorous analysis using Landau-Lifshitz-Gilbert equation solutions for terahertz spin wave generation in mesoscopic length scales is not presented here.

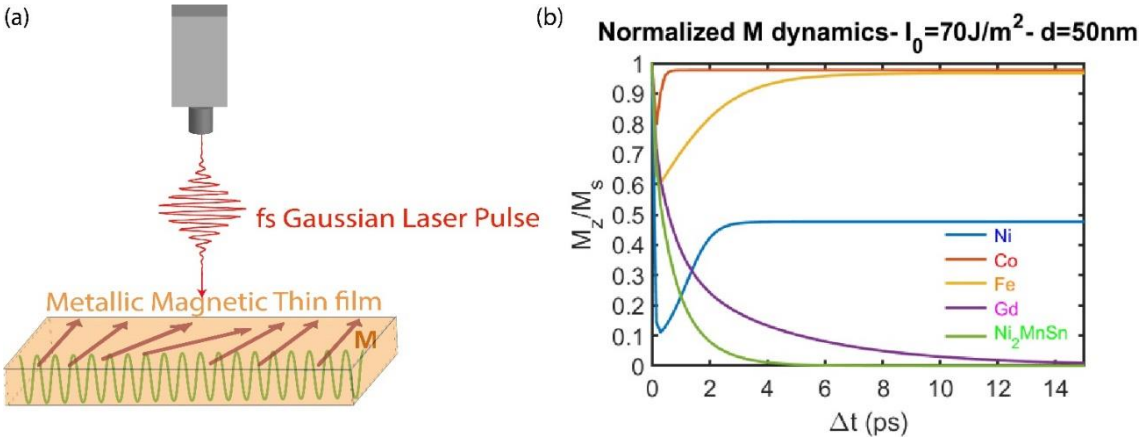

Figure 5.1: Effect of fs laser pulse on metallic magnetic thin films. (a) Ultrafast and local manipulation of spins in metallic magnetic thin films after illumination with ultrashort laser pulse. (b) Transient magnetization dynamics of 50 nm thick Fe, Co, Ni, Gd, and Ni_2MnSn Heusler alloy films illuminated with 100 fs laser pulse with 70 $J \cdot m^{-2}$ fluence. The sub-picosecond ultrafast magnetization dynamics of these metallic magnetic thin films are included in Appendix B, which shows the fs timescales of magnetization decrease after the laser illumination.

Figure 5.1b shows the calculated time-dependence of the magnetic moment magnitude of 50 nm thick Fe, Ni, Co, Gd, and Ni_2MnSn upon each receiving a 100 fs-long pulse with a moderate (70 $J \cdot m^{-2}$) fluence. According to Figure 5.1b, magnetizations in Fe, Ni, Co (type I) reach the dip in less than 200 fs and reach steady state moments in 6, 3, and 0.7 ps, respectively.

We group Fe, Co, and Ni as type I since their Curie temperatures greatly exceed room temperature (Fe: 1043 K, Co: 1388 K, Ni: 627 K). Thus, these films never undergo thermal demagnetization after interacting with fs laser pulse using 70 $J \cdot m^{-2}$ fluence. On the other hand, Gd and Ni_2MnSn (type II) with Curie temperatures near room temperature (Gd: 297 K, Ni_2MnSn: 319 K) undergo thermal demagnetization upon interacting with the fs laser pulse and reach zero magnetization within 15 and 6 ps, respectively. The laser-induced loss of spin angular momentum is attributed to spin-flip scattering with phonons and hot electrons (electron-phonon/electron-electron interaction), known as Elliot-Yafet scattering [248, 249]. In addition, the recovered fraction of magnetization after a few picoseconds is higher in Fe and Co ($|M_z|/M_s > 97\%$) compared to Ni ($|M_z|/M_s \sim 50\%$). The recovered fraction of magnetization increases with increasing the film thickness.

In the rest of this section, the effect of film thickness, fs laser pulse fluence and pulse width on the magnetization dynamics in both type I and II films are investigated.

5.1.4 Thin films with type I dynamics (Fe, Co, Ni)

Type I dynamics is defined as the ultrafast decrease of magnetization in fs timescales, followed by slow recovery of magnetization in picosecond timescales. Hot electrons excite transient magnetization loss and could trigger a subsequent excitation of spin waves (magnons) due to exchange coupling. Magnons undergo inelastic scattering with phonons and electronic charges in the lattice. The lattice serves as a reservoir for absorbed, dissipated and scattered energy and causes evanescent decay of the generated spin waves. Magnetization recovery time is slightly longer than electron-lattice relaxation time due to the different coupling strengths among lattice, phonon and electron temperatures (i.e. strength of Hamiltonian terms for each quasiparticle). In our model, we do not consider the quantum nature of these baths or their Hamiltonians and lump their couplings into G_{ep}, G_{es}, G_{ps} parameters. These parameters are known for the metallic magnetic thin films in our study [83]. Figure 5.2a shows the magnetization dynamics of (i) 20 nm and (ii) 100 nm thick Fe films under illumination with a 100 fs Gaussian laser pulse.

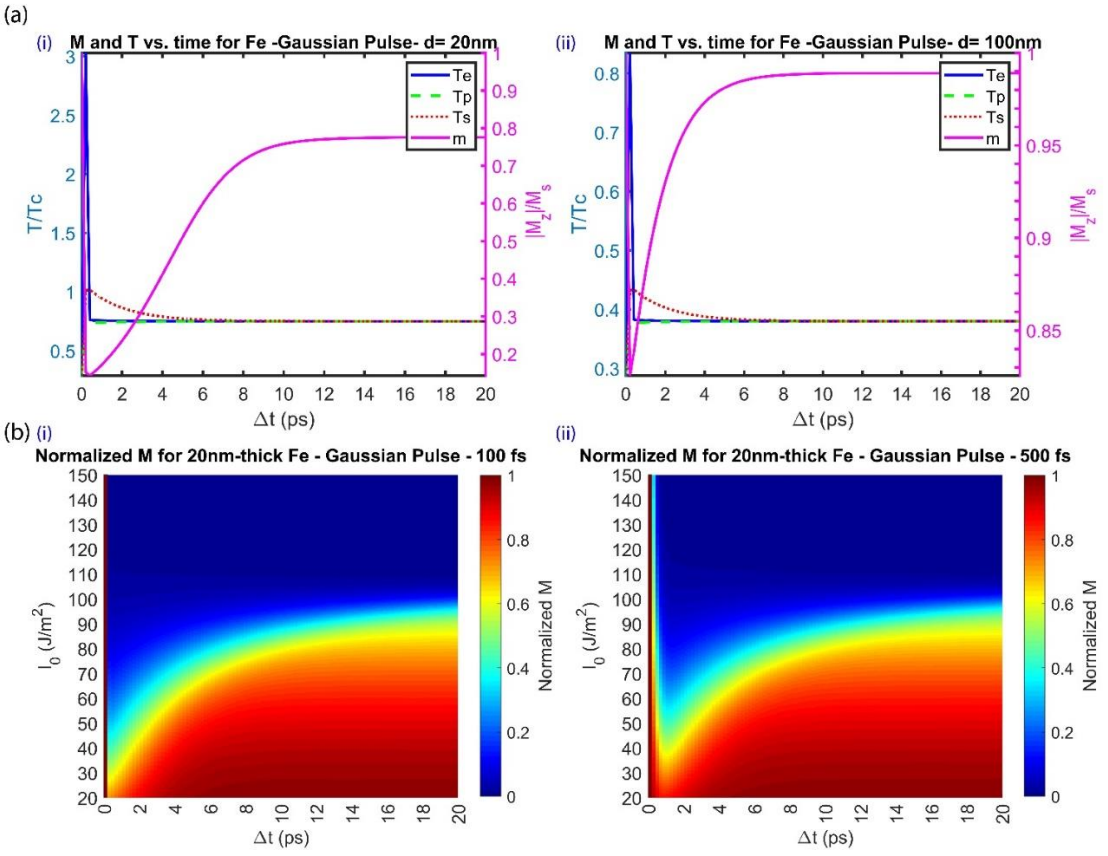

Figure 5.2: Effect of film thickness, fs laser fluence (I_0) and pulse width on magnetization dynamics and lattice temperature of Fe thin film. (a) Transient electron (T_e), phonon (T_p), spin (T_s) temperatures and magnetization ($m=|M_z|/M_s$) of (i) 20 nm and (ii) 100 nm thick Fe, illuminated with 100 fs laser pulse with 70 $J \cdot m^{-2}$ fluence. (b) Fluence and pulse width dependence of magnetization in 20 nm thick Fe film illuminated with (i) 100 fs and (ii) 500 fs laser pulse.

Following type I dynamics, magnetization of Fe starts switching around 300 fs for 20 nm film and slightly shorter than that for 100 nm Fe film. The perpendicular magnetization starts recovering and eventually reaches ~78% of saturation moment after 12 ps in 20 nm Fe film. The recovered magnetization fraction reaches 99% for 100 nm thick film after 8 ps. Due to the interaction of spins with the fs laser pulse, the electron, spin and lattice temperatures increase. Although the electron temperature undergoes a sudden increase to above Curie temperature (T_C) of Fe, due to lower heat capacity of electron (C_e), it drops quickly and the equilibrium lattice temperature (T_p) stays below T_C. Thus, both 20 and 100 nm Fe films retain their magnetization.

In Figure 5.3a, the magnetization dynamics of (i) 20 and (ii) 100 nm thick Co, are shown after illumination with Gaussian single pulse with 100 fs duration and 70 $J \cdot m^{-2}$ fluence. Co magnetization (type I) decreases within 250 fs in 20 nm film and recovers back to 75% of its saturation moment in around 10 ps. Magnetic moment in 100 nm Co starts switching in ~160 fs and almost completely recovers (~99.5%) its saturation state after 800 fs. In this case, $T_p/T_C < 1$ so the film does not demagnetize completely.

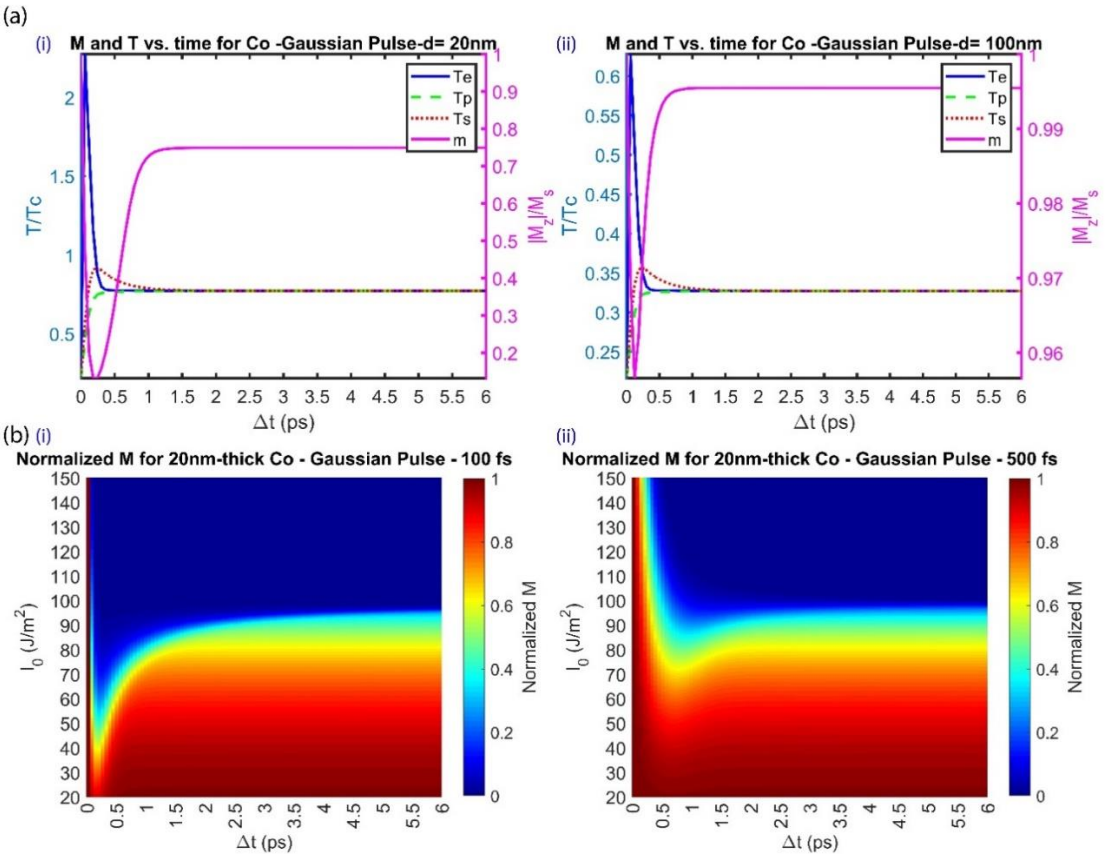

Figure 5.3: Effect of film thickness, fs laser fluence and pulse width on magnetization dynamics and lattice temperature of Co thin film. (a) Transient electron (T_e), phonon (T_p), spin (T_s) temperatures, and normalized

magnetization ($m=|M_z|/M_s$) of (i) 20 nm and (ii) 100 nm thick Co illuminated with 100 fs laser pulse with 70 $J \cdot m^{-2}$ fluence. (b) Fluence and pulse width dependence of normalized magnetization of 20 nm thick Co film illuminated with (i) 100 fs and (ii) 500 fs laser pulse.

In Figure 5.4, the magnetization dynamics of (i) 20 and (ii) 100 nm thick Ni thin films upon illumination with 100 fs Gaussian pulses are shown. The 20 nm Ni film demagnetizes completely after 130 fs, since the lattice temperature (T_p) greatly exceeds nickel's Curie temperature. Nickel's T_C (627 K) is lower than those of Fe (1043 K) and Co (1388 K); so 20 nm thick Ni film cannot retain its magnetization after interacting with the 70 $J \cdot m^{-2}$ fluence and 100 fs laser pulse. However, the thicker Ni film (100 nm) exhibits type I dynamic similar to Fe and Co films due to its larger heat capacity and thermal mass. The film's magnetic moment decreases in ~170 fs and recovers ~83% of its saturation moment within 1.2 ps. Increasing Ni film thickness decreases both magnetization drop and recovery times, but it increases the recovered fraction of magnetization. The fluence and pulse width dependence of magnetizations for 20 nm Fe (Figure 5.2b), Co (Figure 5.3b), Ni (Figure 5.4b) films are shown. The magnetization dynamics have been calculated for fluences from 20 to 150 $J \cdot m^{-2}$. Illuminated with both 100 fs (Figure 5.2b (i), Figure 5.3b (i), Figure 5.4b (i)) and 500 fs (Figure 5.2b (ii), Figure 5.3b (ii), Figure 5.4b (ii)), both magnetization decrease and recovery times of 20 nm films increase with increasing laser fluence. The recovered magnetization fraction, however, decreases with increasing laser fluence. In addition, there is a threshold fluence above which the films are thermally demagnetized completely. This threshold fluence depends on the film type (T_C, G_{ep}, and C_p), thickness and pulse width. Increasing the pulse width increases the response time of the films, which is attributed to the larger energy injected and dissipated with the films. The recovered fraction of magnetization is higher in case of thicker films, since the higher thermal mass prevents the excess heat accumulation and magnetization disturbance in these films. The fluence dependence of magnetization dynamics of 100 nm films are presented in the Appendix B.

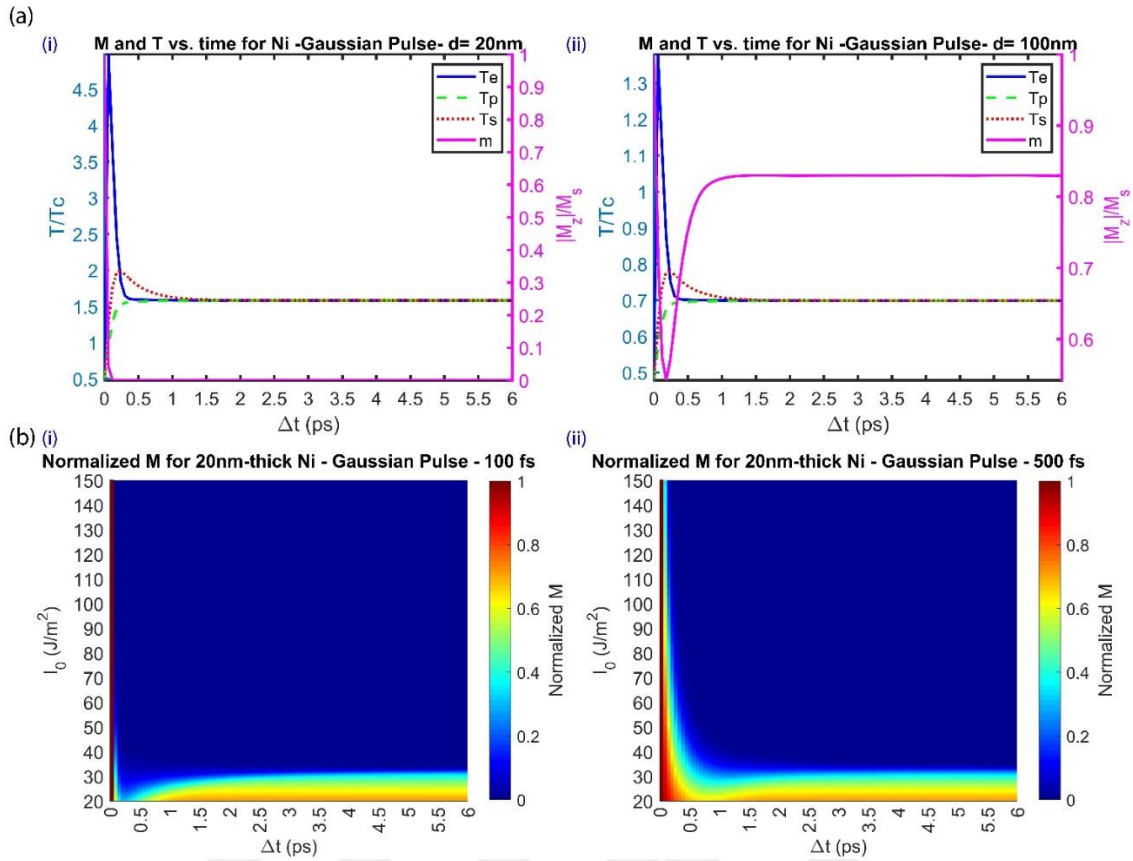

Figure. 5.4: Effect of film thickness, fs laser fluence and pulse width on magnetization dynamics and lattice temperature of Ni thin film. (a) Transient electron (T_e), phonon (T_p), spin (T_s) temperatures, and normalized magnetization ($m=|M_z|/M_s$) of (i) 20 nm and (ii) 100 nm thick Co illuminated with 100 fs laser pulse with 70 $J \cdot m^{-2}$ fluence. (b) Fluence and pulse width dependence of normalized magnetization of 20 nm thick Co film illuminated with (i) 100 fs and (ii) 500 fs laser pulse.

5.1.5 Thin films with type II dynamics (Gd, Ni_2MnSn)

Type II magnetization dynamics arise when the films with low phonon heat capacity and low Curie temperature undergo thermal demagnetization (magnetic moment decays to zero in tens of picoseconds). Figures 5.5 and 5.6 show the magnetization dynamics of type II films, Gd and Ni_2MnSn. Figure 5.5a (i) and (ii) show the temporal change of T_e, T_p, T_s, and the magnetization of 20 nm and 100 nm Gd thin films after interacting with a 100 fs Gaussian single laser pulse of 70 $J \cdot m^{-2}$ fluence. The spin-flip ratio of Gd is small ($R= 0.092 \times 10^{12}$ s^{-1}) compared to the type I metallic magnetic thin films; so the magnetization vanishes slowly after 2.5 ps in 20 nm film and 50 ps in 100 nm Gd film. Since the Curie temperature of Gd is near room temperature (297 K), the equilibrium electron, spin and the lattice temperatures exceed the Curie temperature and the film is thermally demagnetized completely with the laser pulse. The equilibrium lattice temperature of 20 nm thick Gd film (Figure 5.5a (i)) is higher compared to the 100 nm thick film (Figure 5.5a (ii)) due to the lower thermal mass of the thinner film. Similarly,

Ni_2MnSn also undergoes thermal demagnetization and its magnetization decays faster than Gd due to the alloy's larger spin-flip ratio ($R=0.1\times10^{12}s^{-1}$) and Curie temperature (319 K). Demagnetization times of 20 nm and 100 nm thick Ni_2MnSn films are 1 ps and 35 ps, respectively, showing that a larger thermal mass delays thermal equilibration. Figures 5.5b and 5.6b show the dependence of magnetization dynamics to the laser pulse fluence and duration.

Similar to type I dynamics, increasing the laser fluence and pulse duration, increases the response time in both type II films. On the other hand, excitation of the films with smaller laser fluences keeps the films magnetized for longer times. Unlike type I films, the response time increases in type II by increasing the film thickness and perturbation of the magnetic moments inside the thicker films occurs in a longer time due to the increased thermal mass. According to Figures 5.5b and Figure 5.6b, increasing the incoming laser pulse width increases the response time.

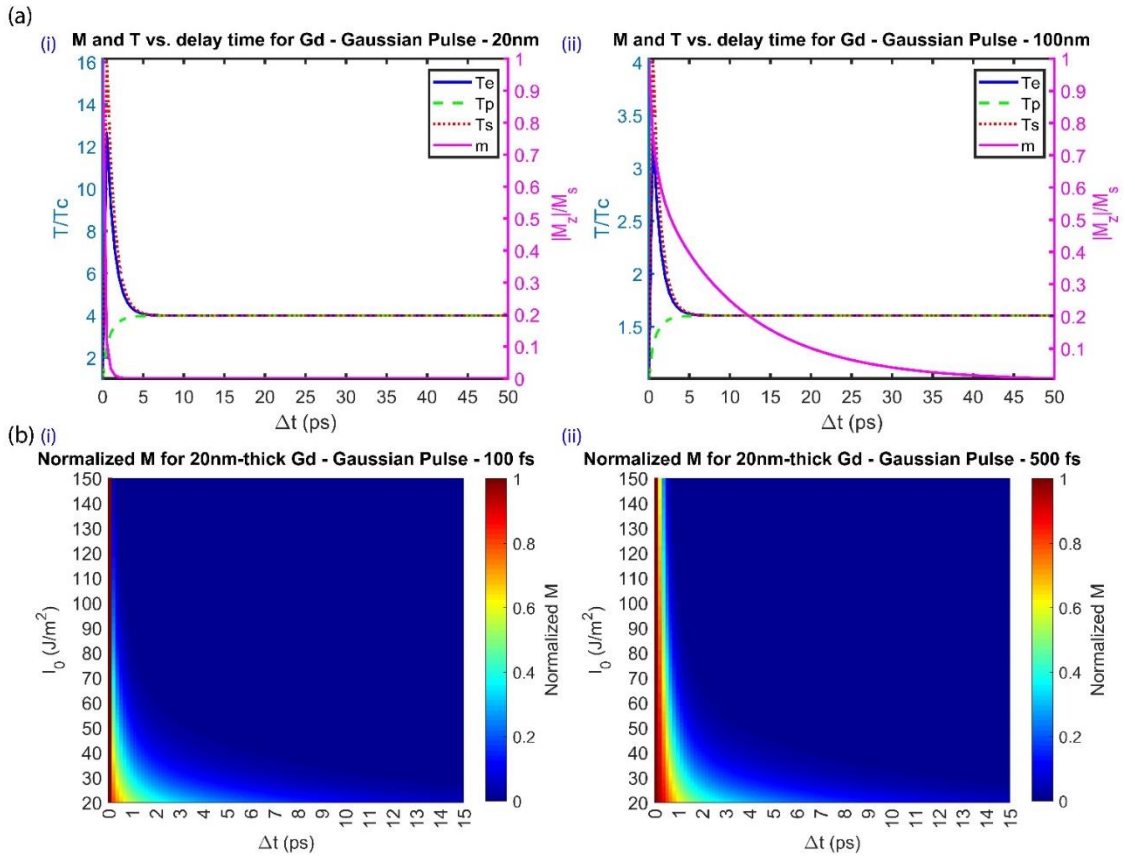

Figure 5.5: Effect of film thickness, fs laser fluence and pulse width on magnetization dynamics and lattice temperature of Gd magnetic thin film. (a) transient electron (T_e), phonon (T_p), spin (T_s) temperatures, and normalized magnetization ($m=|M_z|/M_s$) of (i) 20 nm and (ii) 100 nm thick Gd illuminated with 100 fs laser pulse with 70 $J\cdot m^{-2}$ fluence. (b) Fluence and pulse width dependence of normalized magnetization of 20 nm thick Gd film illuminated with (i) 100 fs and (ii) 500 fs Gaussian laser pulse.

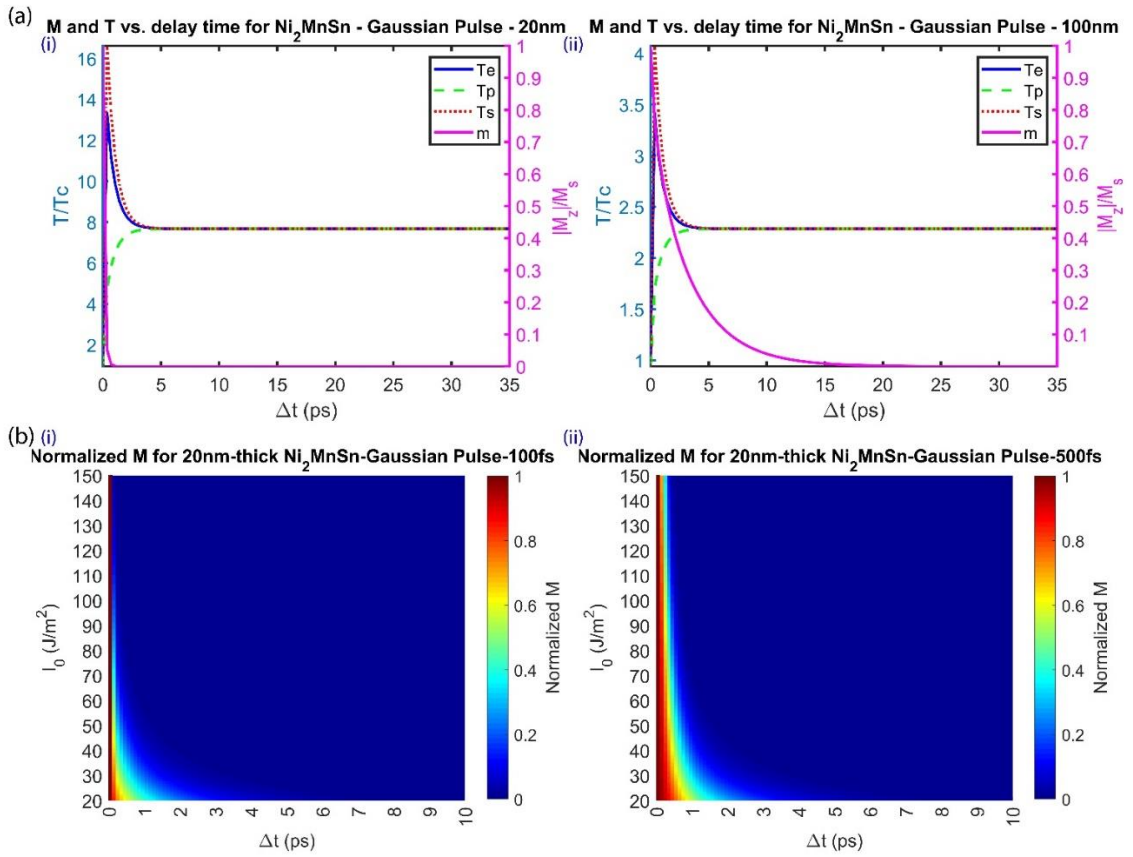

Figure 5.6: Effect of film thickness, fs laser fluence and pulse width on magnetization dynamics and lattice temperature of Ni_2MnSn magnetic thin film. (a) transient electron (T_e), phonon (T_p), spin (T_s) temperatures, and normalized magnetization ($m=|M_z|/M_s$) of (i) 20 nm and (ii) 100 nm thick Gd illuminated with 100 fs laser pulse with 70 $J \cdot m^{-2}$ fluence. (b) Fluence and pulse width dependence of normalized magnetization of 20 nm thick Gd film illuminated with (i) 100 fs and (ii) 500 fs Gaussian laser pulse.

5.1.6 Effect of laser fluence, film thickness and pulse shape on magnetization dynamics in extended M3TM model

We developed our model to investigate the effect of laser pulse fluence (I_0), pulse shape and film thickness on normalized magnetization dynamics. We applied various laser fluences in range of 20 - 150 $J \cdot m^{-2}$ with pulse duration of 100 fs on 20 nm (Figures 5.7a and 5.7c) and 100 nm (Figures 5.7b and 5.7d) Ni thin films. Figure 5.7 shows the sensitivity of normalized magnetization dynamics to laser fluence for sinc and chirp pulses.

In the previous part, we explained that 20 nm thick Ni film completely demagnetizes after interaction with a fs Gaussian laser pulse. According to Figures 5.7a and 5.7c, Ni thin film with 20 nm thickness completely demagnetizes after less than 1 fs when exposed to both sinc and chirp pulses with 100 fs duration. The thermal demagnetization time is

slightly longer when exposed to chirp pulse, compared to sinc pulse. Increasing I_0 increases the thermal demagnetization time, as in Gaussian pulse case.

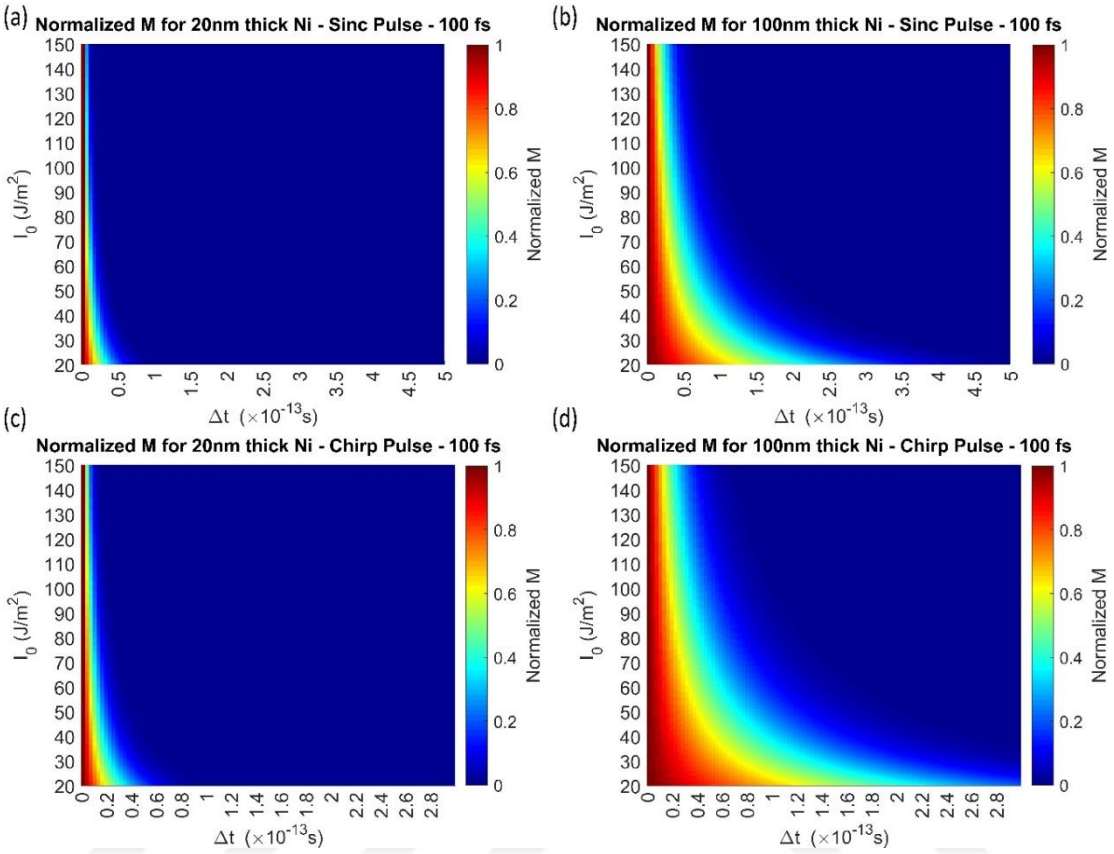

Figure 5.7: Effect of film thickness, laser pulse fluence and pulse shape on magnetization dynamics of (a) and (c) 20 nm and (b) and (d) 100 nm thick Ni thin film under 100 fs (a) and (b) sinc pulse and (c) and (d) chirp pulse.

After illumination with sinc pulse and chirp pulse with the same duration, as shown in Figure 5.7, both 20 nm and 100 nm thick Ni films demagnetize completely. Thermal demagnetization time of 100 nm thick Ni is longer than that for the thinner film, because the excess heat concentrated within the 20 nm Ni film increases its lattice temperature to above T_C.

As a result, Figure 5.7 show that thermal demagnetization time increases with increasing I_0 and film thickness when exposed to 100 fs laser pulse with different pulse shapes.

5.1.7 Conclusions

We present a modified three-temperature model to explain the energy transfer from fs laser pulse to coupled electron, phonon, spin, and normalized magnetization in Fe, Co, Ni (type I films), Gd and Ni_2MnSn (type II films). Our model and numerical solutions show that type I metallic thin films with Curie temperatures much higher than room temperature

recover most of their magnetization. The films were first illuminated with Gaussian single laser pulse. Then, the magnetization vector decreases briefly within the next 130-200 fs and reverts to its initial orientation. In the following 1-2 ps, the magnetization settles to its steady-state orientation. Increasing the laser pulse width and fluence increases the film response time and decreases its recovered fraction of magnetization. Type II films undergo thermal demagnetization gradually in about 35-50 ps after interaction with Gaussian laser pulse. Although higher laser fluences and pulse widths result in higher response times in these films, similar to type I films, increasing the thickness does not shorten the thermal demagnetization time. In thicker type I films (i.e. 100 nm), unlike type II films, the response time of magnetization is shorter.

Illuminating the Ni thin film with 100 fs sinc and chirp laser pulses of any fluence in the range of 20-150 $J \cdot m^{-2}$ results in complete thermal demagnetization of both 20 nm and 100 nm thick Ni film.

Our study suggests the need for optimizing the experimental parameters, such as laser pulse width and energy, film type and thickness for more energy efficient and faster response. Such an optimized set of material and excitation parameter conditions could help tune THz spin waves generated using ultrafast lasers.

5.2 All Optical Control of Magnetization in Quantum Confined Ultrathin Magnetic Metals

This section is based on the manuscript *"All Optical Control of Magnetization in Quantum Confined Ultrathin Magnetic Metals"* S. Mokarian Zanjani, M.T. Naseem, O. Mustecaplioglu, M. C. Onbasli, arXiv preprint arXiv:2104.02608 (2021) (under review).

All-optical control of magnetization dynamics in sub-10 nm metallic thin films are investigated, as these films with quantum confinement undergo unique interactions with femtosecond laser pulses. Our theoretical derivations based on the free electron model show that the density of states at Fermi level (DOS_F) and electron-phonon coupling coefficients (G_{ep}) in ultrathin metals have very high sensitivity to film thickness within a few Ångströms. As DOS_F and G_{ep} depend on thickness, we show that completely different magnetization dynamics characteristics emerge compared with bulk metals. Our model suggests highly-efficient energy transfer from fs laser photons to spin waves due to minimal energy absorption by phonons. This sensitivity to thickness and efficient energy transfer offers an opportunity to obtain ultrafast on-chip magnetization dynamics.

5.2.1 Introduction

Quantum confined magnetic nanomaterials such as magnetic ultrathin metals and alloys, and diluted magnetic semiconductors (DMS), provide rich emerging new physics [247, 250, 251]. There is also significant research on the quantum confinement effect in the atomic thin semiconductors for novel spin-based photonic quantum technologies and applications [252]. Metallic magnetic thin films have been investigated in applications such as femtosecond (fs) laser pulse switching of magnetization [83, 153, 253, 254]. Elemental magnetic metals with low spin-orbit coupling are ideal for this purpose. The mechanism of all-optical switching (AOS) of magnetization includes the electron bath thermalization after illumination by a fs laser pulse, followed by spin and phonon baths coupling with electrons via the electron-phonon coupling. Magnetic metallic ultrathin films (thicknesses less than 10 nm) behave differently to the fs laser pulse because of the change in the density of state at the Fermi level due to the quantum confinement [247, 255, 256]. The free-electron theory of metals provides the opportunity to understand the quantum effects associated with the film thickness. Because of its simplicity, the thin-film quantum well is appropriate and provides an introductory justification to the quantum size effects [257]. This effect directly changes the electron heat capacity constant (known

as Sommerfeld coefficient, γ) and coupling between electron and phonon. This concept is defined as all-optical quantum manipulation of magnetization.

In this study, we theoretically investigate the magnetization dynamics for sub-10 nm isolated, free-standing metallic thin films after exposure to a femtosecond laser pulse, the schematic description of which is shown in Figure 5.8. The laser pulse power is directly transferred to the electron bath, and the electron temperature (T_e) increases quickly in the sub-picosecond timescale. Electron thermalization results in a sharp decrease in the magnetization of the thin film. Due to the electron-phonon coupling, as shown on Figure 5.8, T_e balances its energy with a phonon bath, and reaches thermal equilibrium. The magnetization of the film is recovered in the following picoseconds. This energy transfer has been studied with microscopic three temperature model (M3TM) [258, 259]. To investigate the quantum confinement effects on the magnetization dynamics, first, we calculate the electron density of state at Fermi level (DOS_F), electron-phonon coupling coefficient (G_{ep}), Sommerfeld coefficient (γ), and magnetization dynamics in quantum-confined magnetic metals using M3TM [93, 94]. Next, we analyze the variability of magnetization dynamics as a function of film thickness. Previous studies investigated the laser light interaction with magnetic material [79, 89][260-262], however, quantum effects associated with the film thickness on the magnetization dynamics have not been examined.

The magnetization behavior is captured by the Landau-Lifshitz-Bloch equation (LLB) [246], which describes the time and temperature dependent change of the magnetization after interaction with a fs laser pulse. This model, though, does not study the energy balance between the electron and phonon baths. M3TM does not include the coupling of spins with electrons and phonons. The magnetization dynamics is influenced by the energy balance parameters such as G_{ep}, γ, and spin-flip ratio (R) determining the timescales of magnetization change. A more comprehensive model is needed to include both magnetization dynamics and electron (phonon) bath equilibrium.

In many magnetic materials, weak spin-orbit interactions significantly reduce spin-electron and spin-phonon scattering. Magnetic metallic systems with large spin-orbit coupling, such as transition metal interfaces, 2D electron gas or emergent phenomena such as $SrTiO_3/LaTiO_3$ interfaces which yield emergent superconductivity and large spin-orbit coupling [263], and also transition metal dichalcogenides [264-266] are excluded

from the scope of this study. Our models here is advantageous due to eliminating some scattering events such as Elliot-Yafet (E-Y) scattering [248].

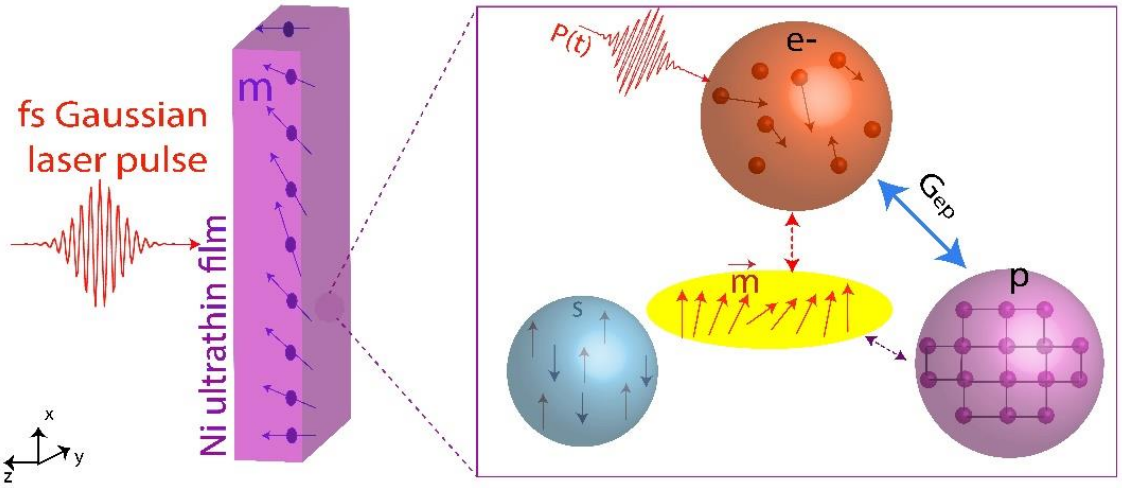

Figure 5.8: (Left) The schematic of ultrashort (femtosecond) laser pulse interaction with metallic magnetic ultrathin film. (Right) Coupled interaction between electron, phonon, and magnetization is shown. We investigate the energy transfer by employing extended microscopic three temperature model.

5.2.2 Quantum confinement effects on electron density of state at fermi level (DOS_F), electron-phonon coupling coefficient (G_{ep}), and Sommerfeld coefficient (γ)

Our physical system, which consists of a ferromagnetic ultrathin metal illuminated by an ultrashort (femtosecond) laser pulse, can be microscopically described by a generic Hamiltonian for interacting electron and phonon baths that reads,

$$H=H_e+H_p+H_{ep} \tag{5.5}$$

where H_e and H_p are the Hamiltonians of free electrons and phonons, respectively. H_{ep} models the electron-scattering from the lattice, ignoring the spin flips. We remark that the baths are, in fact, not exactly free. The calculation of the electron-phonon coupling parameter G_{ep} in the two-temperature model proceeds by application of the Fermi's golden rule using H_{ep}. In the Appendix C, we present a more extensive review on the derivation in ref. [255], which is based upon pioneering works [267]. It allows for including beyond free electron theory effects and arbitrary DOS.

We can write the temperature gradient between the baths such that:

$$C_e \frac{dT_e}{dt} = -G_{ep}(T_e - T_p) \tag{5.6}$$

Electron-phonon coupling factor G_{ep} is given by:

$$G_{ep} = \pi\hbar\lambda\langle\omega^2\rangle g_F \tag{5.7}$$

, where k_B is the Boltzmann constant, λ is the electron-phonon mass enhancement parameter [268], and $\langle\omega^2\rangle$ is the second moment of the phonon [269]. At low temperatures, we can take $C_e = \gamma T_e$, where $\gamma = \pi^2 k_B^2 g_F/3$, according to the Sommerfeld expansion [270]. Numerical examination of C_e for different metals at higher temperatures, which is beyond the scope of the present contribution, can be found in the literature [247]. A similar equation can be obtained for the phonon bath. These equations can be changed to temperature rate equations using the corresponding specific heats. Finally, introducing the additional terms for the laser pulse absorption and heat diffusion, the two-temperature model [271] can be developed.

The sensitivity of g_F to the variations of the thickness of the ultrathin film, L_z, allows for additional control over the electron-phonon coupling G_{ep}. We use the free electron model, while the electrons are confined in a potential well of size L_z and depth V_0. This limits k_z to be always less than $k_{top} = (2mV_0)^{1/2}/\hbar$. Quantization of k_z, according to [256], reduces the finding temperature-dependent Fermi energy is a counting problem of electrons living on disks confined in the Fermi sphere with temperature-dependent radius.

$$K_z L_z = n_z\pi - 2\sin^{-1}\left(\frac{K_z}{K_{top}}\right) \tag{5.8}$$

Allowed k_z form a set k_z whose dimension is temperature dependent. The physical reason for the oscillations with L_z is due to the discreteness of the electronic wave number along the finite thickness direction, k_z.

At zero temperature, the number of electrons can be determined by [256].

$$N = 2\frac{L_x L_y}{4\pi^2}\sum_{k_z \le k_F}\pi(k_F^2 - k_z^2) \tag{5.9}$$

, where L_x, L_y are the long, transverse sizes of the ultrathin film ($L_z \ll L_x$, L_y). At finite temperatures, we should use $N = 2\sum_k f_k$, where the Fermi-Dirac distribution would contain temperature-dependent Fermi energy $\mu(T)$ such that

$$N = 2\frac{L_x L_y}{4\pi^2}\sum_{k_z \epsilon K_z}\int dk_x dk_y \frac{1}{e^{(E(k)-\mu(T))/k_B T}+1} \tag{5.10}$$

Using:

$$E(k) = \frac{\hbar^2}{2m}(k_x^2 + k_y^2 + k_z^2) \quad (5.11)$$

The integral can be evaluated analytically such that:

$$n = \frac{T}{\pi L_z}\sum_{k_z \epsilon K_z} \ln[1 + \exp(\frac{k_\mu^2 - k_z^2}{T})] \quad (5.12)$$

, where k_μ is the temperature-dependent Fermi wavenumber. We use scaled variables such that the length scale is a_B, the temperature scale is T_B, and the energy scale is E_B. This equation generalizes the zero temperature counting problem in equation 5.9, which determines the quantum confinement effect on DOS at Fermi energy to finite temperatures. In Appendix B, we describe a method in ref. [256] with which one could find how the L_z dependence of DOS at Fermi level changes with temperature, to be able to take into account this size effect for G_{ep}. At the range of temperatures we are interested in, the temperature dependence of G_{ep} is negligibly different than the zero temperature results.

5.2.3 Microscopic three temperature model (M3TM) and magnetization dynamics

We solve the M3TM coupled with magnetization dynamics (extended M3TM) in the equations 5.13-5.15 based on Koopmans's model [83]. These differential equations describe the energy transfer from femtosecond laser pulse (shown as P(t): time-dependent Gaussian single pulse) to electron, phonon, and magnetization (**m**=$|M_z|/M_s$).

$$C_e \frac{dT_e}{dt} = -G_{ep}(T_e - T_p) + P(t) \quad (5.13)$$

$$C_p \frac{dT_p}{dt} = -G_{ep}(T_p - T_e) \quad (5.14)$$

$$\frac{dm}{dt} = Rm\frac{T_p}{T_C}\,(1 - m\coth(m\frac{T_C}{T_e})) \quad (5.15)$$

The parameters used in the equations 5.13-5.15 are shown in Table 5.2 for Ni thin film.

Table 5.2: Parameters used in extended microscopic M3TM

Parameter	Explanation	Value
C_p	Heat capacity of phonon	2.33×10^6 ($J\cdot m^{-3}\cdot K^{-1}$) [83]
C_e	Heat capacity of electron (dependent of electron temperature (T_e)	$C_e=\gamma T_e$ ($J\cdot m^{-3}\cdot K^{-1}$) [83]

γ	$\gamma_0 \cdot DOS_F$	Calculated in part 5.2.2 ($J \cdot m^{-3} \cdot K^{-2}$) [247]
γ_0	Sommerfeld coefficient ($C_p/5T_C$)	743.22 ($J \cdot m^{-3} \cdot K^{-2}$) [83]
G_{ep}	$G_0 \cdot DOS_F$	Thickness-dependent e-p coupling coefficient [247]
G_0	$(\pi K_B/\hbar) \cdot \lambda(\omega^2)$	Calculated in part 5.2.2 ($W \cdot m^{-3} \cdot K^{-1}$) [247]
R	R= Spin-flip ratio = $R_0 \times DOS_F$	17.2×10^{12} (s^{-1}) [83, 248]
T_C	Curie Temperature of Ni	627 (K) [83]

We consider the incoming laser pulse power as a Gaussian single pulse per unit volume as

$$P(t) = \frac{P_0}{\sqrt{2\pi}} \exp\left(-\frac{1}{2}\left(\frac{t}{t_0}\right)^2\right) \quad (5.16)$$

where $P_0 = \frac{I_0}{d.t_0}$, and I_0 and t_0 are the laser pulse fluence in $J \cdot m^{-2}$, pulse width (fs), respectively. The injected laser fluence is normalized to a fixed thickness, d, to capture the pulse energy per unit volume. The parameters used in the equations 5.13-5.15 are shown in Table 5.2 for Ni thin film.

We have considered simplifications in the differential equations which describe the electron and phonon temperature profile. Immediately after the illumination by the sub-picosecond laser pulse, two competing processes occur at the non-equilibrium state of the excited electrons. The non-thermalized electrons move with a velocity close to the Fermi velocity and continue to thermalize into a Fermi–Dirac distribution through collision. It takes a finite time for the excited electrons to travel and complete thermalization [272]. But in our study, electron thermalization time is considerably shorter than the laser pulse duration. Moreover, for sub-picosecond pulses, the laser energy is primarily absorbed by the free electrons on the film's surface. Most of the electron thermal energy is then transferred to the lattice; meanwhile, another part of the energy diffuses to the electrons in the deeper sub-surfaces. Because the pulse duration is too short, the laser is turned off

before thermal equilibrium between the electrons and lattice is reached [273]. In fact, on the picosecond time scale, longitudinal temperature gradients and transverse heat propagation are neglected due to the small sample thickness [89].

To the best of our knowledge, there is no former experimental or modelling study on all-optical control of magnetization dynamics of quantum confined ultrathin metals, which considers the thickness dependence of G_{ep} and γ in the extended M3TM. Due to the low thickness of the thin films and quantum confinement effects, the electron-phonon coupling (G_{ep}) changes dramatically with the film thickness in the nm regime. However, there is an experimental report on the effect of thickness on the laser induced demagnetization time of the Co/Pd multilayers with a few nm thickness of each layer, by measuring the Kerr signal of different laser excitation and various number of layers [274]. Due to the quantum confinement in the electron density of states at the Fermi level (DOS_F), both the e-p coupling (G_{ep}) and Sommerfeld coefficient (γ) cannot be considered constant. Our model assumes that C_p is not dependent on the thickness and temperature in the considered time and thickness regime. The spin-flip ratio (R) in equation 5.15 of Ni is a parameter that determines the kinetics of the transient magnetization change. R is dependent of the G_{ep} according to ref. [83], which is also a function of DOS_F and L_z-dependent. In finite-size systems, such as thin metallic films, confinement effects could influence the thermal properties of the lattice phonons, too. Size effects are most significant for thermal transport [275]. On the other hand, thermodynamic properties, such as specific heat, do not change significantly with the size if the temperatures of interest are much lower than the Debye temperature. The primary effect of the finite size is to have fewer states to count in the calculation of specific heat. In strict mathematical terms, the continuum approximation to the states in the k-space cannot be made in finite size systems, and the sum over the states cannot be replaced by an integral. However, the ratio of the exact specific heat determined by the summation to the integral calculation of the specific heat is close to one. For example, it is about ~ 0.9856 for Aluminum thin film at low temperature, using the Debye model phonon dispersion relation [276]. Accordingly, neglecting the size effects on phonon bath by using the typical bulk value of phonon specific heat is a reasonable approximation in our calculations.

5.2.4 Effect of film thickness (L_z) on chemical potential (μ), Fermi level electronic density of states (g_F), electron-phonon, Sommerfeld coefficient (γ), and coupling (G_{ep})

In Figures 5.9a and 5.9b, the L_z dependence of chemical potential μ (or temperature-dependent Fermi energy) and DOS at Fermi energy are plotted, respectively. Both μ and g_F are dimensionless, normalized with their corresponding bulk values. Figure 5.9c shows G_{ep} changes with L_z. We take parameters for Ni for which $\lambda\langle\omega^2\rangle = 49.5$ meV^2 and is converted to J^2 in our calculations. The depth of the metallic confinement potential is assumed to be $V_z = 10$ eV. The temperature is fixed to $T_e = 5 \times 10^{-3}\, T_B$, where $T_B = E_B/k_B$ being the Bohr temperature corresponding to the Bohr energy $E_B = 13.6$ eV. Electronic density is used as $n = 3/4\pi r_s^3$ with $r_s = 4a_B$, and a_B being the Bohr radius. The size-dependent oscillations disappear after $\sim$ 50 Å. This maximum length is a characteristic value given by $d = 10\lambda_F$, where λ_F is the Fermi wavenumber for the bulk. For the electronic density, n, used in the plot, we find $d \sim 50$ Å. In addition, the effect of film thickness (L_z) on the Sommerfeld coefficient is plotted in Figure 5.9d. The graphs are plotted for the electronic temperature corresponding to the Bohr energy $E_B = 13.6$ eV. Electronic density is used as $n = 3/4\pi r_s^3$ with $r_s = 4a_B$, and a_B being the Bohr radius. Similar plots are included in the Appendix C for the electron temperature of $T_e = 0$ K. The depth of the metallic confinement potential is taken to be $V_z = 10$ eV. The V_z value is theoretically infinite, however, in the FEM simulations, its value is considered as a finite number comparable to its bulk Fermi value [256]. In the following sections, we have shown the results of our calculations of μ, g_F, γ, G_{ep}, as well as magnetization dynamics, based on free electron model (FEM), for V_z=10 eV. The results of our calculations for different potential well depths (V_z =5, 15, and 20 eV) are also included in Appendix C.

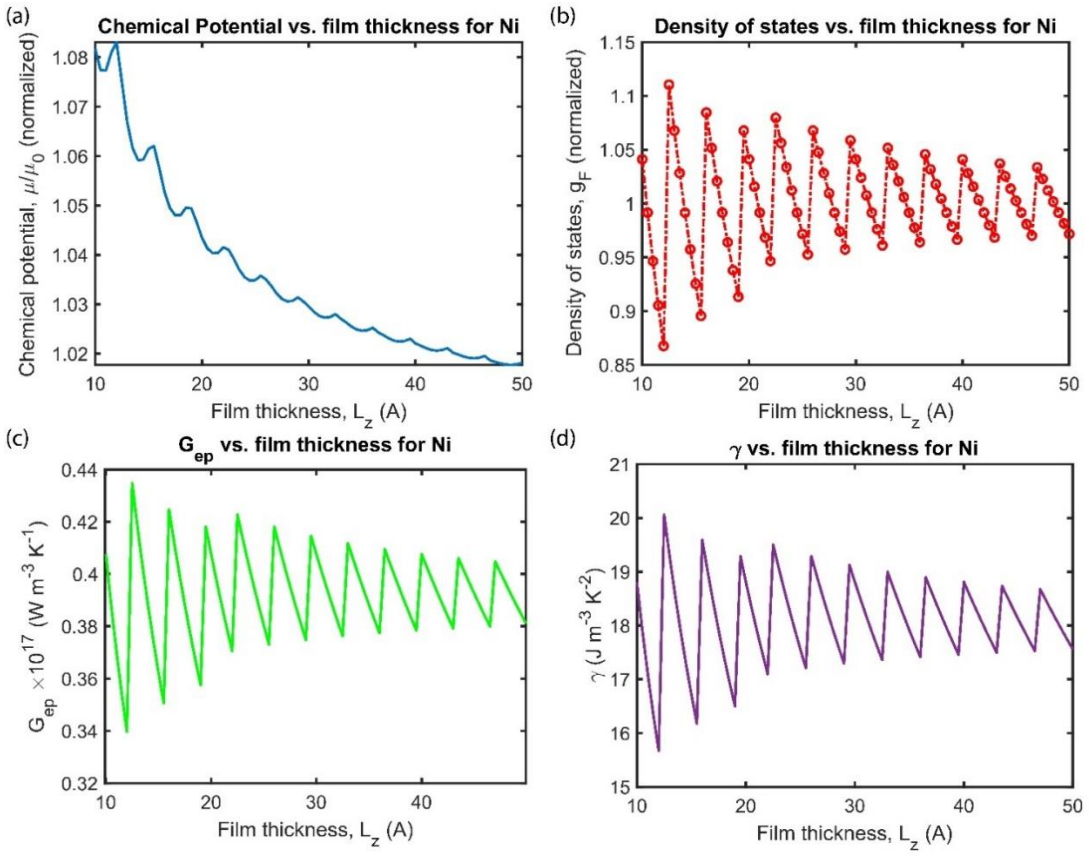

Figure 5.9: Thickness dependent quantum-confinement effect. (a) Chemical potential μ/μ_o (finite temperature Fermi energy), (b) density of states at the Fermi energy g_F, (c) electron-phonon coupling coefficient G_{ep}, and (d) Sommerfeld coefficient γ as a function of ultrathin film thickness L_z. Both μ/μ_o and g_F are dimensionless, normalized with their corresponding bulk values. The parameters are considered of Ni thin film and details are given in Table 5.2.

The FEM perfectly reflects the oscillations in the DOS_F, G_{ep}, and C_e as the result of quantum confinement for the metals whose valance electrons lie in p-band such as Al. Since Ni is a transition metal with an almost full d-band structure [247], the possible complexity in the configuration of electrons in the Fermi level would require beyond free electron methods to determine the DOS_F, such as density functional theory (DFT). However, FEM still captures the essential physics behind the quantum size effects even for transition metals and more complex structures [257]. Ab initio methods confirm the conclusions of the free electron model [277, 278].

The oscillations of G_{ep} (Figure 5.9c) and γ (Figure 5.9d) are due to the Fermi level oscillations translated to DOS_F, arising from the quantum confinement (cf. equation 5.8). This essential physics (discreteness of the k_z) remains the same irrespective of the simplicity or complexity of the Fermi surface. Failure of the continuum approximation in the confined direction yields discrete plateaus for the electronic states. Accordingly, the

formation of such quantum well states (QWS) in the confined direction captures the basic physics of the quantum size effects, manifested as size-dependent oscillations in physical observables [279-282]. We show the Fermi level oscillations in Figure 5.9c, which translates to DOS_F, hence to G_{ep} and C_e. For Ni, although the d-band structure leads to a more complicated Fermi level than Al, which decreases the magnitude of G_{ep} compared to the values used in the experimental studies [247]. Even if the decrease in these terms is not entirely in agreement quantitatively with the reported values, our model still reflects the effect qualitatively. FEM predicts quantum size effect oscillations in the magnetization but should be regarded as a qualitative description for the magnetic metals with more complex Fermi configurations such as Ni. The effect can be studied more rigorously and quantitatively using ab initio calculations of the band structure, Fermi level, and DOS_F. Furthermore, it can be optimized by considering more complex materials using beyond FEM analysis. In this work, we will be presenting the essential physics and predicting quantum size effect in magnetization in the same spirit of quantum size effects in electronic conduction.

5.2.5 Microscopic three temperature model coupled with magnetization dynamics and temporal response

Here, we discuss the quantum confinement effect on the magnetization dynamics for Ni thin film. In Figure 5.10, the magnetization dynamics and transient electron and phonon temperatures calculated from the extended M3TM are shown for 20 Å Ni thin film. According to Figure 5.10, illuminated with a Gaussian single laser pulse of $I_0 = 28\ mJ \cdot m^{-2}$, the magnetization of the Ni thin film decreases in sub-100 fs due to the thermalization of the electron bath and E-Y scattering. Due to the low heat capacity of the electrons, T_e reaches $1.5T_c$ of Ni (940.5 K). However, due to electron-phonon coupling, T_e cools down to an equilibrium temperature with phonon (lattice) in 200 fs, and the magnetization recovers to close to its initial value (> 96%), in around 1 ps. Note that T_p in Figure 5.10 (b) is not constant (since the magnetization recovery is not completed in 500 fs), and its increasing rate is very low compared to T_e and it is not completely visible on the Figure 5.10b (T_p(100fs) = 302.3 K, T_p(500fs) = 302.7 K).

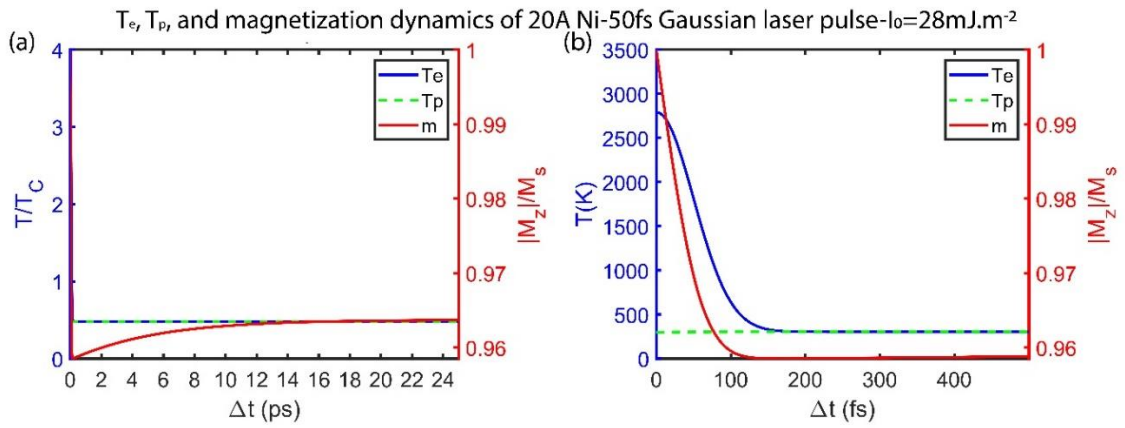

Figure 5.10: (a) Transient T_e, T_p, and normalized magnetization (m = $|M_z|/M_s$) for 20 Å thick Ni film illuminated with $I_0 = 28$ mJ·m^{-2} Gaussian single laser pulse of 50 fs width. (b) Zoomed-in version of (a) 500 fs after illumination. Note that the Y-axis units are different in (a) and (b).

Note that Figure 5.10b shows the temporal change of the magnetization, electron, and phonon temperatures, before reaching the equilibrium (which occurs 15 ps after laser pulse incidence). The sudden rise of the T_e, due to the lower electron heat capacity, in the non-equilibrium state is in the range of a few fs.

We also calculated the effect of the pulse width on the magnetization dynamics and electron and phonon temperature. The results are shown in the Appendix C Figures C.9-C.11. Increasing the pulse width decreases the laser power injected to the thin film, which leads to increase in the demagnetization time as well as electron equilibration time. Choosing very long pulse durations, suppresses the injected laser power and increases the laser fluence needed for recovery of the magnetization after quenching. In addition, we have considered the condition where the incoming laser fluence is in the range of the experimental values, with only 20% absorption in the quantum confined thin film. We compared the results of M3TM for the nm-thick non-quantum confined and Ångström-thick quantum confined Ni film, the results of which are shown in Appendix C Figure C.12. For more extensive investigation, we also compared the effect of laser pulse width (both in fs and ps regimes) on the temporal behavior of the magnetization, electron, and phonon temperatures in nm-thick and angstrom-thick Ni film, in supplementary Appendix C Figure C.13 and C.14.

5.2.6 Dependence of the magnetization dynamics on film thickness (L_z)

Figure 5.11a shows the magnetization dynamics based on the extended M3TM for different thickness of Ni thin film. Results show that the film thickness has a minimal influence on timescales of the demagnetization and recovery. However, it changes the

demagnetization ratio (the dip on the magnetization curve). The effect of thickness on the magnetization dip is shown in Figure 5.11b for different L_z values 10−50 Å. In Figure 5.9, due to the change in the DOS_F at sub-5nm (50 Å) thickness regime, the electron-phonon coupling, and Sommerfeld coefficient change considerably with increasing film thickness. In Figure 5.11a-b, the dips have the same positions, however, their amplitudes are different. This indicates that the change in the rate (G_{ep}) triggers a stronger magnetization loss/recovery without altering the spin wave emission spectra.

Figure 5.11c and 5.11d show the dependence of T_e and T_p maxima on the film thickness, respectively. The modulation of the electron temperature maxima with increasing the film thickness is similar to the behavior of G_{ep} (Figure 5.9) and demagnetization dip (Figure 5.11b). The electron temperature and the magnetization dip change sharply for certain values of thickness, e.g., 22 to 22.5 Å (or 25.5 to 26 Å, 29 to 29.5 Å, 32.5 to 33 Å, 36 to 36.6 Å, 39.5 to 40 Å, 43 to 43.5 Å, 46.5 to 46 Å). The electron temperature can go up to 3300 K depending on L_z. The extreme sensitivity of electron temperature (i.e. 3300 to 2620 K) to the thickness L_z (22 to 22.5 Å) shows that piezoelectric modulation can be a viable method for controlling "hot electrons". The fact that electron temperature exceeds the Curie temperature does not prevent the nanomagnets from recovering magnetization. Due to increasing electron temperature, chemical potential gradient causes charge currents within metallic nanomagnets (see μ as a function of T_e in Appendix C Figure C.2a). Still, since the highest electron temperature never exceeds 3300 K, the chemical potential difference is less than 1%.

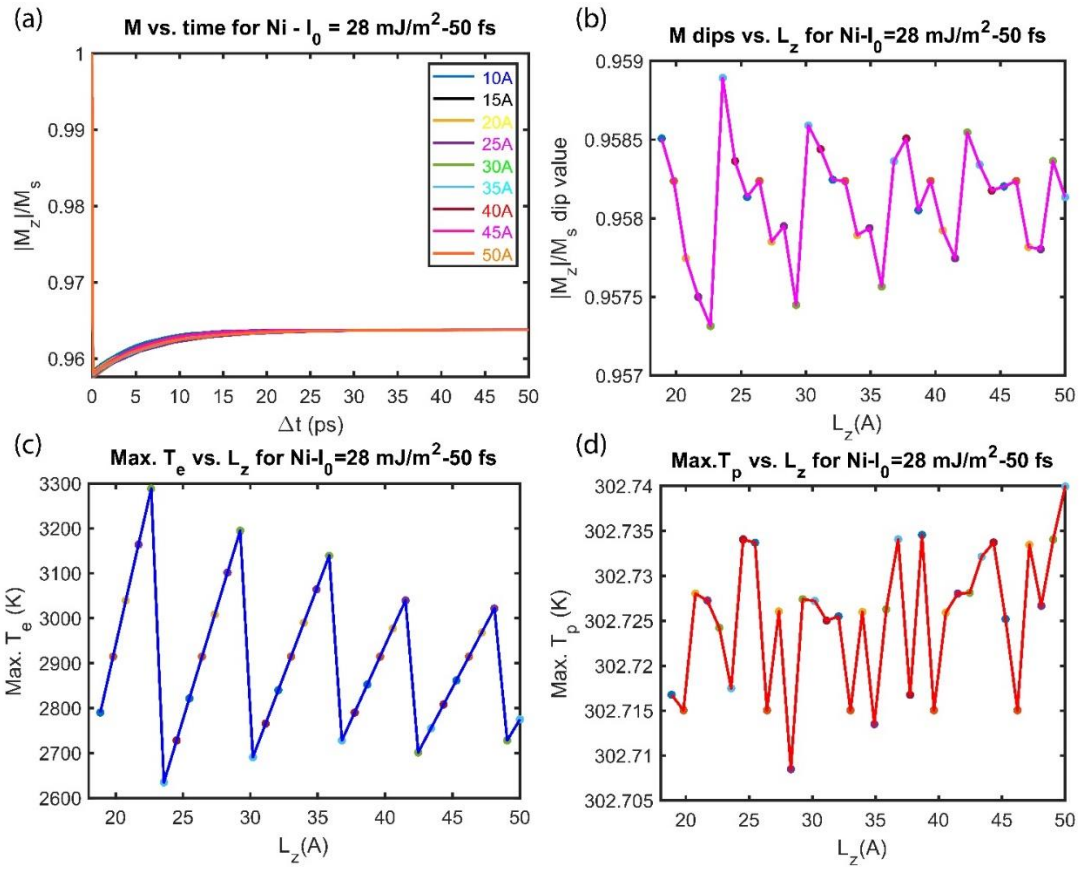

Figure 5.11: Effect of Ni film thickness L_z on (a) magnetization dynamics, (b) demagnetization dip, (c) maximum of electron temperature T_e, and (d) maximum of phonon temperature T_p for L_z = 10 Å, 15 Å, 20 Å, 25 Å, 30 Å, 35 Å, 40 Å, 45 Å, and 50 Å. The Ni thin film is illuminated with I_0 = 28 mJ·m^{-2} Gaussian single laser pulse. Rest of the parameters are given in Table 1. The zoomed-in version of panel (a) is included in Appendix C (Figure C.3).

The finite size of the potential well, does not change the qualitative predictions of our model. The calculations results for the various potential well depths (V_z = 5, 10, 15, and 20 eV) shows that only in case of sub-20 Å film thicknesses, V_z size might result in a few percent difference in the calculations. However, it does not influence the qualitative predictions of our model on decrease and oscillations in the electron density of states and electron-phonon coupling as the result of quantum confinement effect. In other words μ increases slightly (~3%), in sub-20 Å range, from V_z = 5 eV to V_z = 10 eV, but the oscillations are not considerable when V_z changes from 10 eV to 15 eV or 20 eV. Accordingly, g_F, G_{ep}, and γ oscillations decrease (~4%) changing from V_z = 5 eV to V_z = 10 eV, while remains unchanged for other V_z values. We also investigated the sensitivity of the Figure 5.11 results to the size of V_z. Despite similar negligible variations for V_z = 5 eV in case of low film thicknesses, changing the depth of the potential well did not influence the conclusions of the quantum confinement effect on the oscillations of the

magnetization dynamics as well as electron and phonon temperatures (see Appendix C Figures C.6 and C.7). Since the decrease (inversely proportional to the film thickness) in the chemical potential is averagely monotonic [256] (the amplitude of the oscillations does not exceed a few percent), the qualitative results of our calculations are consistent using different potential well depths. In other words, independent of the quantum well depth, quantum confinement effect reduces G_{ep}, and consequently effects the transient magnetization behavior as well as the electron and phonon temperatures, as discussed extensively in the previous part.

The quantization of energy levels in the direction perpendicular to the film due to the thin film's electron confinement leads to the oscillatory dependence of many properties on the film thickness due to quantum size effects. Despite the quantitative small oscillations as the result of quantum confinement, the effect is measurable by various experimental means such as magneto-thermoelectric measurements [283], Kelvin probe force microscopy [284], Hall-bar magnetoresistance measurement [285], and scanning tunneling spectroscopy (STS) technique [286]. These methods are reported to measure the quantum size effect in different metallic and also more complex thin films.

5.2.7 Energy transfer from fs laser pulse to magnon system

Considering the lack of spin coupling, the fs laser pulse manipulates the magnetization without excess energy concentration in the lattice, resulting in the minimal change of phonon temperature. If we assume that the heat capacity of the nm thick Ni film is equal to the bulk value, with the Gaussian laser pulse fluence of $I_0 = 28\ mJ \cdot m^{-2}$ and the spot size of 100 μm, the temperature change of a 2 nm-thick Ni film with the density of 8900 $Kg \cdot m^{-3}$, is calculated as $E_{laser} = 2.184 \times 10^{-10}\ J = M \times c \times \Delta T \cdot M\ (mass) = \rho_{Ni} \cdot V = 1.4 \times 10^{-13}\ kg$ and the specific heat capacity of Ni (c) is 440 $J \cdot (Kg \cdot °C)^{-1}$. As a result, the temperature change in the thin film is $\Delta T = 3.545°C$. The laser fluence ranges for ultrafast magnetization switching of metallic magnetic thin films vary from 1-14 $mJ \cdot cm^{-2}$ (10-140 $J \cdot m^{-2}$) in the literature [152, 258, 287]. Even if we consider an upper limit of 10 $J \cdot m^{-2}$ as incoming laser energy, the thin film temperature change would be $\Delta T = 1276°C$, which is still below the melting point of the Ni (1455°C). Therefore, as long as the fluence is low, there is no significant thermal drift in the metal.

After equilibration with the electron bath all the laser pulse energy goes to the phonon bath. So the energy absorbed by the phonon is equal to $E_p = C_p \cdot \Delta T_p$. The maximum

phonon temperature change is for the film with the thickness around 35 Å, which is around 0.022 K. So the energy absorbed by the phonons is simply $E_p = (2.33 \times 10^6\ J \cdot m^{-3} \cdot K) \times (\pi/4 \times (100 \times 10^{-6}\ m)^2) \times (3.5 \times 10^{-9}\ m) \times (0.022\ K) = 1.4 \times 10^{-12}$ J. From thermodynamic standpoint, phonon energy change (heat) is the difference between the injected energy into the system from laser pulse and the energy change in the spins (work done). The efficiency of work done by laser pulse on spins is $\eta = 1 - Q_{phonon}/Q_{laser}$. The absorbed energy for increasing the lattice temperature is $Q_{phonon} = 1.4 \times 10^{-12}$ J and the laser energy is 2.184×10^{-10} J. The efficiency is $\eta = 99.36\%$. In Appendix C, we consider a condition where the spin-electron, and spin-phonon scattering are not neglected. Since a part of a laser energy is lost due to the scattering phenomena, the laser energy needed to manipulate and recover the magnetization increases. Considering the laser fluence of 35 $mJ \cdot m^{-2}$ ($Q_{laser} = 2.73 \times 10^{-10}$ J), the increase in the phonon temperature maxima for 35 Å film does not considerably change, which is shown in appendix C Figure C.8b in the Appendix C. However, due to the excess laser energy needed for recovery of the magnetization, the work done by the laser on the spins increases which increases the efficiency to $\eta = 99.48\%$.

5.2.8 Conclusions

In summary, we investigated the all-optical magnetization dynamics in the quantum confined magnetic Ni ultrathin films. Our theoretical model shows that due to the quantum confinement in the films with the thicknesses of a few tens of Ångströms, the electron-phonon coupling coefficient (G_{ep}) in the M3TM is highly sensitive to the film thickness and could not be considered constant. This effect changes the amount of magnetization drop after interaction with the fs laser pulse, but not the timescales of the magnetization. In addition, we show that our qualitative predictions of magnetization dynamics in the quantum-confined ultrathin magnetic films are not sensitive to the size of the quantum well. We show that, laser-induced magnetization dynamics could drive ultrafast exchange-driven magnetization oscillations [288]. Furthermore, the quantum confinement effect decreases the lattice temperature change due to the lower density of phonons and lower laser fluences are needed for magnetization control in Ni ultrathin film. Thus, energy efficiency of exciting spin waves with lasers could be enhanced [289].

Our study shows that the choice of the film thickness in the angstrom regime could help modulation of magnetization with around three orders of magnitude lower laser fluences compared to the reported experimental values. We also show that the energy transfer rate

from the laser pulse to the lattice is so low that the lattice temperature stays far below both Curie temperature and the melting point of the Ni. The quantization of energy levels perpendicular to the film due to the thin film's electron confinement leads to the oscillatory dependence of many properties on the film thickness due to quantum size effects. Despite the small oscillations as the result of quantum confinement, the effect is measurable by various experimental means including magneto-thermoelectric measurements [283], Kelvin probe force microscopy [284], Hall-bar magnetoresistance measurement [285], and scanning tunneling spectroscopy (STS) technique [286]. These methods might be useful in measuring the quantum size effects in different metallic and also more complex thin films.

Chapter 6

CONCLUSIONS

Many spintronic applications necessitate the use of perpendicular magnetic anisotropy (PMA) materials with low damping or enhanced magnetotransport characteristics. These applications include memory, spin-orbit torque switching, and logic devices using Rashba-Edelstein and spin-Hall effects. PMA helps achieve fast and reliable response. Rare earth iron garnet (REIG) thin films such as Yttrium iron garnet (YIG) are insulating magnetic materials which are proper candidates for a subset of these applications, due to insulating garnets' low heat dissipation, low Gilbert damping and their effective magnetic anisotropy energies, which can be tuned by engineering their stoichiometry and lattice strain during their growth processes. REIG stoichiometries could be tuned during growth and their total effective magnetic anisotropy could be engineered with PLD growth conditions. Despite the need for new PMA REIGs with different magnetic saturation fields and magnetic anisotropies, few PMA REIGs were reported previously. Therefore, more PMA REIGs are necessary to explore new spintronic mechanisms and devices.

To summarize, in this thesis work:

- We have systematically calculated the shape, magnetocrystalline, and magnetoelastic anisotropy energy density terms for epitaxial rare earth iron garnet thin films when grown on different garnet substrates. We used the convention of K_{eff} <0 which corresponds to perpendicular magnetic anisotropy (PMA). To have magnetic thin film with PMA, it is necessary for magnetoelastic anisotropy energy density to be negative and large to eliminate the demagnetizing effect of shape anisotropy. The magnetoelastic term could exceed the shape term when both λ_{111} and the strain type (compressive or tensile) have the same signs. So in both compressive (λ_{111}<0) and tensile strain (λ_{111}>0) states, thin films can be PMA as long as shape anisotropy is lower than the negative ME effects. We have studied ten various epitaxial lattice-matched RE iron garnet thin films ($X_3Fe_5O_{12}$, X = Y, Tm, Dy, Ho, Er, Yb, Tb, Gd, Sm, Eu) on five garnet substrates which are available commercially and oriented in (111) direction. A total of fifty REIG/substrate pairs have been investigated using the contributing energy terms in their magnetic anisotropy, and we predict twenty different cases which could exhibit PMA. These substrates include $Gd_3Ga_5O_{12}$ (GGG), $Nd_3Ga_5O_{12}$ (NGG), $Y_3Al_5O_{12}$ (YAG), $Gd_3Sc_2Ga_3O_{12}$ (SGGG), and $Tb_3Ga_5O_{12}$ (TGG).

With our numerical model, we have been able to predict magnetic anisotropy state in all fifty cases of garnet/substrate pairs. Among the predicted PMA cases, only a few cases shown partial deviation from the previous experimental reports. Using the precise and correct material properties in the model, under cube-on-cube epitaxy conditions, the anisotropy state and field values can be estimated very accurately. Choosing substrates which have smaller lattice constants than that of the films helps induce compressive in-plane strain inside the thin films along with the negative and large λ_{111} to eliminate the magnetostatic effect of the shape anisotropy and yields PMA. In addition, according to the anisotropy field values we calculated, we predict HoIG films to be PMA ($\varepsilon_{\parallel} < 0$ results $K_{eff} < 0$, and $H_a < 0$), when epitaxially grown on TGG, GGG, and YAG. Increased film thickness would result in strain relaxation since the lattice matching might vanish in those thickness regimes. Consequently, saturation fields decrease in thicker films, due to their lower strain and we might reach more feasible and reduced fields for spin-orbit or magnon device applications. HoIG with less than their critical thickness is PMA, when grown on GGG substrates. Above this critical thickness, HoIG film experiences around 40% strain relaxation and its easy axis becomes IP. Thus, to have PMA, one needs to grow HoIG films thinner than the critical thickness on GGG substrates for spintronic device applications. We also found that YIG/YAG, HoIG/GGG, SmIG/NGG, HoIG/TGG and SmIG/SGGG film-substrate pairs are sensitive to slight variations in strain and M_s induced by off-stoichiometry or growth process effects.

Our predictions are experimentally testable. Therefore, the model can help capture the contributing factors with high quantitative accuracy. Besides, our model has highlighted the sensitivity of film anisotropy to the film properties. We highlighted the need for precise and more detailed reporting of measured film data. The lower magnitude of the anisotropy fields ($H_a < 0.5$ T) and M_s are desired as they require less energy for magnetization switching and possess lower Gilbert damping which make them appropriate candidates for integrated magnonic devices and circuits.

- We provided, for the first time, an optimized method for pulsed laser deposition of HoIG epitaxial thin films on GGG (111) and TGG (111) garnet substrates for achieving PMA. HoIG thin films were grown on Si (001) and silicon-on-insulator (SOI) substrate, for silicon integration.

- We optimized the PLD growth recipe and the film quality by running two calibration processes on GGG and Si substrates: first, HoIG was grown under 150 mTorr, 650 ˚C

substrate temperature, and 150000 laser shots which yielded highly relaxed 420 nm thick film. Second, the oxygen partial pressure, substrate temperature, and the number of laser shots have been reduced to 10 mTorr, 800 ˚C, and 20000 shots, respectively. The second calibration run resulted in 67 nm film thickness. We show that despite 420 nm thick HoIG, the 67 nm HoIG which is grown under lower oxygen partial pressure and higher substrate temperature, shows better epitaxial single crystalline structure with a compressive in-plane strain, which helps obtain partial PMA. The surface roughness of the film gained from AFM characterization, also shows a better epitaxial quality in case of 67 nm (RMS roughness = 0.3 nm), compared to the 420 nm-thick film. In-plane (IP) and out-of-plane VSM magnetic hysteresis loops for 67 nm and 420 nm show out of plane magnetic anisotropy in the thinner film with bulk-like M_s, low coercivity and remanence which is advantageous both for low-energy spin switching and low Gilbert damping in FMR measurements. Overall, the IP hysteresis loop measurements show a coercivity value of around 7 Oe and M_s of around 29 emu·cm^{-3} for the 420 nm HoIG thin film, with a tilted magnetic moment the IP component of which is dominant. The 67 nm film exhibit clear perpendicular magnetic anisotropy. Its IP hysteresis loops show a coercivity of less than 1 Oe, low saturation fields (H_{sat} = 30 Oe) and M_s of 62 emu·cm^{-3} which is near the bulk M_s of the HoIG, but the remanence is negligible. Because of negligible remanence, these films are not IP easy axis although they are very soft magnetic films. The OP hysteresis loops of 67 nm film show PMA due to $M_r/M_s \sim 0.5$, with a coercivity of around 11 Oe and $H_{sat} \sim 150$ Oe. The 420 nm film with a dominant IP magnetic moment component showed a coercivity higher than the 67 nm film (7 Oe). The IP magnetic hysteresis loop shape for the 420 nm film shows a gradual magnetization reversal with a remanence, unlike the 67 nm film. We attribute this loop shape difference to the polycrystalline structure with multiple crystalline grain orientations of the 420 nm film. For the thinner film, crystalline structure is closer to a more strained epitaxial film. Finally, we conclude that decreased film thicknesses with high epitaxial qualities will result in more robust perpendicular magnetic anisotropy in HoIG epitaxial, which is in agreement with our earlier theoretical predictions [64, 65].

Magnetization manipulation in metallic magnetic thin films with ultrashort laser pulse has been a subject of rigorous research in the past decades [226-228, 290]. Femtosecond (fs) laser pulse interaction with metallic magnetic thin films and their phonon, spin and electron baths could provide the foundations for promising future spintronic applications such as high-precision sensing, spectroscopy [234], and on-chip communications [235, 236] using THz spin waves generated as a result of ultrafast magnetization control [237-245]. A detailed understanding of how the key material and laser parameters determine the laser-driven magnetization dynamics is essential for controlling phonon, spin and photon interactions for faster and more energy-efficient response in spintronic devices.

- We quantitatively modeled the energy transfer from fs laser pulse to coupled electron, phonon, spin, and normalized magnetization in Fe, Co, Ni (type I films), Gd and Ni_2MnSn (type II films). Our model and numerical solutions show that type I metallic thin films (T_C >> room temperature) recover most of their magnetization in 1-2 ps when excited with a single Gaussian laser pulse, following the magnetization quenching within 130-200 fs. Increasing the laser pulse width and fluence increases the film response time and decreases its recovered fraction of magnetization. In thicker type I films (i.e. 100 nm), unlike type II films, the response time of magnetization is shorter. Type II films undergo thermal demagnetization gradually in about 35-50 ps after interaction with a Gaussian laser pulse. In addition, we investigated the laser pulse waveform on the magnetization dynamics of type I Ni thin film. Illuminating the Ni thin film with 100 fs sinc and chirp laser pulses of any fluence in the range of 20-150 $J \cdot m^{-2}$ results in complete thermal demagnetization of both 20 nm and 100 nm thick Ni films. Our study suggests the need for optimizing the experimental parameters, such as laser pulse width and energy, film type and thickness for more energy efficient and faster response. Such an optimized set of material and excitation parameter conditions could help tune THz spin waves generated using ultrafast lasers.

- We investigated, for the first time, the all-optical magnetization dynamics in the quantum confined magnetic Ni ultrathin films. Our theoretical model shows that due to the quantum confinement in the films with the thicknesses of a few tens of Ångströms, the electron-phonon coupling coefficient (G_{ep}) in the M3TM is highly sensitive to the film thickness and shows an oscillatory behavior rather than a constant value, as considered in the previous theoretical and experimental studies. This effect changes the amount of magnetization quenching but not the timescales of the magnetization. We show that,

laser-induced magnetization dynamics could drive ultrafast exchange-driven magnetization oscillations [288]. Furthermore, the quantum confinement effect decreases the lattice temperature change due to the lower laser fluences needed for magnetization control in Ni ultrathin film as spin-phonon scattering dramatically decreases due to reduced density of phonon states. Thus, energy efficiency of exciting spin waves with lasers could be enhanced [289].

Overall, our studies hold several contributions to the scientific community. First, our focus to control and predict the magnetic anisotropy state in rare earth iron garnets provides a testable range of new PMA garnets and help optimize new REIG candidates with robust PMA for spintronic devices. Many emerging spintronic logic and memory devices require fast and reliable magnetization switching mechanisms and REIG films with PMA could offer such functionalities through picosecond or few nanosecond spin-orbit torques [291], all-optical switching [292] and other enhanced magnetotransport characteristics due to low damping, Dzyaloshinskii-Moriya Interaction parameter and low exchange constants with respect to magnetic metals [293]. Other areas of intense research that could benefit include PMA garnet-based spin Seebeck effects, spin wave devices, current-driven domain wall logic, tunneling magnetoresistance studies, and magnetooptical investigations of thin film PMA iron garnets. These garnet films offer also allow for testing under a variety of growth and post-processing conditions.

Second, for the first time, we optimized and tested a pulsed laser deposition and growth process for HoIG thin film with PMA. Our guidelines provide a perspective for the optimization of REIG materials growth and characterization for the spintronics research community to achieve robust perpendicular magnetic anisotropy. This experimental test confirmed our PMA hypothesis and the validity of our model for predicting PMA.

Third, we modelled the all-optical fs laser-induced magnetization dynamics of the metallic magnetic thin films with the focus on ultrafast sub-atomic interactions, which provide a better understanding of the materials and laser parameters affecting the timescales of the ultrafast magnetization switching. Our study suggests the requirement of optimization of the materials and the laser pulse properties for sub-picosecond magnetization which could be used in THz communication, spectroscopy and spintronic sensors.

Fourth, for the first time, we investigated the quantum size effect on the laser-induced magnetization dynamics, which as film thicknesses are lowered towards the Ångström regime, more energy efficient laser-induced magnetization control is feasible due to reduced density of phonon states and reduced likelihood of spin-phonon scattering. Quantum-confinement leads to quantization of energy levels along the confinement axis. As a result, electron-phonon coupling behaves in an oscillatory way with increasing film thickness. Our model could serve as a qualitative predictor of quantum size oscillations for the thermal demagnetization of nanomagnetic layers. Thus, metallic magnetic nanolayers could eventually be used for efficient energy transfer from fs laser photon pulses to spins in the THz regime. These functionalities could enable a new class of spin-based room temperature THz detectors with high internal quantum efficiency, where these detectors could be used in 6G and beyond telecommunication applications. We believe that our predictions might trigger further experiments on the predicted quantum size oscillations in the magnetization of ultrathin quantum-confined metallic magnetic nanolayers.

As a result of our studies, I published three articles as first-author in the journals including *AIP Advances*, *Journal of Magnetism and Magnetic Materials*, *Data in Brief*, one conference paper at *OSA Digital Library, Ultrafast Phenomena Conference 2020 proceedings*, and submitted two manuscripts which are under review.

APPENDIX A

COMPLETE LIST OF IRON GARNET FILMS PREDICTED TO HAVE PERPENDICULAR MAGNETIC ANISOTROPY

We present the calculated plots of sensitivity of magnetic anisotropy field and anisotropy energy density for 49 epitaxial rare earth iron garnet (REIG) film/substrate pairs (YIG, TmIG, DyIG, HoIG, ErIG, YbIG, TbIG, GdIG, SmIG, and EuIG thin films on GGG, YAG, SGGG, TGG, and NGG substrates respectively.

A.1 Sensitivity of anisotropy field and energy density of REIG to strain and saturation magnetic moment

Figures A.1-A.15 exclude the Gadolinium Iron Garnet (GdIG) film on substituted Gadolinium Gallium Garnet (SGGG) substrate because there is no lattice mismatch between the film and the substrate. Each anisotropy term consist of the following parameters: $K_{eff} = -\frac{3}{2}\lambda_{111}\frac{Y}{1-\nu}\varepsilon_{||} + 2\pi {M_s}^2 + K_1$. The energy density was calculated based on the parameters reported in previous references [101, 166, 171, 173, 177, 294] and calculated terms according to their formulae (i.e. $\varepsilon_{||} = \frac{a_{sub}-a_{film}}{a_{film}}$). First-order magnetocrystalline anisotropy, K_1, is an intrinsic temperature-dependent constant reported for each REIG material. Young's modulus (Y), Poisson's ratio (ν) and magnetostriction constant (λ_{111}) parameters evolving in the magnetoelastic anisotropy energy density term (first term) are considered to be constant according to the values previously reported. For shape anisotropy energy calculations (second term), bulk saturation magnetization (M_s) for each film was used. Since each film may exhibit variability in M_s with respect to bulk, the model presented here yields the most accurate predictions when the experimental film M_s, λ_{111}, Y, ν and K_1, and in-plane strain values are entered for each term. Table A.1 shows the parameters and calculation results of anisotropy energy density terms and contributing parameters. In addition, in Table A.1, we present a comparison of our model's predictions with the previous experimental studies. Anisotropy fields were calculated using $H_A = 2\frac{K_{eff}}{M_s}$ formula and its change with M_s and strain variability was shown in Figures A.1-A.15. For HoIG/GGG, HoIG/TGG, SmIG/SGGG, SmIG/NGG, YIG/YAG, the PMA is vanished as the result of increased saturation magnetic moment (higher shape anisotropy) and film relaxation (lower

magnetoelastic anisotropy). The original Microsoft Excel and MATLAB files used for generating the data for Figures A.1-A.15 are also presented [64].

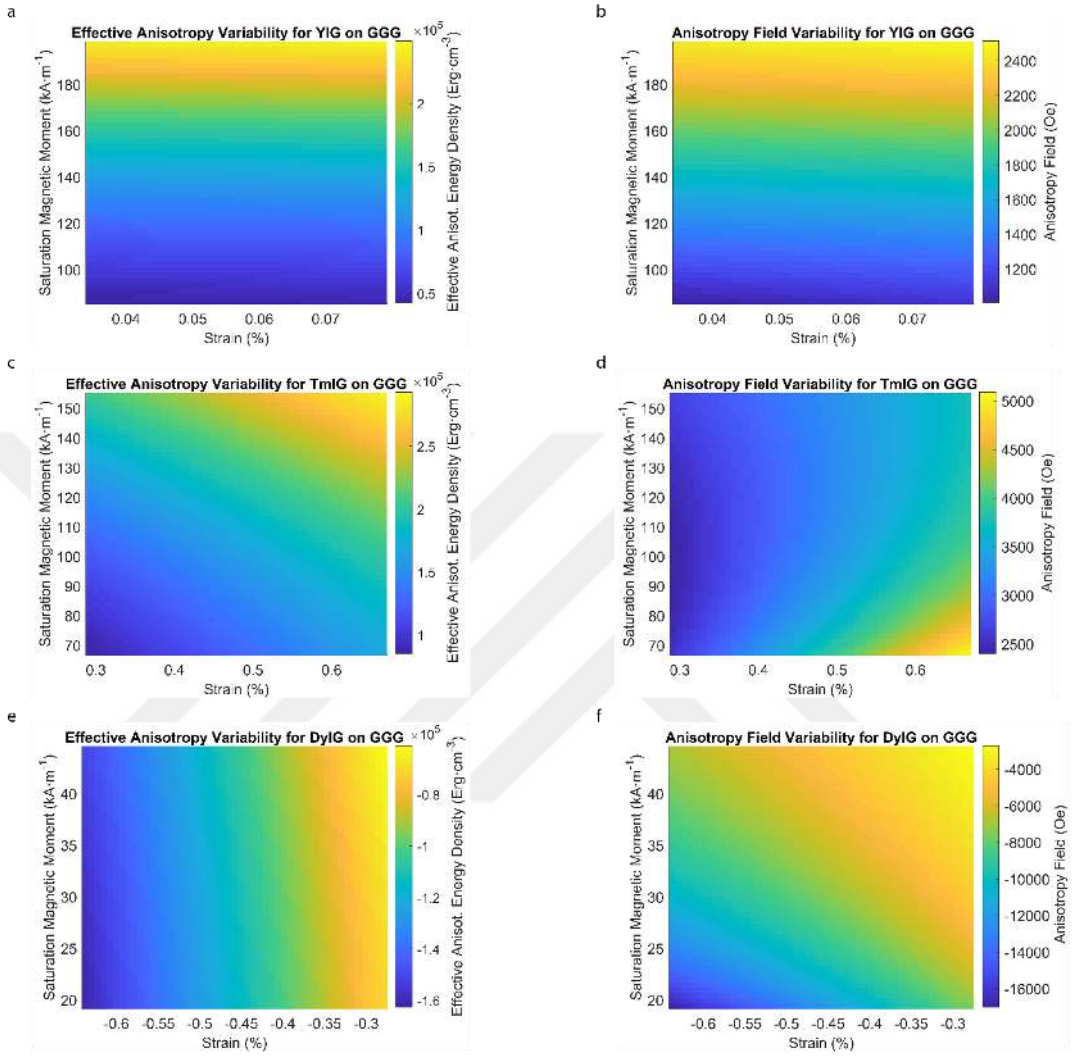

Figure A.1: Effect of partial film relaxation or additional strain and saturation magnetic moment variability on the film effective anisotropy energy density and anisotropy field. Variation of effective magnetic anisotropy energy density and anisotropy field, respectively, for (a) and (b) YIG, (c) and (d) TmIG, (e) and (f) DyIG grown on GGG substrate.

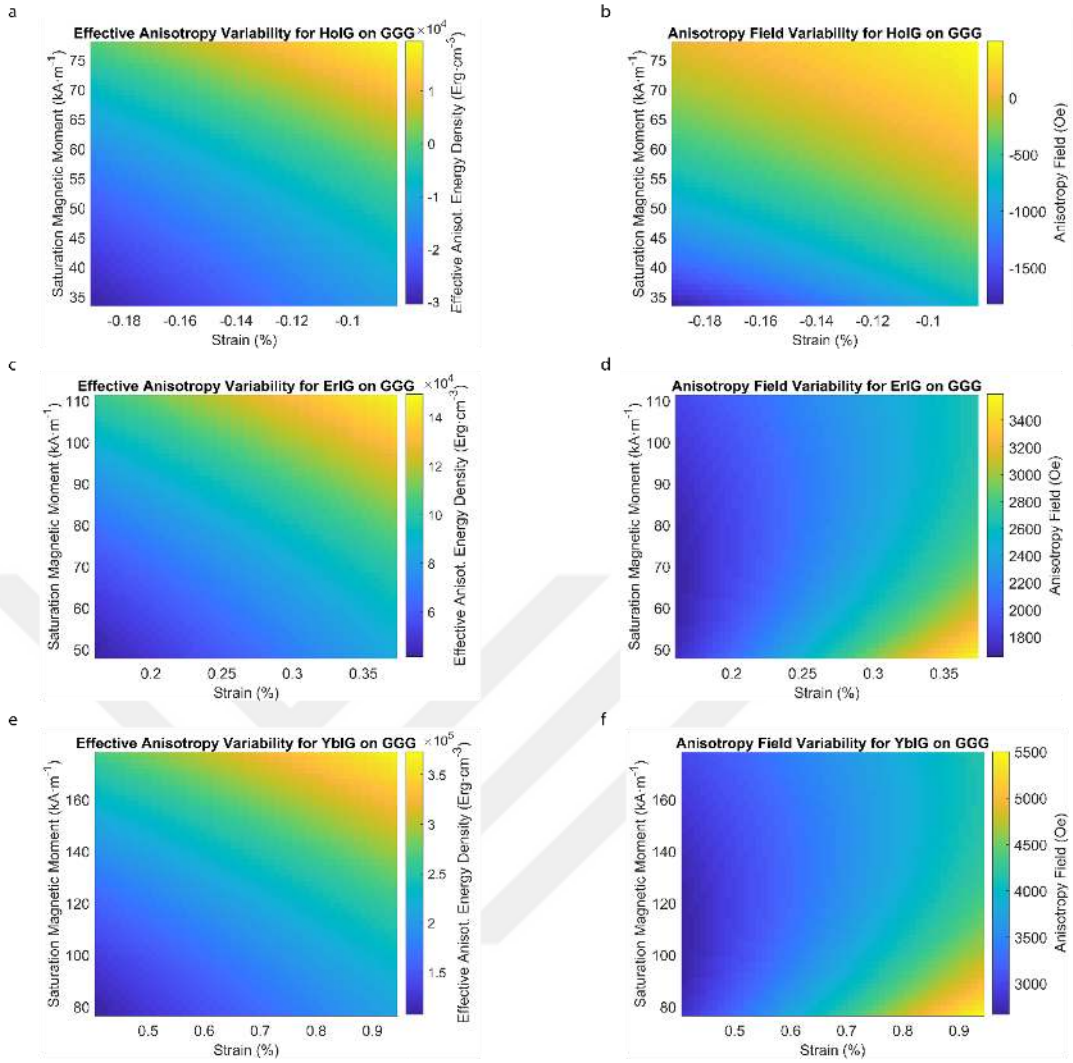

Figure A.2: Effect of partial film relaxation or additional strain and saturation magnetic moment variability on the film effective anisotropy energy density and anisotropy field. Variation of effective magnetic anisotropy energy density and anisotropy field, respectively, for (a) and (b) HoIG, (c) and (d) ErIG, (e) and (f) YbIG grown on GGG substrate.

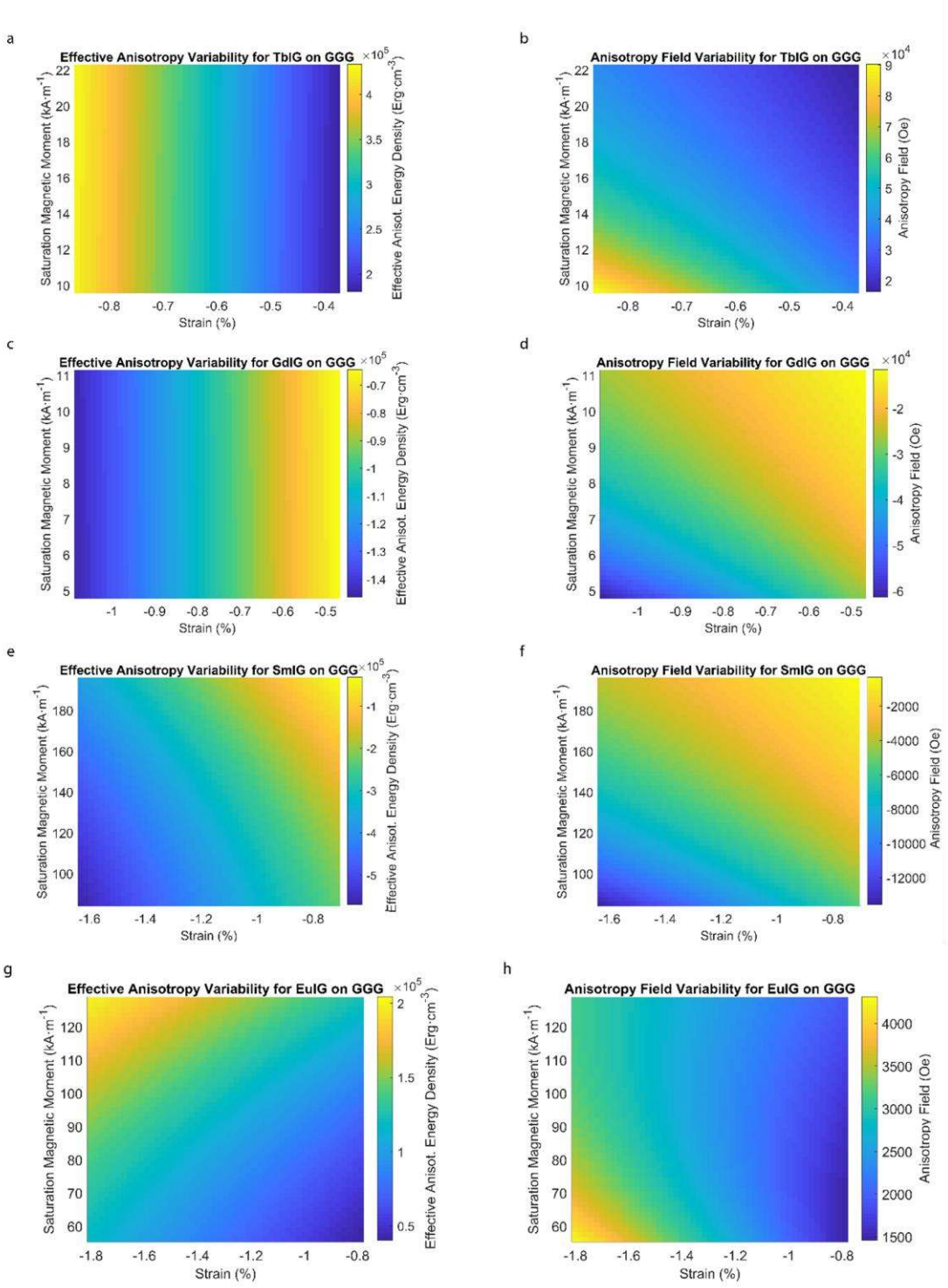

Figure A.3: Effect of partial film relaxation or additional strain and saturation magnetic moment variability on the film effective anisotropy energy density and anisotropy field. Variation of effective magnetic anisotropy energy density and anisotropy field, respectively, for (a) and (b) TbIG, (c) and (d) GdIG, (e) and (f) SmIG, (g) and (h) EuIG grown on GGG substrate.

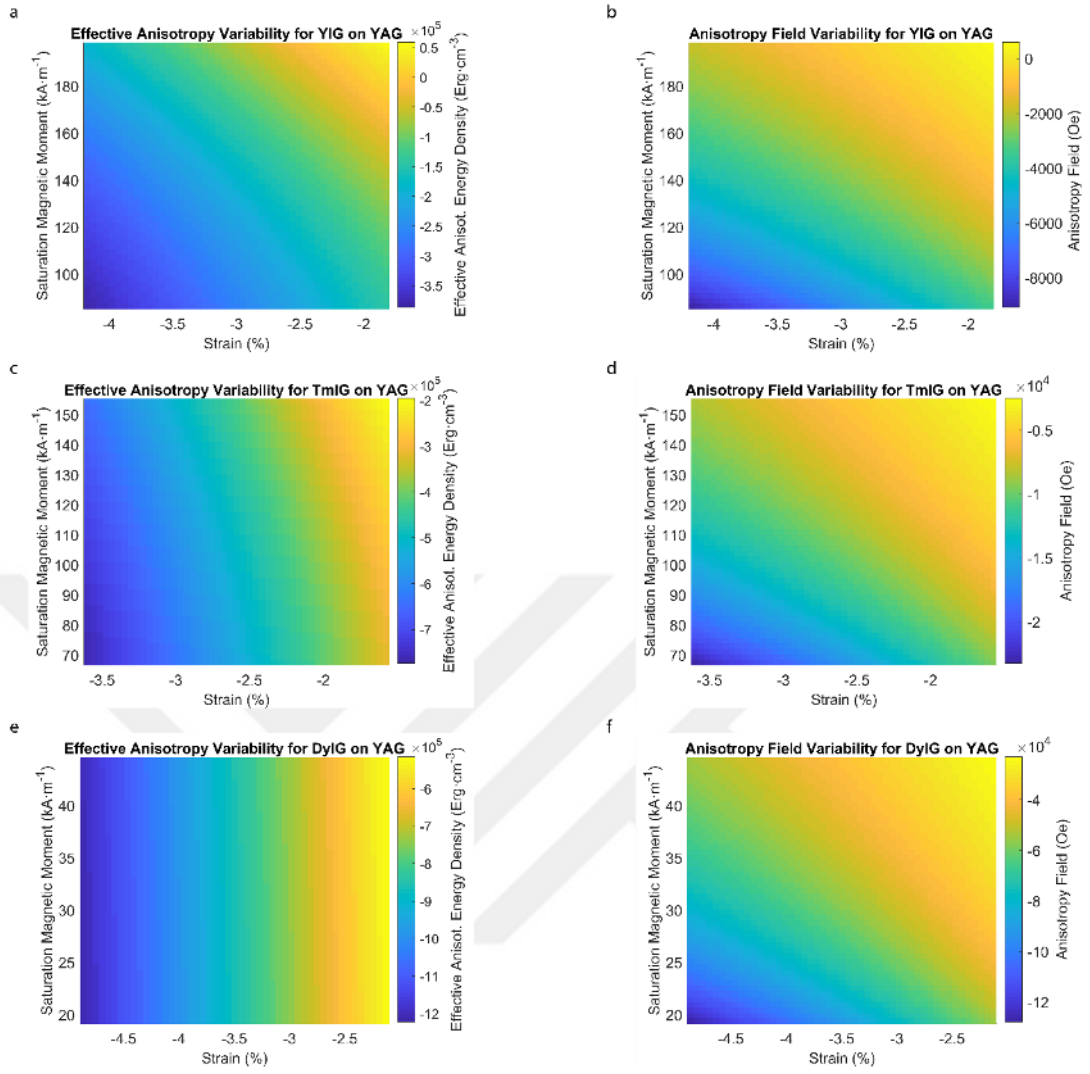

Figure A.4: Effect of partial film relaxation or additional strain and saturation magnetic moment variability on the film effective anisotropy energy density and anisotropy field. Variation of effective magnetic anisotropy energy density and anisotropy field, respectively, for (a) and (b) YIG, (c) and (d) TmIG, (e) and (f) DyIG grown on YAG substrate.

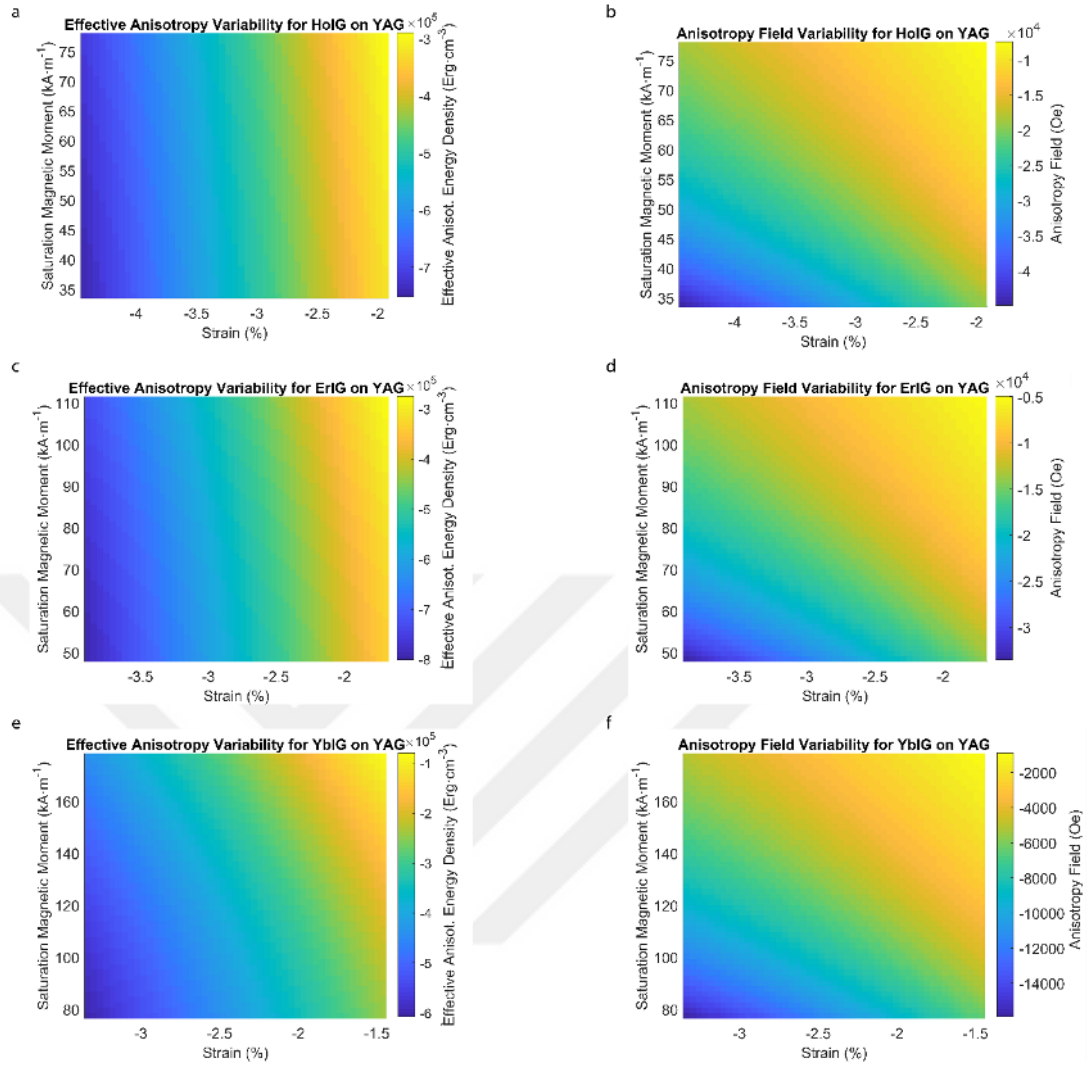

Figure A.5: Effect of partial film relaxation or additional strain and saturation magnetic moment variability on the film effective anisotropy energy density and anisotropy field. Variation of effective magnetic anisotropy energy density and anisotropy field, respectively, for (a) and (b) HoIG, (c) and (d) ErIG, (e) and (f) YbIG grown on YAG substrate.

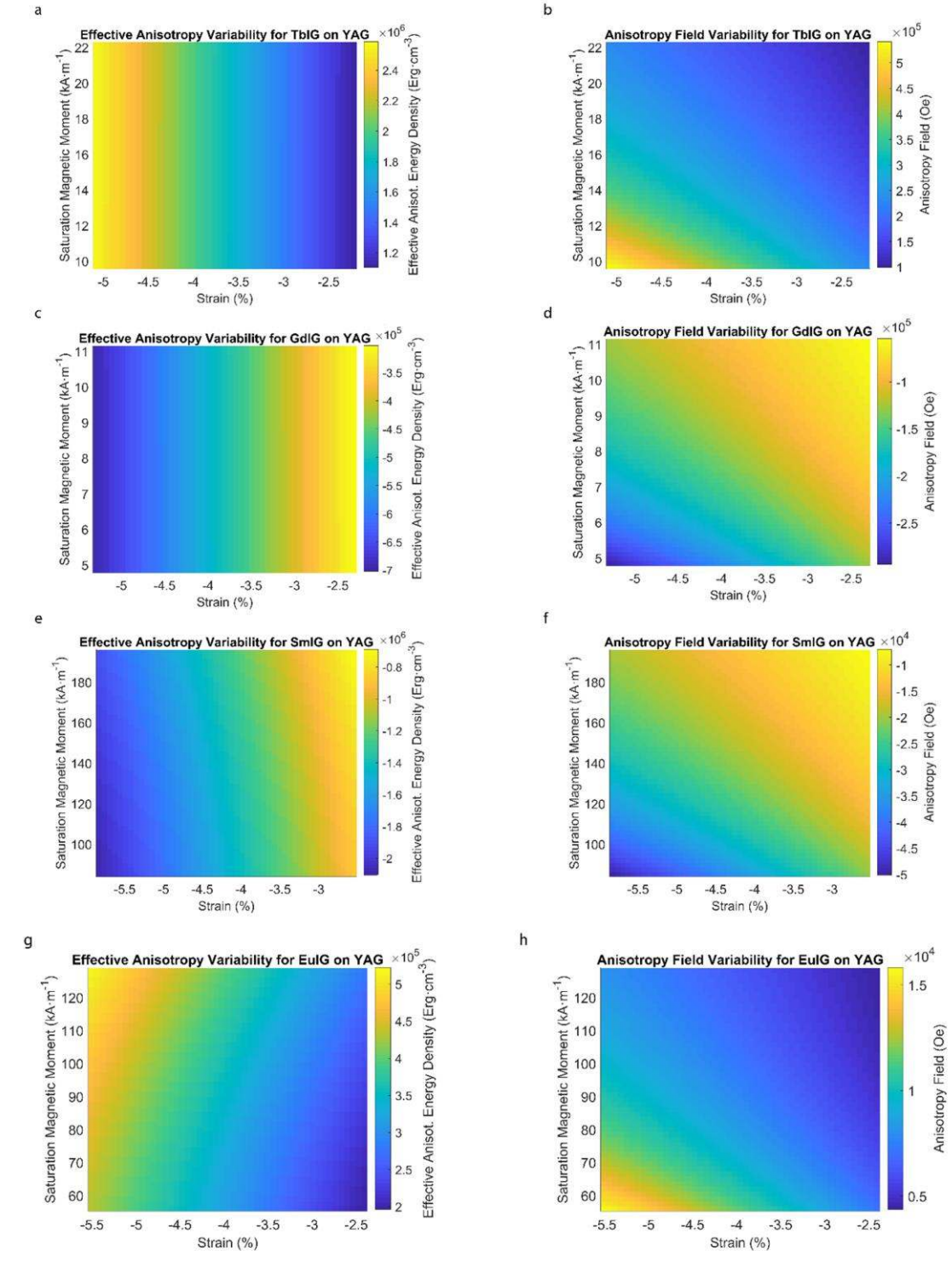

Figure A.6: Effect of partial film relaxation or additional strain and saturation magnetic moment variability on the film effective anisotropy energy density and anisotropy field. Variation of effective magnetic anisotropy energy density and anisotropy field, respectively, for (a) and (b) TbIG, (c) and (d) GdIG, (e) and (f) SmIG, (g) and (h) EuIG grown on YAG substrate.

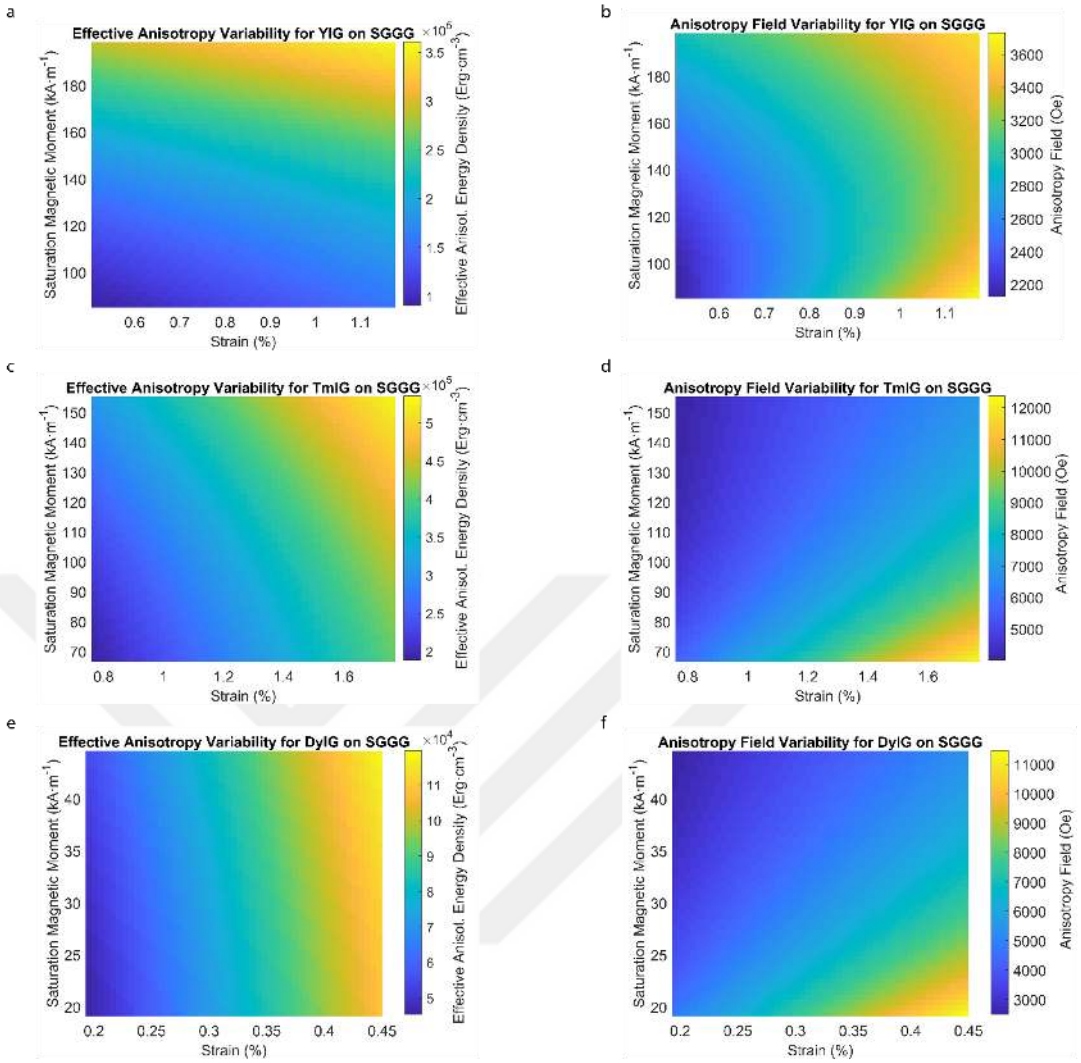

Figure A.7: Effect of partial film relaxation or additional strain and saturation magnetic moment variability on the film effective anisotropy energy density and anisotropy field. Variation of effective magnetic anisotropy energy density and anisotropy field, respectively, for (a) and (b) YIG, (c) and (d) TmIG, (e) and (f) DyIG grown on SGGG substrate.

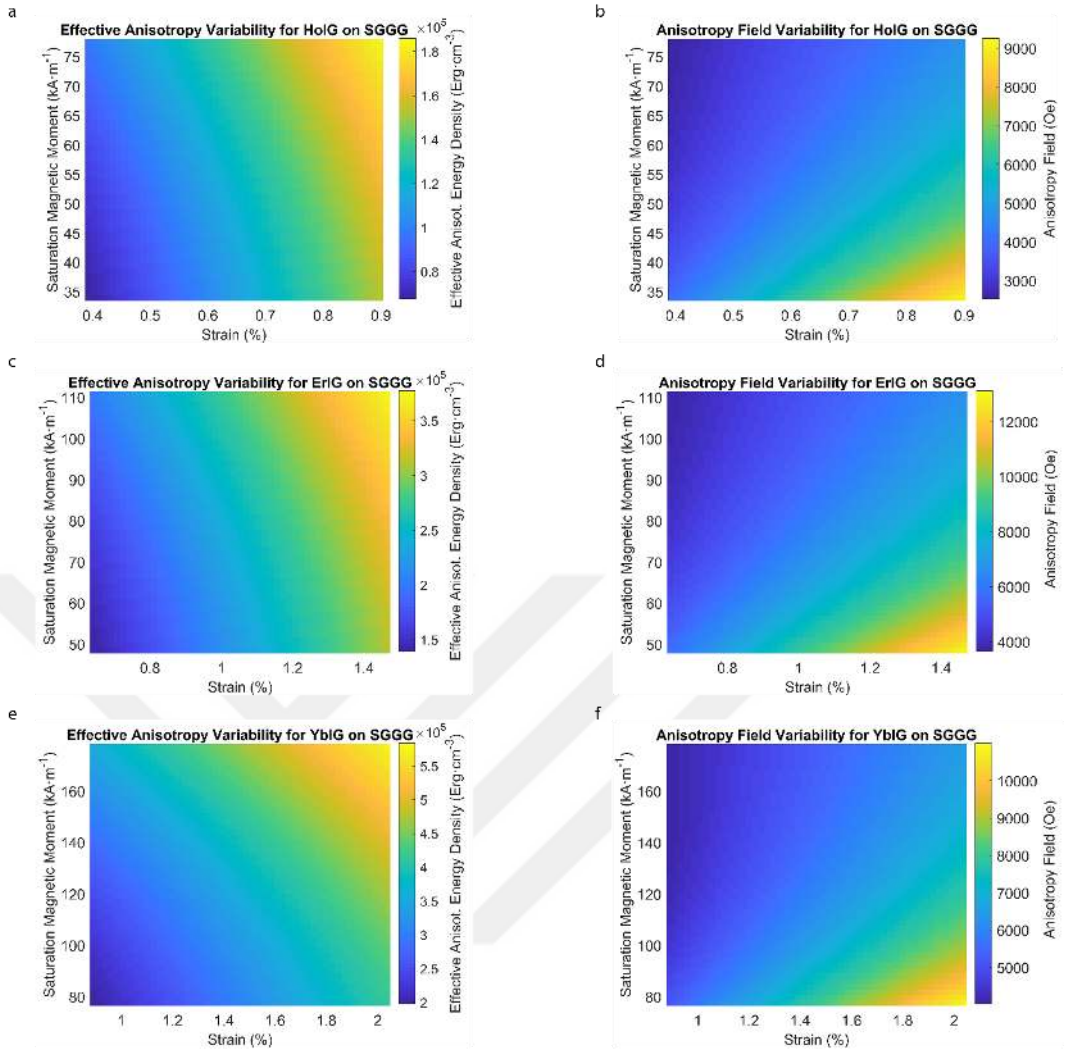

Figure A.8: Effect of partial film relaxation or additional strain and saturation magnetic moment variability on the film effective anisotropy energy density and anisotropy field. Variation of effective magnetic anisotropy energy density and anisotropy field, respectively, for (a) and (b) HoIG, (c) and (d) ErIG, (e) and (f) YbIG grown on SGGG substrate.

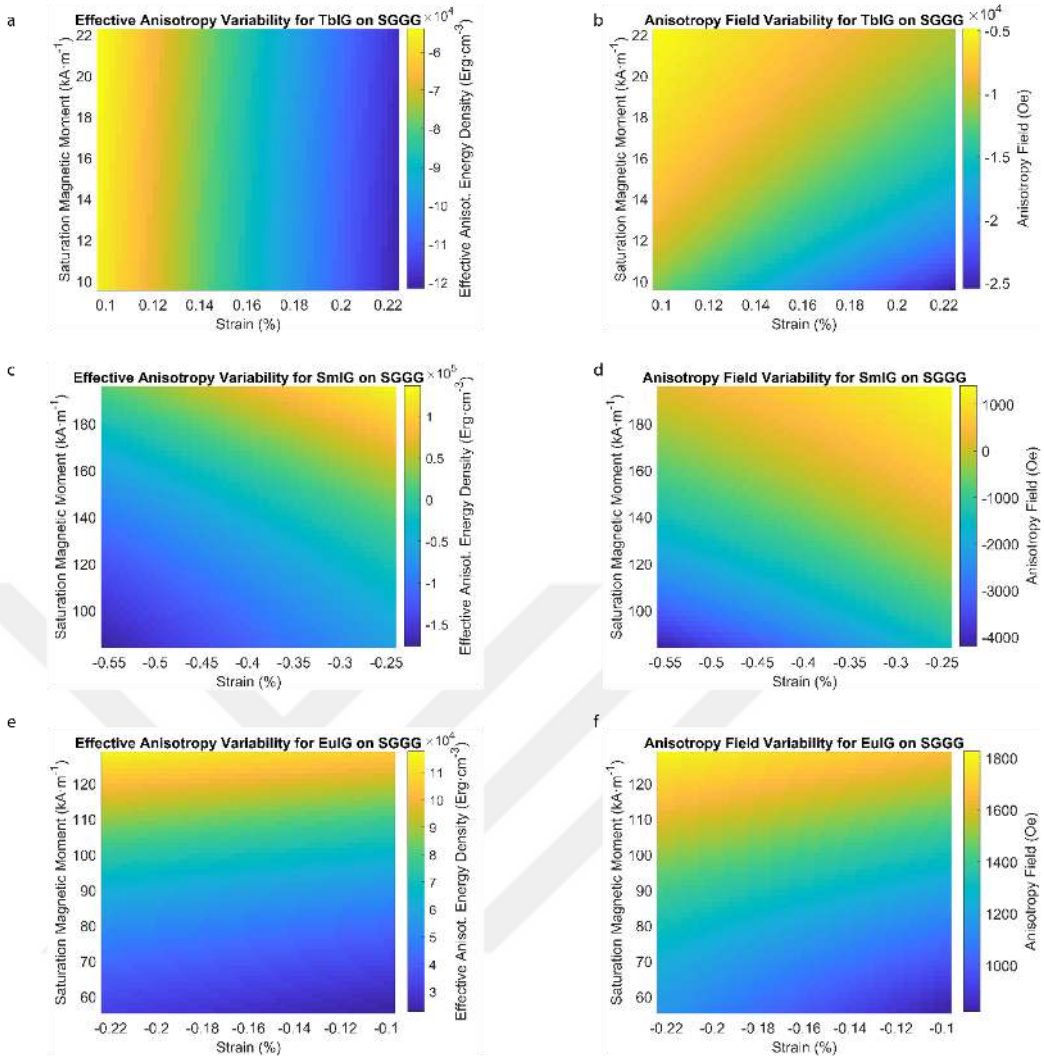

Figure A.9: Effect of partial film relaxation or additional strain and saturation magnetic moment variability on the film effective anisotropy energy density and anisotropy field. Variation of effective magnetic anisotropy energy density and anisotropy field, respectively, for (a) and (b) TbIG, (c) and (d) SmIG, (e) and (f) EuIG grown on SGGG substrate.

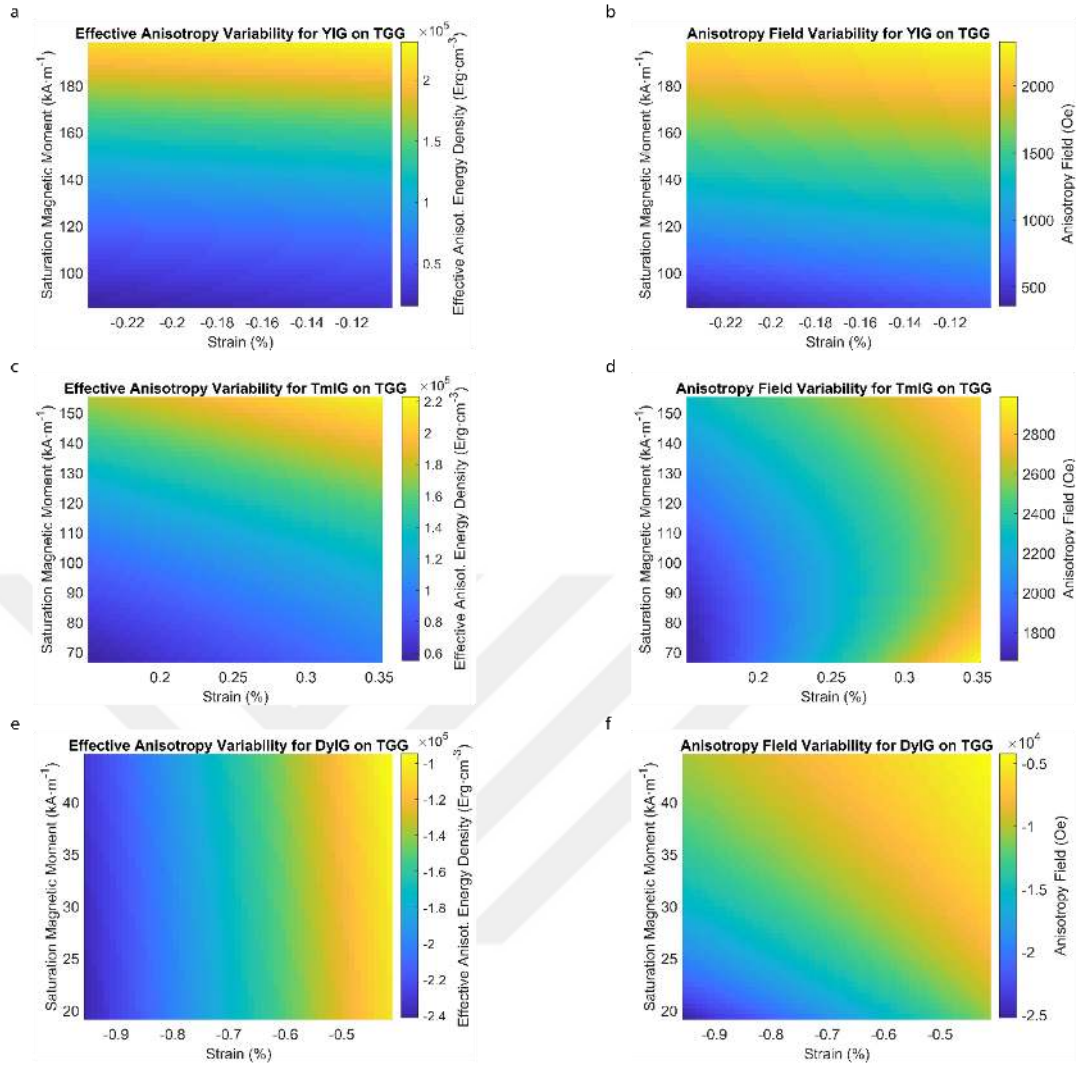

Figure A.10: Effect of partial film relaxation or additional strain and saturation magnetic moment variability on the film effective anisotropy energy density and anisotropy field. Variation of effective magnetic anisotropy energy density and anisotropy field, respectively, for (a) and (b) YIG, (c) and (d) TmIG, (e) and (f) DyIG grown on TGG substrate.

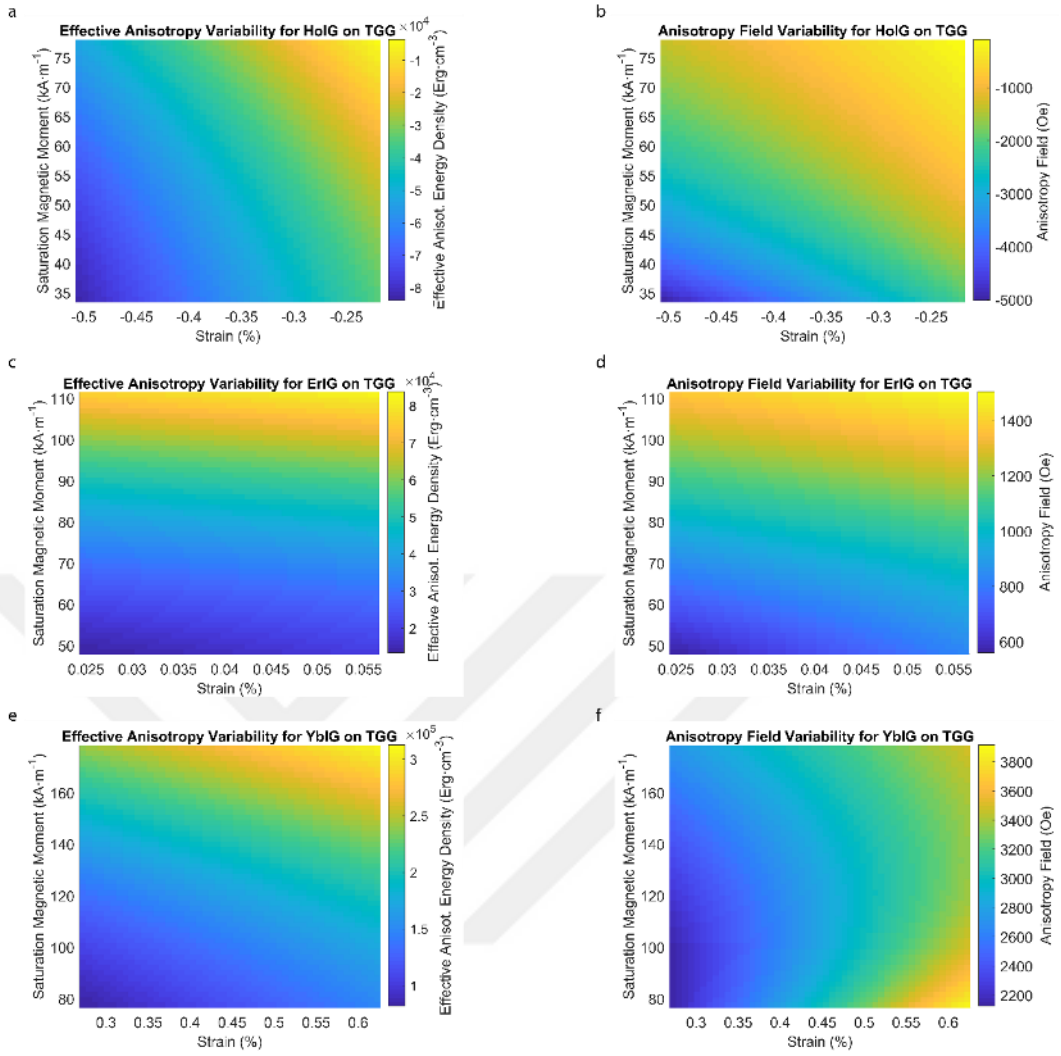

Figure A.11: Effect of partial film relaxation or additional strain and saturation magnetic moment variability on the film effective anisotropy energy density and anisotropy field. Variation of effective magnetic anisotropy energy density and anisotropy field, respectively, for (a) and (b) HoIG, (c) and (d) ErIG, (e) and (f) YbIG grown on TGG substrate.

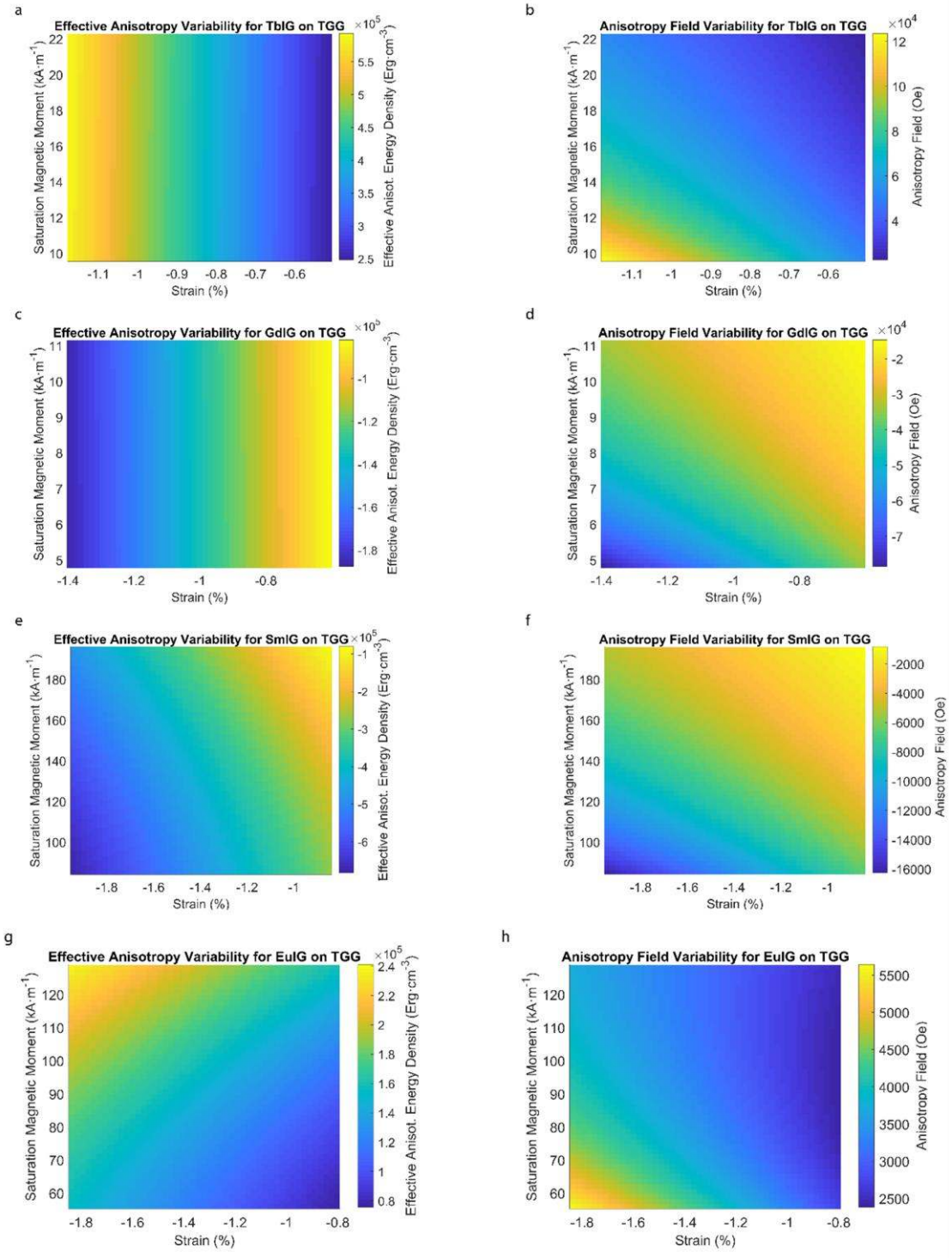

Figure A.12: Effect of partial film relaxation or additional strain and saturation magnetic moment variability on the film effective anisotropy energy density and anisotropy field. Variation of effective magnetic anisotropy energy density and anisotropy field, respectively, for (a) and (b) TbIG, (c) and (d) GdIG, (e) and (f) SmIG, (g) and (h) EuIG grown on TGG substrate.

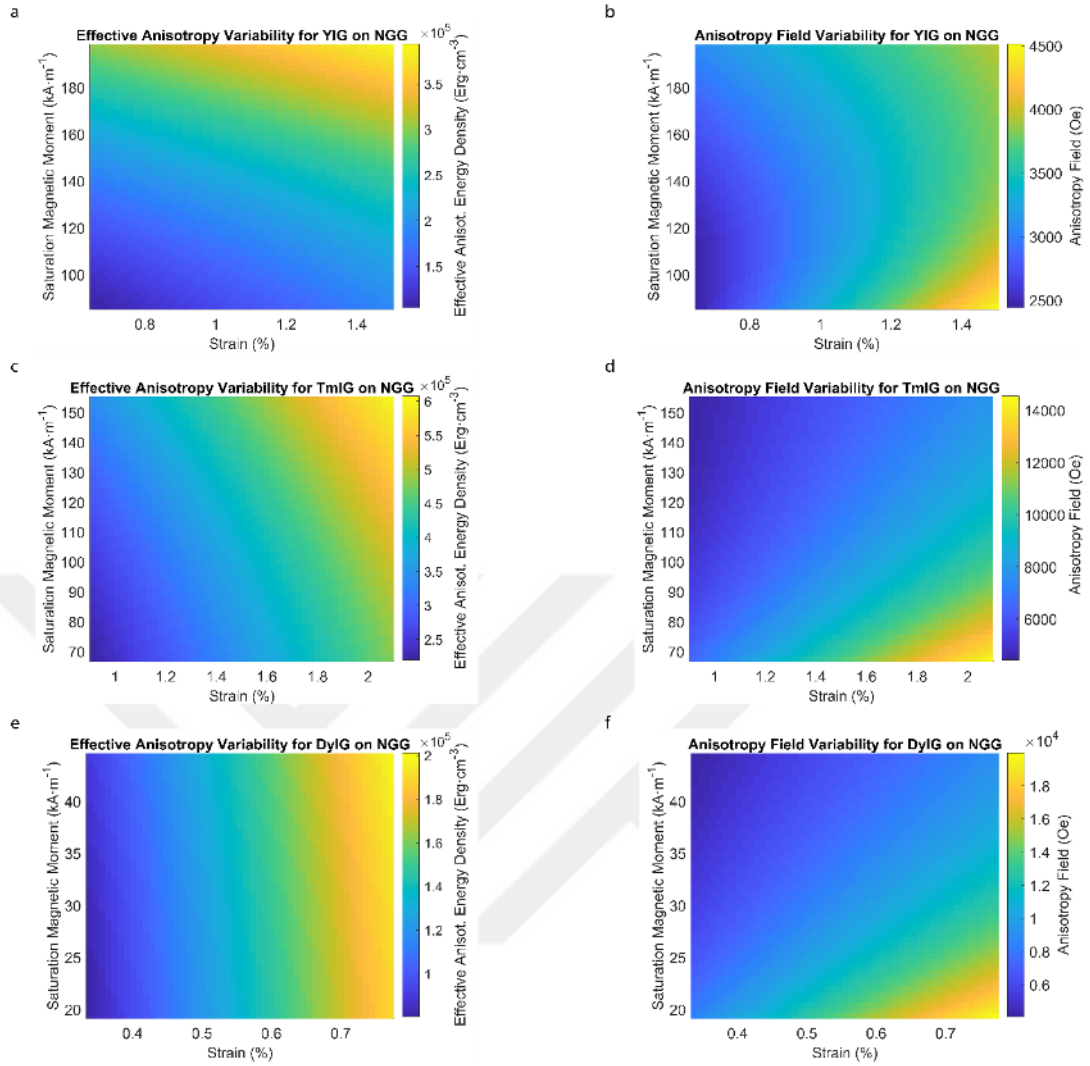

Figure A.13: Effect of partial film relaxation or additional strain and saturation magnetic moment variability on the film effective anisotropy energy density and anisotropy field. Variation of effective magnetic anisotropy energy density and anisotropy field, respectively, for (a) and (b) YIG, (c) and (d) TmIG, (e) and (f) DyIG grown on NGG substrate.

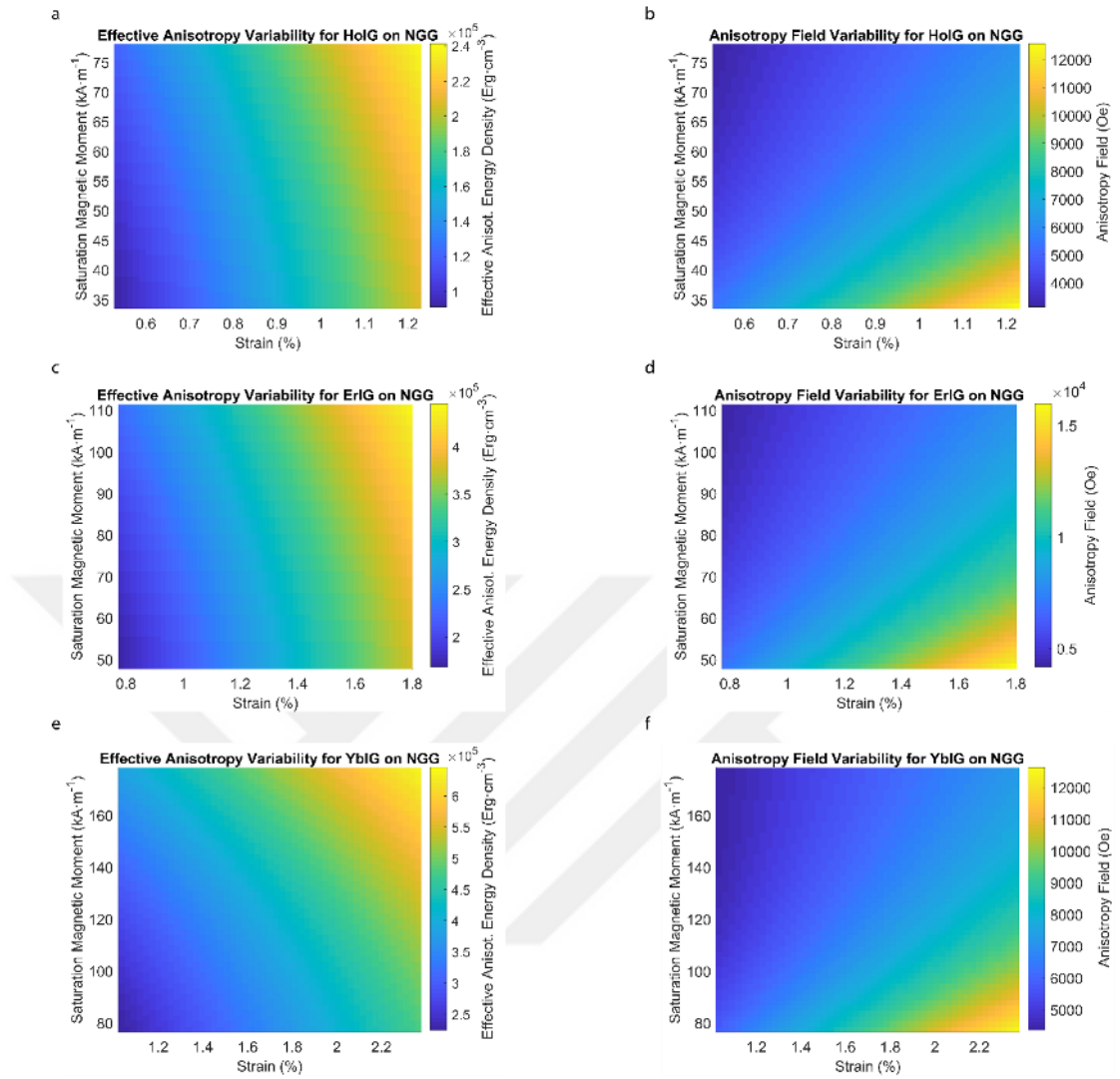

Figure A.14: Effect of partial film relaxation or additional strain and saturation magnetic moment variability on the film effective anisotropy energy density and anisotropy field. Variation of effective magnetic anisotropy energy density and anisotropy field, respectively, for (a) and (b) HoIG, (c) and (d) ErIG, (e) and (f) YbIG grown on NGG substrate.

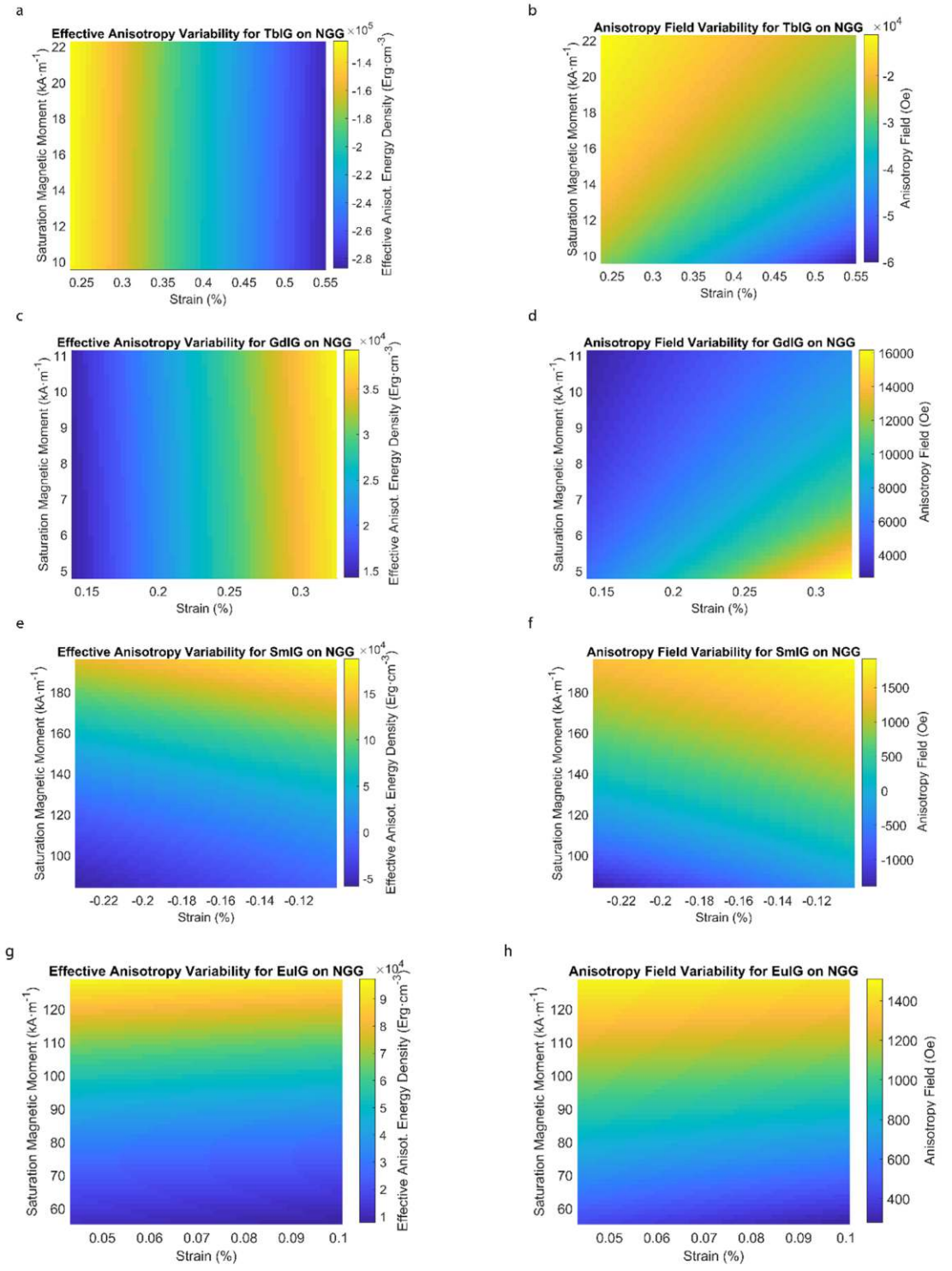

Figure A.15: Effect of partial film relaxation or additional strain and saturation magnetic moment variability on the film effective anisotropy energy density and anisotropy field. Variation of effective magnetic anisotropy energy density and anisotropy field, respectively, for (a) and (b) TbIG, (c) and (d) GdIG, (e) and (f) SmIG, (g) and (h) EuIG grown on NGG substrate.

Table A.1: Calculation of contributing terms to effective magnetic anisotropy energy density (K_{eff}).

a_{GGG}=12.383Å

RIG	M_s (kA·m^{-1})	K_{shape} (erg·cm^{-3} =10^{-1} J.m^{-3})	a_f (Å)	$\varepsilon_{\parallel}$	$\sigma_{\parallel}$ (dyn·cm^{-2} =10^{-1} N.m^{-2})	λ_{111}	K_{indu} (erg·cm^{-3}=10^{-1} J.m^{-3})	K_1 (300K) (erg·cm^{-3}=10^{-1} J.m^{-3})	K_{eff} (erg·cm^{-3}=10^{-1} J.m^{-3})	Experimental Demonstration
YIG	141.7	1.26×10^{5}	12.376	5.66×10^{-4}	1.59×10^{9}	-2.40×10^{-6}	5.74×10^{3}	-6.10×10^{3}	1.26×10^{5}	**[106]** (Bi-Doped)
TmIG	110.9	7.72×10^{4}	12.324	4.79×10^{-3}	1.35×10^{10}	-5.20×10^{-6}	1.05×10^{3}	-5.80×10^{3}	1.77×10^{5}	
DyIG	31.8	6.37×10^{3}	12.44	-4.58×10^{-3}	-1.29×10^{10}	-5.90×10^{-6}	-1.14×10^{5}	-5.00×10^{3}	-1.13×10^{5}	**[196]** (doped stoichiometry)
HoIG	55.7	1.95×10^{4}	12.4	-1.37×10^{-3}	-3.86×10^{9}	-4.00×10^{-6}	-2.32×10^{4}	-5.00×10^{3}	-8.66×10^{3}	**[46]**
ErIG	79.6	3.98×10^{4}	12.35	2.67×10^{-3}	7.53×10^{9}	-4.90×10^{-6}	5.53×10^{4}	-6.00×10^{3}	8.91×10^{4}	
YbIG	127.4	1.02×10^{5}	12.3	6.75×10^{-3}	1.90×10^{10}	-4.50×10^{-6}	1.28×10^{5}	-6.10×10^{3}	2.24×10^{5}	
TbIG	15.9	1.59×10^{3}	12.46	-6.18×10^{-3}	-1.74×10^{10}	1.20×10^{-5}	3.13×10^{5}	-8.20×10^{3}	3.07×10^{5}	
GdIG	7.9	3.98×10^{2}	12.48	-7.77×10^{-3}	-2.19×10^{10}	-3.10×10^{-6}	-1.02×10^{5}	-4.10×10^{3}	-1.06×10^{5}	**[48]**
SmIG	140	1.23×10^{5}	12.53	-1.17×10^{-2}	-3.30×10^{10}	-8.60×10^{-6}	-4.26×10^{5}	-1.74×10^{4}	-3.21×10^{5}	**[38]**
EuIG	92.1	5.33×10^{4}	12.5	-1.30×10^{-2}	-3.65×10^{10}	1.80×10^{-6}	9.86×10^{4}	-3.80×10^{4}	1.14×10^{5}	**[295]** (PMA on GGG(001))

a_{YAG}=12.005Å

RIG	M_s (kA·m^{-1})	K_{shape} (erg·cm^{-3} =10^{-1} J.m^{-3})	a_f (Å)	$\varepsilon_{\parallel}$	$\sigma_{\parallel}$ (dyn·cm^{-2}=10^{-1} N.m^{-2})	λ_{111}	K_{indu} (erg·cm^{-3}=10^{-1} J.m^{-3})	K_1 (300K) (erg·cm^{-3}=10^{-1} J.m^{-3})	K_{eff} (erg·cm^{-3}=10^{-1} J.m^{-3})	Experimental Demonstration
YIG	141.7	1.26×10^{5}	12.376	-3.00×10^{-2}	-8.44×10^{10}	-2.40×10^{-6}	-3.04×10^{5}	-6.10×10^{3}	-1.84×10^{5}	
TmIG	110.9	7.72×10^{4}	12.324	-2.59×10^{-2}	-7.29×10^{10}	-5.20×10^{-6}	-5.69×10^{5}	-5.80×10^{3}	-4.97×10^{5}	
DyIG	31.8	6.37×10^{3}	12.44	-3.50×10^{-2}	-9.85×10^{10}	-5.90×10^{-6}	-8.72×10^{5}	-5.00×10^{3}	-8.70×10^{5}	
HoIG	55.7	1.95×10^{4}	12.4	-3.19×10^{-2}	-8.97×10^{10}	-4.00×10^{-6}	-5.38×10^{5}	-5.00×10^{3}	-5.24×10^{5}	
ErIG	79.6	3.98×10^{4}	12.35	-2.79×10^{-2}	-7.87×10^{10}	-4.90×10^{-6}	-5.78×10^{5}	-6.00×10^{3}	-5.45×10^{5}	
YbIG	127.4	1.02×10^{5}	12.3	-2.40×10^{-2}	-6.76×10^{10}	-4.50×10^{-6}	-4.56×10^{5}	-6.10×10^{3}	-3.60×10^{5}	
TbIG	15.9	1.59×10^{3}	12.46	-3.65×10^{-2}	-1.03×10^{11}	1.20×10^{-5}	1.85×10^{6}	-8.20×10^{3}	1.84×10^{6}	
GdIG	7.9	3.98×10^{2}	12.48	-3.81×10^{-2}	-1.07×10^{11}	-3.10×10^{-6}	-4.99×10^{5}	-4.10×10^{3}	-5.02×10^{5}	
SmIG	140	1.23×10^{5}	12.53	-4.19×10^{-2}	-1.18×10^{11}	-8.60×10^{-6}	-1.52×10^{6}	-1.74×10^{4}	-1.42×10^{6}	
EuIG	92.1	5.33×10^{4}	12.5	-3.96×10^{-2}	-1.12×10^{11}	1.80×10^{-6}	3.01×10^{5}	-3.80×10^{3}	3.51×10^{5}	

a_{SGGG}=12.48Å

RIG	M_s (kA·m^{-1})	K_{shape} (erg·cm^{-3} =10^{-1} J.m^{-3})	a_f (Å)	$\varepsilon_{\parallel}$	$\sigma_{\parallel}$ (dyn·cm^{-2}=10^{-1} N.m^{-2})	λ_{111}	K_{indu} (erg·cm^{-3}=10^{-1} J.m^{-3})	K_1 (300K) (erg·cm^{-3}=10^{-1} J.m^{-3})	K_{eff} (erg·cm^{-3}=10^{-1} J.m^{-3})	Experimental Demonstration
YIG	141.7	1.26×10^{5}	12.376	8.40×10^{-3}	2.37×10^{10}	-2.40×10^{-6}	8.52×10^{4}	-6.10×10^{3}	2.05×10^{5}	**[160], [106]** (Bi-Doped)
TmIG	110.9	7.72×10^{4}	12.324	1.27×10^{-2}	3.57×10^{10}	-5.20×10^{-6}	2.78×10^{5}	-5.80×10^{3}	3.50×10^{5}	**[39]**
DyIG	31.8	6.37×10^{3}	12.44	3.22×10^{-3}	9.06×10^{9}	-5.90×10^{-6}	8.02×10^{4}	-5.00×10^{3}	8.15×10^{4}	
HoIG	55.7	1.95×10^{4}	12.4	6.45×10^{-3}	1.82×10^{10}	-4.00×10^{-6}	1.09×10^{5}	-5.00×10^{3}	1.24×10^{5}	
ErIG	79.6	3.98×10^{4}	12.35	1.05×10^{-2}	2.97×10^{10}	-4.90×10^{-6}	2.18×10^{5}	-6.00×10^{3}	2.52×10^{5}	
YbIG	127.4	1.02×10^{5}	12.3	1.46×10^{-2}	4.12×10^{10}	-4.50×10^{-6}	2.78×10^{5}	-6.10×10^{3}	3.74×10^{5}	

TbIG	15.9	1.59×10^{3}	12.46	1.61×10^{-3}	4.52×10^{9}	1.20×10^{-5}	-8.14×10^{4}	-8.20×10^{3}	-8.80×10^{5}	**[40]**
GdIG	7.9	3.98×10^{2}	12.48	0	0	-3.10×10^{-6}	0	-4.10×10^{3}	-3.70×10^{3}	
SmIG	140	1.23×10^{5}	12.53	-3.99×10^{-3}	-1.12×10^{10}	-8.60×10^{-6}	-1.45×10^{5}	-1.74×10^{4}	-3.93×10^{4}	
EuIG	92.1	5.33×10^{4}	12.5	-1.60×10^{-3}	-4.51×10^{9}	1.80×10^{-6}	1.22×10^{4}	-3.80×10^{3}	6.16×10^{4}	

a_{TGG}=12.355Å

RIG	M_s (kA·m^{-1})	K_{shape} (erg·cm^{-3} =10^{-1} J.m^{-3})	a_f (Å)	$\varepsilon_{\parallel}$	$\sigma_{\parallel}$ (dyn·cm^{-2} =10^{-1} N.m^{-2})	λ_{111}	K_{indu} (erg·cm^{-3}=10^{-1} J.m^{-3})	K_1 (300K) (erg·cm^{-3}=10^{-1} J.m^{-3})	K_{eff} (erg·cm^{-3}=10^{-1} J.m^{-3})	Experimental Demonstration
YIG	141.7	1.26×10^{5}	12.376	-1.70×10^{-3}	-4.78×10^{9}	-2.40×10^{-6}	-1.72×10^{4}	-6.10×10^{3}	1.03×10^{5}	
TmIG	110.9	7.72×10^{4}	12.324	2.52×10^{-3}	7.09×10^{9}	-5.20×10^{-6}	5.53×10^{4}	-5.80×10^{3}	1.27×10^{5}	
DyIG	31.8	6.37×10^{3}	12.44	-6.83×10^{-3}	-1.92×10^{10}	-5.90×10^{-6}	-1.70×10^{5}	-5.00×10^{3}	-1.69×10^{5}	
HoIG	55.7	1.95×10^{4}	12.4	-3.63×10^{-3}	-1.02×10^{10}	-4.00×10^{-6}	-6.13×10^{4}	-5.00×10^{3}	-4.68×10^{4}	
ErIG	79.6	3.98×10^{4}	12.35	4.05×10^{-4}	1.14×10^{9}	-4.90×10^{-6}	8.38×10^{3}	-6.00×10^{3}	4.22×10^{4}	
YbIG	127.4	1.02×10^{5}	12.3	4.47×10^{-3}	1.26×10^{10}	-4.50×10^{-6}	8.50×10^{4}	-6.10×10^{3}	1.81×10^{5}	
TbIG	15.9	1.59×10^{3}	12.46	-8.43×10^{-3}	-2.37×10^{10}	1.20×10^{-5}	4.27×10^{5}	-8.20×10^{3}	4.21×10^{5}	
GdIG	7.9	3.98×10^{2}	12.48	-1.00×10^{-2}	-2.82×10^{10}	-3.10×10^{-6}	-1.31×10^{5}	-4.10×10^{3}	-1.35×10^{5}	
SmIG	140	1.23×10^{5}	12.53	-1.40×10^{-2}	-3.93×10^{10}	-8.60×10^{-6}	-5.08×10^{5}	-1.74×10^{4}	-4.02×10^{5}	
EuIG	92.1	5.33×10^{4}	12.5	-1.32×10^{-2}	-3.72×10^{10}	1.80×10^{-6}	1.00×10^{5}	-3.80×10^{3}	1.50×10^{5}	

a_{NGG}=12.509Å

RIG	M_s (kA·m^{-1})	K_{shape} (erg·cm^{-3} =10^{-1} J.m^{-3})	a_f (Å)	$\varepsilon_{\parallel}$	$\sigma_{\parallel}$ (dyn·cm^{-2} =10^{-1} N.m^{-2})	λ_{111}	K_{indu} (erg·cm^{-3}=10^{-1} J.m^{-3})	K_1 (300K) (erg·cm^{-3}=10^{-1} J.m^{-3})	K_{eff} (erg·cm^{-3}=10^{-1} J.m^{-3})	Experimental Demonstration
YIG	141.72	1.26×10^{5}	12.376	1.07×10^{-2}	3.03×10^{10}	-2.40×10^{-6}	1.09×10^{5}	-6.10×10^{3}	2.29×10^{5}	**[160]**
TmIG	110.908	7.72×10^{4}	12.324	1.50×10^{-2}	4.23×10^{10}	-5.20×10^{-6}	3.30×10^{5}	-5.80×10^{3}	4.01×10^{5}	
DyIG	31.847	6.37×10^{3}	12.44	5.55×10^{-3}	1.56×10^{10}	-5.90×10^{-6}	1.38×10^{5}	-5.00×10^{3}	1.40×10^{5}	
HoIG	55.732	1.95×10^{4}	12.4	8.79×10^{-3}	2.48×10^{10}	-4.00×10^{-6}	1.49×10^{5}	-5.00×10^{3}	1.63×10^{5}	
ErIG	79.618	3.98×10^{4}	12.35	1.29×10^{-2}	3.63×10^{10}	-4.90×10^{-6}	2.67×10^{5}	-6.00×10^{3}	3.00×10^{5}	
YbIG	127.389	1.02×10^{5}	12.3	1.70×10^{-2}	4.79×10^{10}	-4.50×10^{-6}	3.23×10^{5}	-6.10×10^{3}	4.19×10^{5}	
TbIG	15.924	1.59×10^{3}	12.46	3.93×10^{-3}	1.11×10^{10}	1.20×10^{-5}	-1.99×10^{5}	-8.20×10^{3}	-2.06×10^{5}	
GdIG	7.962	3.98×10^{2}	12.48	2.32×10^{-3}	6.55×10^{9}	-3.10×10^{-6}	3.04×10^{4}	-4.10×10^{3}	2.67×10^{4}	
SmIG	140	1.23×10^{5}	12.53	-1.68×10^{-3}	-4.72×10^{9}	-8.60×10^{-6}	-6.09×10^{4}	-1.74×10^{4}	4.48×10^{4}	
EuIG	92.1	5.33×10^{4}	12.5	7.20×10^{-4}	2.03×10^{9}	1.80×10^{-6}	-5.48×10^{3}	-3.80×10^{3}	4.40×10^{4}	

APPENDIX B

ALL-OPTICAL MAGNETIZATION CONTROL IN MAGNETIC METALLIC THIN FILMS USING DUFFERENT LASER PULSE PARAMETERS

B.1 Magnetization dynamics of metallic thin films using different laser pulse width and fluence and thin film thickness

In section 5.1, we solved four coupled differential equations, which describe the energy transfer between electron, phonon (lattice), spin baths and the normalized magnetization, after interaction with femtosecond (fs) Gaussian single laser pulse. We have shown the magnetization dynamics and transient change of three temperature baths (T_e: electron, T_p: phonon/lattice, T_s: spin) for five different metallic thin films: Iron (Fe), Cobalt (Co), Nickel (Ni), Gadolinium (Gd), and Ni_2MnSn Heusler alloy. We applied our model to films with different thicknesses when they are illuminated with different laser pulse widths.

This appendix is organized to present the magnetization dynamics of the metallic magnetic thin films in the sub-picoseconds timescales after illumination of the femtosecond laser pulse. The transient magnetization of the thin films is presented in the Figure 5.1b of the main text. The Figure B.1 specifically shows the magnetization decrease time of the type I thin films at the beginning of the ultrafast magnetization reorientation. In addition, this appendix includes the calculated plots of sensitivity of the transient magnetization to the incoming laser pulse fluence and film thickness after illumination with 500 fs pulse width. Figures B.2 and B.3 show the sensitivity of the magnetization dynamics to the laser fluence and pulse width for 100 nm thick type I and type II thin films, respectively.

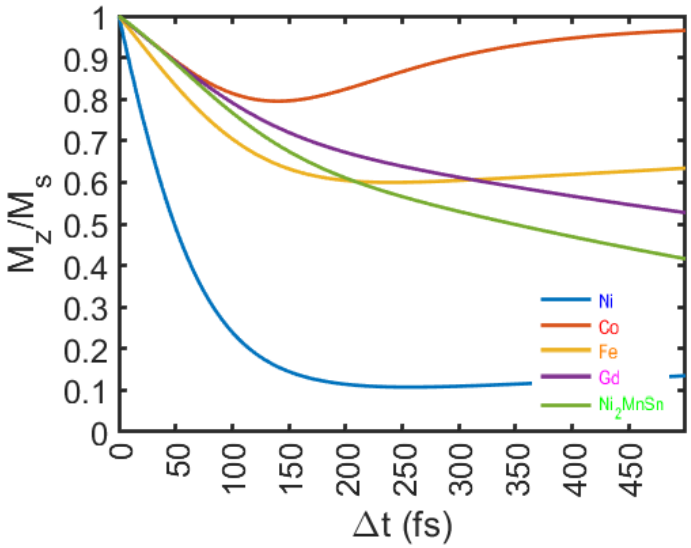

Figure B.1: Sub-picosecond magnetization dynamics of 50 nm thick Fe, Co, Ni, Gd, and Ni_2MnSn Heusler alloy films illuminated with 100 fs laser pulse with 70 $J \cdot m^{-2}$ fluence.

The fluence dependence of magnetization dynamics of 20 nm films are presented in the part 5.1 in Chapter 5. The sensitivity of magnetization to fluence and pulse width for 100 nm thick Fe, Co, and Ni films are shown in Figures B.2a-c, respectively. The magnetization dynamics have been calculated for fluences from 20 to 150 $J \cdot m^{-2}$. Illuminated with both 100 fs (Figures B.2a(i), b(i), c(i)) and 500 fs (Figures B.2a(ii), b(ii), c(ii)), both magnetization switching and recovery times of 100 nm-thick films increase with increasing laser fluence. The recovered magnetization fraction, however, decreases with increasing laser fluence. There is a threshold fluence above which the films are thermally demagnetized. This threshold fluence depends on the film type, thickness and pulse width. Increasing the pulse width increases the response time of the films.

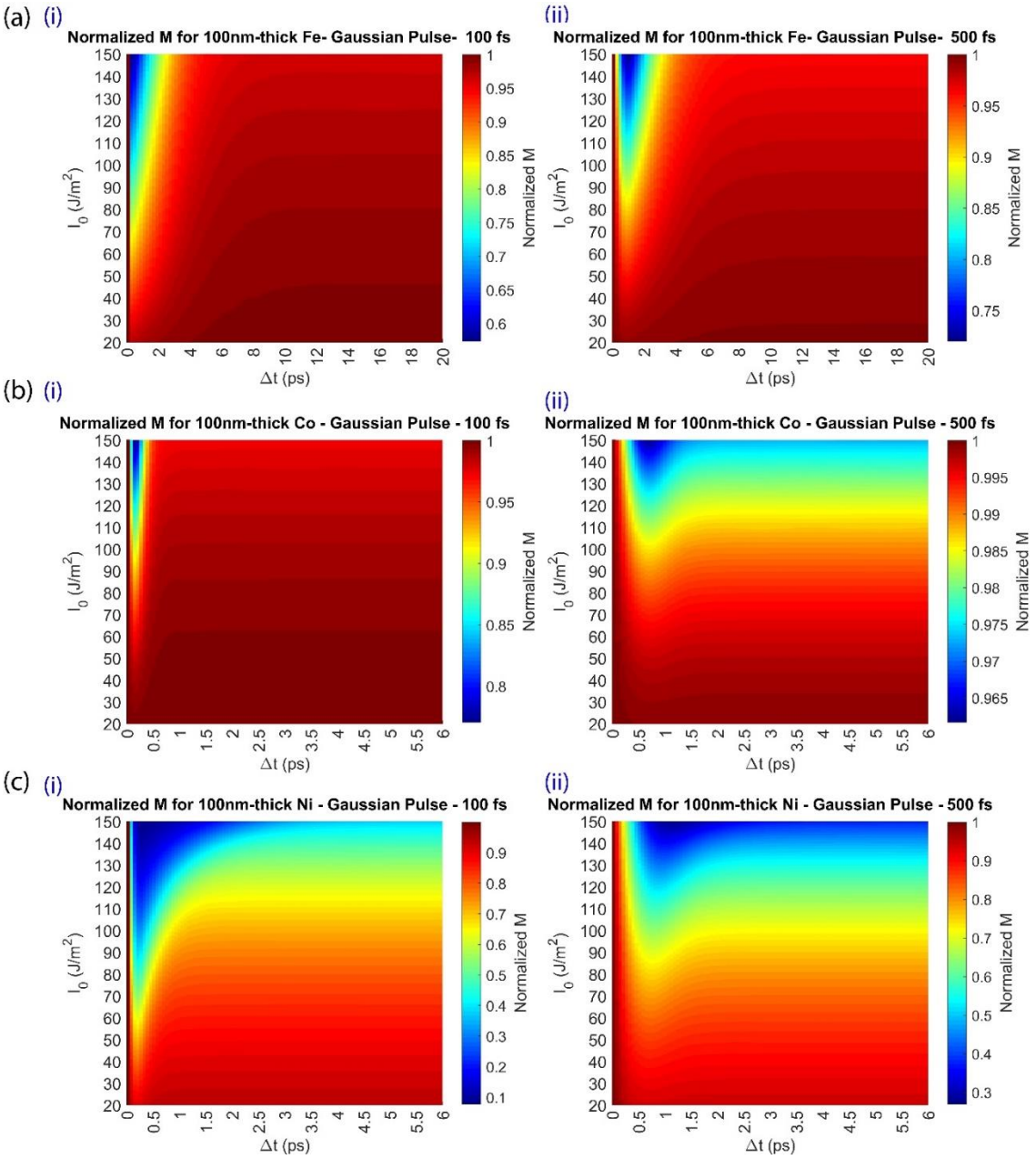

Figure B.2: Effect of fs laser fluence and pulse width on magnetization dynamics and lattice temperature of type I magnetic thin films. Sensitivity of transient magnetization ($m=|M_z|/M_s$) of 100 nm thick (a) Fe, (b) Co, and (c) Ni under illumination of (i) 100 fs and (ii) 500 fs laser pulse widths.

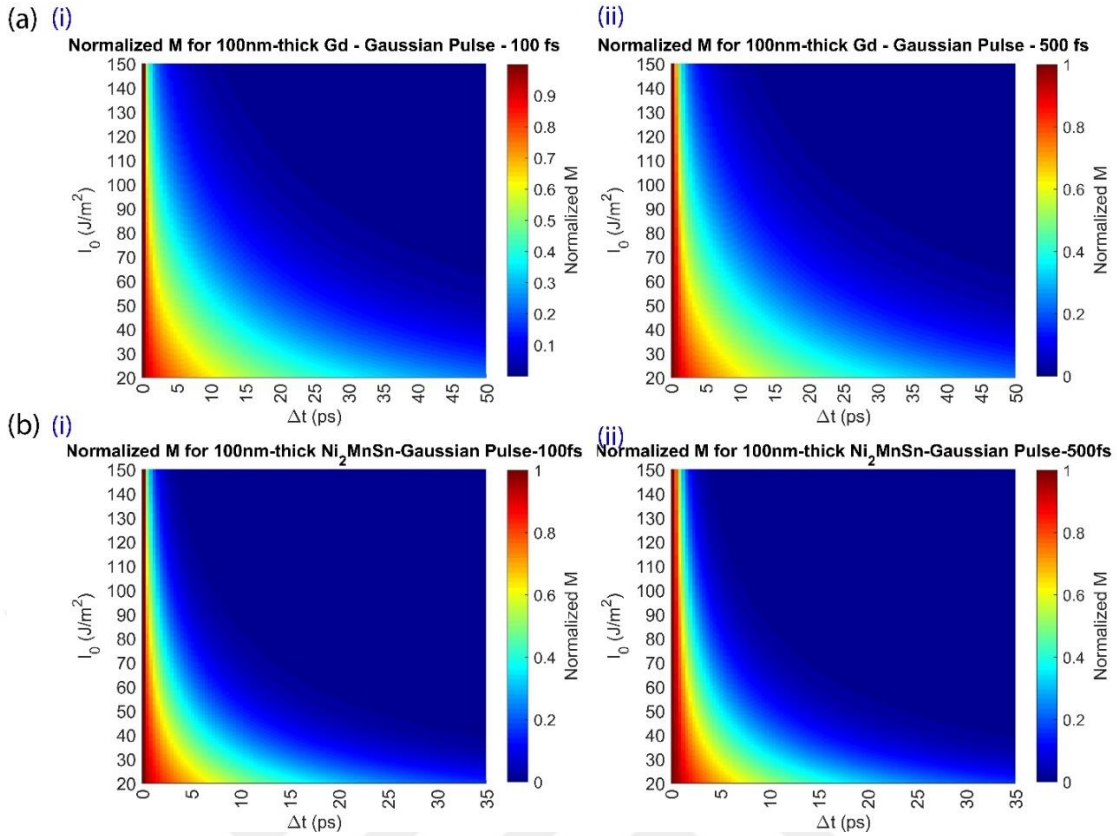

Figure B.3: Effect of fs laser fluence and pulse width on magnetization dynamics and lattice temperature of magnetic type II thin films. Sensitivity of transient magnetization ($m=|M_z|/M_s$) of 100 nm thick (a) Gd, (b) Ni_2MnSn under illumination of (i) 100 fs and (ii) 500 fs laser pulse widths.

Figures B.3a and B.3b show the dependence of magnetization dynamics to the pulse fluence and pulse width for 100 nm thick Gd and Ni_2MnSn films, respectively. Type II films, unlike type I, undergo total thermal demagnetization and their moments cannot be recovered. Similar to type I dynamics, increasing the laser fluence and pulse duration increases the response time in both type II films. On the other hand, excitation of the films with smaller laser fluences keeps the films magnetized for longer times. Unlike type I films, the response time increases in type II films by increasing the film thickness. Besides, increasing the incoming laser pulse width increases the response time in both films, as shown in Figures B.3a(ii) and b(ii).

APPENDIX C

QUNTUM SIZE EFFECT ON ULTRAFAST MAGNETIZATION MANIPULATION IN QUANTUM-CONFINED METALS

This study has been completed in collaboration with Prof. Özgür E. Müstecaplıoğlu, who derived the key relations on the density of electronic states and related properties on quantum-confined metallic magnetic nanofilms. S. Mokarian Zanjani contributed to calculations of electron, phonon, spin temperatures and magnitude of magnetization as functions of time using the microscopic three temperature model.

This appendix has three main parts. In the first part, we present the complete derivation of the three temperature model, which we explained and used in part 5.2 in Chapter 5. In the second part, we compare the thickness dependence of chemical potential and the Fermi level electronic density of states for two different electron temperature (T_e). Furthermore, we investigate the sensitivity of our results presented in section 5.2 to potential well depth (V_z). In the third part, we present with our model the condition of spin-electron and spin-phonon coupling for explaining highly-efficient energy transfer from laser to spins using quantum-confinement in all-optical magnetization manipulation.

C.1 Derivation of the microscopic three temperature model

Here, we present the derivation of the microscopic three temperature model based on the pioneering works [255, 267], including free electron theory. Then, the effect of ultrathin film thickness on the electron density of states at the Fermi level and the electron-phonon coupling coefficient are theoretically modeled.

This section is organized to present our theoretical derivation of the microscopic three temperature model. A ferromagnetic ultrathin metal illuminated by an ultrashort (femtosecond) laser pulse can be microscopically described by a generic Hamiltonian for interacting electron and phonon baths as the following:

$$H = H_e + H_p + H_{ep} \tag{C.1}$$

H_e and H_p are the Hamiltonians of free electrons and phonons, respectively. H_{ep} models the electron-scattering from the lattice, ignoring spin flips. We remark that the baths are not exactly free. The interactions in the same subsystems H_{ee} and H_{pp} lead to fast equilibration and hence, they are dropped after instant thermalization assumptions. Their effects are implicit in the dynamics; we will not present them here explicitly. Ignoring the

spin degree of freedom of the electrons, their non-interacting electron gas has the Hamiltonian:

$$H_e = \sum_k E(\mathbf{k}) \mathbf{c}_\mathbf{k}^\dagger \mathbf{c}_\mathbf{k} \quad (C.2)$$

Here $c_\mathbf{k}$ ($c^\dagger_\mathbf{k}$) annihilates (generates) an electron with excitation energy $E(\mathbf{k})$ in Bloch state $|\mathbf{k}\rangle$. Initially, the gas in metal is in equilibrium at an ambient temperature T_0. After the ultrashort pulse excitation, this gas can quickly reach a new temperature due to (screened) Coulomb interaction H_{ee}.

An ensemble of non-interacting quantum harmonic oscillators describes the bath of lattice vibrations, phonons, with the Hamiltonian:

$$H_p = \sum_q \hbar\omega_q (\mathbf{a}_\mathbf{q}^\dagger \mathbf{a}_\mathbf{q} + 1/2) \quad (C.3)$$

Here the operators $a^\dagger_\mathbf{q}$ and $a_\mathbf{q}$ generate and annihilate phonons with quasi-momentum $\mathbf{q}$, respectively. Phonons obey the Bose-Einstein statistics. Einstein model is the simplest choice to describe them, while Debye model is also possible.

Fröchlich interaction describes the scattering of spinless electrons from the lattice as

$$H_{ep} = \sum_{kk'q} V_{kk'q} \mathbf{c}_\mathbf{k}^\dagger \mathbf{c}_{\mathbf{k}'} (\mathbf{a}_\mathbf{q}^\dagger + \mathbf{a}_\mathbf{q}) \quad (C.4)$$

, where we denote the matrix element of the scattering process with $V_{\mathbf{kk'q}}$.

The calculation of electron-phonon coupling parameter G_{ep} in the two-temperature model proceeds applying of the Fermi's golden rule using H_{ep}. We will present a brief review of the derivation in ref. [255], which is based upon pioneering works [267] , and allows for including beyond free electron theory effects and arbitrary DOS. Accordingly, we write the energy transfer rate from electrons to the lattice E_e as

$$\frac{\partial E_e}{\partial t} = \frac{4\pi}{\hbar} \sum_{kk'} \hbar\omega_q |V_{kk'}|^2 S(k,k') \delta(E(k) - E(k') + \hbar\omega_q) \quad (C.5)$$

Here,

$$S(k,k') = (f_k - f_{k'}) n_q - f_{k'}(1 - f_k) \quad (C.6)$$

is the thermal factor, that depends on the Fermi-Dirac ($f_\mathbf{k}$) and Bose-Einstein ($n_\mathbf{q}$) distribution functions of the electron and phonon baths in their "local" thermal equilibrium states [255]. Explicitly they are defined as $f_\mathbf{k} = 1/(1 + \exp(E(k) - \mu)/k_B T_e)$

and $n_{\mathbf{q}} = 1/(\exp(\hbar\omega_q/k_B T_p - 1)$. Near room temperature, after the conversion of the k summation to continuum energy integrals, we can write

$$\frac{\partial E_e}{\partial t} = 2\pi g_F \int d\Omega \alpha^2 F(\Omega)(\hbar\Omega)^2 \left[n(\hbar\Omega, T_p) - n(\hbar\Omega, T_e)\right] \quad (C.7)$$

With g_F denoting the electronic DOS at Fermi level. The limitation of the DOS to the Fermi level value assumes that only those electrons near the Fermi energy could contribute to the scattering process from the lattice vibrations around room temperature. The term $\alpha^2F(\Omega)$ is the Eliashberg spectral function [269]. If we assume temperatures are below Debye temperatures but higher than phonon mode energy $\hbar\Omega \ll k_B T_p, k_B T_e$, then we can replace the population distributions with a temperature gradient between the baths such that

$$C_e \frac{dT_e}{dt} = -G_{ep}(T_e - T_p) \quad (C.8)$$

, where we used $dE_e = C_e dT_e$. Electron-phonon coupling factor G_{ep} is given by

$$G_{ep} = \pi\hbar\lambda\langle\omega^2\rangle g_F \quad (C.9)$$

, where k_B is the Boltzmann constant, λ is the electron-phonon mass enhancement parameter [268], and $\langle\omega^2\rangle$ is the second moment of the phonon [269]. At low temperatures, we can take $C_e = \gamma T_e$, where $\gamma = \pi^2 k_B^2 g_F/3$, according to the Sommerfeld expansion [270]. Numerical examination of C_e for different metals at higher temperatures, which is beyond the scope of the present contribution, can be found in the literature [247].

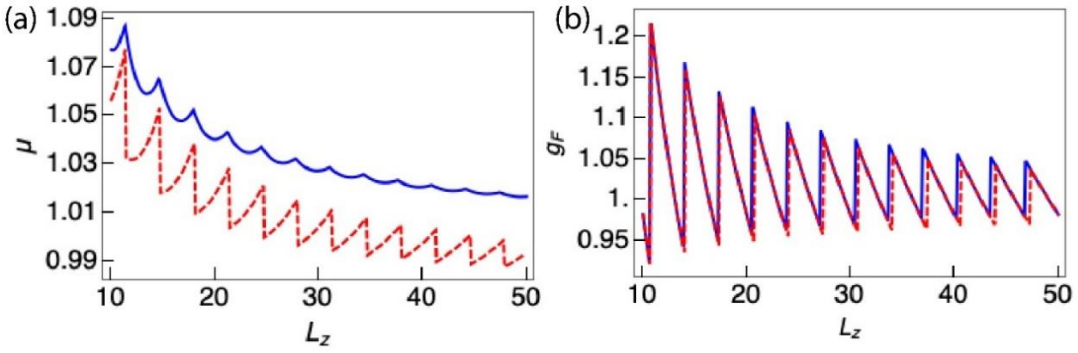

Figure. C.1: (a) Chemical potential (finite temperature Fermi energy) μ and (b) Density of states (DOS) at the Fermi energy as a function of ultrathin film thickness L_z (in units of A). Both μ and g_F are dimensionless, normalized with their corresponding bulk values. Solid blue lines are the zero temperature results. Dashed red lines are for the electronic temperature $T_e = 5 \times 10^{-3} T_B$, where $T_B = E_B/k_B$ being the Bohr temperature corresponding to the Bohr energy $E_B = 13.6$ eV. Depth of the metallic confinement potential is taken to be $V_z = 10$ eV. Electronic density is used as $n = 3/4\pi r_s^3$ with $r_s = 4a_B$, and a_B being the Bohr radius.

C.2 Dependence of DOS on temperature

Here, we describe a theoretical method with which the dependence of DOS at Fermi level changes with temperature, to be able to take into account this size effect for G_{ep}.

Our numerical method starts with taking k_z for $n_z = 1$ in equation C.4 as a guess set of K_z to evaluate k_μ by solving equation C.8 in part 5.2. We then compare k_z with k_μ; if $k_z < k_\mu$, then we increase the size of K_z by increasing n_z one more. The iteration repeats till the largest k_z in K_z is more than calculated k_μ. The results for corresponding chemical potential μ (or temperature-dependent Fermi energy) and DOS at Fermi energy are plotted in Figure C.1. Both μ and g_F are dimensionless, normalized with their corresponding bulk values. Generalizing the methods in ref. [256] to this temperature-dependent Fermi energy case, we found how the L_z dependence of DOS at Fermi level changes with temperature, to be able to take into account this size effect for G_{ep}.

In Figure C.2, the electron temperature dependence of chemical potential and density of states and Fermi level are shown. The electron-phonon coupling coefficient is shown in Figure C.2c. Both DOS_F and G_{ep} are independent of the electron temperature at the temperature ranges applicable in our calculations (where maximum electron temperature does not exceed 2000 K).

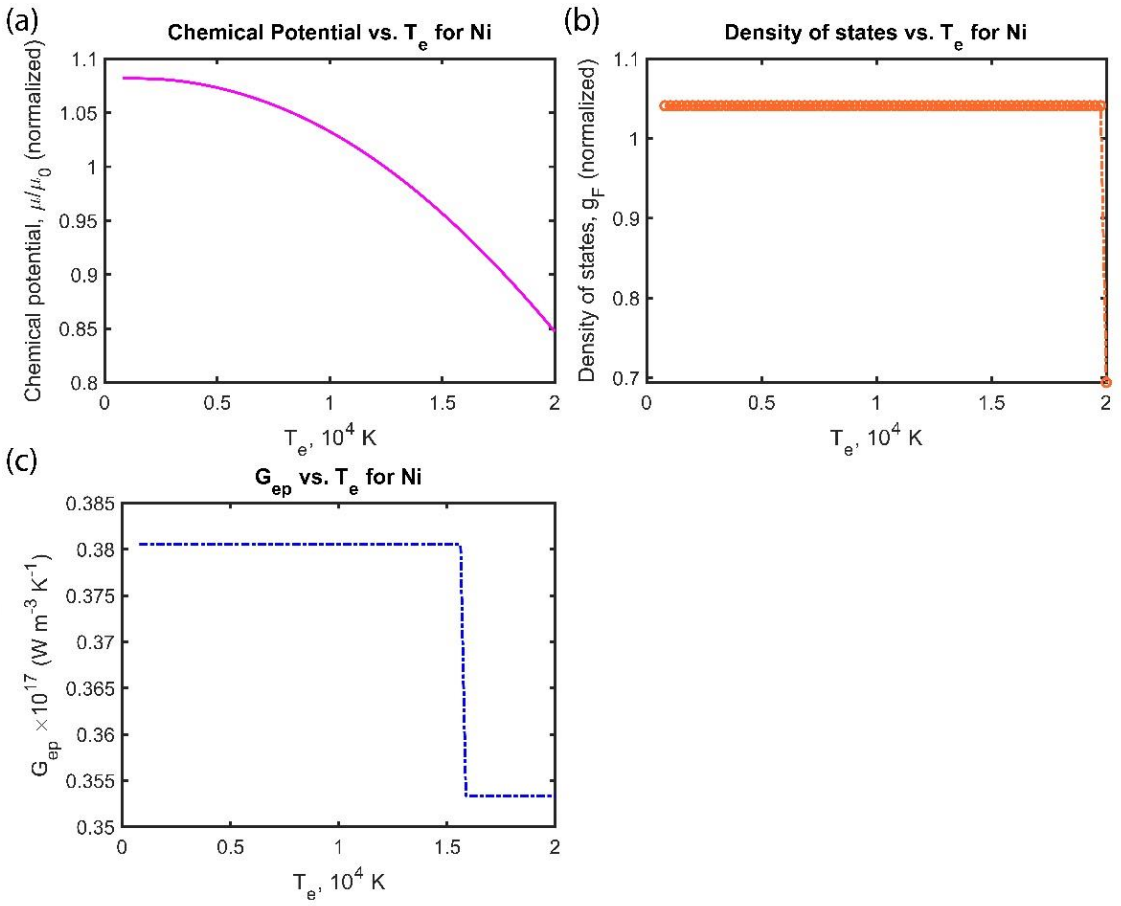

Figure C.2: The dependence of the Fermi level (a) chemical potential (*m*), (b) density of states, and (c) electron phonon coupling (G_{ep}) on the electron temperature (T_e).

The effect of substrate (especially if it is non-magnetic) might be negligible in changing magnetic order. However, the substrate might influence the contributing electron and phonon density and hence, G_{ep}. Nevertheless, assuming an isolated thin film is reasonable for wide band gap non-magnetic insulator substrates, similar to previous studies [83, 89].

In Figure 5.10, we showed the magnetization dynamics of the Ni ultrathin film for different film thicknesses. A zoomed-in version of the magnetization dynamics at a smaller time ranges are shown in Figure C.3.

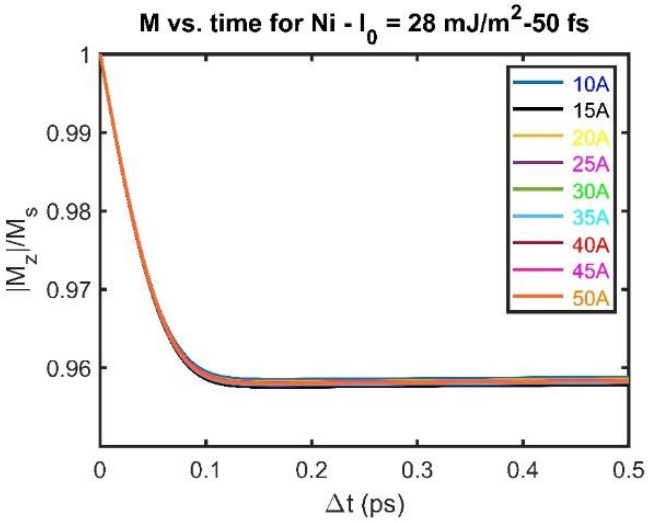

Figure C.3: Magnetization dynamics of the Ni ultrathin film in 300 fs after interaction with the laser pulse.

C.3 Sensitivity of quantum confinement effect of magnetic ultrathin films to the potential well depth (Vz)

In part 5.2, we reported our calculation results of quantum confinement effect in Figures 5.8 and 5.10, using the potential well depth of $V_z = 10$ eV. In this section, we present the sensitivity of our results to the size of the potential well. Practically, the V_z is an infinite value, however, in the FEM calculations, a finite value is given to it. We consider three extra cases of $V_z = 5$ eV, 15 eV, and 20 eV.

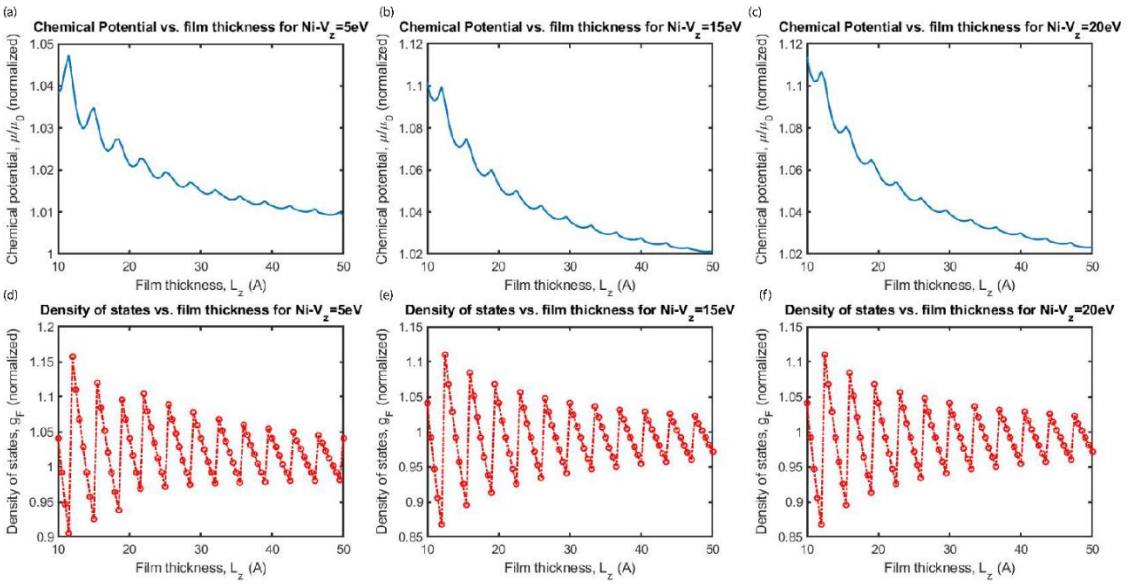

Figure C.4: Thickness dependent (a) chemical potential of the quantum confined Ni ultrathin film with quantum well depth of V_z=5 eV, (b) 15 eV, (c) 20 eV, and (d) Fermi level electron density of states for V_z = 5 eV (e) 15 eV (f) 20 eV.

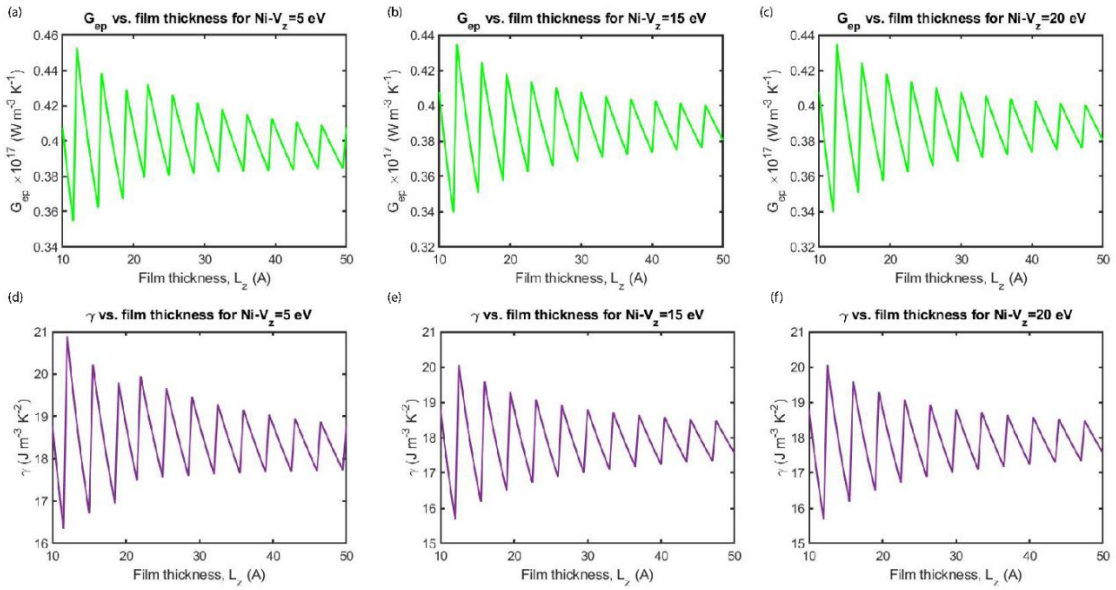

Figure C.5: Thickness dependent (a) electron-phonon coupling coefficient the quantum confined Ni ultrathin film with quantum well depth of V_z = 5 eV, (b) 15 eV, (c) 20 eV, and (d) Sommerfeld coefficient for V_z = 5 eV (e) 15 eV (f) 20 eV.

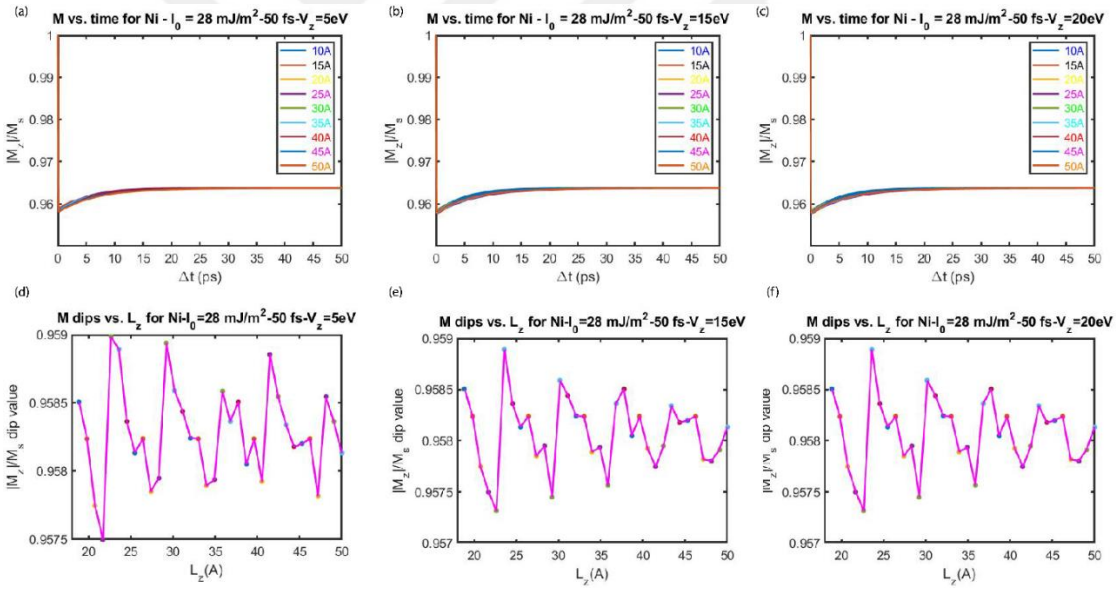

Figure C.6: Thickness dependent (a) magnetization dynamics of the quantum confined Ni ultrathin film with quantum well depth of V_z =5 eV, (b) 15 eV, (c) 20 eV, and (d) demagnetization dip for V_z = 5 eV (e) 15 eV (f) 20 eV.

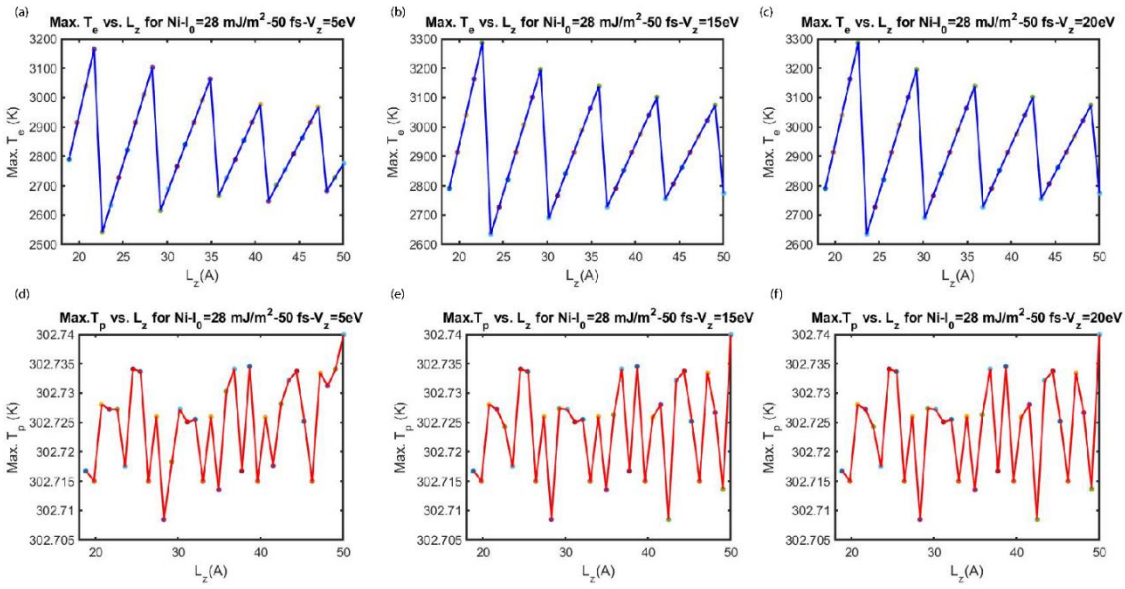

Figure C.7: Thickness dependent (a) maximum electron temperature of the quantum confined Ni ultrathin film with quantum well depth of V_z=5 eV, (b) 15 eV, (c) 20 eV, and (d) maximum phonon temperature for V_z= 5 eV (e) 15 eV (f) 20 eV.

The calculation results for the various potential well depths (V_z = 5, 10, 15, and 20 eV) show that only in the case of sub-20 Å film thicknesses, V_z size might result in a few per cent difference in the calculations. However, it does not influence the qualitative predictions of our model on decrease and oscillations in the electron density of states and electron-phonon coupling as the result of quantum confinement effect. μ increases slightly (~ 3%) in sub-20 Å range, from V_z = 5 to 10 eV, but the oscillations are not considerable when V_z changes from 10 to 15 or 20 eV. Accordingly, g_F, G_{ep}, and γ oscillations decrease (~ 4%) changing from V_z = 5 to 10 eV, while g_F, G_{ep}, and γ remain unchanged for other V_z values. We also investigated the sensitivity of the Figure 5.10 results to the size of V_z. Despite similar negligible variations for V_z = 5 eV in case of low film thicknesses, changing the depth of the potential well did not influence the conclusions of the quantum confinement effect on the oscillations of the magnetization dynamics as well as electron and phonon temperatures (Figures C.6-C.7). Increasing V_z from 5 eV leads to a small increase (~ 3%) in the maximum electron temperature and a decrease in demagnetization dip was observed for sub-20 Å thin films. However, for other V_z values, the results remain unchanged. Since the decrease in the chemical potential and consequently g_F and G_{ep}, is monotonic when averaged [256] (the oscillation amplitude does not exceed a few percent of total amplitude), the qualitative results of our calculations are consistent using different potential well depths.

C.4 M3TM model considering spin-phonon and spin-electron scattering

In this section, we calculated the effect of film thickness including the spin-phonon, and spin-electron scattering in the M3TM models shown in Figure C.8a. We used the following equations:

$$C_e \frac{dT_e}{dt} = -G_{ep}(T_e - T_p) - G_{es}(T_e - T_s) + P(t) \quad (C.10)$$

$$C_p \frac{dT_p}{dt} = -G_{ep}(T_p - T_e) - G_{ps}(T_p - T_s) \quad (C.11)$$

$$C_s \frac{dT_s}{dt} = -G_{es}(T_s - T_e) - G_{ps}(T_s - T_p) \quad (C.12)$$

$$\frac{dm}{dt} = Rm\frac{T_p}{T_C}\left(1 - m\coth\left(m\frac{T_C}{T_e}\right)\right) \quad (C.13)$$

, where C_s is the spin heat capacity, G_{es}, and G_{ps} are the electron-spin and phonon-spin coupling coefficients, respectively. T_s represents the spin temperature. Note that both G_{ep} and R change with the film thickness, as mentioned in part 5.2. If we heuristically assume that G_{es} and G_{ps} have similar size dependence as with G_{ep}, through their dependence to DOS_F, we find that our results with constant G_{ep}, and G_{es} do not change significantly. We therefore estimate that the size dependence of G_{es} and G_{ps} are negligible on T_e and T_p dynamics, which determine the magnetization evolution.

According to Figure C.8a, due to the energy loss to the spin-phonon scattering, the laser fluence needed to recover the magnetization is larger compared to the condition where the spin-lattice scattering is neglected (I_0=35 mJ·m^{-2}). In addition, the magnetization drop time is slightly longer, while the recovered magnetization ratio is slightly lower as the result of spin scattering. Figure C.8b shows the thickness dependence of lattice temperature. According to this figure, the maximum lattice temperature increases due to the energy exchange between spin and phonon baths. However, maximum T_p does not exceed 305.976 K, which is still well below the Curie temperature of Ni.

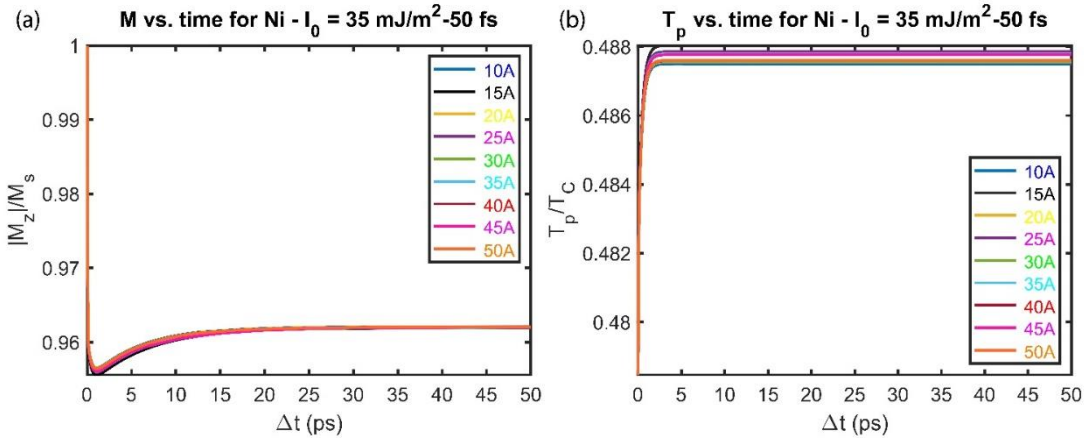

Figure C.8: Effect of Ni film thickness on (a) magnetization dynamics for L_z = 10 Å, 15 Å , 20 Å, 25 Å, 30 Å, 35 Å, 40 Å, 45 Å, and 50 Å thick Ni films, (b) T_p/T_C, illuminated with I_0 = 35 mJ·m^{-2} Gaussian single laser pulse.

In the previous studies, the easy axis of the Ni changes from perpendicular to in-plane when the film thickness changes from around 12-14 Å to 24 Å [296]·[297]. The size-dependent change in the magnetic anisotropy is due to shape anisotropy (dominant anisotropy in the thicker films that dictate the in-plane easy axis), which is completely geometry dependent. In our magnetization dynamics model, "m" stands for the normalized magnetization vector magnitude ($|M_z/M_s|$). After interaction with the low-fluence fs laser pulse, the magnetization vector orientation might change but may not switch completely. The motion is described as precession or canting from an initial stable orientation, which we assume to be $m_0 = 1$. The magnetization magnitude, which changes due to spin reorientation, does not influence the temperature dynamics in the 2TM or M3TM. The easy axis, magnetization vector field and magnetic anisotropy effects are studied using Landau-Lifshitz-Gilbert (LLG) equation, which is beyond the scope of this study [298-301].

C.5 Effect of the femtosecond laser pulse width on the magnetization dynamics of the quantum confined ultrathin Ni film

According to the laser pulse power distribution, $P(t) = \frac{P_0}{\sqrt{2\pi}} \exp\left(-\frac{1}{2}\left(\frac{t}{t_0}\right)^2\right)$ the wider pulse leads to smaller power/energy injected to the thin film ($P_0 = \frac{I_0}{d.t_0}$, and I_0 and t_0 are the laser pulse fluence in J·m^{-2}, pulse width (fs), respectively). It leads to increase in the time of the demagnetization and also electron temperature equilibration. Moreover, for wider pulses such as 200 fs and 500 fs, the injected energy is small such that the quenched magnetization does not recover back and stays constant, and the demagnetization ratio is

smaller compared to the lower pulse widths. Electron temperature rises to the lower amounts in case of wide laser pulses, due to the lower laser energy injection and similar to the magnetization quenching time, the electron equilibration time increases by increasing the pulse width. This effect is also reflected in the maximum electron temperature, which is considerably smaller for 200 fs and 500 fs pulse width, compared to 50 fs. In addition, Figures C9-C11 show that for each specific pulse width, the behavior of the magnetization dip oscillation and maximum T_e and T_p are almost similar. In conclusion, increasing the pulse width decreases the laser power injected to the thin film which leads to increase in the demagnetization time as well as electron equilibration time. Choosing very long pulse durations, increases the laser fluence needed for recovery of the magnetization after quenching, which is not favorable for the scope of our study.

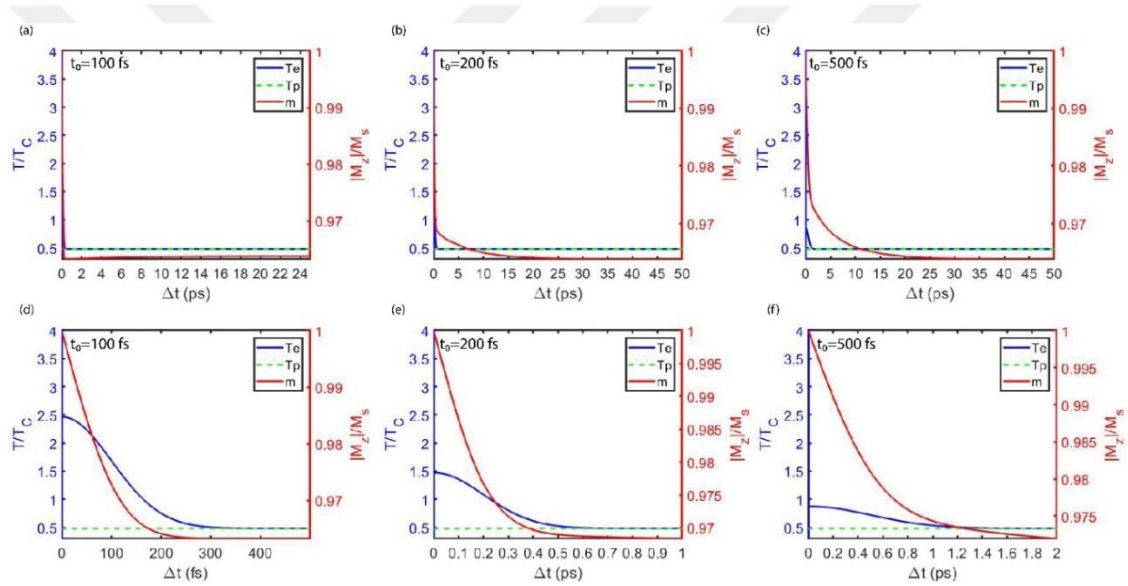

Figure C.9. Magnetization dynamics of 20Å Ni film under 28 mJ·m^{-2} laser pulse fluence of (a) 100 fs (b) 200 fs and (c) 500 fs pulse width. The figures (d)-(f) show the zoomed-in version of the (a)-(c) respectively.

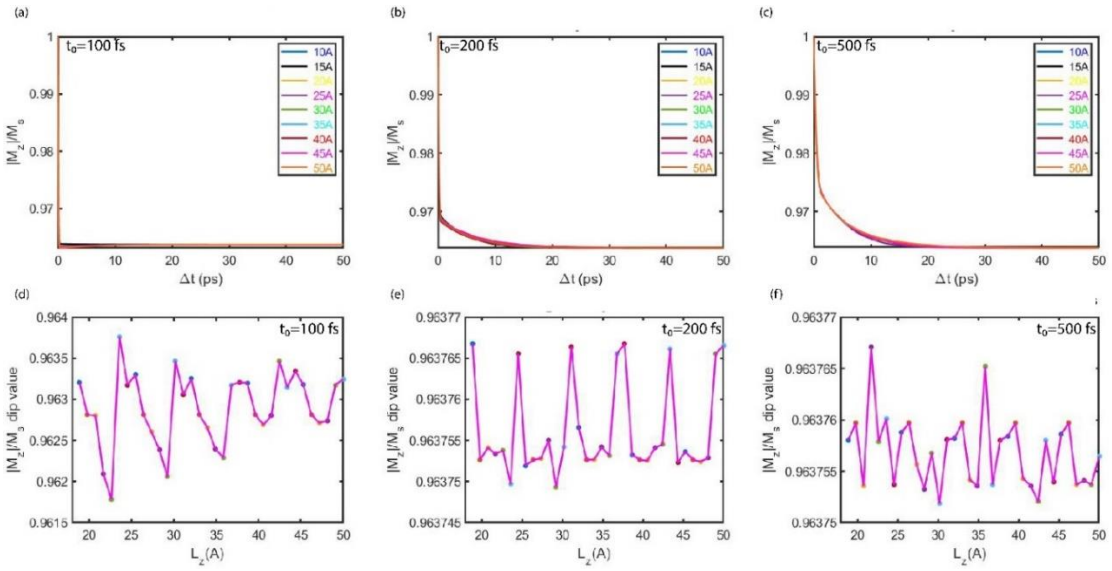

Figure C.10. Thickness dependence of magnetization dynamics of Ni ultrathin film under 28 mJ·m^{-2} laser pulse fluence of (a) 100 fs (b) 200 fs and (c) 500 fs pulse width. The figures (d)-(f) show the magnetization dip values in (a)-(c) respectively.

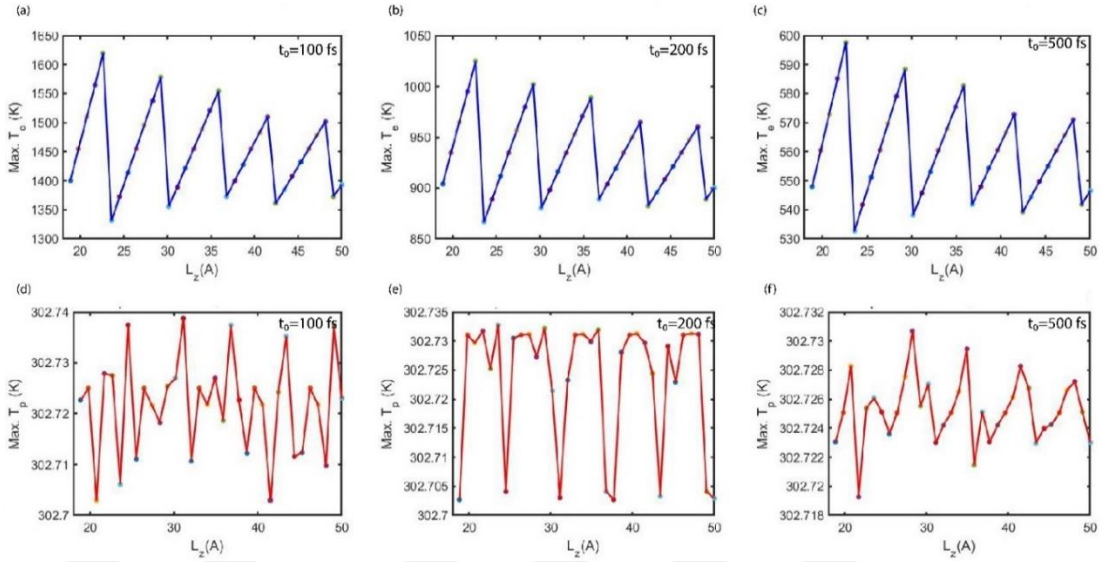

Figure C.11. Thickness dependence of maximum electron temperaturein Ni ultrathin film under 28 mJ·m^{-2} laser pulse fluence of (a) 100 fs (b) 200 fs and (c) 500 fs pulse width. The figures (d)-(f) show the thickness dependence of maximum phonon temperature values for the pulse widths in (a)-(c) respectively.

C.6 Effect of laser pulse fluence on magnetization dynamics, and temporal electron and phonon temperatures

In the laser-driven all-optical switching experiments, not all the incoming laser energy is absorbed by the ultrathin Ni film; we investigate the case of Ni thin films with a few nm thickness, in which only 20% of the incoming laser fluence is absorbed by the thin film and most of it is transmitted through the Ni sample. We have also calculated using incoming laser fluences of 2, 5, 7, and 10 mJ·cm^{-2} (ranges used in the experiments [152, 258, 287]) for both nm-thick Ni film using M3TM model of Koopmans, and quantum confined Ni thin film. The results are shown in Figure C.12.

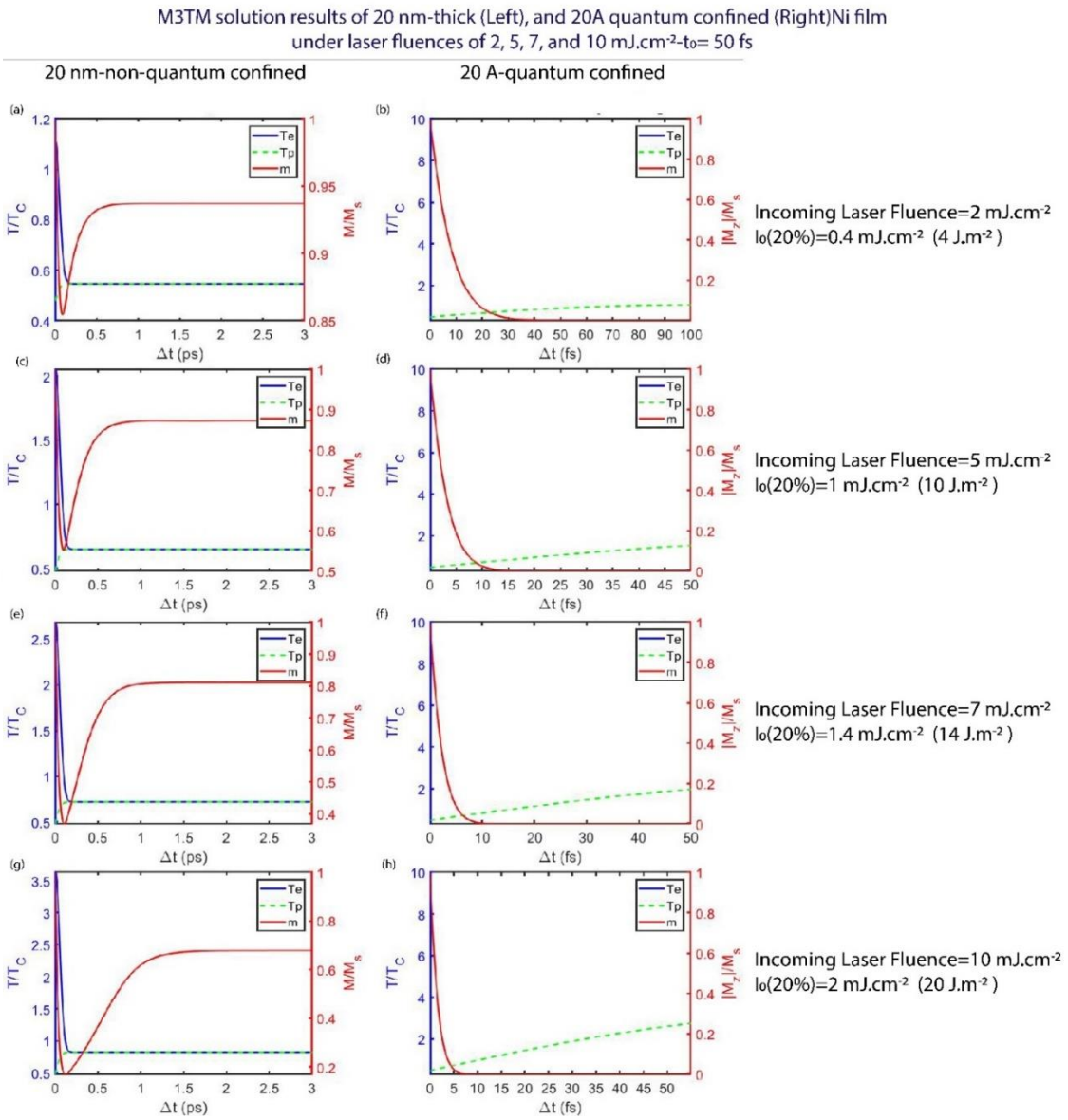

Figure C.12: M3TM solution results of 20 nm-thick (a, c, e, g), and 20 Å quantum-confined (b, d, f, h) Ni film when it absorbs 20% of the incoming laser fluences. Incident laser fluences are (a, b) 0.4 mJ·cm^{-2}, (c, d) 1 mJ·cm^{-2}, (e, f) 1.4 mJ·cm^{-2}, and (g, h) 2 mJ·cm^{-2}. Note that the plots of the quantum confined film (right) are a zoomed-in version (to show the complete thermal demagnetization and T_p exceeding T_C), before the equilibration of electron and phonon temperatures.

The results of Figure C.12 show that using the same experimental parameters for solving M3TM, results in magnetization drop in sub-200 fs and recovery to near 65%-95% of its initial stage in 1-2 ps (depending on the laser fluence). The plots on the right side of Figure C.12 show that, despite the nm-thick Ni film, using similar laser fluences, the lattice temperature exceeds the Curie temperature in the quantum confined 20 Å Ni film and results in complete thermal demagnetization, even before the electron-phonon equilibration (in case the material is not evaporated).

C.7 Effect of laser pulse width on the magnetization dynamics, and temporal electron and phonon temperatures

The effect of the laser pulse duration (width) appears in the incident laser power to the thin film. According to the $P(t) = \frac{P_0}{\sqrt{2\pi}} \exp\left(\frac{-1}{2}\left(\frac{t}{t_0}\right)^2\right)$ formula, by increasing the pulse duration, t_0, the injected laser energy to the thin film decreases which leads to a lower rise in T_e, when the pulse width is higher.

We have shown and compared the results of M3TM both for nm-thick (experimental parameters [83, 89]) and quantum confined Ni film for different pulse widths in fs and ps range, shown in Figures C.13 and C.14 of this appendix, respectively. We show that using the pulse width in sub 500 fs timescales, the sudden rise in the electron temperature is inevitable due to the excess energy concentration and low heat capacity of the electron. The conclusions from Figures C.13 and C.14 are as follows:

1) In the case of illumination with the pulse widths in the picosecond regime, the rise in the electron temperature happens more smoothly.

2) For wider fs laser pulses, the magnetization recovery is suppressed, and magnetism stabilizes after quenching.

3) The timescales of magnetization quenching and recovery increase in the case of wider pulses, which is undesirable for ultrafast manipulation of magnetization.

4) Electron temperature equilibration time increases with increasing the pulse width/duration.

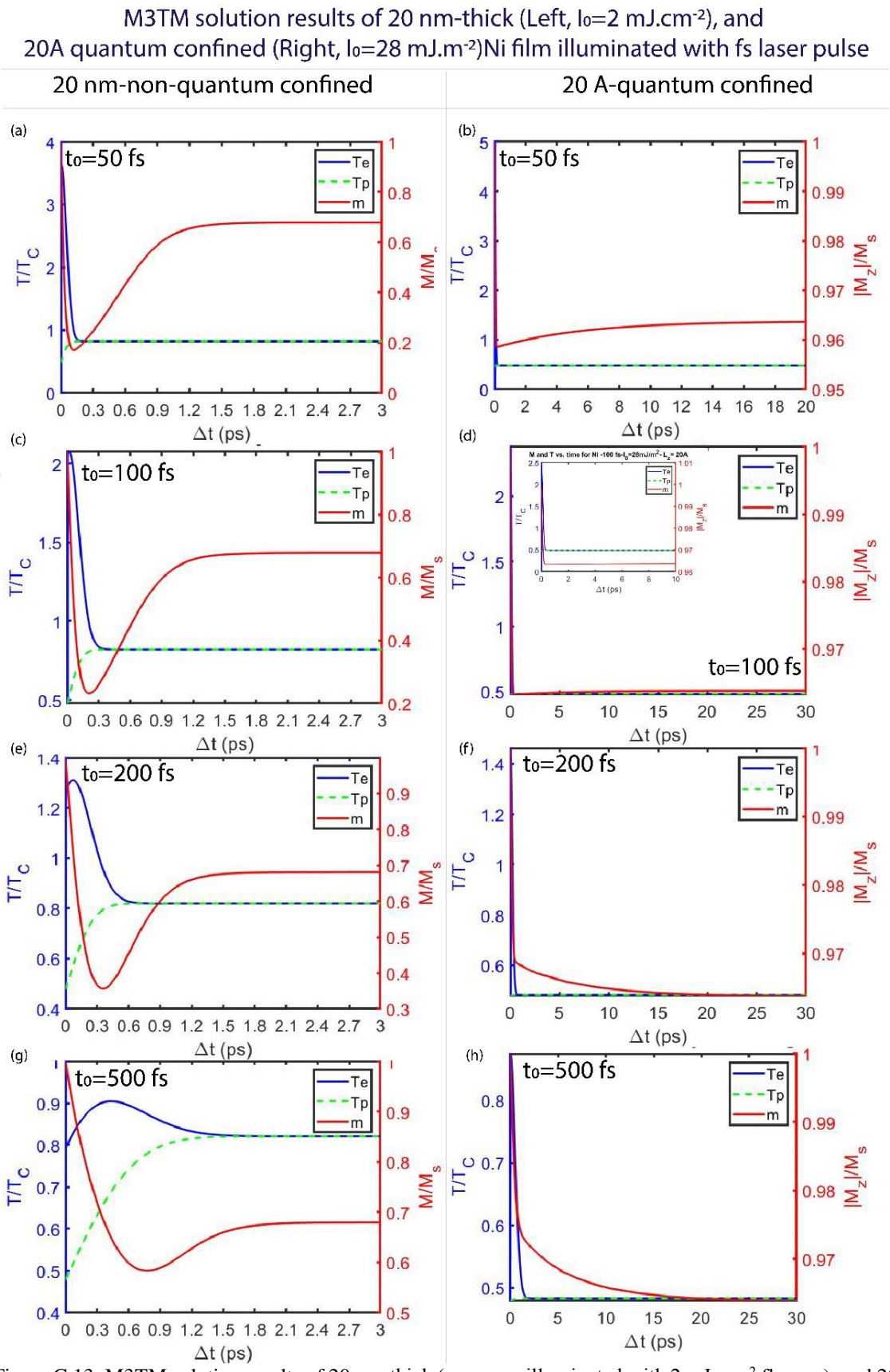

Figure C.13: M3TM solution results of 20 nm-thick (a, c, e, g: illuminated with 2 mJ·cm^{-2} fluence), and 20 Å quantum-confined (b, d, f, h: illuminated with 2 mJ·cm^{-2} fluence) Ni film using a pulse width of (a, b) 50 fs, (c, d) 100 fs, (e, f) 200 fs, and (g, h) 500 fs.

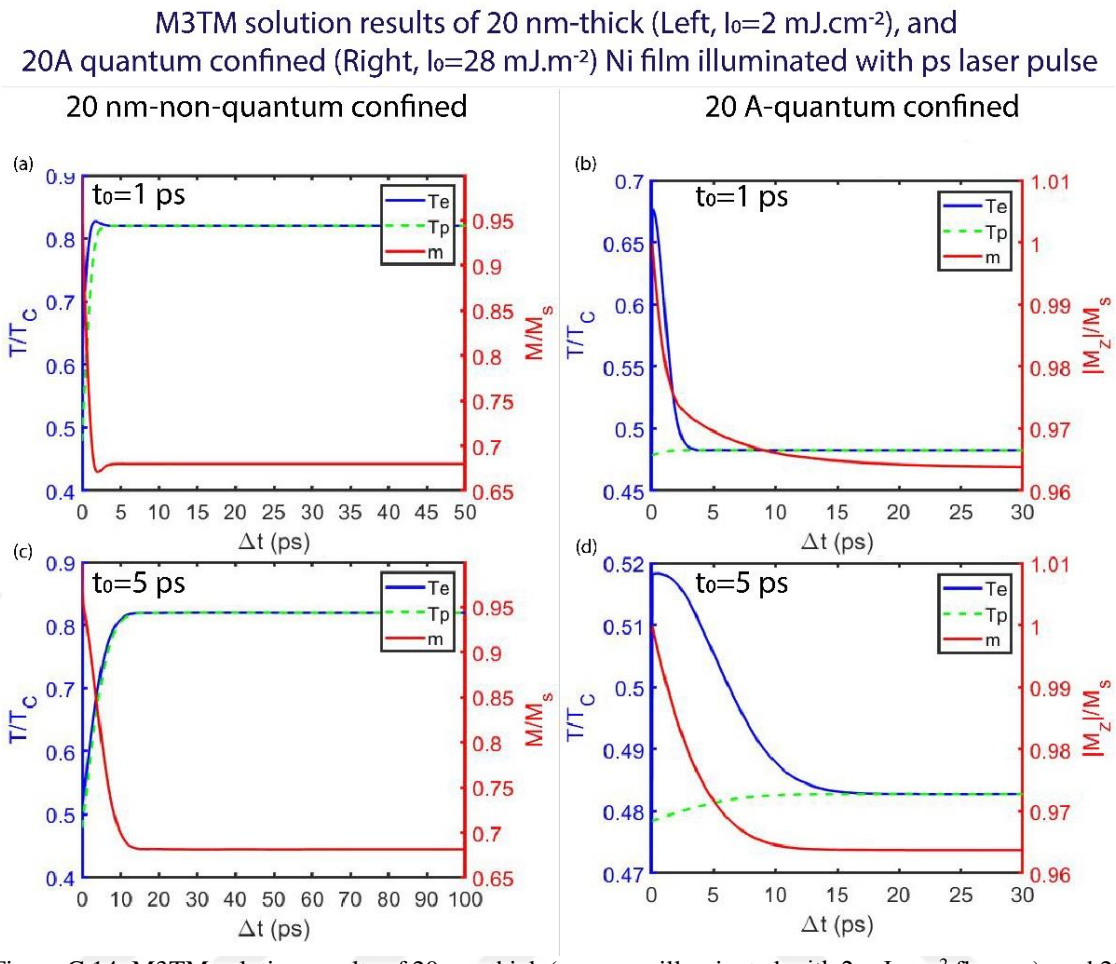

Figure C.14: M3TM solution results of 20 nm-thick (a, c, e, g: illuminated with 2 mJ·cm^{-2} fluence), and 20 Å quantum-confined (b, d, f, h: illuminated with 2 mJ·cm^{-2} fluence) Ni film using a pulse width of (a, b) 1 ps, and (c, d) 5 ps.

APPENDIX D

STRUCTURAL AND MAGNETIC CHARACTERIZATION OFEPITAXIAL YIG AND TmIG FILMS ON GGG (111) SUBSTRATES

This appendix includes the structural and magnetic anisotropy characterization of Yttrium iron garnet (YIG), and Thulium iron garnet (TmIG) grown on GGG (111) single crystalline substrates. X-ray diffraction (XRD) measurement results of YIG and TmIG are shown in Figure D.1. The magnetic hysteresis loop measurements of the samples were done by using vibrating sample magnetometer (VSM), the results of which are shown in Figures D.2 and D.3.

According to Figure D.1a, YIG thin film lattice parameter is calculated based on Bragg's law. The out-of-plane lattice parameter of the YIG thin film shown in Figure D.1a is 12.623 Å, which is greater than the bulk YIG value (12.376 Å). This result shows that the YIG film is stretched out of plane and is under compressive in-plane strain. In Figure D.1b, the out-of-plane lattice parameter of the YIG film, 12.302 Å is smaller than 12.376 Å; so the YIG film is under in-plane tensile strain. Figure D.1c shows the XRD results of the TmIG thin film. According to the TmIG peak position, the out of plain lattice parameter of the TmIG is calculated as 12.369 Å. The bulk lattice parameter of the TmIG is 12.324 Å. Therefore, the TmIG thin film is under compressive strain.

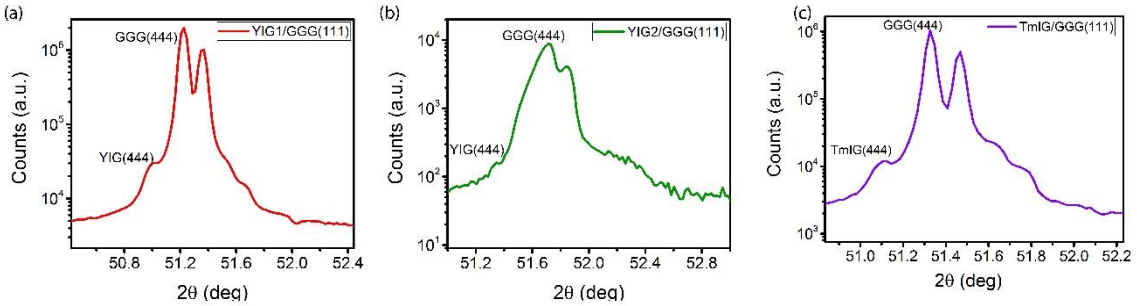

Figure D.1: XRD measurement results of epitaxial (a,b) YIG, and (c) TmIG grown on GGG (111) substrate.

The out of plane lattice parameters of the YIG and TmIG thin films are presented in Table D.1.

Table D.1: Peak positions and out of plane lattice parameters of the YIG and TmIG thin films grown on GGG (111) substrate

Thin film	**YIG I**	**YIG II**	**TmIG**
Peak Position 2Θ (°)	50	51.4	51.1
Lattice Parameter (Å)	12.62	12.30	12.37
Bulk Lattice Parameter	12.37		12.32

The VSM measurements of the TmIG thin film are shown in Figure D.2. According to the magnetic hysteresis loop measurements of the TmIG film (Figure D.2a), the saturation magnetization (M_s) is 70 emu·cm^{-3} and the coercivity (H_c) is 27 Oe, while the applied magnetic field is perpendicular to the film plane. Figure D.2) shows that the in- plane field of 100 Oe cannot saturate the sample properly. The comparison between IP and OP hysteresis loop of the TmIG sample (Figure D.2c) shows that the TmIG films have clear perpendicular magnetic anisotropy.

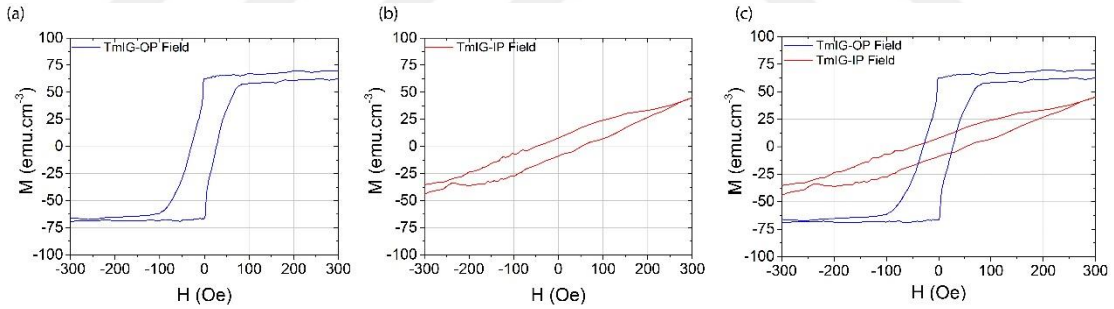

Figure D.2: Magnetic hysteresis loop measurement of TmIG/GGG thin film under (a) out of plane (OP), and (b) in plane (IP) magnetic field. (c) The comparison between the IP and OP field response of the TmIG thin film.

Figure D.3a shows the IP hysteresis loop measurement result of the YIG sample. According to this figure, the YIG film is saturated easily with a field of around 12 Oe up to 156 emu·cm^{-3}. The coercivity value of the YIG thin film under IP magnetic field is very small (H_c < 1 Oe, below or near Gaussmeter magnetic field sensitivity limit). When the applied field is perpendicular to the sample plane (Figure D.3b), an unsaturated minor loop is observed. The coercivity of the YIG sample under OP magnetic field is very large (~15 Oe) compared to that of IP magnetic field. The comparison between IP and OP

hysteresis loops of the YIG sample (Figure D.3c) shows that the YIG film has in-plane magnetic easy axis.

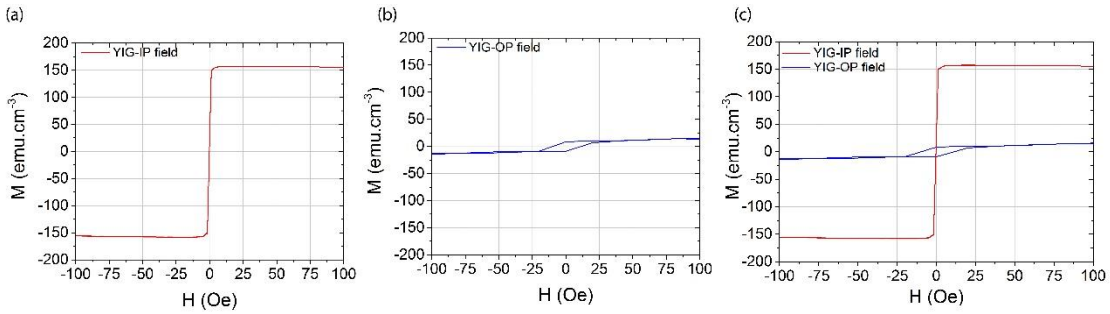

Figure D.3: Magnetic hysteresis loop measurement of YIG/GGG thin film under (a) in-plane (IP), and (b) out-of-plane (OP) magnetic field. (c) The IP and OP field hysteresis loops of the YIG film are compared.

The VSM results of YIG and TMIG are presented in Table D.2.

Table D.2: Magnetic hysteresis loop measurement results of TmIG and YIG under IP and OP applied magnetic field

Thin Film	**Magnetic Field Orientation**	**H_c (Oe)**	**M_s (emu/cm^3)**	**M_r (emu/cm^3)**	**H_s (Oe)**
TmIG	IP	51	No Saturation	~10	No Saturation
	OP	27	70	~1	<10
YIG	IP	0	156	~1	12
	OP	11.5	15	<12	15

BIBLIOGRAPHY

[1] S. M. Yakout, "Spintronics: Future Technology for New Data Storage and Communication Devices," *Journal of Superconductivity and Novel Magnetism,* vol. 33, pp. 2557-2580, 2020.

[2] H. Kaeslin, *Top-down digital VLSI design: from architectures to gate-level circuits and FPGAs*: Morgan Kaufmann, 2014.

[3] D. L. Shinder and M. Cross, *Scene of the Cybercrime*: Elsevier, 2008.

[4] T. Datta-Chaudhuri, P. Abshire, and E. Smela, "Packaging commercial CMOS chips for lab on a chip integration," *Lab on a Chip,* vol. 14, pp. 1753-1766, 2014.

[5] R. Comstock, "Review modern magnetic materials in data storage," *Journal of Materials Science: Materials in Electronics,* vol. 13, pp. 509-523, 2002.

[6] J. S. Meena, S. M. Sze, U. Chand, and T.-Y. Tseng, "Overview of emerging nonvolatile memory technologies," *Nanoscale research letters,* vol. 9, pp. 1-33, 2014.

[7] T. Welsh and M. Wright, *Information literacy in the digital age: An evidence-based approach*: Elsevier, 2010.

[8] S. Bhatti, R. Sbiaa, A. Hirohata, H. Ohno, S. Fukami, and S. Piramanayagam, "Spintronics based random access memory: a review," *Materials Today,* vol. 20, pp. 530-548, 2017.

[9] W. Liu, P. K. J. Wong, and Y. Xu, "Hybrid spintronic materials: Growth, structure and properties," *Progress in Materials Science,* vol. 99, pp. 27-105, 2019.

[10] V. K. Joshi, "Spintronics: A contemporary review of emerging electronics devices," *Engineering science and technology, an international journal,* vol. 19, pp. 1503-1513, 2016.

[11] S. C. Ray, *Magnetism and spintronics in carbon and carbon nanostructured materials*: Elsevier, 2020.

[12] J. Lu, E. Chen, M. Kabir, M. Stan, and S. Wolf, "Spintronics technology: past, present and future," *International Materials Reviews,* vol. 61, pp. 456-472, 2016.

[13] V. L. Kalyani and V. Agrawal, "Spintronics—a vision for future in electronics and computers," *J. Manag. Eng. Inf. Technol,* vol. 2, pp. 30-36, 2015.

[14] A. El-Ghazaly, J. Gorchon, R. B. Wilson, A. Pattabi, and J. Bokor, "Progress towards ultrafast spintronics applications," *Journal of Magnetism and Magnetic Materials,* vol. 502, p. 166478, 2020.

[15] S. D. Sarma, "Spintronics: A new class of device based on electron spin, rather than on charge, may yield the next generation of microelectronics," *American Scientist,* vol. 89, pp. 516-523, 2001.

[16] J. Puebla, J. Kim, K. Kondou, and Y. Otani, "Spintronic devices for energy-efficient data storage and energy harvesting," *Communications Materials,* vol. 1, pp. 1-9, 2020.

[17] J. Ferrer and V. M. Garcia-Suarez, "From microelectronics to molecular spintronics: an explorer's travelling guide," *Journal of Materials Chemistry,* vol. 19, pp. 1696-1717, 2009.

[18] M. N. Baibich, J. M. Broto, A. Fert, F. N. Van Dau, F. Petroff, P. Etienne*, et al.*, "Giant magnetoresistance of (001) Fe/(001) Cr magnetic superlattices," *Physical review letters,* vol. 61, p. 2472, 1988.

[19] G. Binasch, P. Grünberg, F. Saurenbach, and W. Zinn, "Enhanced magnetoresistance in layered magnetic structures with antiferromagnetic interlayer exchange," *Physical review B,* vol. 39, p. 4828, 1989.

[20] H. Zabel, "Progress in spintronics," *Superlattices and microstructures,* vol. 46, pp. 541-553, 2009.

[21] A. Fert, "Origin, development, and future of spintronics (Nobel lecture)," *Angewandte Chemie International Edition,* vol. 47, pp. 5956-5967, 2008.

[22] W. P. McCray, "How spintronics went from the lab to the iPod," *Nature nanotechnology,* vol. 4, pp. 2-4, 2009.

[23] S. V. Garimella, T. Persoons, J. Weibel, and L.-T. Yeh, "Technological drivers in data centers and telecom systems: Multiscale thermal, electrical, and energy management," *Applied energy,* vol. 107, pp. 66-80, 2013.

[24] P. Corcoran and A. Andrae, "Emerging trends in electricity consumption for consumer ICT," *National University of Ireland, Galway, Connacht, Ireland, Tech. Rep,* 2013.

[25] A. S. Andrae and T. Edler, "On global electricity usage of communication technology: trends to 2030," *Challenges,* vol. 6, pp. 117-157, 2015.

[26] C. Pan and A. Naeemi, "Nonvolatile spintronic memory array performance benchmarking based on three-terminal memory cell," *IEEE Journal on Exploratory Solid-State Computational Devices and Circuits,* vol. 3, pp. 10-17, 2017.

[27] S. Yuasa, T. Nagahama, A. Fukushima, Y. Suzuki, and K. Ando, "Giant room-temperature magnetoresistance in single-crystal Fe/MgO/Fe magnetic tunnel junctions," *Nature materials,* vol. 3, pp. 868-871, 2004.

[28] J. C. Slonczewski, "Current-driven excitation of magnetic multilayers," *Journal of Magnetism and Magnetic Materials,* vol. 159, pp. L1-L7, 1996.

[29] J. Katine, F. Albert, R. Buhrman, E. Myers, and D. Ralph, "Current-driven magnetization reversal and spin-wave excitations in Co/Cu/Co pillars," *Physical review letters,* vol. 84, p. 3149, 2000.

[30] D. C. Ralph and M. D. Stiles, "Spin transfer torques," *Journal of Magnetism and Magnetic Materials,* vol. 320, pp. 1190-1216, 2008.

[31] S. Ikeda, K. Miura, H. Yamamoto, K. Mizunuma, H. Gan, M. Endo*, et al.*, "A perpendicular-anisotropy CoFeB–MgO magnetic tunnel junction," *Nature materials,* vol. 9, pp. 721-724, 2010.

[32] H. Liu, D. Bedau, D. Backes, J. Katine, J. Langer, and A. Kent, "Ultrafast switching in magnetic tunnel junction based orthogonal spin transfer devices," *Applied Physics Letters,* vol. 97, p. 242510, 2010.

[33] K. Garello, C. O. Avci, I. M. Miron, M. Baumgartner, A. Ghosh, S. Auffret*, et al.*, "Ultrafast magnetization switching by spin-orbit torques," *Applied Physics Letters,* vol. 105, p. 212402, 2014.

[34] Y. Otani, M. Shiraishi, A. Oiwa, E. Saitoh, and S. Murakami, "Spin conversion on the nanoscale," *Nature Physics,* vol. 13, pp. 829-832, 2017.

[35] A. Mellnik, J. Lee, A. Richardella, J. Grab, P. Mintun, M. H. Fischer*, et al.*, "Spin-transfer torque generated by a topological insulator," *Nature,* vol. 511, pp. 449-451, 2014.

[36] Y. Fan, P. Upadhyaya, X. Kou, M. Lang, S. Takei, Z. Wang*, et al.*, "Magnetization switching through giant spin–orbit torque in a magnetically doped topological insulator heterostructure," *Nature materials,* vol. 13, pp. 699-704, 2014.

[37] L. Liu, C.-F. Pai, Y. Li, H. Tseng, D. Ralph, and R. Buhrman, "Spin-torque switching with the giant spin Hall effect of tantalum," *Science,* vol. 336, pp. 555-558, 2012.

[38] H. Yamahara, M. Mikami, M. Seki, and H. Tabata, "Epitaxial strain-induced magnetic anisotropy in Sm3Fe5O12 thin films grown by pulsed laser deposition," *Journal of Magnetism and Magnetic Materials,* vol. 323, pp. 3143-3146, 2011.

[39] C. Li, Z. Zang, W. Chen, Z. Hu, X. Tang, W. Hu*, et al.*, "Highly pure green light emission of perovskite CsPbBr 3 quantum dots and their application for green light-emitting diodes," *Optics express,* vol. 24, pp. 15071-15078, 2016.

[40] E. R. Rosenberg, L. Beran, C. O. Avci, C. Zeledon, B. Song, C. Gonzalez-Fuentes*, et al.*, "Magnetism and spin transport in rare-earth-rich epitaxial terbium and europium iron garnet films," *Physical Review Materials,* vol. 2, p. 094405, 2018.

[41] C. O. Avci, A. Quindeau, C.-F. Pai, M. Mann, L. Caretta, A. S. Tang*, et al.*, "Current-induced switching in a magnetic insulator," *Nature materials,* vol. 16, p. 309, 2017.

[42] A. Chumak, V. Vasyuchka, A. Serga, and B. Hillebrands, "Magnon spintronics," *Nature Physics,* vol. 11, p. 453, 2015.

[43] M. Onbasli, A. Kehlberger, D. Kim, G. Jakob, M. Kläui, A. Chumak*, et al.*, "Pulsed laser deposition of epitaxial yttrium iron garnet films with low Gilbert damping and bulk-like magnetization," *APL Materials,* vol. 2, p. 106102, 2014.

[44] A. Serga, A. Chumak, and B. Hillebrands, "YIG magnonics," *Journal of Physics D: Applied Physics,* vol. 43, p. 264002, 2010.

[45] C. O. Avci, E. Rosenberg, L. Caretta, F. Büttner, M. Mann, C. Marcus*, et al.*, "Interface-driven chiral magnetism and current-driven domain walls in insulating magnetic garnets," *Nature nanotechnology,* p. 1, 2019.

[46] A. Kalashnikova, V. Pavlov, A. Kimel, A. Kirilyuk, T. Rasing, and R. Pisarev, "Magneto-optical study of holmium iron garnet Ho3Fe5O12," *Low Temperature Physics,* vol. 38, pp. 863-869, 2012.

[47] M. Kubota, A. Tsukazaki, F. Kagawa, K. Shibuya, Y. Tokunaga, M. Kawasaki*, et al.*, "Stress-induced perpendicular magnetization in epitaxial iron garnet thin films," *Applied Physics Express,* vol. 5, p. 103002, 2012.

[48] H. Maier-Flaig, S. Geprägs, Z. Qiu, E. Saitoh, R. Gross, M. Weiler*, et al.*, "Perpendicular magnetic anisotropy in insulating ferrimagnetic gadolinium iron garnet thin films," *arXiv preprint arXiv:1706.08488,* 2017.

[49] C. Tang, C.-Z. Chang, G. Zhao, Y. Liu, Z. Jiang, C.-X. Liu*, et al.*, "Above 400-K robust perpendicular ferromagnetic phase in a topological insulator," *Science Advances,* vol. 3, p. e1700307, 2017.

[50] H. Wang, C. Du, P. C. Hammel, and F. Yang, "Strain-tunable magnetocrystalline anisotropy in epitaxial Y 3 Fe 5 O 12 thin films," *Physical Review B,* vol. 89, p. 134404, 2014.

[51] J. D. Adam, L. E. Davis, G. F. Dionne, E. F. Schloemann, and S. N. Stitzer, "Ferrite devices and materials," *IEEE Transactions on Microwave Theory and Techniques,* vol. 50, pp. 721-737, 2002.

[52] B. Calhoun, J. Overmeyer, and W. Smith, "Ferrimagnetic Resonance in Gadolinium Iron Garnet," *Physical Review,* vol. 107, p. 993, 1957.

[53] G. F. Dionne, "Molecular Field and Exchange Constants of Gd3+-Substituted Ferrimagnetic Garnets," *Journal of Applied Physics,* vol. 42, pp. 2142-2143, 1971.

[54] S. Geprägs, A. Kehlberger, F. Della Coletta, Z. Qiu, E.-J. Guo, T. Schulz*, et al.*, "Origin of the spin Seebeck effect in compensated ferrimagnets," *Nature communications,* vol. 7, p. 10452, 2016.

[55] V. Lauer, M. Schneider, T. Meyer, T. Brächer, P. Pirro, B. Heinz*, et al.*, "Temporal evolution of auto-oscillations in an yttrium-iron-garnet/platinum microdisk driven by pulsed spin Hall effect-induced spin-transfer torque," *IEEE Magnetics Letters,* vol. 8, pp. 1-4, 2017.

[56] M. Evelt, C. Safranski, M. Aldosary, V. Demidov, I. Barsukov, A. Nosov*, et al.*, "Spin Hall-induced auto-oscillations in ultrathin YIG grown on Pt," *Scientific reports,* vol. 8, p. 1269, 2018.

[57] G. E. Bauer, E. Saitoh, and B. J. Van Wees, "Spin caloritronics," *Nature materials,* vol. 11, p. 391, 2012.

[58] L. Cornelissen, J. Liu, R. Duine, J. B. Youssef, and B. Van Wees, "Long-distance transport of magnon spin information in a magnetic insulator at room temperature," *Nature Physics,* vol. 11, p. 1022, 2015.

[59] X. Y. Sun, Q. Du, T. Goto, M. C. Onbasli, D. H. Kim, N. M. Aimon*, et al.*, "Single-step deposition of cerium-substituted yttrium iron garnet for monolithic on-chip optical isolation," *Acs Photonics,* vol. 2, pp. 856-863, 2015.

[60] J. Walowski and M. Münzenberg, "Perspective: Ultrafast magnetism and THz spintronics," *Journal of applied Physics,* vol. 120, p. 140901, 2016.

[61] W. Han, Y. Otani, and S. Maekawa, "Quantum materials for spin and charge conversion," *NPJ Quantum Materials,* vol. 3, p. 27, 2018.

[62] Q. Du, T. Fakhrul, Y. Zhang, J. Hu, and C. A. Ross, "Monolithic magneto-optical oxide thin films for on-chip optical isolation," *MRS Bulletin,* vol. 43, pp. 413-418, 2018.
[63] T. Mizumoto, R. Baets, and J. E. Bowers, "Optical nonreciprocal devices for silicon photonics using wafer-bonded magneto-optical garnet materials," *MRS Bulletin,* vol. 43, pp. 419-424, 2018.
[64] S. Mokarian Zanjani and M. C. Onbaşlı, "Predicting new iron garnet thin films with perpendicular magnetic anisotropy," *Journal of Magnetism and Magnetic Materials,* vol. 499, p. 166108, 2020/04/01/ 2020.
[65] S. M. Zanjani and M. C. Onbasli, "Thin film rare earth iron garnets with perpendicular magnetic anisotropy for spintronic applications," *AIP Advances,* vol. 9, p. 035024, 2019/03/01 2019.
[66] M. Guillot, A. Marchand, F. Tcheou, and H. Le Gall, "Magnetic properties on holmium iron garnet in high magnetic field. Optical absorption spectra in the infra-red region," *Zeitschrift für Physik B Condensed Matter,* vol. 49, pp. 221-228, 1982/09/01 1982.
[67] A. J. Di Pasqua, K. J. Balkus Jr, I. S. Munaweera, and Y. Shi, "Iron garnet nanoparticles for cancer radiotherapy and chemotherapy," ed: Google Patents, 2019.
[68] M. M. Selvi, D. Chakraborty, and C. Venkateswaran, "Magnetodielectric coupling in multiferroic holmium iron garnets," *Journal of Magnetism and Magnetic Materials,* vol. 423, pp. 39-45, 2017.
[69] J. Scott, "Multiferroic memories," *Nature materials,* vol. 6, pp. 256-257, 2007.
[70] W. Eerenstein, N. Mathur, and J. F. Scott, "Multiferroic and magnetoelectric materials," *nature,* vol. 442, pp. 759-765, 2006.
[71] N. Hur, S. Park, P. Sharma, S. Guha, and S.-W. Cheong, "Colossal Magnetodielectric Effects in D y M n 2 O 5," *Physical review letters,* vol. 93, p. 107207, 2004.
[72] N. A. Spaldin and M. Fiebig, "The renaissance of magnetoelectric multiferroics," *Science,* vol. 309, pp. 391-392, 2005.
[73] H. Schmid, "Multi-ferroic magnetoelectrics," *Ferroelectrics,* vol. 162, pp. 317-338, 1994.
[74] G. Catalan and J. F. Scott, "Physics and applications of bismuth ferrite," *Advanced materials,* vol. 21, pp. 2463-2485, 2009.
[75] M. Fiebig, "Revival of the magnetoelectric effect," *Journal of physics D: applied physics,* vol. 38, p. R123, 2005.
[76] P. Larsen and R. Metselaar, "Electrical properties of yttrium iron garnet at high temperatures," *Physical Review B,* vol. 14, p. 2520, 1976.
[77] N. Hur, S. Park, S. Guha, A. Borissov, V. Kiryukhin, and S.-W. Cheong, "Low-field magnetodielectric effect in terbium iron garnets," *Applied Physics Letters,* vol. 87, p. 042901, 2005.
[78] J. Su, X. Lu, C. Zhang, J. Zhang, H. Sun, C. Ju*, et al.*, "Study on dielectric and magnetic properties of H03Fe5O12 ceramics," *Physica B: Condensed Matter,* vol. 407, pp. 485-488, 2012.
[79] A. Kirilyuk, A. V. Kimel, and T. Rasing, "Ultrafast optical manipulation of magnetic order," *Reviews of Modern Physics,* vol. 82, pp. 2731-2784, 09/22/ 2010.
[80] J. Åkerman, "Toward a universal memory," *Science,* vol. 308, pp. 508-510, 2005.
[81] K. Jhuria, J. Hohlfeld, A. Pattabi, E. Martin, A. Y. A. Córdova, X. Shi*, et al.*, "Spin–orbit torque switching of a ferromagnet with picosecond electrical pulses," *Nature Electronics,* vol. 3, pp. 680-686, 2020.
[82] F. Hellman, A. Hoffmann, Y. Tserkovnyak, G. S. Beach, E. E. Fullerton, C. Leighton*, et al.*, "Interface-induced phenomena in magnetism," *Reviews of modern physics,* vol. 89, p. 025006, 2017.

[83] B. Koopmans, G. Malinowski, F. Dalla Longa, D. Steiauf, M. Fähnle, T. Roth*, et al.*, "Explaining the paradoxical diversity of ultrafast laser-induced demagnetization," *Nature materials,* vol. 9, pp. 259-265, 2010.
[84] M. Vomir, M. Albrecht, and J.-Y. Bigot, "Single shot all optical switching of intrinsic micron size magnetic domains of a Pt/Co/Pt ferromagnetic stack," *Applied Physics Letters,* vol. 111, p. 242404, 2017.
[85] G. Kichin, M. Hehn, J. Gorchon, G. Malinowski, J. Hohlfeld, and S. Mangin, "From multiple-to single-pulse all-optical helicity-dependent switching in ferromagnetic Co/Pt multilayers," *Physical Review Applied,* vol. 12, p. 024019, 2019.
[86] A. Schellekens, K. Kuiper, R. De Wit, and B. Koopmans, "Ultrafast spin-transfer torque driven by femtosecond pulsed-laser excitation," *Nature communications,* vol. 5, pp. 1-7, 2014.
[87] M. Lalieu, R. Lavrijsen, R. Duine, and B. Koopmans, "Investigating optically excited terahertz standing spin waves using noncollinear magnetic bilayers," *Physical Review B,* vol. 99, p. 184439, 2019.
[88] M. L. Lalieu, R. Lavrijsen, and B. Koopmans, "Integrating all-optical switching with spintronics," *Nature communications,* vol. 10, pp. 1-6, 2019.
[89] E. Beaurepaire, J. C. Merle, A. Daunois, and J. Y. Bigot, "Ultrafast Spin Dynamics in Ferromagnetic Nickel," *Physical Review Letters,* vol. 76, pp. 4250-4253, 05/27/ 1996.
[90] K. Carva, P. Baláž, and I. Radu, "Laser-induced ultrafast magnetic phenomena," *Handbook of magnetic materials,* vol. 26, pp. 291-463, 2017.
[91] J.-Y. Bigot and M. Vomir, "Ultrafast magnetization dynamics of nanostructures," *Annalen der Physik,* vol. 525, pp. 2-30, 2013/02/01 2013.
[92] S. Iida, "Magnetostriction Constants of Rare Earth Iron Garnets," *Journal of the Physical Society of Japan,* vol. 22, pp. 1201-1209, 1967/05/15 1967.
[93] S. Nolte, C. Momma, H. Jacobs, A. Tünnermann, B. N. Chichkov, B. Wellegehausen*, et al.*, "Ablation of metals by ultrashort laser pulses," *JOSA B,* vol. 14, pp. 2716-2722, 1997.
[94] A. M. Prokhorov, *Laser heating of metals*: CRC Press, 2018.
[95] S. Geller and M. Gilleo, "Structure and ferrimagnetism of yttrium and rare-earth–iron garnets," *Acta Crystallographica,* vol. 10, pp. 239-239, 1957.
[96] S. Geller and M. Gilleo, "The crystal structure and ferrimagnetism of yttrium-iron garnet, Y3Fe2 (FeO4) 3," *Journal of Physics and Chemistry of solids,* vol. 3, pp. 30-36, 1957.
[97] F. B. Hagedorn, W. J. Tabor, and L. G. Van Uitert, "Growth-induced magnetic anisotropy in seven different mixed rare-earth iron garnets," *Journal of Applied Physics,* vol. 44, pp. 432-437, 1973/01/01 1973.
[98] R. Nakamoto, B. Xu, C. Xu, H. Xu, and L. Bellaiche, "Properties of rare-earth iron garnets from first principles," *Physical Review B,* vol. 95, p. 024434, 2017.
[99] C. N. Wu, C. C. Tseng, Y. T. Fanchiang, C. K. Cheng, K. Y. Lin, S. L. Yeh*, et al.*, "High-quality thulium iron garnet films with tunable perpendicular magnetic anisotropy by off-axis sputtering – correlation between magnetic properties and film strain," *Scientific Reports,* vol. 8, p. 11087, 2018/07/23 2018.
[100] O. Ciubotariu, A. Semisalova, K. Lenz, and M. Albrecht, "Strain-induced perpendicular magnetic anisotropy and Gilbert damping of Tm3Fe5O12 thin films," *Scientific Reports,* vol. 9, p. 17474, 2019/11/25 2019.
[101] G. F. Dionne, *Magnetic oxides* vol. 14: Springer, 2009.
[102] S. M. Wu, J. E. Pearson, and A. Bhattacharya, "Paramagnetic spin Seebeck effect," *Physical Review Letters,* vol. 114, p. 186602, 2015.
[103] B. T. Zhou, K. Taguchi, Y. Kawaguchi, Y. Tanaka, and K. T. Law, "Spin-orbit coupling induced valley Hall effects in transition-metal dichalcogenides," *Communications Physics,* vol. 2, pp. 1-7, 2019.

[104] C. O. Avci, E. Rosenberg, M. Baumgartner, L. Beran, A. Quindeau, P. Gambardella*, et al.*, "Fast switching and signature of efficient domain wall motion driven by spin-orbit torques in a perpendicular anisotropy magnetic insulator/Pt bilayer," *Applied Physics Letters,* vol. 111, p. 072406, 2017.

[105] M. Imai, H. Chudo, M. Ono, K. Harii, M. Matsuo, Y. Ohnuma*, et al.*, "Angular momentum compensation manipulation to room temperature of the ferrimagnet H03− x Dy x Fe5O12 detected by the Barnett effect," *Applied Physics Letters,* vol. 114, p. 162402, 2019.

[106] L. Soumah, N. Beaulieu, L. Qassym, C. Carrétéro, E. Jacquet, R. Lebourgeois*, et al.*, "Ultra-low damping insulating magnetic thin films get perpendicular," *Nature communications,* vol. 9, pp. 1-6, 2018.

[107] N. Zhu, H. Chang, A. Franson, T. Liu, X. Zhang, E. Johnston-Halperin*, et al.*, "Patterned growth of crystalline Y3Fe5O12 nanostructures with engineered magnetic shape anisotropy," *Applied Physics Letters,* vol. 110, p. 252401, 2017.

[108] B. Heinrich and J. F. Cochran, "Magnetic ultrathin films," *Handbook of Magnetism and Advanced Magnetic Materials,* 2007.

[109] R. Eason, *Pulsed laser deposition of thin films: applications-led growth of functional materials*: John Wiley & Sons, 2007.

[110] H. Jenniches, J. Shen, C. V. Mohan, S. S. Manoharan, J. Barthel, P. Ohresser*, et al.*, "Structure and magnetism of pulsed-laser-deposited ultrathin films of Fe on Cu (100)," *Physical Review B,* vol. 59, p. 1196, 1999.

[111] M. Bellardita, A. Di Paola, S. Yurdakal, and L. Palmisano, "Preparation of Catalysts and Photocatalysts Used for Similar Processes," in *Heterogeneous Photocatalysis*, ed: Elsevier, 2019, pp. 25-56.

[112] M. Zharnikov, A. Dittschar, W. Kuch, C. Schneider, and J. Kirschner, "Interplay between structure and magnetism in Fe/Cu (1 0 0) upon temperature variation," *Journal of magnetism and magnetic materials,* vol. 174, pp. 40-56, 1997.

[113] P. Ohresser, J. Shen, J. Barthel, M. Zheng, C. V. Mohan, M. Klaua*, et al.*, "Growth, structure, and magnetism of fcc Fe ultrathin films on Cu (111) by pulsed laser deposition," *Physical Review B,* vol. 59, p. 3696, 1999.

[114] Q. Zhang, D. Sando, and V. Nagarajan, "Chemical route derived bismuth ferrite thin films and nanomaterials," *Journal of Materials Chemistry C,* vol. 4, pp. 4092-4124, 2016.

[115] H. J. Scheel, "Introduction to liquid phase epitaxy," *Liquid Phase Epitaxy of Electronic, Optical and Optoelectronic Materials,* vol. 19, 2007.

[116] I. Nistor, "Development of magnetic field sensors using Bismuth-substituted garnets thin films with in-plane magnetization," 2006.

[117] M. Guillot, H. Le Gall, J. Gouzerh, J. Desvignes, and M. Artinian, "Bi–DyIG films: Enhancement of the Dy contribution to the Faraday rotation," *Journal of applied physics,* vol. 79, pp. 5932-5934, 1996.

[118] F. Starecki, W. Bolaños, G. Brasse, A. Benayad, M. Morales, J.-L. Doualan*, et al.*, "Rare earth doped LiYF4 single crystalline films grown by liquid phase epitaxy for the fabrication of planar waveguide lasers," *Journal of crystal growth,* vol. 401, pp. 537-541, 2014.

[119] R. Kingi, Y. Wang, S. J. Fonash, O. Awadelkarim, and J. Mehlhaff, "Comparison between rapid thermal and furnace annealing for a-Si solid phase crystallization," *MRS Online Proceedings Library Archive,* vol. 424, 1996.

[120] https://www.slideshare.net/HotLookingCoolGuy/sputtering-process

[121] A. J. Ptak, "Principles of molecular beam epitaxy," in *Handbook of Crystal Growth*, ed: Elsevier, 2015, pp. 161-192.

[122] https://www.openpr.com/news/2138968/global-molecular-beam-epitaxy-mbe-market-expected-to-witness

[123] Ü. Özgür, Y. Alivov, and H. Morkoç, "Microwave ferrites, part 1: fundamental properties," *Journal of Materials Science: Materials in Electronics,* vol. 20, pp. 789-834, 2009.

[124] Ü. Özgür, Y. Alivov, and H. Morkoç, "Microwave ferrites, part 2: passive components and electrical tuning," *Journal of Materials Science: Materials in Electronics,* vol. 20, pp. 911-952, 2009.
[125] J. Pesek and M. Matyska, "Spectroscopic characterization of chemically modified oxide surfaces," in *Studies in Surface Science and Catalysis*. vol. 120, ed: Elsevier, 1999, pp. 117-142.
[126] A. Passian and G. Siopsis, "Quantum state atomic force microscopy," *Physical Review A,* vol. 95, p. 043812, 2017.
[127] B. J. Inkson, "2 - Scanning electron microscopy (SEM) and transmission electron microscopy (TEM) for materials characterization," in *Materials Characterization Using Nondestructive Evaluation (NDE) Methods*, G. Hübschen, I. Altpeter, R. Tschuncky, and H.-G. Herrmann, Eds., ed: Woodhead Publishing, 2016, pp. 17-43.
[128] Y. Yan, "7 - Tribology and tribo-corrosion testing and analysis of metallic biomaterials," in *Metals for Biomedical Devices*, M. Niinomi, Ed., ed: Woodhead Publishing, 2010, pp. 178-201.
[129] A. S. Ali, "Application of nanomaterials in environmental improvement," in *Nanotechnology and the Environment*, ed: IntechOpen, 2020.
[130] S. J. Pennycook, "Transmission electron microscopy," 2005.
[131] T. Khare, U. Oak, V. Shriram, S. K. Verma, and V. Kumar, "Chapter Ten - Biologically synthesized nanomaterials and their antimicrobial potentials," in *Comprehensive Analytical Chemistry*. vol. 87, S. K. Verma and A. K. Das, Eds., ed: Elsevier, 2019, pp. 263-289.
[132] C. Suchomski, C. Reitz, C. T. Sousa, J. P. Araujo, and T. Brezesinski, "Room temperature magnetic rare-earth iron garnet thin films with ordered mesoporous structure," *Chemistry of Materials,* vol. 25, pp. 2527-2537, 2013.
[133] M. Rafique, "Study of the Magnetoelectric Properties of Multiferroic Thin Films and Composites for Device Applications," COMSATS Institute of Information Technology, Islamabad-Pakistan, 2014.
[134] F. E. Luborsky, J. D. Livingston, and G. Y. Chin†, "CHAPTER 29 - MAGNETIC PROPERTIES OF METALS AND ALLOYS," in *Physical Metallurgy (Fourth Edition)*, R. W. Cahn and P. Haasen†, Eds., ed Oxford: North-Holland, 1996, pp. 2501-2565.
[135] M. Getzlaff, *Fundamentals of magnetism*: Springer Science & Business Media, 2007.
[136] P. Gruszecki, C. Banerjee, M. Mruczkiewicz, O. Hellwig, A. Barman, and M. Krawczyk, "Chapter Two - The influence of the internal domain wall structure on spin wave band structure in periodic magnetic stripe domain patterns," in *Solid State Physics*. vol. 70, R. L. Stamps and H. Schultheiß, Eds., ed: Academic Press, 2019, pp. 79-132.
[137] M. D. Kuz'min and M. Richter, "Magnetic Anisotropy Calculations: Materials of Technological Interest," in *Encyclopedia of Materials: Science and Technology*, K. H. J. Buschow, R. W. Cahn, M. C. Flemings, B. Ilschner, E. J. Kramer, S. Mahajan*, et al.*, Eds., ed Oxford: Elsevier, 2007, pp. 1-7.
[138] B. Cullity, "Introduction to Magnetic Materials, Addison," ed: Wiley, Reading, 1972.
[139] R. C. O'handley, *Modern magnetic materials: principles and applications*: Wiley, 2000.
[140] A. Aharoni, "Introduction to the Theory of Ferromagnetism Oxford University Press," ed: Oxford, 1996.
[141] M. S. S. Brooks, M. Richter, and L. M. Sandratskii, "Density Functional Theory: Magnetism," in *Encyclopedia of Materials: Science and Technology*, K. H. J. Buschow, R. W. Cahn, M. C. Flemings, B. Ilschner, E. J. Kramer, S. Mahajan*, et al.*, Eds., ed Oxford: Elsevier, 2001, pp. 2059-2070.

[142] H. Kirchmayr, "Magnetic Anisotropy," in *Encyclopedia of Materials: Science and Technology*, K. H. J. Buschow, R. W. Cahn, M. C. Flemings, B. Ilschner, E. J. Kramer, S. Mahajan*, et al.*, Eds., ed Oxford: Elsevier, 2001, pp. 4754-4757.
[143] R. M. Bozorth, "Ferromagnetism, Chap. 18," ed: D. Van Nostrand Company Inc., New York, 1951.
[144] D. L. Atherton and J. Beattie, "A mean field Stoner-Wohlfarth hysteresis model," *IEEE transactions on magnetics,* vol. 26, pp. 3059-3063, 1990.
[145] C. Tannous and J. Gieraltowski, "The Stoner–Wohlfarth model of ferromagnetism," *European journal of physics,* vol. 29, p. 475, 2008.
[146] T. Kakeshita, T. Takeuchi, T. Fukuda, M. Tsujiguchi, T. Saburi, R. Oshima*, et al.*, "Giant magnetostriction in an ordered Fe 3 Pt single crystal exhibiting a martensitic transformation," *Applied Physics Letters,* vol. 77, pp. 1502-1504, 2000.
[147] A. Makarov, "Modeling of emerging resistive switching based memory cells," *Institute for Microelectronics, TU Wien, Vienna,* 2014.
[148] J. Bigot, "Mircea., V., Beaurepaire, E., Coherent ultrafast magnetism induced by femtosecond laser pulses," *Nature Phys,* vol. 5, pp. 515-520, 2009.
[149] M. Battiato, K. Carva, and P. M. Oppeneer, "Superdiffusive spin transport as a mechanism of ultrafast demagnetization," *Physical review letters,* vol. 105, p. 027203, 2010.
[150] G. Malinowski, F. Dalla Longa, J. Rietjens, P. Paluskar, R. Huijink, H. Swagten*, et al.*, "Control of speed and efficiency of ultrafast demagnetization by direct transfer of spin angular momentum," *Nature Physics,* vol. 4, pp. 855-858, 2008.
[151] N. Bergeard, M. Hehn, S. Mangin, G. Lengaigne, F. Montaigne, M. Lalieu*, et al.*, "Hot-electron-induced ultrafast demagnetization in Co/Pt multilayers," *Physical review letters,* vol. 117, p. 147203, 2016.
[152] M. S. El Hadri, P. Pirro, C.-H. Lambert, S. Petit-Watelot, Y. Quessab, M. Hehn*, et al.*, "Two types of all-optical magnetization switching mechanisms using femtosecond laser pulses," *Physical review B,* vol. 94, p. 064412, 2016.
[153] J. Kimling, J. Kimling, R. Wilson, B. Hebler, M. Albrecht, and D. G. Cahill, "Ultrafast demagnetization of FePt: Cu thin films and the role of magnetic heat capacity," *Physical Review B,* vol. 90, p. 224408, 2014.
[154] M. Agranat, S. Ashitkov, A. Granovskii, and G. Rukman, "Interaction of picosecond laser pulses with the electron, spin, and phonon subsystems of nickel," *Zh. Eksp. Teor. Fiz,* vol. 86, p. 10, 1984.
[155] J. Hirsch, "Spin hall effect," *Physical review letters,* vol. 83, p. 1834, 1999.
[156] B. Koopmans, J. Ruigrok, F. Dalla Longa, and W. De Jonge, "Unifying ultrafast magnetization dynamics," *Physical review letters,* vol. 95, p. 267207, 2005.
[157] A. Schellekens and B. Koopmans, "Comparing ultrafast demagnetization rates between competing models for finite temperature magnetism," *Physical review letters,* vol. 110, p. 217204, 2013.
[158] A. Quindeau, C. O. Avci, W. Liu, C. Sun, M. Mann, A. S. Tang*, et al.*, "Tm3Fe5O12/Pt heterostructures with perpendicular magnetic anisotropy for spintronic applications," *Advanced Electronic Materials,* vol. 3, 2017.
[159] R. Skomski, H.-P. Oepen, and J. Kirschner, "Unidirectional anisotropy in ultrathin transition-metal films," *Physical Review B,* vol. 58, p. 11138, 1998.
[160] T. Yoshimoto, T. Goto, K. Shimada, B. Iwamoto, Y. Nakamura, H. Uchida*, et al.*, "Static and Dynamic Magnetic Properties of Single-Crystalline Yttrium Iron Garnet Films Epitaxially Grown on Three Garnet Substrates," *Advanced Electronic Materials,* p. 1800106, 2018.
[161] M. Kubota, K. Shibuya, Y. Tokunaga, F. Kagawa, A. Tsukazaki, Y. Tokura*, et al.*, "Systematic control of stress-induced anisotropy in pseudomorphic iron garnet thin films," *Journal of Magnetism and Magnetic Materials,* vol. 339, pp. 63-70, 2013.

[162] P. Dorsey, S. Bushnell, R. Seed, and C. Vittoria, "Epitaxial yttrium iron garnet films grown by pulsed laser deposition," *Journal of Applied Physics,* vol. 74, pp. 1242-1246, 1993.
[163] M. Duan, A. Grishin, K. Rao, and T. Suzuki, "Laser deposited bismuth doped iron garnet films with perpendicular anisotropy," *IEEE transactions on magnetics,* vol. 31, pp. 3245-3246, 1995.
[164] Y. Krockenberger, K.-S. Yun, T. Hatano, S. Arisawa, M. Kawasaki, and Y. Tokura, "Layer-by-layer growth and magnetic properties of Y 3 Fe 5 O 12 thin films on Gd 3 Ga 5 O 12," *Journal of Applied Physics,* vol. 106, p. 123911, 2009.
[165] E. Popova, N. Keller, F. Gendron, L. Thomas, M.-C. Brianso, M. Guyot*, et al.*, "Perpendicular magnetic anisotropy in ultrathin yttrium iron garnet films prepared by pulsed laser deposition technique," *Journal of Vacuum Science & Technology A: Vacuum, Surfaces, and Films,* vol. 19, pp. 2567-2570, 2001.
[166] J. Fu, M. Hua, X. Wen, M. Xue, S. Ding, M. Wang*, et al.*, "Epitaxial growth of Y3Fe5O12 thin films with perpendicular magnetic anisotropy," *Applied Physics Letters,* vol. 110, p. 202403, 2017.
[167] Y. Jie-Hui, M. Sheng-Can, and X. You, "Theoretical analysis of the anisotropy of the magnetization of the Ho3+ ion in holmium iron garnet single crystals," *Chinese Physics B,* vol. 17, p. 710, 2008.
[168] C. Suchomski, C. Reitz, D. Pajic, Z. Jaglicic, I. Djerdj, and T. Brezesinski, "Large-pore mesoporous Ho3Fe5O12 thin films with a strong room-temperature perpendicular magnetic anisotropy by sol–gel processing," *Chemistry of Materials,* vol. 26, pp. 2337-2343, 2014.
[169] S. A. Manuilov and A. M. Grishin, "Pulsed laser deposited Y 3 Fe 5 O 12 films: Nature of magnetic anisotropy II," *Journal of Applied Physics,* vol. 108, p. 013902, 2010.
[170] S. A. Manuilov, S. Khartsev, and A. M. Grishin, "Pulsed laser deposited Y 3 Fe 5 O 12 films: nature of magnetic anisotropy I," *Journal of Applied Physics,* vol. 106, p. 123917, 2009.
[171] S. Geller, H. Williams, R. Sherwood, J. Remeika, and G. Espinosa, "Magnetic study of the lighter rare-earth ions in the iron garnets," *Physical Review,* vol. 131, p. 1080, 1963.
[172] D. Sander, "The correlation between mechanical stress and magnetic anisotropy in ultrathin films," *Reports on Progress in Physics,* vol. 62, p. 809, 1999.
[173] W. H. Von Aulock, *Handbook of microwave ferrite materials*: ProQuest, 1965.
[174] A. Paoletti, *Physics of Magnetic Garnets: Proceedings of the International School of Physics' Enrico Fermi', Course LXX, Varenna on Lake Como, Villa Monastero, 27th June-9th July 1977*: Elsevier Science & Technology, 1978.
[175] C. Tang, "Materials Development and Spin Transport Study of Magnetic Insulator Based Heterostructures," UC Riverside, 2017.
[176] B. Dodrill, J. Lindemuth, and J. Krause, "Magnetic Anisotropy: Measurements with a Vector Vibrating Sample Magnetometer."
[177] D. Huber, "B. Magnetoelastic properties of the iron garnets," in *Part A*, ed: Springer, 1970, pp. 346-348.
[178] E. Popova, N. Keller, F. Gendron, M. Guyot, M.-C. Brianso, Y. Dumond*, et al.*, "Structure and magnetic properties of yttrium–iron–garnet thin films prepared by laser deposition," *Journal of Applied Physics,* vol. 90, pp. 1422-1428, 2001.
[179] A. Quindeau, C. O. Avci, W. Liu, C. Sun, M. Mann, A. S. Tang*, et al.*, "Tm3Fe5O12/Pt heterostructures with perpendicular magnetic anisotropy for spintronic applications," *Advanced Electronic Materials,* vol. 3, p. 1600376, 2017.
[180] L. Soumah, N. Beaulieu, L. Qassym, C. Carrétéro, E. Jacquet, R. Lebourgeois*, et al.*, "Ultra-low damping insulating magnetic thin films get perpendicular," *arXiv preprint arXiv:1806.00658,* 2018.

[181] F. Monzon, D. Patterson, and M. Roukes, "Characterization of individual nanomagnets by the local Hall effect," *Journal of magnetism and magnetic materials,* vol. 195, pp. 19-25, 1999.

[182] J.-H. Park, H. Takagi, K. Nishimura, H. Uchida, M. Inoue, D.-H. Lee*, et al.*, "Magnetic softening of switching field of magnetic garnet films by controlling groove depth," *Journal of applied physics,* vol. 93, pp. 8522-8524, 2003.

[183] J. Chen, F. Heimbach, T. Liu, H. Yu, C. Liu, H. Chang*, et al.*, "Spin wave propagation in perpendicularly magnetized nm-thick yttrium iron garnet films," *Journal of Magnetism and Magnetic Materials,* vol. 450, pp. 3-6, 2018.

[184] W. DA, J. Sato, M. Hosoda, and H. Shimizu, "Preparation and Characterization of Bi substituted gadolinium iron garnet BixGd3-xFe5O12 films with x= 1 to 2.5 by Enhanced Metal Organic Decomposition method," *Journal of the Magnetics Society of Japan,* vol. 40, pp. 107-114, 2016.

[185] I. J. Park, K. U. Kang, and C. S. Kim, "Temperature-dependent magnetic properties of bismuth substituted terbium–iron garnets," *IEEE transactions on magnetics,* vol. 42, pp. 2882-2884, 2006.

[186] H. Guo, S. Dong, P. D. Rack, J. D. Budai, C. Beekman, Z. Gai*, et al.*, "Strain doping: Reversible single-axis control of a complex oxide lattice via helium implantation," *Physical review letters,* vol. 114, p. 256801, 2015.

[187] M. Guillot, A. Marchand, J. Desvignes, H. Le Gall, T. Merceron, and M. Guillaud, "High magnetic field properties of mixed terbium-yttrium ferrite garnets," *Zeitschrift für Physik B Condensed Matter,* vol. 74, pp. 335-339, 1989.

[188] M. Lang, M. Montazeri, M. C. Onbasli, X. Kou, Y. Fan, P. Upadhyaya*, et al.*, "Proximity induced high-temperature magnetic order in topological insulator-ferrimagnetic insulator heterostructure," *Nano letters,* vol. 14, pp. 3459-3465, 2014.

[189] T. Yoshimoto, T. Goto, K. Shimada, B. Iwamoto, Y. Nakamura, H. Uchida*, et al.*, "Static and Dynamic Magnetic Properties of Single-Crystalline Yttrium Iron Garnet Films Epitaxially Grown on Three Garnet Substrates," *Advanced Electronic Materials,* vol. 4, p. 1800106, 2018.

[190] G. Li, H. Bai, J. Su, Z. Zhu, Y. Zhang, and J. Cai, "Tunable perpendicular magnetic anisotropy in epitaxial Y3Fe5O12 films," *APL Materials,* vol. 7, p. 041104, 2019.

[191] C. Wu, C. Tseng, Y. Fanchiang, C. Cheng, K. Lin, S. Yeh*, et al.*, "High-quality thulium iron garnet films with tunable perpendicular magnetic anisotropy by off-axis sputtering–correlation between magnetic properties and film strain," *Scientific reports,* vol. 8, p. 11087, 2018.

[192] T. Goto, M. C. Onbaşlı, and C. A. Ross, "Magneto-optical properties of cerium substituted yttrium iron garnet films with reduced thermal budget for monolithic photonic integrated circuits," *Optics express,* vol. 20, pp. 28507-28517, 2012.

[193] M. C. Hickey and J. S. Moodera, "Origin of intrinsic Gilbert damping," *Physical review letters,* vol. 102, p. 137601, 2009.

[194] E. Baños-López, C. Cortés-Escobedo, F. Sánchez-De Jesús, A. Barba-Pingarrón, and A. Bolarín-Miró, "Crystal structure and magnetic properties of cerium-doped YIG: Effect of doping concentration and annealing temperature," *Journal of Alloys and Compounds,* vol. 730, pp. 127-134, 2018.

[195] G. Lou, T. Kato, S. Iwata, and T. Ishibashi, "Magneto-optical properties and magnetic anisotropy of Nd 0.5 Bi 2.5 Fe 5-y Ga y O 12 thin films on glass substrates," *Optical Materials Express,* vol. 7, pp. 2248-2259, 2017.

[196] M. Nur-E-Alam, M. Vasiliev, V. Kotov, and K. Alameh, "Recent developments in magneto-optic garnet-type thin-film materials synthesis," *Procedia Engineering,* vol. 76, pp. 61-73, 2014.

[197] J. Ostorero and M. Guillot, "High field induced magnetic anisotropy of Al-substituted erbium iron garnet single crystals," *IEEE transactions on magnetics,* vol. 37, pp. 2441-2444, 2001.

[198] C. Wu, C. Tseng, K. Lin, C. Cheng, S. Yeh, Y. Fanchiang, *et al.*, "High-quality single-crystal thulium iron garnet films with perpendicular magnetic anisotropy by off-axis sputtering," *AIP Advances,* vol. 8, p. 055904, 2018.
[199] M. Schreier, T. Chiba, A. Niedermayr, J. Lotze, H. Huebl, S. Geprägs, *et al.*, "Current-induced spin torque resonance of a magnetic insulator," *Physical Review B,* vol. 92, p. 144411, 2015.
[200] A. Hamadeh, O. d. A. Kelly, C. Hahn, H. Meley, R. Bernard, A. Molpeceres, *et al.*, "Full control of the spin-wave damping in a magnetic insulator using spin-orbit torque," *Physical review letters,* vol. 113, p. 197203, 2014.
[201] M. Montazeri, P. Upadhyaya, M. C. Onbasli, G. Yu, K. L. Wong, M. Lang, *et al.*, "Magneto-optical investigation of spin–orbit torques in metallic and insulating magnetic heterostructures," *Nature communications,* vol. 6, pp. 1-9, 2015.
[202] J. Li, G. Yu, C. Tang, Y. Liu, Z. Shi, Y. Liu, *et al.*, "Deficiency of the bulk spin Hall effect model for spin-orbit torques in magnetic-insulator/heavy-metal heterostructures," *Physical Review B,* vol. 95, p. 241305, 2017.
[203] Y. Kajiwara, K. Harii, S. Takahashi, J.-i. Ohe, K. Uchida, M. Mizuguchi, *et al.*, "Transmission of electrical signals by spin-wave interconversion in a magnetic insulator," *Nature,* vol. 464, pp. 262-266, 2010.
[204] T. Yoshimoto, T. Goto, R. Isogai, Y. Nakamura, H. Takagi, C. Ross, *et al.*, "Magnetophotonic crystal with cerium substituted yttrium iron garnet and enhanced Faraday rotation angle," *Optics express,* vol. 24, pp. 8746-8753, 2016.
[205] L. Bi, J. Hu, P. Jiang, D. H. Kim, G. F. Dionne, L. C. Kimerling, *et al.*, "On-chip optical isolation in monolithically integrated non-reciprocal optical resonators," *Nature Photonics,* vol. 5, p. 758, 2011.
[206] M. A. Schoen, D. Thonig, M. L. Schneider, T. Silva, H. T. Nembach, O. Eriksson, *et al.*, "Ultra-low magnetic damping of a metallic ferromagnet," *Nature Physics,* vol. 12, pp. 839-842, 2016.
[207] A. Krysztofik, L. E. Coy, P. Kuświk, K. Załęski, H. Głowiński, and J. Dubowik, "Ultra-low damping in lift-off structured yttrium iron garnet thin films," *Applied Physics Letters,* vol. 111, p. 192404, 2017.
[208] M. Shalaby, F. Vidal, M. Peccianti, R. Morandotti, F. Enderli, T. Feurer, *et al.*, "Terahertz macrospin dynamics in insulating ferrimagnets," *Physical Review B,* vol. 88, p. 140301, 2013.
[209] T. Fischer, M. Kewenig, D. Bozhko, A. Serga, I. Syvorotka, F. Ciubotaru, *et al.*, "Experimental prototype of a spin-wave majority gate," *Applied Physics Letters,* vol. 110, p. 152401, 2017.
[210] T. Bayaraa, C. Xu, D. Campbell, and L. Bellaiche, "Tuning magnetization compensation and Curie temperatures in epitaxial rare earth iron garnet films," *Physical Review B,* vol. 100, p. 214412, 12/12/ 2019.
[211] E. Baños-López, F. Sánchez-De Jesús, C. A. Cortés-Escobedo, A. Barba-Pingarrón, and A. M. Bolarín-Miró, "Enhancement in Curie Temperature of Yttrium Iron Garnet by Doping with Neodymium," *Materials (Basel, Switzerland),* vol. 11, p. 1652, 2018.
[212] M. Collet, X. De Milly, O. d. A. Kelly, V. V. Naletov, R. Bernard, P. Bortolotti, *et al.*, "Generation of coherent spin-wave modes in yttrium iron garnet microdiscs by spin–orbit torque," *Nature communications,* vol. 7, pp. 1-8, 2016.
[213] D. Apalkov, B. Dieny, and J. Slaughter, "Magnetoresistive random access memory," *Proceedings of the IEEE,* vol. 104, pp. 1796-1830, 2016.
[214] W. Jiang, P. Upadhyaya, W. Zhang, G. Yu, M. B. Jungfleisch, F. Y. Fradin, *et al.*, "Blowing magnetic skyrmion bubbles," *Science,* vol. 349, pp. 283-286, 2015.
[215] A. Chumak, A. Serga, M. Jungfleisch, R. Neb, D. Bozhko, V. Tiberkevich, *et al.*, "Direct detection of magnon spin transport by the inverse spin Hall effect," *Applied Physics Letters,* vol. 100, p. 082405, 2012.
[216] V. Castel, N. Vlietstra, J. Ben Youssef, and B. J. van Wees, "Platinum thickness dependence of the inverse spin-Hall voltage from spin pumping in a hybrid

yttrium iron garnet/platinum system," *Applied Physics Letters,* vol. 101, p. 132414, 2012.
[217] K. Ando and E. Saitoh, "Spin pumping driven by bistable exchange spin waves," *Physical review letters,* vol. 109, p. 026602, 2012.
[218] N. Vlietstra, J. Shan, V. Castel, B. Van Wees, and J. B. Youssef, "Spin-Hall magnetoresistance in platinum on yttrium iron garnet: Dependence on platinum thickness and in-plane/out-of-plane magnetization," *Physical Review B,* vol. 87, p. 184421, 2013.
[219] J. Han, A. Richardella, S. A. Siddiqui, J. Finley, N. Samarth, and L. Liu, "Room-Temperature Spin-Orbit Torque Switching Induced by a Topological Insulator," *Physical Review Letters,* vol. 119, p. 077702, 08/18/ 2017.
[220] C. Jermain, H. Paik, S. Aradhya, R. Buhrman, D. Schlom, and D. Ralph, "Low-damping sub-10-nm thin films of lutetium iron garnet grown by molecular-beam epitaxy," *Applied Physics Letters,* vol. 109, p. 192408, 2016.
[221] H. Chang, P. Li, W. Zhang, T. Liu, A. Hoffmann, L. Deng*, et al.*, "Nanometer-thick yttrium iron garnet films with extremely low damping," *IEEE Magnetics Letters,* vol. 5, pp. 1-4, 2014.
[222] S. Geller, J. Remeika, R. Sherwood, H. Williams, and G. Espinosa, "Magnetic study of the heavier rare-earth iron garnets," *Physical Review,* vol. 137, p. A1034, 1965.
[223] R. Pearson, "Magnetocrystalline anisotropy of rare-earth iron garnets," in *Proceedings of the Seventh Conference on Magnetism and Magnetic Materials*, 1962, pp. 1236-1242.
[224] J. Bauer, E. Rosenberg, and C. Ross, "Perpendicular magnetic anisotropy and spin mixing conductance in polycrystalline europium iron garnet thin films," *Applied Physics Letters,* vol. 114, p. 052403, 2019.
[225] T. Fakhrul, S. Tazlaru, L. Beran, Y. Zhang, M. Veis, and C. A. Ross, "Magneto-optical Bi: YIG films with high figure of merit for nonreciprocal photonics," *Advanced Optical Materials,* vol. 7, p. 1900056, 2019.
[226] E. Beaurepaire, G. Turner, S. Harrel, M. Beard, J.-Y. Bigot, and C. Schmuttenmaer, "Coherent terahertz emission from ferromagnetic films excited by femtosecond laser pulses," *Applied Physics Letters,* vol. 84, pp. 3465-3467, 2004.
[227] T. Roth, A. Schellekens, S. Alebrand, O. Schmitt, D. Steil, B. Koopmans*, et al.*, "Temperature dependence of laser-induced demagnetization in Ni: A key for identifying the underlying mechanism," *Physical Review X,* vol. 2, p. 021006, 2012.
[228] C. Stanciu, F. Hansteen, A. Kimel, A. Kirilyuk, A. Tsukamoto, A. Itoh*, et al.*, "All-optical magnetic recording with circularly polarized light," *Physical review letters,* vol. 99, p. 047601, 2007.
[229] T. S. Seifert, S. Jaiswal, J. Barker, S. T. Weber, I. Razdolski, J. Cramer*, et al.*, "Femtosecond formation dynamics of the spin Seebeck effect revealed by terahertz spectroscopy," *Nature communications,* vol. 9, p. 2899, 2018.
[230] S. Zhang, Z. Jin, X. Liu, W. Zhao, X. Lin, C. Jing*, et al.*, "Photoinduced terahertz radiation and negative conductivity dynamics in Heusler alloy Co 2 MnSn film," *Optics letters,* vol. 42, pp. 3080-3083, 2017.
[231] T. Huisman, R. Mikhaylovskiy, J. Costa, F. Freimuth, E. Paz, J. Ventura*, et al.*, "Femtosecond control of electric currents in metallic ferromagnetic heterostructures," *Nature nanotechnology,* vol. 11, p. 455, 2016.
[232] R. Moreno, T. Ostler, R. Chantrell, and O. Chubykalo-Fesenko, "Conditions for thermally induced all-optical switching in ferrimagnetic alloys: Modeling of TbCo," *Physical Review B,* vol. 96, p. 014409, 2017.
[233] M. Ellis and R. Chantrell, "Switching times of nanoscale FePt: Finite size effects on the linear reversal mechanism," *Applied Physics Letters,* vol. 106, p. 162407, 2015.

[234] Y.-J. Lin, S. Cakmakyapan, N. Wang, D. Lee, M. Spearrin, and M. Jarrahi, "Plasmonic heterodyne spectrometry for resolving the spectral signatures of ammonia over a 1-4.5 THz frequency range," *Optics Express,* vol. 27, pp. 36838-36845, 2019.

[235] X. Chen, X. Wu, S. Shan, F. Guo, D. Kong, C. Wang*, et al.*, "Generation and manipulation of chiral broadband terahertz waves from cascade spintronic terahertz emitters," *Applied Physics Letters,* vol. 115, p. 221104, 2019.

[236] Y. Yang, Y. Yamagami, X. Yu, P. Pitchappa, B. Zhang, M. Fujita*, et al.*, "Terahertz topological photonics for on-chip communication," *arXiv preprint arXiv:1904.04213,* 2019.

[237] J. A. Fülöp, S. Tzortzakis, and T. Kampfrath, "Laser-Driven Strong-Field Terahertz Sources," *Advanced Optical Materials,* vol. 8, p. 1900681, 2020.

[238] B. Fischer, M. Walther, and P. U. Jepsen, "Far-infrared vibrational modes of DNA components studied by terahertz time-domain spectroscopy," *Physics in Medicine & Biology,* vol. 47, p. 3807, 2002.

[239] K. M. Mølster, T. Sørgård, H. Laurell, C. Canalias, V. Pasiskevicius, F. Laurell*, et al.*, "Time-domain spectroscopy of KTiOPO 4 in the frequency range 0.6–7.0 THz," *OSA Continuum,* vol. 2, pp. 3521-3538, 2019.

[240] P. Upadhya, Y. Shen, A. Davies, and E. Linfield, "Terahertz time-domain spectroscopy of glucose and uric acid," *Journal of Biological Physics,* vol. 29, pp. 117-121, 2003.

[241] M. Walther, B. M. Fischer, A. Ortner, A. Bitzer, A. Thoman, and H. Helm, "Chemical sensing and imaging with pulsed terahertz radiation," *Analytical and bioanalytical chemistry,* vol. 397, pp. 1009-1017, 2010.

[242] Z.-P. Zheng, W.-H. Fan, and H. Yan, "Terahertz absorption spectra of benzene-1, 2-diol, benzene-1, 3-diol and benzene-1, 4-diol," *Chemical Physics Letters,* vol. 525, pp. 140-143, 2012.

[243] M. Leahy-Hoppa, M. Fitch, X. Zheng, L. Hayden, and R. Osiander, "Wideband terahertz spectroscopy of explosives," *Chemical Physics Letters,* vol. 434, pp. 227-230, 2007.

[244] H. Qiu, K. Kato, K. Hirota, N. Sarukura, M. Yoshimura, and M. Nakajima, "Layer thickness dependence of the terahertz emission based on spin current in ferromagnetic heterostructures," *Optics express,* vol. 26, pp. 15247-15254, 2018.

[245] D. Yang, J. Liang, C. Zhou, L. Sun, R. Zheng, S. Luo*, et al.*, "Powerful and tunable THz emitters based on the Fe/Pt magnetic heterostructure," *Advanced Optical Materials,* vol. 4, pp. 1944-1949, 2016.

[246] U. Atxitia, D. Hinzke, and U. Nowak, "Fundamentals and applications of the Landau–Lifshitz–Bloch equation," *Journal of Physics D: Applied Physics,* vol. 50, p. 033003, 2016.

[247] Z. Lin, L. V. Zhigilei, and V. Celli, "Electron-phonon coupling and electron heat capacity of metals under conditions of strong electron-phonon nonequilibrium," *Physical Review B,* vol. 77, p. 075133, 2008.

[248] K. Bühlmann, R. Gort, G. Salvatella, S. Däster, A. Fognini, T. Bähler*, et al.*, "Ultrafast demagnetization in iron: Separating effects by their nonlinearity," *Structural Dynamics,* vol. 5, p. 044502, 2018.

[249] B. Y. Mueller, T. Roth, M. Cinchetti, M. Aeschlimann, and B. Rethfeld, "Driving force of ultrafast magnetization dynamics," *New Journal of Physics,* vol. 13, p. 123010, 2011.

[250] D. Steil, J. Walowski, F. Gerhard, T. Kiessling, D. Ebke, A. Thomas*, et al.*, "Efficiency of ultrafast optically induced spin transfer in Heusler compounds," *Physical Review Research,* vol. 2, p. 023199, 2020.

[251] S. Sapra, D. Sarma, S. Sanvito, and N. A. Hill, "Influence of quantum confinement on the electronic and magnetic properties of (Ga, Mn) As diluted magnetic semiconductor," *Nano Letters,* vol. 2, pp. 605-608, 2002.

[252] M. Atatüre, D. Englund, N. Vamivakas, S.-Y. Lee, and J. Wrachtrup, "Material platforms for spin-based photonic quantum technologies," *Nature Reviews Materials,* vol. 3, pp. 38-51, 2018.
[253] S. M. Zanjani and M. C. Onbaşlı, "Effect of Laser Pulse Fluence, Waveform and Film Thickness on Ultrafast Magnetization Dynamics in Nickel," in *The 22nd International Conference on Ultrafast Phenomena 2020*, Washington, D.C., 2020, p. M4A.31.
[254] S. M. Zanjani and M. C. Onbaşlı, "Ultrafast All Optical Magnetization Control for Broadband Terahertz Spin Wave Generation," *arXiv preprint arXiv:2005.03493,* 2020.
[255] P. B. Allen, "Theory of thermal relaxation of electrons in metals," *Physical review letters,* vol. 59, p. 1460, 1987.
[256] J. Rogers III, P. Cutler, T. Feuchtwang, and A. Lucas, "Quantum size effects in the fermi energy and electronic density of states in a finite square well thin film model," *Surface Science,* vol. 181, pp. 436-456, 1987.
[257] W. Atkinson and A. Slavin, "A free-electron calculation for quantum size effects in the properties of metallic islands on surfaces," *American Journal of Physics,* vol. 76, pp. 1099-1101, 2008.
[258] Z. Du, C. Chen, F. Cheng, Y. Liu, and L. Pan, "Prediction of deterministic all-optical switching of ferromagnetic thin film by ultrafast optothermal and optomagnetic couplings," *Scientific reports,* vol. 7, pp. 1-11, 2017.
[259] T. Qiu and C. Tien, "Heat transfer mechanisms during short-pulse laser heating of metals," 1993.
[260] L. Avilés-Félix, A. Olivier, G. Li, C. Davies, L. Álvaro-Gómez, M. Rubio-Roy*, et al.*, "Single-shot all-optical switching of magnetization in Tb/Co multilayer-based electrodes," *Scientific reports,* vol. 10, pp. 1-8, 2020.
[261] C. Davies, T. Janssen, J. Mentink, A. Tsukamoto, A. Kimel, A. van der Meer*, et al.*, "Pathways for Single-Shot All-Optical Switching of Magnetization in Ferrimagnets," *Physical Review Applied,* vol. 13, p. 024064, 2020.
[262] A. Kirilyuk, A. V. Kimel, and T. Rasing, "Ultrafast optical manipulation of magnetic order," *Reviews of Modern Physics,* vol. 82, p. 2731, 2010.
[263] H. Y. Hwang, Y. Iwasa, M. Kawasaki, B. Keimer, N. Nagaosa, and Y. Tokura, "Emergent phenomena at oxide interfaces," *Nature materials,* vol. 11, pp. 103-113, 2012.
[264] M. Claassen, C. Jia, B. Moritz, and T. P. Devereaux, "All-optical materials design of chiral edge modes in transition-metal dichalcogenides," *Nature communications,* vol. 7, pp. 1-8, 2016.
[265] D. Xiao, G.-B. Liu, W. Feng, X. Xu, and W. Yao, "Coupled spin and valley physics in monolayers of MoS 2 and other group-VI dichalcogenides," *Physical review letters,* vol. 108, p. 196802, 2012.
[266] W. Feng, Y. Yao, W. Zhu, J. Zhou, W. Yao, and D. Xiao, "Intrinsic spin Hall effect in monolayers of group-VI dichalcogenides: A first-principles study," *Physical Review B,* vol. 86, p. 165108, 2012.
[267] M. Kaganov, E. Lifshitz, and L. Tanatarov, "Relaxation between electrons and the crystalline lattice," *Soviet Physics-JETP,* vol. 4, pp. 173-178, 1957.
[268] G. Grimvall, "The electron-phonon interaction in metals," 1981.
[269] W. McMillan, "Transition temperature of strong-coupled superconductors," *Physical Review,* vol. 167, p. 331, 1968.
[270] N. W. Ashcroft and N. D. Mermin, "Solid state physics [by] Neil W. Ashcroft [and] N. David Mermin," ed: New York: Holt, Rinehart and Winston, 1976.
[271] S. Anisimov, B. Kapeliovich, and T. Perelman, "Electron emission from metal surfaces exposed to ultrashort laser pulses," *Zh. Eksp. Teor. Fiz,* vol. 66, pp. 375-377, 1974.

[272] J. Chen, D. Tzou, and J. Beraun, "A semiclassical two-temperature model for ultrafast laser heating," *International journal of heat and mass transfer,* vol. 49, pp. 307-316, 2006.
[273] J. Chen and J. Beraun, "Numerical study of ultrashort laser pulse interactions with metal films," *Numerical Heat Transfer: Part A: Applications,* vol. 40, pp. 1-20, 2001.
[274] S. Pan, O. Hellwig, and A. Barman, "Controlled coexcitation of direct and indirect ultrafast demagnetization in Co/Pd multilayers with large perpendicular magnetic anisotropy," *Physical Review B,* vol. 98, p. 214436, 2018.
[275] R. D. Mountain and R. A. MacDonald, "Thermal conductivity of crystals: A molecular-dynamics study of heat flow in a two-dimensional crystal," *Physical Review B,* vol. 28, p. 3022, 1983.
[276] L. Yao, S. Qing-Lin, and X. Shan-Hong, "Calculation of specific heat for aluminium thin films," *Chinese Physics Letters,* vol. 22, p. 2346, 2005.
[277] M. C. Tringides, M. Jalochowski, and E. Bauer, "Quantum size effects in metallic nanostructures," *Physics Today,* vol. 60, p. 50, 2007.
[278] N. Binggeli and M. Altarelli, "Surface reactivity and quantum-size effects on the electronic density decay length of ultrathin metal films," *Physical review letters,* vol. 96, p. 036805, 2006.
[279] R. Otero, A. L. V. de Parga, and R. Miranda, "Observation of preferred heights in Pb nanoislands: A quantum size effect," *Physical Review B,* vol. 66, p. 115401, 2002.
[280] M. Bouhassoune, B. Zimmermann, P. Mavropoulos, D. Wortmann, P. H. Dederichs, S. Blügel*, et al.*, "Quantum well states and amplified spin-dependent Friedel oscillations in thin films," *Nature communications,* vol. 5, pp. 1-6, 2014.
[281] E. Ogando, N. Zabala, E. V. Chulkov, and M. J. Puska, "Quantum size effects in Pb islands on Cu (111): Electronic structure calculations," *Physical Review B,* vol. 69, p. 153410, 2004.
[282] A. Shanenko, M. Croitoru, and F. Peeters, "Oscillations of the superconducting temperature induced by quantum well states in thin metallic films: Numerical solution of the Bogoliubov–de Gennes equations," *Physical Review B,* vol. 75, p. 014519, 2007.
[283] R. Bi, Z. Feng, X. Li, J. Zhao, J. Fan, Y. Shi*, et al.*, "Quantum oscillations of thermopower in WTe 2 thin films," *Physical Review B,* vol. 100, p. 235405, 2019.
[284] T. Späth, M. Popp, C. P. León, M. Marz, and R. Hoffmann-Vogel, "Near-equilibrium measurement of quantum size effects using Kelvin probe force microscopy," *Nanoscale,* vol. 9, pp. 7868-7874, 2017.
[285] P. Cheng, C. Zhang, Y. Liu, X. Yuan, F. Song, Q. Sun*, et al.*, "Thickness-dependent quantum oscillations in Cd3As2 thin films," *New Journal of Physics,* vol. 18, p. 083003, 2016.
[286] B. Sun, P. Zhang, S. Duan, X.-G. Zhao, J. Shi, and Q.-K. Xue, "First-principles calculations of Cu (001) thin films: quantum size effect in surface energetics and surface chemical reactivities," *arXiv preprint cond-mat/0701294,* 2007.
[287] Y. Xu, M. Hehn, W. Zhao, X. Lin, G. Malinowski, and S. Mangin, "From single to multiple pulse all-optical switching in GdFeCo thin films," *Physical Review B,* vol. 100, p. 064424, 2019.
[288] R. Mikhaylovskiy, T. Huisman, V. Gavrichkov, S. Polukeev, S. Ovchinnikov, D. Afanasiev*, et al.*, "Resonant Pumping of d– d Crystal Field Electronic Transitions as a Mechanism of Ultrafast Optical Control of the Exchange Interactions in Iron Oxides," *Physical review letters,* vol. 125, p. 157201, 2020.
[289] Q. Remy, J. Igarashi, S. Iihama, G. Malinowski, M. Hehn, J. Gorchon*, et al.*, "Energy Efficient Control of Ultrafast Spin Current to Induce Single Femtosecond Pulse Switching of a Ferromagnet," *Advanced Science,* p. 2001996, 2020.
[290] E. Beaurepaire, J.-C. Merle, A. Daunois, and J.-Y. Bigot, "Ultrafast spin dynamics in ferromagnetic nickel," *Physical review letters,* vol. 76, p. 4250, 1996.

[291] Q. Shao, P. Li, L. Liu, H. Yang, S. Fukami, A. Razavi*, et al.*, "Roadmap of spin-orbit torques," *IEEE Transactions on Magnetics,* 2021.

[292] A. Stupakiewicz, K. Szerenos, M. D. Davydova, K. A. Zvezdin, A. K. Zvezdin, A. Kirilyuk*, et al.*, "Selection rules for all-optical magnetic recording in iron garnet," *Nature Communications,* vol. 10, p. 612, 2019/02/05 2019.

[293] Q. Shao, Y. Liu, G. Yu, S. K. Kim, X. Che, C. Tang*, et al.*, "Topological Hall effect at above room temperature in heterostructures composed of a magnetic insulator and a heavy metal," *Nature Electronics,* vol. 2, pp. 182-186, 2019/05/01 2019.

[294] C. Tang, *Materials Development and Spin Transport Study of Magnetic Insulator Based Heterostructures*: University of California, Riverside, 2017.

[295] V. H. Ortiz, M. Aldosary, J. Li, Y. Liu, P. Sellappan, C. Warren*, et al.*, "Strain induced perpendicular magnetic anisotropy in epitaxial europium iron garnet thin films," *Bulletin of the American Physical Society,* 2018.

[296] B. Schulz and K. Baberschke, "Crossover from in-plane to perpendicular magnetization in ultrathin Ni/Cu (001) films," *Physical Review B,* vol. 50, p. 13467, 1994.

[297] U. Parlak, M. Akoz, S. Tokdemir Ozturk, and M. Erkovan, "Thickness dependent magnetic properties of polycrystalline nickel thin films," *Acta Physica Polonica A,* vol. 127, pp. 995-997, 2015.

[298] M. A. Corrêa and F. Bohn, "Manipulating the magnetic anisotropy and magnetization dynamics by stress: Numerical calculation and experiment," *Journal of Magnetism and Magnetic Materials,* vol. 453, pp. 30-35, 2018.

[299] M. d'Aquino, "Nonlinear magnetization dynamics in thin-films and nanoparticles," *http://wpage. unina. it/mdaquino/PhD_thesis/main/main. html,* 2004.

[300] C. Giuffrida, C. Ragusa, and M. Repetto, "Magnetization dynamics in metallic thin films by finite formulation," *Journal of magnetism and magnetic materials,* vol. 290, pp. 475-478, 2005.

[301] G. Malinowski, K. Kuiper, R. Lavrijsen, H. Swagten, and B. Koopmans, "Magnetization dynamics and Gilbert damping in ultrathin Co 48 Fe 32 B 20 films with out-of-plane anisotropy," *Applied Physics Letters,* vol. 94, p. 102501, 2009.